Kinetic, Spectroscopic, and Computational Insight into the Proton-Coupled Electron Transfer Reactivity of Manganese Complexes Supported by Pentadentate Ligands

By

Derek B. Rice

Submitted to the graduate degree program in Chemistry and the Graduate Faculty of the University of Kansas in partial fulfillment of the requirements for the degree of Doctor of Philosophy

Chairperson: Dr. Timothy A. Jackson

Dr. Mikhail V. Barybin

Dr. James D. Blakemore

Dr. Ward H. Thompson

Dr. Alan M. Allgeier

Date Defended: October 25, 2018

The Dissertation Committee for Derek B. Rice

certifies that this is the approved version of the following dissertation:

Kinetic, Spectroscopic, and Computational Insight into the Proton-Coupled Electron Transfer Reactivity of Manganese Complexes Supported by Pentadentate Ligands

_____

Chairperson: Dr. Timothy A. Jackson

Date Approved: November 27, 2018

Abstract

In biological systems, manganese enzymes have been shown to perform vital proton-coupled electron transfer (PCET) reactions. In manganese lipoxygenase, a mid-valent Mn^{III}–hydroxo moiety is proposed to abstract a hydrogen atom from poly-unsaturated fatty acids to initiate substrate peroxidation. In the oxygen evolving complex (OEC) of photosystem II (PSII), a Mn_4Ca cluster performs water oxidation involving the abstraction of 4 protons and 4 electrons and the formation of dioxygen. Reactivity of the OEC has been shown to shut down upon the removal of the Ca^{2+}. However, the exact role of the Ca^{2+} is not well understood. Understanding how these enzymes achieve their reactivity is of ongoing interest, and relevant model complexes can be used to probe how changing the electronic structure can modulate reactivity. However, the number of Mn^{III}–OH complexes capable of performing PCET are scarce, with only $[Mn^{III}(OH)(PY5)]^{2+}$, $[Mn^{III}(OH)(S^{Me2}N_4(tren))]^{+}$, and $[Mn^{III}(OH)(dpaq)]^{+}$ previously reported. These complexes have a wide range of reported PCET rates, but due to the significant variation in ligand design it can be difficult to identify the exact structure-function relationship.

To address this, a more systematic approach to complex variability was utilized through modification of the $[Mn^{III}(OH)(dpaq)]^{+}$ complex. The first of such complexes, $[Mn^{III}(OH)(dpaq^{2Me})](OTf)$, which contains a methyl group at the 2-position of the quinoline, was synthesized. The goal of this complex was to provide steric bulk near the reaction center. With the substrate TEMPOH, $[Mn^{III}(OH)(dpaq^{2Me})]^{+}$ was shown to react at rates more than two orders of magnitude faster than the unsubstituted complex. The methyl-substitution near the reaction center of the 2Me derivative was shown to increase reactivity with small substrates by increasing the reduction center of the manganese center. However, the $[Mn^{III}(OH)(dpaq^{2Me})]^{+}$ was shown to react with the C–H bonds of xanthene at rates similar to the initial complex. This damping of reaction

rate was determined to be due to steric interactions of the methyl substitution, which hindered reactivity with bulkier substrates.

X-ray absorption spectroscopy (XAS) experiments were then performed on the solid and frozen solution samples of both $[Mn^{III}(OH)(dpaq^{R})]^{+}$ (R = H, 2Me) complexes and their Mn^{II} precursor to gain insight into structural and electronic properties. An interesting result was observed, where $[Mn^{III}(OH)(dpaq)]^{+}$ showed evidence of a dimeric species in acetonitrile (MeCN), but the expected monomeric species in H_2O. This result differed from that of the $[Mn^{III}(OH)(dpaq^{2Me})]^{+}$ complex, which showed only the monomeric species in MeCN. The relevance of these results was initially uncertain, as the XAS experiments were performed at cryogenic temperatures (ca. 10 K), while all kinetic experiments were performed above 238 K. To address this, ^{1}H NMR experiments were performed on the $[Mn^{III}(OH)(dpaq)]^{+}$, and revealed the presence of a mixture of a paramagnetic species, as expected, as well as an antiferromagnetically coupled species as determined by temperature dependent ^{1}H NMR. Combining XAS, density functional theory (DFT), and the ^{1}H NMR results, it was determined that this species was a $[Mn^{III}Mn^{III}(\mu\text{–}O)(dpaq)_2]^{2+}$ dimer that existed in equilibrium with the $[Mn^{III}(OH)(dpaq)]^{+}$ monomer. Meanwhile, the $[Mn^{III}(OH)(dpaq^{2Me})]^{+}$ showed no mixture of species in solution, due to the steric bulk of the methyl group disfavoring the formation of such a dimer. Through the addition of a small amount of H_2O to $[Mn^{III}(OH)(dpaq)]^{+}$ in MeCN, the equilibrium could be shifted to favor the monomer in solution, and the kinetics with TEMPOH were reevaluated. The rates obtained for the $[Mn^{III}(OH)(dpaq)]^{+}$ were now two orders of magnitude faster, and nearly as fast as $[Mn^{III}(OH)(dpaq^{2Me})]^{+}$. These studies demonstrated potential hurdles with Mn^{III}–OH model complexes, where their proclivity to form an oxo-bridged $Mn^{III}Mn^{III}$ dimer in non-hydroxylic solvents could complicate kinetic and spectroscopic results.

With the reactivity difference between the two complexes reconciled, additional modifications could be made to the ligand in order to test other effects. The next series of complexes synthesized were $[Mn^{III}(OH)(dpaq^{R})]^{+}$ (R = 5OMe, 5Cl, $5NO_2$), where electron donating and withdrawing groups were appended away from the reactive site. Crystal structures were obtained of the $[Mn^{III}Mn^{III}(\mu\text{–}O)(dpaq^{R})_2]^{2+}$ dimers, confirming the results from the above spectroscopic studies. Kinetic studies were performed with the derivatives in the presence of H_2O, and these complexes showed only a modest variation in reactivity with the fastest (R = $5NO_2$) being only 9 times faster than the slowest (R = 5OMe). It was shown with DFT calculations that the substitutions of electron withdrawing groups create a more favorable electron transfer, but disfavors proton transfer. Overall the electron withdrawing group created a more potent PCET oxidant, but the results were somewhat dampened by the increased acidity and minor modulation of reduction potential.

With the small variance in reactivity by the ligand modifications, a different approach was used where $[Mn^{III}(OH)(dpaq)]^{+}$ was modified by the addition of $Sc(OTf)_3$. In the presence of $Sc(OTf)_3$, a new intermediate is formed that is able to abstract hydrogen atoms from substrates with moderately strong C–H bonds such as ethylbenzene. This shows significant enhancement over reactivity of the complex in the absence of $Sc(OTf)_3$, and is approaching the reactivity of the more reactive Mn^{IV}–oxo complexes. Spectroscopic techniques identify the intermediate as a Mn^{III} complex that is similar in structure to $[Mn^{III}(OH)(dpaq)]^{+}$, but the exact mode of interaction between scandium and the manganese complex are still under investigation.

Despite the synthetic efforts so far, Mn^{III}–OH complexes cannot access PCET reactivity of the stronger C–H bonds of substrates such as cyclohexane. Mn^{IV}–oxo complexes, however are often proposed as intermediates in catalytic C-H bond activation reactions. Synthetic Mn^{IV}–O complexes

with varying ligand structures have shown a wide range of reactivity, with some complexes reacting only with very weak C-H bonds, while others are capable of abstracting strong C-H bonds from substrates such as cyclohexane. The understanding for this variability in reactivity is currently lacking. Previous studies from Nam and Shaik utilizing DFT have proposed the involvement of an excited state to explain the rapid reactivity of complexes such as $[Mn^{IV}(O)(N4py)]^{2+}$. To further evaluate this computationally, DFT calculations along with a multireference method, complete active-space self-consistent field (CASSCF) followed by N-electron valence perturbation theory to the second order (NEVPT2) are performed on $[Mn^{IV}(O)(N4py)]^{2+}$ with a substrate with experimental activation parameters. The nature of the multistate reactivity is evaluated, and the energetics are compared with the experimental values.

Acknowledgements

I would like to thank Tim Jackson for providing a wonderful learning environment throughout my graduate career. I was lucky enough to have you teach my introductory inorganic and the spectroscopic methods, where I learned a great deal from you. I believe during a lecture one day you said that you viewed electronic structure and d-orbital splitting with a "pure love". That view came through with the way you taught the classes and approached research, and really resonated with me. I have greatly appreciated the opportunities I've been given in the group to explore and learn about a wide range of techniques and topics.

I would also like to thank all of my committee members. To Misha Barybin, I always appreciate the questions that you ask as well as the help and ideas you've given. To Ward Thompson, I really enjoyed having you teach my intro quantum and statistical thermodynamics courses. You also have been great at giving ideas for improving the calculations I've presented which I greatly appreciate. To James Blakemore, I've always appreciated your enthusiasm for science. To Alan Allgeier, I thank you for being on another defense committee for our group despite being on one so recently. I appreciate all the time you all have given to me.

I would like to thank Justin Douglas for all the help with NMR, especially sitting with me while we figured out how to get the relaxation times for the manganese complexes and the variable temperature NMR.

My great experience in the Jackson group has been due in no small part to my fellow members, past and present. Domenick, though we only overlapped for one semester in the group, our conversations during grading Chem. 150 exams helped convince me to look more into the group, and for that I am grateful. Gayan, you were my mentor in lab and the originator of the dpaq work in our group. I learned a lot of synthetic and kinetic techniques from you and am glad that I

could witness your reign (rain) of terror. Hannah, on the XAS trips we had a lot of good times (pastrami place, Palo Alto in general) and terrible times (the murder hotel). I'm glad we got to share those. Josh, thank for all the conversations about chemistry and music, many times beginning on campus and continuing later while drinking a beer elsewhere. Melissa, you have been a great office-mate and I was very lucky to have you around so that I could bother both you and Josh about anything synthetic related. Sorry I will not stick around to take over ordering for you. Yuri you have also been a great office-mate and source of amusing conversation ("Derek, may I ask a cultural question?"). Melissa and Yuri, you both spoiled me with too many snacks as well. I'm not sure if I'm thankful for that or not. To Jaycee and Liz, I wish you the best of luck in the future. I have also been lucky to mentor many wonderful undergraduate students. Andrew, Anthony, Anna, Shannon, and Travis, you have all helped me learn more about myself as an instructor, and for that I am very grateful. I wish you all the best of luck.

To Nate and Tal, it only feels appropriate to group you two together. I appreciate you letting me stay with you guys during my last bit of time here. I also appreciate all the conversations we've had about chemistry, electronic structure calculations, and many other topics.

To my family, you have always been a wonderful, supportive force in my life. I can always count on you to be there for me. I know you always believe in me and what I can do and push me to be the best I can. I am very grateful for all the work you've put into raising me.

Finally, to Allyssa, I of course must thank you. You have been there for me throughout the entirety of grad school. You helped me when things aren't going well. You always listen when I ramble on about chemistry or other topics. But also, there are all the wonderful experiences we've gotten to and will get to share. I'm excited to see what comes next.

Table of Contents

Abbreviations and Acronyms

Abs	absorption
BDE	bond dissociation enthalpy
BDFE	bond dissociation free energy
CPET	concerted proton electron transfer
CV	cyclic voltammetry
DFT	density functional theory
DHA	9,10-dihydroanthracene
EPR	electron paramagnetic resonance
ET	electron transfer
CASSCF	complete active space self-consistent field
COSMO	conductor-like screening model
CV	cyclic voltammetry
EPR	electron paramagnetic resonance
ESI-MS	electrospray ionization mass spectrometry
EXAFS	extended X-ray absorption fine structure
HAT	hydrogen atom transfer
KIE	kinetic isotope effect
MCD	magnetic circular dichroism
MeCN	acetonitrile
MnLOX	manganese lipoxygenase
MO	molecular orbital
NEVPT2	N-electron valence state perturbation theory to the second order
NMR	nuclear magnetic resonance
OEC	oxygen evolving complex
PCET	proton-coupled electron transfer
PSII	photosystem II
PT	proton transfer
SSRL	Stanford Synchrotron Radiation Lightsource
TD-DFT	time dependent density functional theory
TEMPOH	2,2'-6,6'-tetramethylpiperidine-1-ol
UV	ultraviolet
XANES	X-ray absorption near-edge structure
XAS	X-ray absorption
XRD	X-ray diffraction

Chapter 1

Proton-Coupled Electron Transfer in Manganese Complexes

Adapted with permission from Rice, D. B.; Massie, A. A.; Jackson, T. A. Manganese-Oxygen Intermediates in O-O Bond Activation and Hydrogen-Atom Transfer Reactions. *Acc Chem Res* **2017**, *50*, 2706-2717.

1.1 Introduction

The transfer of a hydrogen atom, a proton and an electron, is a seemingly simple process that is of great importance to both chemistry and biology.[1-25] The transfer of a proton and electron in some coupled way is generally termed proton-coupled electron transfer (PCET). The traditional understanding of PCET comes from the reactivity of p-block radicals with other organic molecules. These reactions proceed in a single kinetic step where the proton and electron are transferred to the radical via a hydrogen atom transfer (HAT) mechanism. It was later realized that many transition metal reactions in enzymes and complexes also perform hydrogen atom abstraction via PCET. In these reactions, the electron is most commonly transferred to the metal center and the proton to a basic ligand bound to the metal. In nature, enzymes utilize this coupled process to avoid unstable intermediates and prevent the buildup of charge in the active sites.

First-row transition metals play an important role in these enzymatic PCET reactions and this reactivity has been of great interest. This interest is due not only to the desire to understand how the enzymes function, but also to further apply this understanding in the generation of catalysts that can perform industrially relevant reactions at more environmentally and economically friendly conditions (closer to standard temperature and pressure). Iron oxidants have formed a large portion of these studies, due both to their prevalence in nature as well as relative ease of spectroscopic characterization.[17, 19, 26-28] The PCET reactivity of manganese complexes has been the subject of fewer studies[29-35] but is a vital metal in manganese dependent enzymes such as manganese lipoxygenase (MnLOX)[36-39] and photosystem II (PSII)[40]. The work presented here focuses on the electronic structure of manganese complexes that are competent PCET oxidants. The role of the ligand in reactivity is evaluated via kinetic, spectroscopic and theoretical methods.

1.2 Proton Coupled Electron Transfer Reactivity

PCET reactions involve the transfer of a proton and an electron in one or multiple kinetic steps. The possible pathways for such a reaction are outlined in Scheme 1.1. The horizontal lines in the scheme indicate a proton transfer from the donor (D) to the acceptor (A) and the vertical lines indicate an electron transfer from the donor to the acceptor. In this scheme the proton and electron are coming from the same donor and ending at the same acceptor, though this need not always be the case. The diagonal line shows the concerted process specified as either hydrogen atom transfer (HAT) or concerted proton-electron transfer (CPET), which are just two of the many acronyms given for the single-step transfer. [21-22, 24, 41] The advantage for such a concerted process can be made based on thermodynamic arguments, where the intermediates formed after the transfer of either a proton or an electron would be too high in energy, often higher than the activation energy as determined from temperature dependent kinetics.[41] In such cases, the reaction must proceed through a concerted process in order to avoid these unstable intermediates.

Scheme 1.1. The four diabatic states in PCET and the possible pathways to get from reactants (top left) to products (bottom right). The sides represent the stepwise pathway while the diagonal represents the concerted pathway. The schematic here depicts a single-site donor-acceptor reaction.

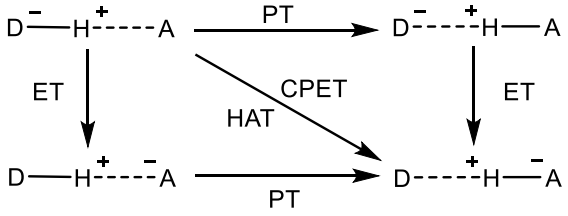

The kinetics of PCET reactions have been described using a Marcus-like relationship, where the reaction can be thought of as two intersecting parabolas in the diabatic regime.[21-22, 24, 41] Unlike Marcus theory, where the curves are associated with the electronic states, these curves are associated with the proton-electron states. On the blue curve, the proton and electron are localized on the

donor molecule. As there is collective inner and outer-sphere reorganization, the molecules approach the curve crossing and the proton and electron become localized on both donor and acceptor. PCET reactions can often display significant electronic coupling between the states near the crossing point. This mixing of states creates an avoided crossing which is depicted by the dashed lines above and below the intersection. In the classical particle view of the proton, this transition state region manifests as a structure with the proton some distance partially between the donor and acceptor and the electron transferred to some degree, often represented by spin or charge density analysis. After the surface crossing or transition state structure, further reorganization occurs that causes the reaction to proceed on the red (product) curve where the proton and electron are localized on the acceptor.

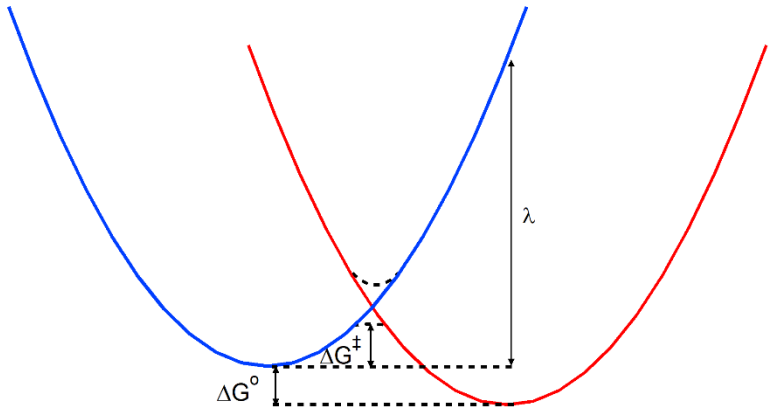

Figure 1.1. Marcus-like free energy curves for the reactant (blue) and product (red) diabatic states along the reaction coordinate. The curved dashed lines indicate the adiabatic potential energy surface that arises from coupling.

The activation energy of the reaction is determined by two main thermodynamic parameters, the free energy of reaction (ΔG^0) and the reorganization energy (λ). The driving force of a PCET reaction can be determined by comparing the bond-dissociation free energy (BDFE) of the reactants and the products. The BDFE for reactants and products can be determined by calculating the stepwise processes for removal of a proton and electron. Therefore, the BDFE can be calculated by

determining the relevant pK_a and reduction potential of the oxidant and substrate. This approach has been used by Mayer extensively and has been shown to be a good predictor of reaction rates.[20, 41-42] Plots of activation energy or log of the rate constant as a function of driving force show linear or quadratic relationships. This free energy relationship leads to the goal of striving for ligand design to target the generation of stronger X–H bonds of the product which will drive reaction rates. Work in chapters 2 and 5 discuss the idea of reactivity rates as a function of driving force.

The reorganization energy is the other thermodynamic parameter that modulates the activation free energy. λ can be viewed as the energy required to distort the reactants to the product geometry *without* crossing to the product diabatic state, or in other words, staying on the blue curve while advancing along the reaction coordinate (Figure 1.1). The other way to think of the reorganization energy is the energy required switch diabatic surfaces *without* heavy-atom rearrangement, or, pictorially, to instantaneously jump from the well of the blue curve vertically to the red curve without progressing along the reaction coordinate. Unlike in ET, where the solvent reorganization energy can be the largest contributor to some reactions, in PCET with metal complexes, λ is often largely dependent on inner-sphere reorganization energy of the metal complex. The importance of the metal complex λ is due to a net neutral charge transfer and has been shown by insensitivity of reaction rates to differing solvents as well, as the possibility for large changes in M–L bond lengths upon reduction of the metal center.

1.3 PCET by Manganese Hydroxides: MnLOX and Model Complexes

The non-heme manganese lipoxygenase (MnLOX) performs substrate dixoygenation of polyunsaturated fatty acid, such as linoleic acid.[37-39] The structure of the Mn^{II} state of the enzyme has recently been determined by XRD, and the local active-site is shown in Figure 1.2 (left) where the six-coordinate manganese is coordinated facially by three His, with one trans to a solvent ligand

(presumably water), as well as a C terminal carboxylate (from Val) and Asn in the equatorial plane. This environment gives an overall negative-one charge from the amino acid ligands. Kinetic experiments of MnLOX with linoleic acid had a large H/D kinetic isotope effect (KIE) greater than 20, showing proton transfer is involved in the rate determining step.[37-38] One proposed mechanism for substrate dioxygenation is outlined in Figure 1.2 (right). Here, a Mn^{III}–OH adduct initiates dixoygenation through PCET from the bis-allylic C–H bond, leading to a Mn^{II}–OH_2 and substrate radical. This radical undergoes rearrangement and then binds to dioxygen, forming a peroxyl radical. This radical species abstracts a hydrogen atom from Mn^{II}–OH_2 to reform Mn^{III}–OH and generate the peroxidized product. Due to the proposed importance of Mn^{III}–OH complexes in MnLOX as well as other enzymes,[40, 43-44] there has been interest in probing the properties and reactivity of synthetic Mn^{III}–OH complexes.[33-35, 45-48]

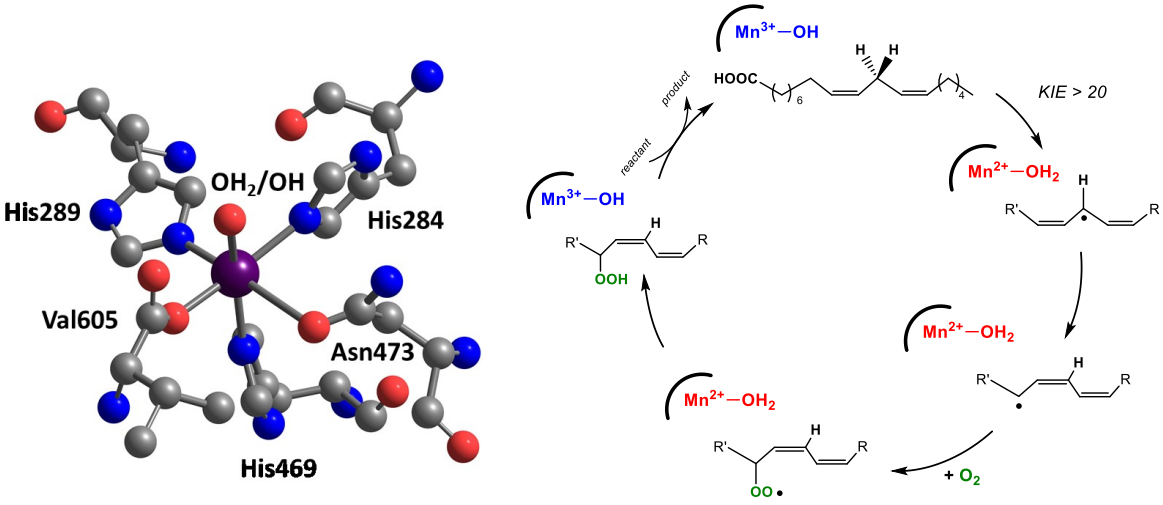

Figure 1.2. Truncated active-site crystal structure of MnLOX from 5FNO (left) and proposed mechanism.[36]

In 2014, our lab began exploring the manganese chemistry of the pentadentate, amide-containing dpaq ligand (dpaq=2-[bis(pyridin-2-ylmethyl)]amino-N-quinolin-8-yl-acetamidate). This ligand, developed by Hitomi and co-workers, was shown to support high-valent Fe oxidants and could be modified to tune steric and electronic properties.[49] Our interest in dpaq stemmed from its monoanionic nature, which mimicked the net charge of amino-acid-derived ligands of mononuclear Mn enzymes, such as MnLOX. (Figure 1.2). Investigations revealed that $[Mn^{II}(dpaq)](OTf)$ reacts with O_2 in MeCN to generate the mononuclear Mn^{III}-hydroxo complex $[Mn^{III}(OH)(dpaq)]^+$ in 98% yield.[33] Such clean reactivity with O_2 is unusual for Mn^{II} complexes. XRD characterization of $[Mn^{III}(OH)(dpaq)]^+$ revealed a six-coordinate Mn^{III} center with the hydroxo *trans* to the amide of dpaq (Figure 1.3, top-left). The high thermal stability of $[Mn^{III}(OH)(dpaq)]^+$ was unanticipated ($t_{1/2}$ in MeCN at 25 °C of ~26 days), as the XRD structure reveals no steric protection of the hydroxo ligand.

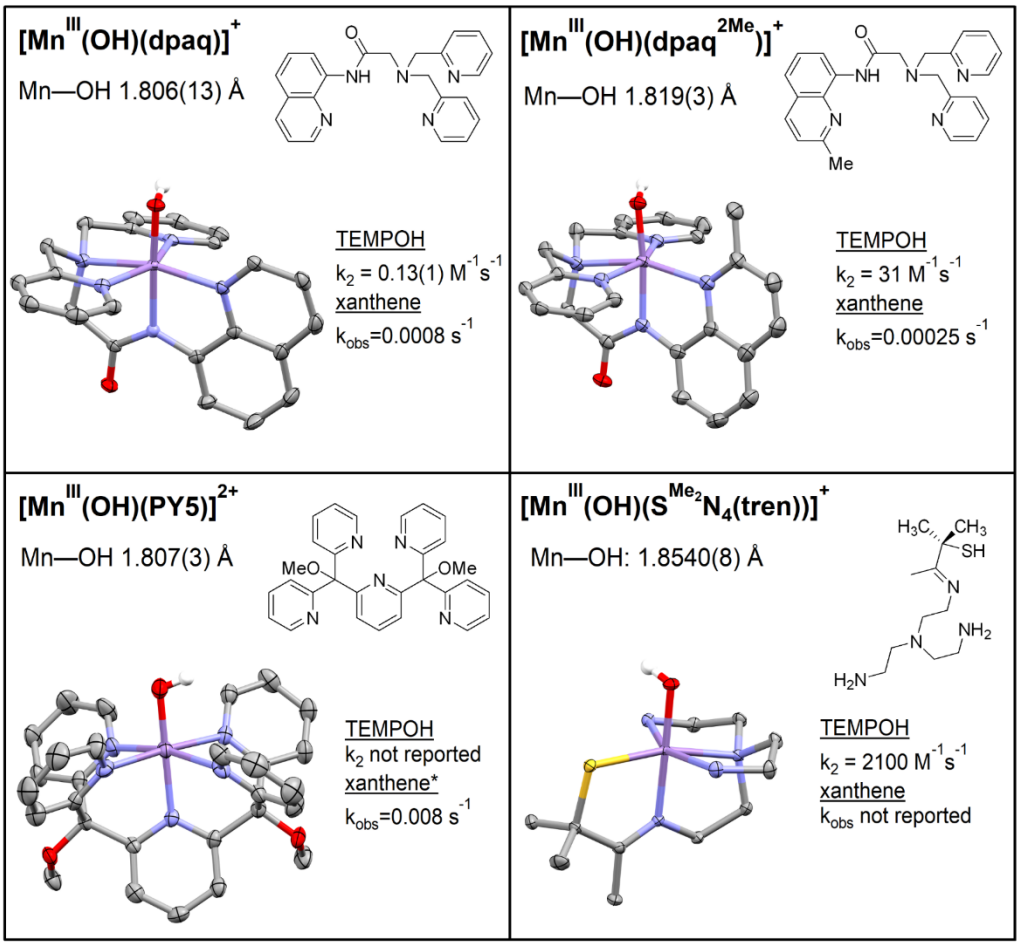

Figure 1.3. ORTEP diagrams of $[Mn^{III}(OH)(dpaq)]^+$, $[Mn^{III}(OH(dpaq^{2Me})]^+$, $[Mn^{III}(OH)(PY5)]^{2+}$, and $[Mn^{III}(OH)(S^{Me2}N_4(tren))]^+$, with Mn–OH bond distance and selected rate constants. k_2 is the second-order rate constant at 25°C; k_{obs} is the pseudo-first-order rate constant at 50°C and 312.5 mM xanthene. *values estimated (see text).

Inspired by the HAT reactivity of the Mn^{III}-hydroxo unit of MnLOX, Wijeratne et al. investigated the ability of $[Mn^{III}(OH)(dpaq)]^+$ to react with the activated C–H bond in xanthene.[33] Xanthene provides an analogue of the polyunsaturated fatty acid substrates of MnLOX, which contain doubly allylic C–H bonds. At 50 °C, the electronic absorption signals of $[Mn^{III}(OH)(dpaq)]^+$ decayed in the presence of 250 equivalents xanthene, yielding a pseudo-first-order rate constant (k_{obs}) of 8×10^{-4} s^{-1}. Although xanthene oxidation is slow, this represented only the second report of a

synthetic Mn^{III}-hydroxo unit attacking a C–H bond. The other example was $[Mn^{III}(OH)(PY5)]^{2+}$ (PY5=2,6-bis(bis(2-pyridyl)methoxymethane)pyridine; Figure 1.3, bottom-left), which features a neutral pentadentate ligand, and can attack a range of C–H bonds, including those of xanthene.[34] By extrapolating the second-order rate constant for xanthene oxidation by $[Mn^{III}(OH)(PY5)]^{2+}$ to 250 equivalents xanthene, we estimate $k_{obs}=8\times10^{-3}$ s^{-1}, which is an order of magnitude faster than that of $[Mn^{III}(OH)(dpaq)]^{+}$. This difference in reactivity can be understood on the basis of the more positive $Mn^{II/III}$ reduction potential of $[Mn^{III}(OH)(PY5)]^{2+}$ compared to $[Mn^{III}(OH)(dpaq^{H})]^{+}$ (+0.14 and -0.73 V, respectively, versus Fc/Fc^{+} in MeCN). The 870 mV difference in reduction potential might suggest that $[Mn^{III}(OH)(PY5)]^{2+}$ should be a far better HAT agent than $[Mn^{III}(OH)(dpaq)]^{+}$. Presumably, the reactivity of $[Mn^{III}(OH)(PY5)]^{2+}$ is dampened by its lower proton affinity, as assessed experimentally by a pK_a of 13 for $[Mn^{II}(OH_2)(PY5)]^{+}$. In comparison, DFT computations indicated a far greater basicity for $Mn^{II}(OH_2)(dpaq)]$ (pK_a=21).[50]

Next the ability of $[Mn^{III}(OH)(dpaq)]^{+}$ to attack O–H bonds was investigated, focusing on the highly activated bond of TEMPOH (2,2',6,6'-tetramethylpiperidine-1-ol), as well as the stronger bonds of *para*-substituted-2,6-di-*tert*-butylphenols. TEMPOH oxidation by $[Mn^{III}(OH)(dpaq)]^{+}$ proceeded with a second-order rate-constant (k_2) of 0.13 $M^{-1}s^{-1}$ at 25 °C, which was obtained by fitting the linear increase in k_{obs} with increasing TEMPOH concentration (Figure 1.4, top). In contrast, k_{obs} values for phenol oxidation showed saturation at higher substrate concentrations, suggestive of a rapid equilibrium prior to a rate-determining step (Figure 1.4, bottom). It was determined that both equilibrium constants (K_{eq}) and first-order rate constants (k_1) for these steps for four *para*-substituted-2,6-di-*tert*-butylphenols. The saturation behavior could arise from several possibilities, the most likely of which are a proton-transfer equilibrium followed by rate-determining electron transfer, or formation of a precursor complex followed by rate-determining HAT. The

latter scenario was supported by an H/D kinetic isotope effect for k_1 and a linear correlation between log(k_1) and phenol BDFE. In addition, there was no correlation between phenol pK_a and the measured K_{eq}, which is inconsistent with a proton-transfer equilibrium. These observations led to the proposal of the formation of H-bonded precursor complex prior to rate-determining HAT (Figure 1.4, bottom). The small equilibrium constant measured for most of the substituted phenols (K_{eq}=8-20) represents a minor stabilization relative to the free reactants.

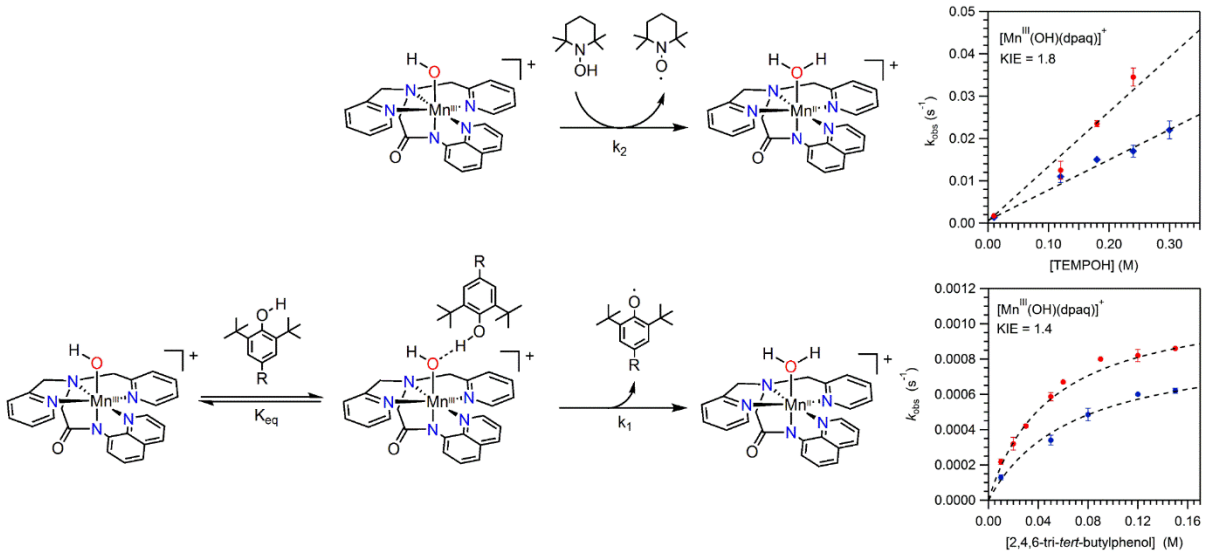

Figure 1.4. Reaction schemes and pseudo-first-order rate constants (k_{obs}) as a function of substrate concentration (-OH, red; -OD, blue) for $[Mn^{III}(OH)(dpaq)]^+$ with TEMPOH (top), and 2,4,6-tri-*tert*-butylphenol (bottom).

The reactivity of $[Mn^{III}(OH)(dpaq)]^+$ towards O–H bonds can be compared with that of the $[Mn^{III}(OH)(S^{Me2}N_4(tren))]^+$ complex of Kovacs and co-workers (Figure 1.3, bottom-right).[35] TEMPOH oxidation by $[Mn^{III}(OH)(S^{Me2}N_4(tren))]^+$ proceeds 10^4-fold more rapidly than $[Mn^{III}(OH)(dpaq)]^+$, but $[Mn^{III}(OH)(S^{Me2}N_4(tren))]^+$ is unable to oxidize O–H bonds stronger than that of TEMPOH (BDFE=66.5 kcal/mol). Thus, a comparison of the reactivities of these complexes offers a conundrum – the $[Mn^{III}(OH)(S^{Me2}N_4(tren))]^+$ complex is far more reactive

towards TEMPOH, but the $[Mn^{III}(OH)(dpaq)]^{+}$ complex is able to attack the stronger O–H bonds of phenols. Such issues underscore the importance of exploring the basis of reactivity for mid-valent metal oxidants as a means of better understanding HAT reactions in general. The work in chapters 2 – 5 focus on understanding the structure-reactivity relationship of these complexes, as well as shedding some light on the perceived reaction difference between $[Mn^{III}(OH)(dpaq)]^{+}$ and $[Mn^{III}(OH)(S^{Me2}N_4(tren))]^{+}$.

1.4 PCET by Pentadentate Manganese Oxo Complexes.

High-valent metal-oxo species have been invoked as intermediates in PCET reactions in biological and synthetic systems.[13-14, 20, 51-58] A majority of the metal-oxo studies with model complexes have focused on characterizing the structure and reactivity has been focused on Fe^{IV}–oxo complexes due to their prevalence in nature. From these studies detailed descriptions of the PCET reactivity have been developed through a combination of spectroscopic, kinetic, and theoretical techniques. Mn^{IV}–oxo complexes have seen considerably fewer studies in comparison. Many of the reported Mn^{IV}–oxo complexes have very limited reactivity when compared to their iron counterparts. Two exceptions to this come from more recent complexes, $[Mn^{IV}(O)(BnTPEN)]^{+}$ as well as $[Mn^{IV}(O)(N4py)]^{2+}$ and its derivatives $[Mn^{IV}(O)(^{DMM}N4py)]^{+}$ and $[Mn^{IV}(O)(2PyN2Q)]^{2+}$.[30-32, 59] These complexes are able to react with significantly stronger C–H bonds, with $[Mn^{IV}(O)(2PyN2Q)]^{2+}$ capable of activating the strong C–H bond of cyclohexane at rates of $k_2 = 6.8 \times 10^{-4}$ $M^{-1}s^{-1}$. The increased reactivity of the complexes relative to other Mn^{IV}–oxo complexes has been postulated to be due to a much more stable Mn^{III}–OH formed after hydrogen atom abstraction.[30] Without pK_a values for the Mn^{III}–OH, the BDFE of the complexes have not been

determined and as such the only thermodynamic parameter available is the $Mn^{IV/III}$ couple. An additional postulate that arose from DFT calculations performed by Shaik and Nam suggest that the complex has increased reactivity due to the ability to access, as they call it, an excited state in order to progress along the reaction.[60] This so-called "excited state" (formally the ^4E state as depicted in Figure 1.5) arises from a promotion of an electron from the Mn $3d_{xz/yz}$ orbital into the Mn $3d_{x2-y2}$. This state was shown to have a lower barrier to reaction and would lead to a more stable high-spin product. This reactivity is in contrast to the reaction along the "ground" state (formally the $^4B_1$ state as depicted in Figure 1.5) that would lead to an intermediate spin product that would need to additionally reorganize to get to the more stable, high-spin product.

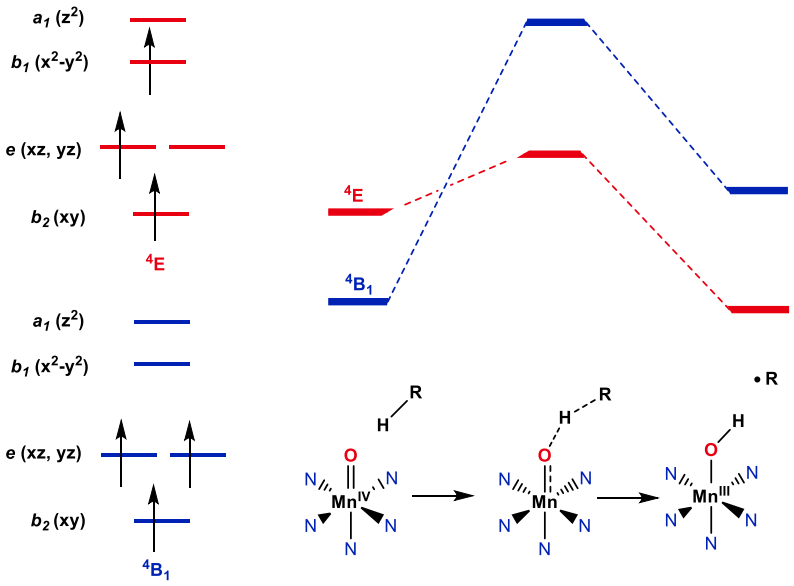

Figure 1.5. Electron configurations for the $^4B_1$ and ^4E states (left) and qualitative HAT reaction coordinate for proposed multistate reactivity.

Synthetic and kinetic work performed by Massie et. al probing this multistate model demonstrated that the reactivity of a series of Mn^{IV}–oxo adducts showed correlation consistent with both the thermodynamic and multistate reactivity.[32] A complementary study by our group utilized

magnetic circular dichroism (MCD) of $[Mn^{IV}(O)(N4py)]^{2+}$ along with DFT and a multireference method, complete active space self-consistent field (CASSCF) with N-electron valence perturbation theory up to second order; NEVPT2 in order to analyze the ground and excited states.[61-62]. This method had been successfully utilized to study Fe^{IV}–oxo complexes to provide insight into the electronic states that control reactivity.[29, 54, 63] A near-IR band was identified using MCD as arising from the ^4E (d_{xz}, d_{yz} → d_{x2-y2}) state which provided experimental support that accessing the ^4E state was energetically feasible. The CASSCF/NEVPT2 calculations were then used to determine the change in energetics and electronic structure of the ^4B and ^4E states as the Mn–oxo bond is elongated (Figure 1.6). Combining these methods, molecular orbital arguments can be used to describe how the states can contribute to reactivity. These scans showed that the ^4E state has significant Mn^{III}–oxyl character in the π direction, which has been predicted to play an important role in PCET reactivity.[60] However, the ^4E state was calculated to be significantly higher in energy than the $^4B_1$ state at the transition state Mn–oxo distance. It was proposed that this lack of state crossing could be due to the ^4E state being stabilized by the presence of substrate, which was not accounted for. The work in chapter 7 looks to address this by inclusion of the substrate to evaluate how the energetics of the states are altered and the role of both states in PCET reactivity.

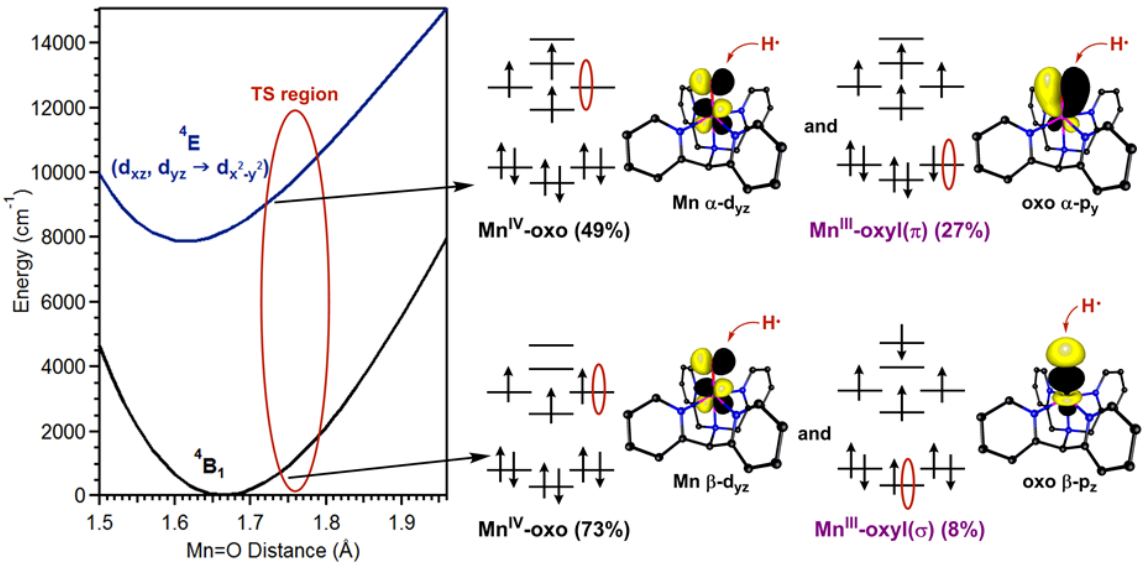

Figure 1.6. CASSCF/NEVPT2 potential energy surfaces for $^4B_1$ and ^4E states (left). Configurations contributing to the CASSCF wave functions, with corresponding surface contour plots (right). The red ellipses in the configuration diagrams represent electron-accepting orbitals for HAT. Reproduced with permission from ref. [29]. Copyright 2016 American Chemical Society.

1.5 Spectroscopic Characterization of Manganese Complexes.

Structural information for model Mn^{III}–OH complexes has readily been obtained from crystal structures.[33-35, 50] This approach allows for accurate comparison of structural differences caused from ligand modifications. These Mn^{III}–OH complexes, however, could be used as a starting material in the generation of a new unstable intermediate for which crystal structures cannot be easily obtained. Additionally, in enzymes such as MnLOX, there are no crystal structures of the Mn^{III}–OH moiety. These highly unstable intermediates require a different method of structural characterization that does not require the growth of crystalline material. For this, X-ray absorption spectroscopy (XAS) can prove an invaluable tool. For manganese complexes, the K-edge XAS can provide a wealth of information about the electronic and atomic structure of the complexes. Mn K-edge XAS involves the excitation of a core Mn 1s electron, which gives a spectrum such as the one

shown in Figure 1.7 (middle). The spectra are characterized by two predominant regions, the X-ray absorption near edge structure (XANES) region, which is within a small energy window around the K-edge, and the extended X-ray absorption fine structure (EXAFS) region.[64]

The XANES region itself consists of multiple important features. The most noticeable is the intense, rising edge, from which an edge energy can be determined. This edge energy can be determined through various ways, one of which is from the inflection point of the rising edge (black dashed line, Figure 1.7, center) and is the energy at which the election is ejected from the metal center. The edge energy is characteristic for every element, and for manganese metal is at 6539 eV. Modulations of this value arises due to coordinate environment of the metal as well as oxidation state. Increases in oxidation state often show an increase in the edge energy by at least 1 eV at parity of coordination environment. Taking ligand modifications and oxidation states together, the edge energy can shift to energies above 6550 eV. Knowing the edge energy of a well-characterized structure serves as a probe for changes in oxidation state upon reaction. The next region of interest in the XANES is the pre-edge, which arises from Mn 1s → 3d transitions into unoccupied 3d orbitals (Figure 1.7, center). These transitions are formally parity-forbidden and therefore have a low intensity. Mixing of the metal 3d-4p orbitals due to lowered symmetry or metal-ligand covalency gives intensity to these transitions. Due to this, peak deconvolution of the pre-edge region to obtain areas can provide geometric information as well as insight into the nature of metal-ligand bonds. Pre-edge areas have been shown to often correlate with the % p character determined from DFT orbitals. The rest of the XANES region has the potential to provide significant information, as it can be highly sensitive to minor changes in geometry, but it is complicated by the fact that there are many contributions to this region. These contributions include excitations into 4p orbitals as well as multiple-scattering pathways.

The other region used to obtain structural characterization is the EXAFS region. The energy of this region is greater than that necessary to ionize the manganese (the edge energy, E_0), and the additional energy is conserved as kinetic energy of the ejected photoelectron. The wavelength of the photoelectron is inversely proportional to the kinetic energy, and therefore scanning energies beyond the edge is equivalent to scanning the wavelength of the photoelectron. The photoelectron will scatter off the electron density of nearby atoms and the backscatter wave will interfere with itself, leading to constructive and destructive interference, depending on the wavelength and distance of the scatterer. In the spectra, this scattering will give an oscillatory shape, where the upper peak is maximum constructive interference and the lower peak is maximum destructive interference. Often the data are plotted as a function of the wavevector (k-space, $Å^{-1}$), which is related to the kinetic energy via the de Broglie equation (Figure 1.7, top right). The oscillatory data can be fit by multiple functions, corresponding to different scattererers, and the distances of the scatterers can be extracted. Often, the Fourier transform of the EXAFS data is taken to show a qualitative depiction in R-space (Å) of the structural information. Overall XAS has proven to be a very powerful technique to identify metastable intermediates, and even with well-characterized complexes it can provide additional information about the electronic structure. The work in chapter 3 focuses on this technique, and further use of the technique is present in chapters 4 and 6.

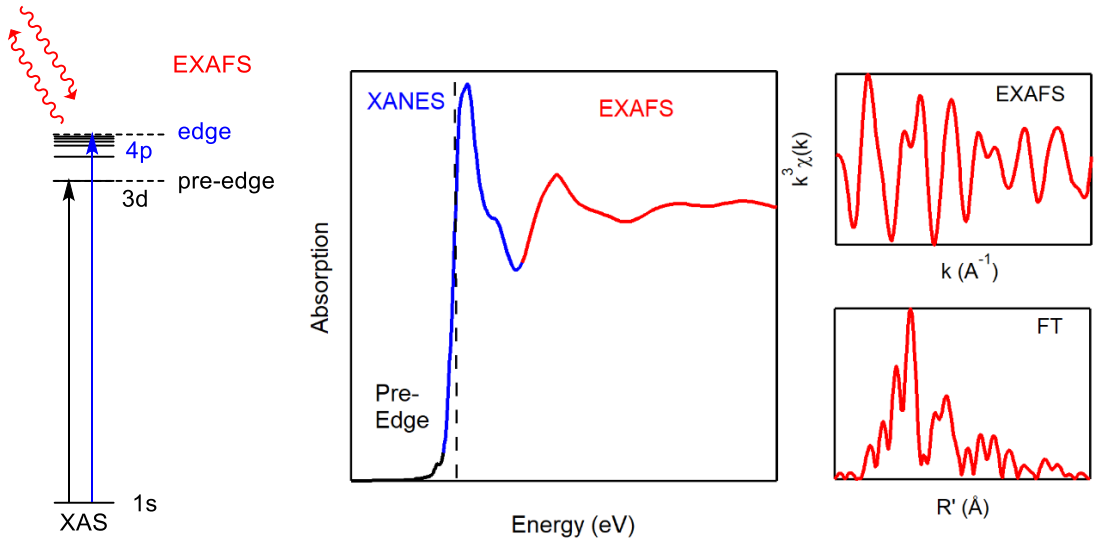

Figure 1.7. Orbital diagram showing the electronic excitation at the K-edge for a first-row transition metal depicting the contributions to the experimental XAS data (left). XAS spectra showing the general regions (middle). EXAFS data plotted in k-space ($Å^{-1}$) and weighted by k^3 (right, top) and its Fourier transform plotted in R-space (Å) (right, bottom).

Due to the S = 2 ground state of Mn^{III}–OH complexes, characterization of the complex by electron paramagnetic resonance (EPR) can prove problematic due to large zero-field splitting. High-field EPR can potentially overcome this dilemma, but such instruments are not readily available. Additionally, EPR experiments would require the sample to be frozen in solution and performed at liquid nitrogen temperatures and below. A different avenue to characterize Mn^{III} complexes is available via NMR experiments. For diamagnetic systems, NMR is well established and often trivial to perform. In paramagnetic complexes, the spin-density of a metal center can propagate throughout the ligand via different mechanisms and cause rapid relaxation, which leads to broadened and greatly shifted NMR resonances. Methods to overcome this difficulty have been developed, such as significantly lowering the acquisition time (and consequently increasing the spectral width) and performing diamagnetic suppression routines via inversion-recovery methods. These approaches have allowed for NMR to be obtained for various high-spin systems. While not as

well-defined as NMR of diamagnetic complexes there are various techniques that have been utilized to characterize these paramagnetic species. Temperature dependent ^{1}H NMR applied to copper dimeric structures demonstrated that the chemical shifts of a ferromagnetically coupled or weakly antiferromagnetically coupled system will follow Curie behavior, while strongly antiferromagnetically coupled species will follow anti-Curie or non-Curie behavior. [65-67] Spin-relaxation measurements as well as selective ligand modifications have allowed for characterization of iron and manganese complexes in solution.[68-72] NMR of paramagnetic and antiferromagnetically complexes play an important role in characterizing structures in solution and this technique is utilized in chapters 4, 5, and 6.

References

1. Zaragoza, J. P. T.; Yosca, T. H.; Siegler, M. A.; Moenne-Loccoz, P.; Green, M. T.; Goldberg, D. P., Direct Observation of Oxygen Rebound with an Iron-Hydroxide Complex. *J Am Chem Soc* **2017**.
2. Kumar, D.; Karamzadeh, B.; Sastry, G. N.; de Visser, S. P., What Factors Influence the Rate Constant of Substrate Epoxidation by Compound I of Cytochrome P450 and Analogous Iron(IV)-Oxo Oxidants? *Journal of the American Chemical Society* **2010,** *132* (22), 7656-7667.
3. Kumar, D.; Hirao, H.; Que, L.; Shaik, S., Theoretical Investigation of C−H Hydroxylation by (N4Py)FeIVO2+: An Oxidant More Powerful than P450? *Journal of the American Chemical Society* **2005,** *127* (22), 8026-8027.
4. Green, M. T.; Dawson, J. H.; Gray, H. B., Oxoiron(IV) in Chloroperoxidase Compound II Is Basic: Implications for P450 Chemistry. *Science* **2004,** *304* (5677), 1653-1656.
5. Kumar, D.; de Visser, S. P.; Sharma, P. K.; Cohen, S.; Shaik, S., Radical Clock Substrates, Their C−H Hydroxylation Mechanism by Cytochrome P450, and Other Reactivity Patterns: What Does Theory Reveal about the Clocks' Behavior? *Journal of the American Chemical Society* **2004,** *126* (6), 1907-1920.
6. Kumar, D.; de Visser, S. P.; Shaik, S., How Does Product Isotope Effect Prove the Operation of a Two-State "Rebound" Mechanism in C−H Hydroxylation by Cytochrome P450? *Journal of the American Chemical Society* **2003,** *125* (43), 13024-13025.
7. Rice, D. B.; Massie, A. A.; Jackson, T. A., Manganese-Oxygen Intermediates in O-O Bond Activation and Hydrogen-Atom Transfer Reactions. *Acc Chem Res* **2017,** *50* (11), 2706-2717.
8. Gupta, R.; Taguchi, T.; Lassalle-Kaiser, B.; Bominaar, E. L.; Yano, J.; Hendrich, M. P.; Borovik, A. S., High-spin Mn–oxo complexes and their relevance to the oxygen-evolving complex within photosystem II. *Proceedings of the National Academy of Sciences* **2015,** *112* (17), 5319-5324.

9. Glockner, C.; Kern, J.; Broser, M.; Zouni, A.; Yachandra, V.; Yano, J., Structural changes of the oxygen-evolving complex in photosystem II during the catalytic cycle. *J Biol Chem* **2013,** *288* (31), 22607-20.
10. Cox, N.; Pantazis, D. A.; Neese, F.; Lubitz, W., Biological water oxidation. *Acc Chem Res* **2013,** *46* (7), 1588-96.
11. Dau, H.; Zaharieva, I.; Haumann, M., Recent developments in research on water oxidation by photosystem II. *Curr Opin Chem Biol* **2012,** *16* (1-2), 3-10.
12. McEvoy, J. P.; Brudvig, G. W., Water-splitting chemistry of photosystem II. *Chem Rev* **2006,** *106* (11), 4455-83.
13. Borovik, A. S., Role of metal-oxo complexes in the cleavage of C-H bonds. *Chemical Society Reviews* **2011,** *40* (4), 1870-1874.
14. Ye, S.; Neese, F., Nonheme oxo-iron(IV) intermediates form an oxyl radical upon approaching the C-H bond activation transition state. *Proc Natl Acad Sci U S A* **2011,** *108* (4), 1228-33.
15. Fukuzumi, S.; Morimoto, Y.; Kotani, H.; Naumov, P.; Lee, Y.-M.; Nam, W., Crystal structure of a metal ion-bound oxoiron(IV) complex and implications for biological electron transfer. *Nat Chem* **2010,** *2* (9), 756-759.
16. Fukuzumi, S.; Fujioka, N.; Kotani, H.; Ohkubo, K.; Lee, Y.-M.; Nam, W., Mechanistic Insights into Hydride-Transfer and Electron-Transfer Reactions by a Manganese(IV)−Oxo Porphyrin Complex. *Journal of the American Chemical Society* **2009,** *131* (47), 17127-17134.
17. Hirao, H.; Que, L.; Nam, W.; Shaik, S., A Two-State Reactivity Rationale for Counterintuitive Axial Ligand Effects on the C□H Activation Reactivity of Nonheme FeIV□O Oxidants. *Chemistry – A European Journal* **2008,** *14* (6), 1740-1756.
18. Lansky, D. E.; Goldberg, D. P., Hydrogen Atom Abstraction by a High-Valent Manganese(V)-Oxo Corrolazine. *Inorg. Chem.* **2006,** *45*, 5119.
19. Hirao, H.; Kumar, D.; Que, L.; Shaik, S., Two-State Reactivity in Alkane Hydroxylation by Non-Heme Iron−Oxo Complexes. *Journal of the American Chemical Society* **2006,** *128* (26), 8590-8606.
20. Mayer, J. M., Understanding Hydrogen Atom Transfer: From Bond Strengths to Marcus Theory. *Accounts of Chemical Research* **2011,** *44* (1), 36-46.
21. Hammes-Schiffer, S., Proton-Coupled Electron Transfer: Moving Together and Charging Forward. *J Am Chem Soc* **2015,** *137* (28), 8860-71.
22. Layfield, J. P.; Hammes-Schiffer, S., Hydrogen Tunneling in Enzymes and Biomimetic Models. *Chemical Reviews* **2014,** *114* (7), 3466-3494.
23. Horvath, S.; Fernandez, L. E.; Soudackov, A. V.; Hammes-Schiffer, S., Insights into proton-coupled electron transfer mechanisms of electrocatalytic H2 oxidation and production. *Proc Natl Acad Sci U S A* **2012,** *109* (39), 15663-8.
24. Hammes-Schiffer, S.; Stuchebrukhov, A. A., Theory of Coupled Electron and Proton Transfer Reactions. *Chemical Reviews* **2010,** *110* (12), 6939-6960.
25. Skone, J. H.; Soudackov, A. V.; Hammes-Schiffer, S., Calculation of Vibronic Couplings for Phenoxyl/Phenol and Benzyl/Toluene Self-Exchange Reactions: Implications for Proton-Coupled Electron Transfer Mechanisms. *Journal of the American Chemical Society* **2006,** *128* (51), 16655-16663.
26. Kupper, C.; Mondal, B.; Serrano-Plana, J.; Klawitter, I.; Neese, F.; Costas, M.; Ye, S.; Meyer, F., Nonclassical Single-State Reactivity of an Oxo-Iron(IV) Complex Confined to Triplet Pathways. *J Am Chem Soc* **2017,** *139* (26), 8939-8949.

27. England, J.; Martinho, M.; Farquhar, E. R.; Frisch, J. R.; Bominaar, E. L.; Munck, E.; Que, L., Jr., A synthetic high-spin oxoiron(IV) complex: generation, spectroscopic characterization, and reactivity. *Angew Chem Int Ed Engl* **2009,** *48* (20), 3622-6.
28. Rasheed, W.; Draksharapu, A.; Banerjee, S.; Young, V. G., Jr.; Fan, R.; Guo, Y.; Ozerov, M.; Nehrkorn, J.; Krzystek, J.; Telser, J.; Que, L., Crystallographic evidence for a sterically induced ferryl tilt in a non-heme oxoiron(IV) complex that makes it a better oxidant. *Angew Chem Int Ed Engl* **2018**.
29. Leto, D. F.; Massie, A. A.; Rice, D. B.; Jackson, T. A., Spectroscopic and Computational Investigations of a Mononuclear Manganese(IV)-Oxo Complex Reveal Electronic Structure Contributions to Reactivity. *J Am Chem Soc* **2016,** *138* (47), 15413-15424.
30. Leto, D. F.; Ingram, R.; Day, V. W.; Jackson, T. A., Spectroscopic properties and reactivity of a mononuclear oxomanganese(iv) complex. *Chemical Communications* **2013,** *49* (47), 5378-5380.
31. Massie, A. A.; Sinha, A.; Parham, J. D.; Nordlander, E.; Jackson, T. A., Relationship between Hydrogen-Atom Transfer Driving Force and Reaction Rates for an Oxomanganese(IV) Adduct. *Inorg Chem* **2018,** *57* (14), 8253-8263.
32. Massie, A. A.; Denler, M. C.; Cardoso, L. T.; Walker, A. N.; Hossain, M. K.; Day, V. W.; Nordlander, E.; Jackson, T. A., Equatorial Ligand Perturbations Influence the Reactivity of Manganese(IV)-Oxo Complexes. *Angewandte Chemie International Edition* **2017,** *56* (15), 4178-4182.
33. Wijeratne, G. B.; Corzine, B.; Day, V. W.; Jackson, T. A., Saturation kinetics in phenolic O-H bond oxidation by a mononuclear Mn(III)-OH complex derived from dioxygen. *Inorg Chem* **2014,** *53* (14), 7622-34.
34. Goldsmith, C. R.; Cole, A. P.; Stack, T. D., C-H activation by a mononuclear manganese(III) hydroxide complex: synthesis and characterization of a manganese-lipoxygenase mimic? *J Am Chem Soc* **2005,** *127* (27), 9904-12.
35. Coggins, M. K.; Brines, L. M.; Kovacs, J. A., Synthesis and structural characterization of a series of Mn(III)OR complexes, including a water-soluble Mn(III)OH that promotes aerobic hydrogen-atom transfer. *Inorg Chem* **2013,** *52* (21), 12383-93.
36. Wennman, A.; Oliw, E. H.; Karkehabadi, S.; Chen, Y., Crystal Structure of Manganese Lipoxygenase of the Rice Blast Fungus Magnaporthe oryzae. *J Biol Chem* **2016,** *291* (15), 8130-9.
37. Wennman, A.; Karkehabadi, S.; Oliw, E. H., Kinetic investigation of the rate-limiting step of manganese- and iron-lipoxygenases. *Archives of Biochemistry and Biophysics* **2014,** *555–556*, 9-15.
38. Su, C.; Sahlin, M.; Oliw, E. H., Kinetics of Manganese Lipoxygenase with a Catalytic Mononuclear Redox Center. *Journal of Biological Chemistry* **2000,** *275* (25), 18830-18835.
39. Su, C.; Oliw, E. H., Manganese Lipoxygenase: PURIFICATION AND CHARACTERIZATION. *Journal of Biological Chemistry* **1998,** *273* (21), 13072-13079.
40. Yano, J.; Yachandra, V., Mn4Ca Cluster in Photosynthesis: Where and How Water is Oxidized to Dioxygen. *Chemical Reviews* **2014,** *114* (8), 4175-4205.
41. Warren, J. J.; Tronic, T. A.; Mayer, J. M., Thermochemistry of Proton-Coupled Electron Transfer Reagents and its Implications. *Chemical Reviews* **2010,** *110* (12), 6961-7001.
42. Saouma, C. T.; Mayer, J. M., Do Spin State and Spin Density Affect Hydrogen Atom Transfer Reactivity? *Chem Sci* **2014,** *5* (1).
43. Jackson, T. A.; Gutman, C. T.; Maliekal, J.; Miller, A. F.; Brunold, T. C., *Inorg. Chem.* **2013,** *52*, 3356.
44. Grove, L. E.; Brunold, T. C., *Comments Inorg. Chem.* **2008,** *29*, 134.
45. Shirin, Z.; Hammes, B. S.; Young, V. G.; Borovik, A. S., Hydrogen Bonding in Metal Oxo Complexes: Synthesis and Structure of a Monomeric Manganese(III)−Oxo Complex and Its Hydroxo Analogue. *Journal of the American Chemical Society* **2000,** *122* (8), 1836-1837.

46. Shirin, Z.; S. Borovik, A.; G. Young Jr, V., Synthesis and structure of a MnIII(OH) complex generated from dioxygen. *Chemical Communications* **1997,** (20), 1967-1968.
47. Gupta, R.; Borovik, A. S., *J. Am. Chem. Soc.* **2003,** *125*, 13234.
48. Gupta, R.; Taguchi, T.; Borovik, A. S.; Hendrich, M. P., *Inorg. Chem.* **2013,** *52*, 12568.
49. Hitomi, Y.; Arakawa, K.; Kodera, M., Electronic Tuning of Iron–Oxo-Mediated C□H Activation: Effect of Electron-Donating Ligand on Selectivity. *Chemistry – A European Journal* **2013,** *19* (43), 14697-14701.
50. Rice, D. B.; Wijeratne, G. B.; Burr, A. D.; Parham, J. D.; Day, V. W.; Jackson, T. A., Steric and Electronic Influence on Proton-Coupled Electron-Transfer Reactivity of a Mononuclear Mn(III)-Hydroxo Complex. *Inorg Chem* **2016,** *55* (16), 8110-20.
51. McDonald, A. R.; Que, L., High-valent nonheme iron-oxo complexes: Synthesis, structure, and spectroscopy. *Coordination Chemistry Reviews* **2013,** *257* (2), 414-428.
52. Nam, W., Synthetic Mononuclear Nonheme Iron–Oxygen Intermediates. *Accounts of Chemical Research* **2015,** *48* (8), 2415-2423.
53. Solomon, E. I.; Wong, S. D.; Liu, L. V.; Decker, A.; Chow, M. S., Peroxo and oxo intermediates in mononuclear nonheme iron enzymes and related active sites. *Current Opinion in Chemical Biology* **2009,** *13* (1), 99-113.
54. Srnec, M.; Wong, S. D.; Solomon, E. I., Excited state potential energy surfaces and their interactions in Fe(IV)=O active sites. *Dalton Trans* **2014,** *43* (47), 17567-77.
55. Ye, S.; Geng, C. Y.; Shaik, S.; Neese, F., Electronic structure analysis of multistate reactivity in transition metal catalyzed reactions: the case of C-H bond activation by non-heme iron(IV)-oxo cores. *Phys Chem Chem Phys* **2013,** *15* (21), 8017-30.
56. Yin, G., Understanding the Oxidative Relationships of the Metal Oxo, Hydroxo, and Hydroperoxide Intermediates with Manganese(IV) Complexes Having Bridged Cyclams: Correlation of the Physicochemical Properties with Reactivity. *Accounts of Chemical Research* **2013,** *46* (2), 483-492.
57. Costas, M.; Mehn, M. P.; Jensen, M. P.; Que, L., Dioxygen Activation at Mononuclear Nonheme Iron Active Sites: Enzymes, Models, and Intermediates. *Chemical Reviews* **2004,** *104* (2), 939-986.
58. Sahu, S.; Goldberg, D. P., Activation of Dioxygen by Iron and Manganese Complexes: A Heme and Nonheme Perspective. *Journal of the American Chemical Society* **2016,** *138* (36), 11410-11428.
59. Wu, X.; Seo, M. S.; Davis, K. M.; Lee, Y.-M.; Chen, J.; Cho, K.-B.; Pushkar, Y. N.; Nam, W., A Highly Reactive Mononuclear Non-Heme Manganese(IV)–Oxo Complex That Can Activate the Strong C–H Bonds of Alkanes. *Journal of the American Chemical Society* **2011,** *133* (50), 20088-20091.
60. Cho, K.-B.; Shaik, S.; Nam, W., Theoretical Investigations into C–H Bond Activation Reaction by Nonheme MnIVO Complexes: Multistate Reactivity with No Oxygen Rebound. *The Journal of Physical Chemistry Letters* **2012,** *3* (19), 2851-2856.
61. Roos, B. O.; Taylor, P. R.; Si≐gbahn, P. E. M., A complete active space SCF method (CASSCF) using a density matrix formulated super-CI approach. *Chemical Physics* **1980,** *48* (2), 157-173.
62. Angeli, C.; Cimiraglia, R.; Evangelisti, S.; Leininger, T.; Malrieu, J.-P., Introduction of n-electron valence states for multireference perturbation theory. *The Journal of Chemical Physics* **2001,** *114* (23), 10252-10264.
63. Srnec, M.; Wong, S. D.; Matthews, M. L.; Krebs, C.; Bollinger, J. M.; Solomon, E. I., Electronic Structure of the Ferryl Intermediate in the alpha-Ketoglutarate Dependent Non-Heme Iron Halogenase SyrB2: Contributions to H Atom Abstraction Reactivity. *J Am Chem Soc* **2016,** *138* (15), 5110-22.

64. Scott, R. A., X-Ray Absorption Spectroscopy. In *Physical Methods in Bioinorganic Chemistry*, Que Jr, L., Ed. University Science Books: 2000; pp 465 - 504.
65. Holz, R. C.; Bradshaw, J. M.; Bennett, B., Synthesis, Molecular Structure, and Reactivity of Dinuclear Copper(II) Complexes with Carboxylate-Rich Coordination Environments. *Inorganic Chemistry* **1998,** *37* (6), 1219-1225.
66. Holz, R. C.; Brink, J. M.; Rose, R. A., J-Dependent Curie or Anti-Curie Behavior of Proton NMR Resonances for Antiferromagnetically Coupled Dinuclear Copper(II) Complexes. *Journal of Magnetic Resonance, Series A* **1996,** *119* (1), 125-128.
67. Asokan, A.; Manoharan, P. T., 1H NMR Studies on Strongly Antiferromagnetically Coupled Dicopper(II) Systems. *Inorganic Chemistry* **1999,** *38* (25), 5642-5654.
68. Klinker, E. J.; Kaizer, J.; Brennessel, W. W.; Woodrum, N. L.; Cramer, C. J.; Que, L., Structures of Nonheme Oxoiron(IV) Complexes from X-ray Crystallography, NMR Spectroscopy, and DFT Calculations. *Angewandte Chemie International Edition* **2005,** *44* (24), 3690-3694.
69. Chiou, Y.-M.; Que, L., Models for .alpha.-Keto Acid-Dependent Non-heme Iron Enzymes: Structures and Reactivity of [FeII(L)(O2CCOPh)](ClO4) Complexes. *Journal of the American Chemical Society* **1995,** *117* (14), 3999-4013.
70. Zang, Y.; Kim, J.; Dong, Y.; Wilkinson, E. C.; Appelman, E. H.; Que, L., Models for Nonheme Iron Intermediates: Structural Basis for Tuning the Spin States of Fe(TPA) Complexes. *Journal of the American Chemical Society* **1997,** *119* (18), 4197-4205.
71. Ciringh, Y.; Gordon-Wylie, S. W.; Norman, R. E.; Clark, G. R.; Weintraub, S. T.; Horwitz, C. P., Multinuclear Paramagnetic NMR Spectra and Solid State X-ray Crystallographic Characterization of Manganese(III) Schiff-Base Complexes. *Inorganic Chemistry* **1997,** *36* (22), 4968-4982.
72. Godbole, M. D.; Hotze, A. C. G.; Hage, R.; Mills, A. M.; Kooijman, H.; Spek, A. L.; Bouwman, E., Stereochemical Influence of the Ligand on the Structure of Manganese Complexes: Implications for Catalytic Epoxidations. *Inorganic Chemistry* **2005,** *44* (25), 9253-9266.

Chapter 2

Steric and Electronic Influence on Proton-Coupled Electron-Transfer Reactivity of a Mononuclear Mn(III)-Hydroxo Complex

2.1 Introduction

Mn^{III}-hydroxo motifs are proposed in the catalytic cycles of Mn lipoxygenase (MnLOX)[1-5] and the oxygen evolving complex (OEC) of photosystem II.[6,7] In MnLOX, a Mn^{III}-hydroxo abstracts an H-atom from a polyunsaturated fatty acid to initiate its dioxygenation. This step proceeds with a large H/D KIE of 20-24, implying a concerted proton-electron transfer (CPET). (CPET is a sub-class of proton-coupled electron-transfer, PCET, reactions, where the proton and electron are transferred in the same kinetic step.) PCET from a Mn^{III}-hydroxo unit is also a possible pathway for stepwise oxidation of the OEC during the water splitting cycle,[6,7] although this mechanism remains disputed. Despite the importance of Mn^{III}-hydroxo complexes in PCET processes, there are few examples of synthetic Mn^{III}-hydroxo complexes known to mediate such reactions. This is in great contrast to the well-studied reactivity of high-valent Mn(IV)-oxo centers in PCET processes.[8-15] Furthermore, of the known hydroxide complexes there is substantial variability in Mn^{III} coordination environment and PCET reactivity.[16,17] For example, the $[Mn^{III}(OH)(PY5)]^{2+}$ complex of Stack and co-workers, which features a neutral N_5 ligand (PY5 = 2,6-bis(bis(2-pyridyl)methoxymethanepyridine)), can oxidize the relatively strong C–H bonds of toluene (bond dissociation free energy, BDFE, of 87 kcal/mol).[16] However, the $[Mn^{III}(OH)(S^{Me2}N_4(tren))]^{+}$ complex of Kovacs and co-workers, which has a N_4S^{-} ligand ($S^{Me2}N_4(tren)$ = 3-((2-(bis(2-aminoethyl)-amino)ethyl)imino-2-methylbutane-2-thiolate), can only attack the weak O–H bond of TEMPOH (2,2'-6,6'-tetramethylpiperidine-1-ol; BDFE = 66.5 kcal/mol).[17] The substantial differences in Mn^{III} environment for this pair of complexes obscure the impact of general factors, such as $Mn^{III/II}$ reduction potentials and steric effects, on PCET reactivity.

We have reported that the Mn^{II} complex of the anionic N5 ligand dpaq (**1-H**; dpaq = 2-[bis(pyridin-2-ylmethyl)]amino-*N*-quinolin-8-yl-acetamidate) forms a hydroxomanganese(III) species

in the presence of O_2 at ambient conditions in MeCN (Scheme 2.1).[18] The $[Mn^{III}(OH)(dpaq)]^+$ (**2-H**) complex abstracts hydrogen atoms from moderate-strength O–H and C–H bonds (BDFE < 79 kcal/mol) by a CPET mechanism. A dimeric bis(μ-oxo)manganese(III,IV) complex supported by the dpaq ligand has also recently been shown capable of initiating hydrogen atom abstraction reactions.[19]

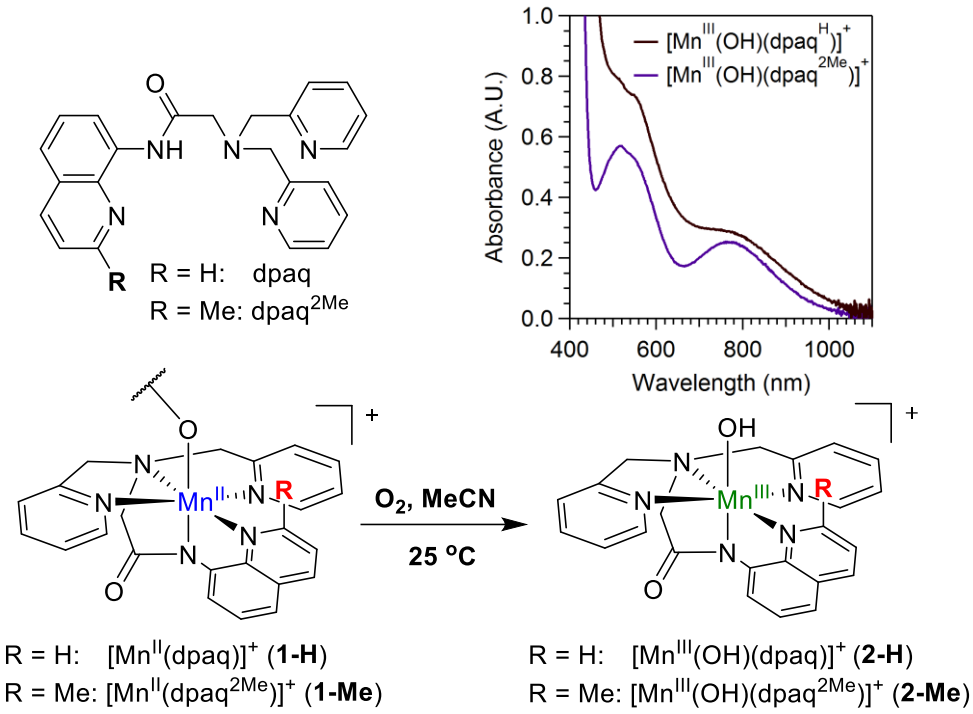

Scheme 2.1. Chemical structure of the $Hdpaq^R$ ligand (top left). Electronic absorption spectra of 2.5 mM MeCN solutions of **2-H** and **2-Me** after full formation upon reaction of Mn^{II} complexes with O_2 gas at 25° C (top right). Reaction scheme for the conversion of $[Mn^{II}(dpaq^R)]^+$ to $[Mn^{III}(OH)(dpaq^R)]^+$ in the presence of O_2 (bottom). In the solid-state structure of **1-H** and **1-Me**, the Mn^{II} coordination sphere is completed by an amide oxygen from a separate Mn^{II} molecule.

Importantly, the dpaq ligand is easily amenable to modification, as employed by Hitomi and co-workers to tune the reactivity of Fe and Mn-NO complexes.[20-24] Here we describe modification of the dpaq ligand through incorporation of a 2-methylquinoline moiety ($dpaq^{2\text{-}Me}$ = 2-[bis(pyridin-2-ylmethyl)]amino-*N*-2-methyl-quinolin-8-yl-acetamidate), providing steric bulk adjacent to the N-

donor function and in proximity to the reaction center (Scheme 2.1). Quinoline and pyridine ligands with methyl-substituents adjacent to the N-donor support longer metal–N interactions, impacting metal electronic structure.[25-27] In this present case, this ligand perturbation dramatically increases the rate of TEMPOH oxidation by the Mn^{III}-hydroxo unit, while the rates of oxidation of bulkier, or more rigid, substrates are largely unaffected. Density functional theory (DFT) computations are used to aid in understanding the electronic and steric factors accounting for this interesting reactivity pattern.

2.2 Experimental and Computational Methods.

Materials and Instrumentation. All chemicals and solvents were obtained from commercial vendors at ACS grade or better and, unless otherwise described, were used without further purification. Acetonitrile, methanol, and ether were dried and degassed using a Pure Solv (2010) solvent purification system. These solvents were degassed in air-tight solvent reservoirs (4 L) by passing Ar gas at room temperature for 20 min. Acetonitrile and ether were dried using air-tight alumina columns, and methanol was dried using a drierite column. Anhydrous dichloromethane and deuterated acetonitrile (MeCN-d_3) were purchased from Acros Organics. All dried, degassed solvents were immediately taken into an argon-filled glove box and were stored in tightly-sealed Schlenk glassware. All experimental procedures were carried out under an argon atmosphere unless otherwise stated. The purity of O_2 gas used was >99% and was further purified using a gas purifier column packed with drierite and 5 Å molecular sieves prior to use. TEMPOH, TEMPOD and 2,4,6-tri-*tert*-butylphenol-d were synthesized as described in literature procedures.[9,28] All ^{1}H NMR spectra were collected on a Bruker DRZ 400 MHz spectrometer. Mass spectrometry experiments were performed using an LCT' Primers MicroMass electrospray time of-flight instrument. EPR

experiments were performed on a Bruker EMXPlus spectrometer with a dual-mode cavity and an Oxford instruments cryostat.

Synthesis of Hdpaq^{2Me}. 2-methylquinolin-8-amine (1.00g, 6.32mmol) and 2-bromoacetyl bromide (0.725mL, 8.32 mmol) were combined in acetonitrile (20mL) along with excess Na_2CO_3 (1.03g, 9.7mmol) under an inert atmosphere, and the resulting solution was stirred for 30 min at 0 °C. The solution was then allowed to warm to room temperature, was filtered through celite, and evaporated to dryness under reduced pressure. The solid product was combined with di-picolyl amine (1.5mL, 8.33mmol) and Na_2CO_3 (1.03g, 9.7mmol) in acetonitrile (40mL), and was stirred overnight at 0 °C under an inert atmosphere. The final reaction mixture was filtered through celite and evaporated to dryness. The crude product was purified by flash chromatography on a silica column using a MeOH:CH_2Cl_2 mixture with an initial composition of 0.5% MeOH that was gradually increased to 5% MeOH. The pure ligand was isolated in good yield (77%) as a brown oil, and was characterized by ^{1}H and ^{13}C NMR methods and ESI-MS. ^{1}H NMR data (400MHz) for Hdpaq^{2Me} ($CDCl_3$, δ) = 11.52 (s, 1H), 8.70 (dd, J=6.4, 2.7Hz, 1H), 8.50 – 8.40 (m, 2H), 8.02 (d, J = 8.3Hz, 1H,) 7.92 (d, J= 7.8 Hz, 2H), 7.54 (td, J = 7.6, 1.9 Hz, 2H), 7.46 – 7.28 (m, 3H), 7.15 – 7.02 (m,2H), 3.93 (s, 4H) 3.45(s, 2H), 2.82 (d, J= 4.3Hz, 3H). ^{13}C NMR data (500MHz) for Hdpaq^{2Me} ($CDCl_3$, δ) = 25.2 (s, *C*H$_3$Qu-), 59.6 (s, -*C*H2 CO-), 61.1 (s, -*C*H2Py), 116.6 (s, Qu6), 121.5 (s; Qu3, Qu5, or Qu7), 122.3 (s; Qu3, Qu5, or Qu7), 122.4 (s, Py5), 123.1 (s, Py3), 126.3 (s,Qu10), 126.5 (s; Qu3, Qu5, or Qu7),133.8 (s, Qu8), 136.6 (s, Qu4), 136.8 (s, Py4), 138.2 (s, Qu9), 149.2 (s, Py6), 156.9 (s, Qu2), 158.5 (s, Py2),169.5 (s, C=O). The numbering of the quinoline carbon atoms refers to the standard numbering scheme, as illustrated in Figure A1.12. ESI-MS: {Hdpaq^{2Me} + Na]$^+$} m/z = 420.1766 (calc. = 420.1800)

Preparation of [Mn^{II}($dpaq^{2-Me}$)](OTf). To a stirred solution of 103 mg (0.26 mmol) of $Hdpaq^{2Me}$ in 2mL of MeOH was added 113 mg (0.26 mmol) of $Mn^{II}(OTf)_2$ in 2mL of MeOH, followed by 25 mg (0.26 mmol) of NaO^{t}Bu in 2mL of MeOH under an inert atmosphere. The $Mn^{II}(OTf)_2$ salt was generated using a previously reported method.[29] The orange colored resultant solution was stirred overnight, then filtered, and evaporated to dryness under vacuum. The solid product was recrystallized by layering Et_2O onto a MeOH solution of the Mn^{II} product to yield yellow crystals of [Mn^{II}($dpaq^{2Me}$)](OTf). Crystals for X-ray diffraction analysis were obtained by subsequent recrystallization of the final solid product in the MeOH:Et_2O solvent system. [Mn^{II}($dpaq^{2Me}$)](OTf) was further characterized by ESI-MS (Figure A1.9), EPR spectroscopy (Figure A1.8), X-ray crystallography (Figure A1.1 and Table A1.1), and elemental analysis. Elemental analysis [Mn^{II}($dpaq^{2Me}$)](OTf): $C_{25}H_{22}F_3MnN_5O_4S$ cal. (%) C 50.01, H 3.69, N 11.66; found (%): C 49.15, H 3.68, N 11.41.

X-ray Diffraction Data Collection and Analysis for [Mn^{II}($dpaq^{2Me}$)](OTf). A yellow colored single-domain crystal of [Mn^{II}($dpaq^{2Me}$)](OTf) was suspended with Paratone N oil on a MiteGen MicroMount and placed on a goniometer head in a cold nitrogen stream at 100 K for a single-crystal X-ray structure determination. Monochromatic X-rays were provided by a Bruker diffractometer equipped with Helios high-brilliance multilayer optics, a Platinum 135 CCD detector and a Bruker MicroStar microfocus rotating anode X-ray source operating at 45 kV and 60 mA. Intensity data (6590 0.5°-wide ω- or f-scan frames with counting times of 4-6 seconds each) were collected with the Bruker program SMART[30] and diffracted intensities were measured with the Bruker program SAINT.[31] The space group[32] and crystallographic data are summarized in Table A1.1. The Bruker software package SHELXTL was used to solve the structure and locate all non-hydrogen atoms with "direct methods" techniques. Each methyl group was incorporated into the structural model as a

fixed rigid group (using idealized sp^3 – hybridized geometry and a C—H bond length of 0.98 Å) with idealized "staggered" geometry. The remaining hydrogen atoms were included in the structural model as idealized atoms (assuming sp^2 – or sp^3 -hybridization of the carbon and C—H bond lengths of 0.95 - 0.99 Å). The isotropic thermal parameters of all idealized hydrogen atoms were fixed at values 1.2 (nonmethyl) or 1.5 (methyl) times the equivalent isotropic thermal parameter of the carbon atom to which they are covalently bonded.

All three triflate anions are 50:50 disordered over two closely separated sites in the unit cell. The first and third triflates are disordered about crystallographic inversion centers at (½, 0, 0) and (½, 0, ½), respectively. The bond lengths and angles of the triflates were mildly restrained to have similar values. All stages of weighted full-matrix least-squares refinement were conducted using F_o^2 data with the SHELXXTL XLMP v2013/4 software package.[33] The final structural model incorporated anisotropic thermal parameters for all non-hydrogen atoms and isotopic thermal parameters for all hydrogen atoms. Figure A1.1 shows two Mn^{II} complexes in the $[Mn^{II}(dpaq^{2Me})](OTf)$ structure.

Preparation of $[Mn^{III}(OH)(dpaq^{2Me})](OTf)$. A 2.5 mM $[Mn^{II}(dpaq^{2Me})](OTf)$ solution (3.0 mg in 2 mL of MeCN) was prepared under an inert atmosphere and transferred to a gas-tight cuvette sealed with a pierceable septum. An excess of O_2 gas was then delivered to the solution by means of a syringe, and the formation of $[Mn^{III}(OH)(dpaq^{2Me})](OTf)$ was monitored by electronic absorption spectroscopy (Figure A1.2). The formation was complete in ~250 min and the resulting dark red solution was evaporated to dryness under reduced pressure. The solid residue was then recrystallized using MeCN:Et_2O (3.2 mg; 98% yield). Synthesis of $[Mn^{III}(OH)(dpaq^{2Me})](OTf)$ on a larger scale was undertaken to obtain suitable material for X-ray crystallographic analysis. In this procedure, O_2 gas was passed through an acetonitrile solution of $[Mn^{II}(dpaq^{2Me})](OTf)$ (20 mg in 5 mL), and the complete formation of $[Mn^{III}(OH)(dpaq^{2Me})](OTf)$ was confirmed by ESI-MS and

electronic absorption spectroscopy. The resulting solution was evaporated to dryness under reduced pressure, and the solid residue was recrystallized using slow diffusion of ether into MeCN. Dark red $[Mn^{III}(OH)(dpaq^{2Me})](OTf)$ crystals of X-ray crystallographic quality were obtained by repetitive recrystallization, and were further characterized by ESI-MS (Figure A1.9), X-band EPR spectroscopy (Figure A1.8), Evans NMR spectroscopy, and elemental analysis. $\mu_{eff} = 4.90$ (by Evan's NMR method). Elemental analysis $[Mn^{III}(OH)(dpaq^{2Me})](OTf)$: $C_{25}H_{23}F_3MnN_5O_5S$ cal. (%) C 48.63, H 3.75, N 11.34; found (%): C 46.70, H 3.74, N 10.74.

X-ray Diffraction Data Collection and Analysis for $[Mn^{III}(OH)(dpaq^{2Me})](OTf)$. A deep red single-domain crystal of $[Mn^{III}(OH)(dpaq^{2Me})](OTf)$ was suspended with Paratone N oil on a MiteGen MicroMount and placed on a goniometer head in a cold nitrogen stream at 100 K for a single-crystal X-ray structure determination. Data were collected and analyzed using the same methods as described above for $[Mn^{II}(dpaq^{2Me})](OTf)$. The space group[32] and crystallographic data are summarized in Table A1.2. Hydrogen atoms were located from a difference Fourier and initially included in the structural model as independent isotropic atoms whose parameters were allowed to vary in least-squares refinement cycles. In the final least-squares refinement cycles, the acetonitrile methyl group was included in the structural model as an idealized sp^3 hybridized rigid rotor (with C–H bond lengths of 0.98 Å) that was allowed to rotate freely about its C–C bond and the isotropic thermal parameter of H(11a) was fixed at a value 1.2 times the equivalent isotropic thermal parameter of carbon atom C(11). The triflate CF_3 group is 88:12 rotationally disordered about the C–S bond and the three minor-occupancy fluorine sites were incorporated in the structural model with isotropic thermal parameters. All stages of weighted full-matrix least-squares refinement were conducted using F_o^2 data with the SHELXTL XLMP v2013/4 software package.[33] The final structural model incorporated anisotropic thermal parameters for all full- and major occupancy non-

hydrogen atoms and isotropic thermal parameters for all hydrogen atoms and the three minor-occupancy fluorine atoms.

Kinetic Studies of $[Mn^{III}(OH)(dpaq^{2Me})]^+$ with TEMPOH. For each experiment, a 1.25 mM $[Mn^{III}(OH)(dpaq^{2Me})]^+$ acetonitrile solution was prepared in an argon glovebox, placed in a gas-tight cuvette, and sealed with a septum. The appropriate amount of TEMPOH (10 – 40 equiv) was dissolved in 100μL of acetonitrile and sealed in a vial with a pierceable cap. The gastight syringe used to inject the TEMPOH was first purged with argon before use. Temperature was maintained using a Unisoku cryostat at -35 °C, and the cuvette was allowed to equilibrate to the temperature for 10 minutes before injection took place. Kinetic measurements were made using an Agilent 8453 spectrophotometer. Variable temperature reactions (-35 - 15 °C) were carried out following the same procedure as above. The final reaction product was analyzed by X-band EPR spectroscopy at 5 K, which showed a signal consistent with a TEMPO radical (Figure A1.8).

Kinetic Studies of $[Mn^{III}(OH)(dpaq^{2Me})]^+$ with 2,4,6-tri-*tert*-butylphenol For each kinetic experiment, a 1.25 mM $[Mn^{III}(OH)(dpaq^{2Me})]^+$ solution was prepared in 2 mL of acetonitrile within an argon-filled glovebox, placed in a gas-tight cuvette, and sealed with a septum. The appropriate amount of 2,4,6-tri-*tert*-butylphenol (10-200 equiv) was dissolved in 100 μL of CH_2Cl_2 and sealed in a vial with a pierceable cap. The gastight syringe used to inject the phenol was first purged with argon before use. Temperature was maintained using a Unisoku cryostat at 50°C and the cuvette was allowed to equilibrate to the temperature for 10 minutes before injection took place. Kinetic measurements were made using an Agilent 8453 spectrophotometer. The final reaction product was analyzed by X-band EPR spectroscopy at 5 K, which showed a signal consistent with a phenoxyl radical (Figure A1.8).

Kinetic Studies of $[Mn^{III}(OH)(dpaq^{2Me})]^+$ with xanthene. For each kinetic experiment, a 1.25 mM $[Mn^{III}(OH)(dpaq^{2Me})]^+$ solution was prepared in 1.8 mL of acetonitrile within an argon-filled glovebox, placed in a gas-tight cuvette, and sealed with a septum. 250 equiv of xanthene was dissolved in 300 μL CH_2Cl_2 and sealed in a vial with a pierceable cap. The gastight syringe used to inject the phenol was first purged with argon before use. Temperature was maintained using a Unisoku cryostat at 50 °C and the cuvette was allowed to equilibrate to the temperature for 10 minutes before injection took place. Figure A1.3 shows data for a representative reaction.

Cyclic Voltammetry of $[Mn^{III}(OH)(dpaq^{H})]^+$ and $[Mn^{III}(OH)(dpaq^{2Me})]^+$. Cyclic voltammetry was performed on a 1 mM solution of each Mn^{III}-hydroxo complex in acetonitrile with 600 μL of H_2O added to the solution. Experiments were performed under nitrogen atmosphere, with the solution being purged with nitrogen gas for 1 hour prior to measurements. A glassy carbon working electrode, a platinum auxiliary electrode, and a AgCl/Ag reference electrode were utilized along with a 0.1 M $Bu_4N(PF_6)$ as the supporting electrolyte. Data were referenced to the $E_{p,c}$ for ferrocenium/ferrocene (Fc^+/Fc) in MeCN.

Electronic Structure Calculations. All DFT calculations were carried out using the *ORCA* 3.0.1 software package.[34] The $[Mn^{III}(OH)(dpaq)]^+$ and $[Mn^{III}(OH)(dpaq^{2Me})]^+$ complexes were optimized starting from the available crystal structures.[18] Geometry optimizations were performed using the BP86 functional[35,36] with the Ahlrichs TZVP basis set with the TZVP/J auxiliary basis set for Mn, N, and O and the smaller SVP basis set with the SVP/J auxiliary basis set for C and H.[37,38] For DFT geometry optimizations involving xanthene, the TZVP basis set was also used for the C involved in HAT. The resolution of identity approximation was used for all optimizations.[39] Solvent was implicitly accounted for in all calculations using the COSMO continuum solvent model with the default parameters for acetonitrile as found in *ORCA*.[40] Numerical frequency calculations were

carried out at the same level of theory as the geometry optimizations. The frequency calculations provided the zero point and thermal corrections to the energy as well as confirmed ground state structures by showing no imaginary frequencies. The transition state was identified first by scanning along the O–H bond distance between the manganese-bound hydroxide oxygen and the hydrogen bound to the oxygen of TEMPOH (or, in the case of the xanthene reactions, the C involved in HAT), then taking the highest energy structure and using the *ORCA* saddle point optimization function following the transition state mode. The transition state was confirmed by having only one imaginary frequency, which corresponded to the O–H vibration. Single point energy calculations were carried out on all structures using the TPSSh functional[41] and the Ahlrichs TZVPP basis set with the TZVPP/J auxiliary basis set on all atoms. The RIJCOSX approximation,[42,43] as well as COSMO, were used in all single point energy calculations. Cartesian coordinates for all DFT-optimized structures considered in this work are included in Supporting Information (Tables S7 – S20).

The rotational and vibrational entropy were accounted for using the default values from numerical frequency calculations performed in *ORCA*. The translational entropy was calculated using a correction model developed by Mammen *et al.* to account for the volume available to the solute.[44] For the calculation of the free volume, the van der Waals radii were used to calculate the molecular volume, the experimental value for the concentration of MeCN was used, and the cubic model in a 3D cubic array was chosen. For the final translational entropy calculation, the model excluding the entropy of condensation was used. The enthalpy was taken as the single point electronic energy plus the zero-point energy. The activation free energy was calculated using the total free energy of the infinitely separated reactants and the free energy of the transition state. The

thermodynamic driving force was calculated using the total free energy of the infinitely separated products and the total free energy of the infinitely separated reactants.

2.3 Results and Discussion

Structure and Properties of Mn^{II} and Mn^{III}-hydroxo Complexes. The crystal structure of $[Mn^{II}(dpaq^{2Me})](OTf)$ (**1-Me**) shows a six-coordinate Mn^{II} center bound by the five nitrogen donors of the dpaq ligand (Figure 2.1). The coordination sphere is completed by binding of the amide oxygen group from an adjacent **1-Me** cation, creating the same polymeric structure previously observed in crystals of $[Mn^{II}(dpaq^{H})](OTf)$ (**1-H**).[18] The most notable differences between **1-Me** and **1-H** are $Mn–N_{quinoline}$ (Mn-N1) and $Mn\text{-}O_{amide}$ (Mn–O2) bond elongations in the **1-Me** structure by 0.054 and 0.037 Å, respectively (see Table 2.2 for a structural comparison). When **1-Me** is dissolved in MeCN, the electronic absorption spectrum shows a weak band at 500nm (ε= 24 $M^{-1}cm^{-1}$), which is presumably a charge-transfer band associated with the Mn^{II} complex. The perpendicular-mode X-band EPR spectrum of a frozen solution of **1-Me** at 5 K shows a large feature centered at g = 2.04, attributed to the mononuclear Mn^{II} center (Figure A1.8). Hyperfine splitting for this feature was not resolved, as was also observed for **1-H**.[18]

Table 2.1. Selected manganese-ligand bond lengths (Å) from the crystal structures of $[Mn^{II}(dpaq^{2Me})](OTf)$ (1-Me), $[Mn^{II}(dpaq)](OTf)$ (1-H), $[Mn^{III}(OH)(dpaq^{2Me})](OTf)$ (2-Me), and $[Mn^{III}(OH)(dpaq)](OTf)$ (2-H).

$[Mn^{II}(dpaq^{R})](OTf)$ (**1-R**)			$[Mn^{III}(OH)(dpaq^{R})](OTf)$ (**2-R**)		
Bond [a]	**1-Me**	**1-H** [b]	Bond [a]	**2-Me**	**2-H** [b]
Mn–O1A	2.116(2)	2.079(2)	Mn–O2	1.819(3)	1.806(13)
Mn–N1B	2.268(3)	2.214(3)	Mn–N1	2.186(3)	2.072(14)
Mn–N2B	2.172(3)	2.191(3)	Mn–N2	1.979(3)	1.975(14)
Mn–N3B	2.317(3)	2.314(3)	Mn–N3	2.203(3)	2.173(14)
Mn–N4B	2.275(3)	2.244(3)	Mn–N4	2.148(3)	2.260(14)
Mn–N5B	2.286(3)	2.286(3)	Mn–N5	2.158(3)	2.216(15)

[a] See Figures 1 and S1 for the atom numbering scheme. [b] Taken from reference 18.

Upon addition of excess O_2, the MeCN solution of **1-Me** changes from orange to a dark purple, with absorption bands appearing at 515 nm (ε = 228 $M^{-1}cm^{-1}$) and 770nm (ε = 100 $M^{-1}cm^{-1}$; see Figure A1.2). These new absorption features are similar to those of **2-H** (λ = 550 and 780 nm, with corresponding ε values of 320 and 130 $M^{-1}cm^{-1}$; see Scheme 2.1). The reaction of **1-Me** with O_2 shows full formation after 150 minutes, approximately five times slower than the reaction of O_2 with **1-H**. The purple solution formed upon oxygenation of **1-Me** is EPR silent in both perpendicular and parallel-modes at X-band frequency (Figure A1.8). Thus, **1-Me** has been completely consumed, and an EPR silent-species is formed. Examination of the purple solution by the NMR method of Evans reveals an effective magnetic moment (μ_{eff}) of 4.90, consistent with a mononuclear, S = 2, Mn^{III} center. Such species are often EPR-silent even in parallel-mode X-band experiments due to a larger zero-field splitting of the Mn^{III} ion.[45]

Definitive assignment for the purple chromophore comes from X-ray diffraction experiments on crystals grown by ether diffusion into the MeCN solution. The X-ray structure shows a mononuclear Mn^{III}-hydroxo complex, $[Mn^{III}(OH)(dpaq^{2Me})](OTf)$, where the Mn^{III} coordination sphere is completed by the five nitrogen donors of the $dpaq^{2Me}$ ligand and with the hydroxo bound

trans to the amide group (Figure 2.1). The structure also contains free triflate, ether, and acetonitrile groups. The $dpaq^{2Me}$ ligand binds in a similar fashion to that previously reported for $dpaq^{H}$, although with a large 0.11 Å elongation in the bond length of the equatorial quinoline (Mn–N1; Table 2.1). This is presumably caused by the steric bulk of the methyl group adjacent to the nitrogen donor. Similar elongations of ~0.1 Å have been observed for Fe^{II} complexes when comparing α-methyl-appended and unsubstituted pyridines, although for the Fe^{II} complexes the introduction of the α-methyl-substituents often results in a change from a low-spin (S = 0) to a high-spin (S = 2) ground state.[25-27] In addition to the Mn–N1 elongation in **2-Me**, there is also a contraction of the two pyridine Mn–N bond distances of 0.1 and 0.06 Å for the Mn–N4 and Mn–N5 bonds, respectively (see Figure 2.1 for the numbering scheme and Table 2.1). Notably, the Mn–OH bond distances of **2-Me** and **2-H** are identical, within the experimental uncertainty (Table 2.1). The **2-Me** structure also displays an extended hydrogen-bonding interaction between the hydroxo ligand and the amide oxygen of a different **2-Me** molecule, with an oxygen-oxygen separation of 2.787 Å, which is approximately 0.05 Å longer than that seen in the **2-H** structure.[18]

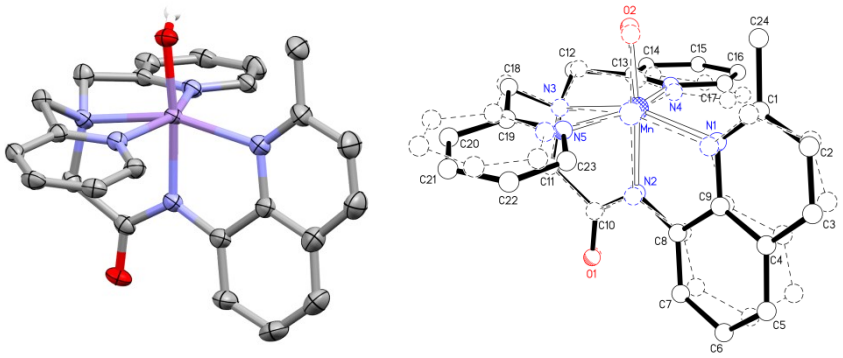

Figure 2.1. Left: ORTEP diagram of $Mn^{III}(OH)(dpaq^{2Me})](OTf)$. Right: ORTEP overlay of $[Mn^{III}(OH)(dpaq^{2Me})]$ (bold) and $[Mn^{III}(OH)(dpaq^{H})]^{+}$. Hydrogen atoms, solvent, and noncoordinating triflate counterions were removed for clarity.

The reduction potential of **2-Me** in MeCN was investigated experimentally using cyclic voltammetry. Reproducible CV data were achieved for experiments run with 600 μL added water. (In the absence of added water, multiple reduction processes were observed. Previous investigations of Mn^{III}-hydroxo and Fe^{IV}-oxo complexes have established the importance of added water in obtaining ideal CV behavior by eliminating competing decay processes following reduction.[46-48] We note that, under these conditions, **2-H** shows a slightly higher reduction peak potential than that previously reported.[18]) Under these conditions, reduction of both **2-Me** and **2-H** are irreversible processes, with peak potentials, $E_{p,c}$, of -0.62 and -0.73 V, respectively (Figure A1.4, all values versus Fc/Fc^+ in MeCN). Thus, **2-Me** shows an increase in peak potential of +0.09 V, indicating a more facile reduction.

Oxidative Reactivity of $[Mn^{III}(OH)(dpaq^{2Me})]^+$. In order to evaluate the effect of these minor perturbations in structure and reduction potential on reactivity, **2-Me** was reacted with various substrates with weak O–H and C–H bonds under an inert atmosphere. We first investigated the reactivity of **2-Me** with TEMPOH. Because of the weak BDFE of TEMPOH (BDFE = 66.5 kcal/mol, in MeCN at 25 °C), as well as its propensity to participate in CPET reactions,[49] this substrate is commonly used to investigate the reactivity of mid-valent oxidants.[17,18,50] Treatment of **2-Me** with 10 equiv of TEMPOH at 25 °C in MeCN led to complete bleaching of the electronic absorption signals of the Mn^{III}-hydroxo within 8 seconds. This apparently rapid reaction was unanticipated, as the reaction of **2-H** with 100 equiv of TEMPOH is complete within 10 minutes.[18] To monitor the kinetics of TEMPOH oxidation by **2-Me**, the Mn^{III}-hydroxo was treated with 10 equiv of substrate in MeCN at -35 °C. In this case, the disappearance of **2-Me** was still rapid (95% complete within 1 minute), but the change in absorbance versus time showed first-order behavior past 5 half-lives, permitting a kinetic analysis (Figure 2.2). The final spectrum after reaction is that of

1-Me in MeCN, which is formed in near 100% yield (Figure 2.2). A perpendicular-mode X-band EPR spectrum collected for frozen MeCN solutions following the reaction shows an intense feature at g = 2.03 which corresponds to the TEMPO radical (Figure A1.8). On the basis of these results, we conclude that **2-Me** reacts with TEMPOH to produce $[Mn^{II}(dpaq^{2Me})]^+$ and the TEMPO radical.

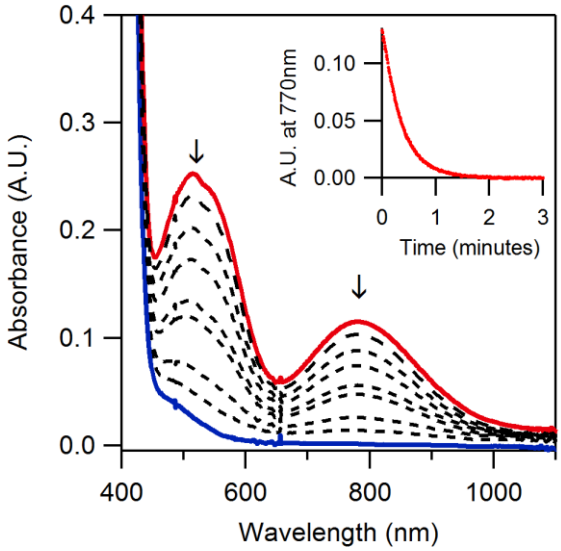

Figure 2.2. Electronic absorption spectra of 1.25 mM $[Mn^{III}(OH)(dpaq^{2Me})]^+$ upon the addition of 10 equiv TEMPOH at -35ºC in MeCN (initial and final spectra are the red and blue traces, respectively). Inset shows the decay of the 770 nm band over time.

A series of reactions of $[Mn^{III}(OH)(dpaq^{2Me})]^+$ with 10 - 40 equiv of TEMPOH (pseudo-first order conditions) were carried out at -35 °C. The reactions provided a linear correlation between TEMPOH concentration and the pseudo-first order rate constant (Figure 2.3). The slope of this relation gives a second order rate constant (k_2) of 3.9(3) $M^{-1}s^{-1}$ at -35 °C. Thus, for the reaction with TEMPOH, **2-Me** has a second-order rate constant, *at -35ºC*, that is 30 times faster than the same reaction with **2-H** *at 25 °C* (k_2 = 0.13(1) $M^{-1}s^{-1}$). The rate is also much larger than that observed for the corresponding Mn^{III}-methoxy complex of the dpaq ligand, $[Mn^{III}(OMe)(dpaq)]^+$ (k_2 = 0.080(1)).[51]

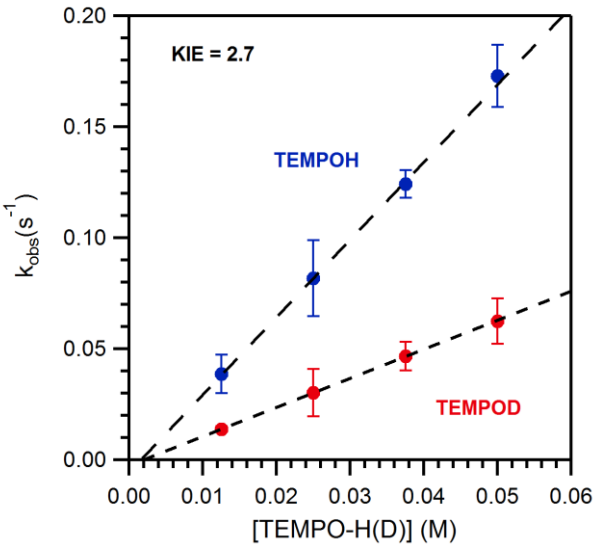

Figure 2.3. Pseudo-first-order rate constants, k_{obs} (s^{-1}) as a function of TEMPOH and TEMPOD concentration for a 1.25 mM solution of 2-Me. The second order rate constant, k_2 (M^{-1} s^{-1}), was calculated from the slope of the linear correlation.

Using TEMPOD, the H/D kinetic isotope effect (KIE) for the reaction with **2-Me** was determined to be 2.7 (Figure 2.3). This KIE suggests that O–H/D bond cleavage is involved in the rate determining step for the reaction. We note that the intercepts for plots of k_{obs} versus substrate concentration for both TEMPOH and TEMPOD are slightly negative; however, the intercepts are similar to each other and both are indistinguishable from zero within the experimental uncertainty.

To determine the activation parameters for the reaction of TEMPOH with **2-Me**, an Eyring analysis was carried out by monitoring TEMPOH oxidation reactions from -35 to 15 °C. This provided $\Delta H^{\ddagger}$ and $\Delta S^{\ddagger}$ of 5.7(3) kcal mol^{-1} and 41(1) cal mol^{-1} K^{-1}, respectively (Table 2.2 and Figure 2.4). This gives, at 25 °C, an activation free energy of 17.9 kcal mol^{-1}, with the entropic contribution being 12.2 kcal mol^{-1}. Utilizing the activation parameters, we can estimate a second order rate constant (k_2) for **2-Me** at 25 °C of 31 $M^{-1}s^{-1}$. Thus, the reaction of **2-Me** with TEMPOH shows a remarkable increase in the rate constant of ~240-fold compared to that of **2-H** (k_2 = 0.13(1) $M^{-1}s^{-1}$

at 25 °C). The nature of the activation barrier has also changed significantly with the addition of the methyl group. A comparison of the kinetic parameters for TEMPOH oxidation for **2-Me**, **2-H**, and the Mn^{III}-methoxy complex $[Mn^{III}(OMe)(dpaq)]^+$ is provided in Table 2.2. Specifically, the activation enthalpy has decreased by nearly a factor of two, from 9.9(9) kcal/mol for **2-H** to 5.7(6) kcal mol^{-1} for **2-Me**, while the entropic contribution, at 25 at 25 °C, is slightly increased (10 versus 12 kcal mol^{-1} for **2-H** and **2-Me**, respectively). This increase in the entropic contribution to the free energy of activation could be accounted for by an increase in steric strain brought about by the proximity of the 2-methyl substituent to the reaction center. However, the decrease in the $\Delta H^{\ddagger}$ dominates the observed reaction rate, demonstrating that the increase in the strain of the transition state is overcome by the more favorable electronics of **2-Me**. TEMPOH is also not a very bulky substrate and is likely to have little direct interaction with the methyl group.

Table 2.2. Reaction Parameters for the Oxidation of TEMPOH, xanthene, and 2,4,6-tri-*tert*-butylphenol by $[Mn^{III}(OR)(dpaq^R)]^+$ Complexes.

Complex	**TEMPOH**				**xanthene**	**2,4,6-tri-*t*-butyl-phenol**
	k_2 (M^{-1} s^{-1})[a]	$\Delta H^{\ddagger}$ [b]	$\Delta S^{\ddagger}$ [c]	$\Delta G^{\ddagger}$ [b]	k_{obs} (s^{-1})[d]	k_2 (M^{-1} s^{-1})[e]
$[Mn^{III}(OH)(dpaq^H)]^+$	0.13(1)	9.9(9)	-35(3)	20.3	0.0008	ND[f]
$[Mn^{III}(OMe)(dpaq^H)]^+$	0.080(1)	11.4(5)	-27(2)	19.4	ND[g]	0.0052(1)
$[Mn^{III}(OH)(dpaq^{2Me})]^+$	31[h]	5.7(3)	-41(1)	17.9	0.00025	0.044(2)

[a] Values at 25 °C. [b] Units of kcal mol^{-1}. [c] Units of cal mol^{-1} K^{-1}. [d] Pseudo-first order rate constant using 250 equivalents of xanthene at 50 °C. [e] Values at 50 °C. [f] The reaction of $[Mn^{III}(OH)(dpaq^H)$ with 2,4,6-tri-*tert*-butylphenol displays saturation kinetics; thus, the reaction cannot be described by a second-order rate constant. [g] Treatment of $[Mn^{III}(OMe)(dpaq^H)]^+$ with xanthene lead to a decay rate of the same order as the self-decay rate of this complex; see reference 51. [h] The second-order rate

constant at 25 °C was determined using the activation parameters and the corresponding rate at constant at -35 °C.

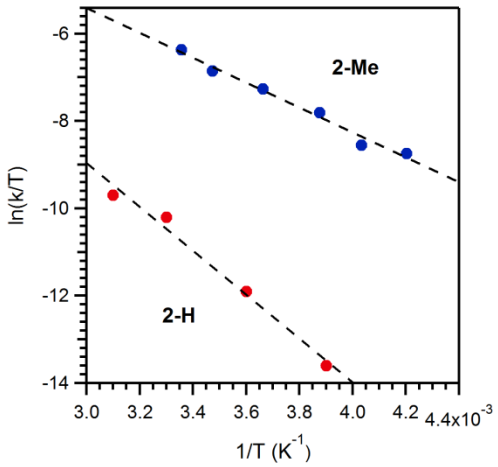

Figure 2.4. Plot of ln(k/T) as a function of 1/T(K^{-1}) for the reaction of 1.25 mM 2-Me with TEMPOH from -35ºC to 15ºC (blue circles). Corresponding data for the reaction of 1.25 mM 2-H with TEMPOH (red circles) are included for comparison.

To date, only two synthetic Mn^{III}-hydroxo species are known to abstract hydrogen atoms from C–H bonds. The $[Mn^{III}(OH)(PY5)]^{2+}$ complex of Goldsmith and Stack can attack the relatively strong C–H bond of toluene (BDFE = 87 kcal/mol in MeCN)[16], while **2-H** attacks the weaker C–H bond of xanthene (BDFE = 73.3 kcal/mol in dimethyl sulfoxide), albeit very slowly (with 250 equiv xanthene, $k_{obs} = 8 \times 10^{-4}$ s^{-1} at 50 °C in MeCN).[18] When **2-Me** was treated with 250 equiv xanthene at 50 °C, the reaction showed a slow decay of the electronic absorption signal from the Mn^{III}-hydroxo species (Figure A1.3). After 16 hours, approximately 85% of **2-Me** had been consumed. A pseudo-first order rate constant of 2.5×10^{-4} s^{-1} was determined, which is a factor of three smaller than that observed for the reaction of **2-H** with xanthene. Thus, the reactivity of **2-Me** with xanthene is comparable to that of **2-H**, which is unanticipated given the large rate differences with TEMPOH.

Because of the seemingly contradictory reactivity of **2-Me** towards TEMPOH and xanthene, we investigated the reactivity of this complex using a substrate with a more sterically-hindered O–H bond. (We also explored the reactivity of **2-Me** with 1,4-cyclohexadiene, which has a less hindered C–H bond. However, the kinetic profile for this reaction was complex. Instead of the expected formation of **1-Me**, this reaction yielded a colored product that has eluded further characterization.) **2-Me** was reacted with 10 to 200 equiv 2,4,6-tri-*tert*-butylphenol at 50 °C under an argon atmosphere. For each reaction, the electronic absorption features associated with the Mn^{III}-hydroxo decayed, while the characteristic 2,4,6-tri-*tert*-butylphenoxyl radical feature (λ_{max} = 628 nm; ε = 400(10) $M^{-1}s^{-1}$)[52] grew in simultaneously (Figure 2.5). Perpendicular-mode X-band EPR data collected following the reaction showed a single derivative feature characteristic of the phenoxyl radical (Figure A1.8). In addition, the absorbance intensity of the 2,4,6-tri-*tert*-butylphenoxyl radical following the reaction indicates 90% formation of this radical relative to **2-Me**. The second order rate constant for this reaction was determined to be 4.4(2) × 10^{-2} M^{-1} s^{-1} from the linear correlation of the k_{obs} and the substrate concentration (Figure 2.6). The H/D KIE for this reaction was found to be 2.1, which is similar to that found for the TEMPOH/TEMPOD reaction and suggests that the reaction is undergoing a CPET mechanism for both substrates. Phenol oxidation by **2-Me** also shows a dramatic shift in the kinetic model compared to the reaction of **2-H** with phenols. With that complex, the reaction was shown to involve saturation kinetics, giving a non-linear rate dependence on substrate concentration (*i.e.*, the k_{obs} values leveled at high substrate concentration).[18] This was attributed to the stabilization of a hydrogen-bonded precursor complex. This change in kinetic model for phenol oxidation by **2-Me** could arise from a destabilization of a hydrogen-bonded structure due to interactions between the bulky *tert*-butyl groups on the substrate and the methyl functionalized quinoline of **2-Me**. This difference in phenol reactivity for **2-H** and **2-Me**

complicates a direct comparison of reaction rates, because the **2-H** reaction cannot be properly described by a second-order rate constant. However, previous work with the Mn^{III}-methoxy analogue of **2-H**, $[Mn^{III}(OMe)(dpaq)]^+$, showed the standard second-order kinetics observed here for **2-Me**.[51] The second-order rate constant for that reaction was 5.2(1) x 10^{-3} $M^{-1}s^{-1}$, which is slightly slower than that observed for **2-Me** (4.4(2) x 10^{-2} M^{-1} s^{-1}). Thus, while **2-Me** reacts with TEMPOH ~390-fold faster than $[Mn^{III}(OMe)(dpaq)]^+$ (Table 2.2), these two complexes show more comparable reaction rates towards the bulkier substrate 2,4,6-tri-*tert*-butylphenol. These results show an increased reactivity of **2-Me** with smaller substrates but similar, or even slower, reaction rates with larger, or rigid, substrates (*i.e.*, phenols and xanthene).[53]

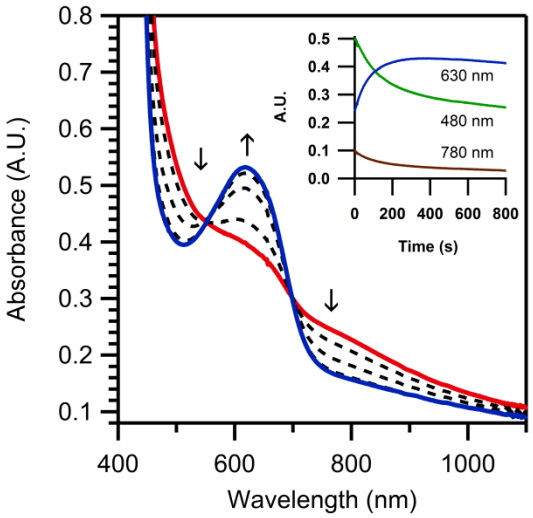

Figure 2.5. Electronic absorption spectra of 1.25 mM 2-Me with the addition of 100 equiv tri-*tert*-butylphenol at 50 °C in MeCN. Inset graphic shows the decay of 2-Me and growth of the phenoxyl radical. The tri-*tert*-butylphenoxyl radical product, which absorbs at 630 nm, reaches maximum concentration at ~200 s, and then slowly decays, as seen in the decrease of the absorbance signals after this time point.

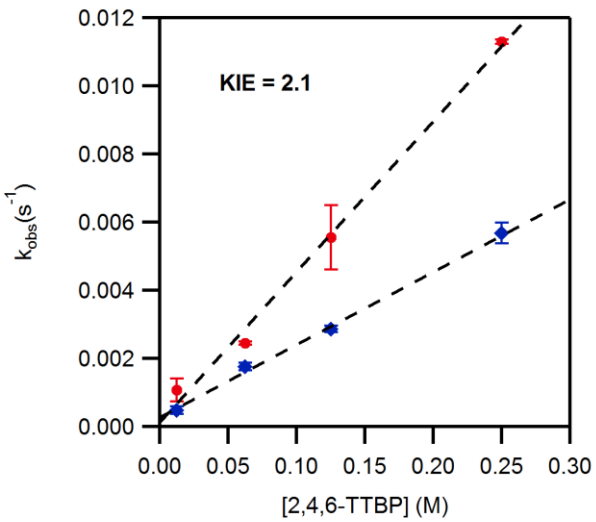

Figure 2.6. Pseudo-first-order rate constant, k_{obs} (s^{-1}) as a function of 2,4,6-tri-tert-butylphenol concentration for a 1.25 mM solution of 2-Me (red circles) and corresponding data for deuterated phenol (blue circles). The second order rate constant, k_2 (M^{-1} s^{-1}), was calculated from the slope of the linear correlation.

Electronic Structure Computations. Electronic structure methods were used to analyze the basis for this intriguing reactivity. DFT-optimized structures for both **2-H** and the **2-Me** are in good agreement of the crystal structures (Tables 1 and S5). The free energy profiles for the reaction of each complex with TEMPOH are shown in Figure 2.7. There is excellent agreement between the calculated free energy activation barriers and the experimentally determined values.[18] This agreement, along with the smaller KIE values found experimentally, suggest that tunneling does not play a large roll in this CPET process. The reaction coordinate takes place along the S = 2 surface, with the resulting TEMPO radical (S = 1/2) and Mn^{II} product (S = 5/2) antiferromagnetically coupled. The structures at the transition state are shown in Figure 2.8A. These illustrate that the hydrogen atom is only partially transferred between the substrate and the Mn-hydroxo, with an O–H bond distance of

1.14 Å for **2-Me** and 1.15 Å for **2-H**. The transition state structure with **2-Me** shows that the TEMPOH is able to orient itself without interacting with the methyl-quinoline group (Figure 2.8A).

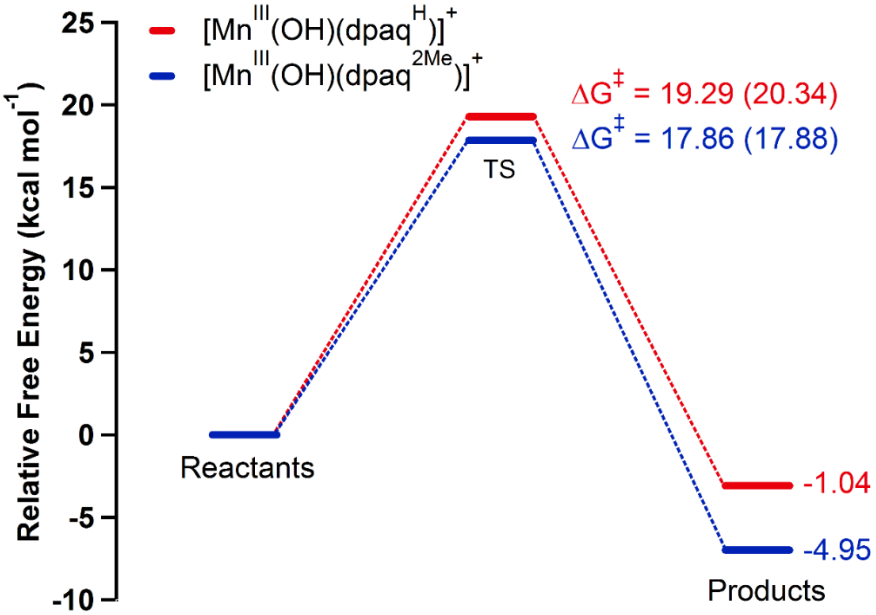

Figure 2.7. DFT-calculated reaction coordinate for 2-H (red) and 2-Me (blue) with TEMPOH. Experimental values are in parenthesis. All values are in kcal mol^{-1}.

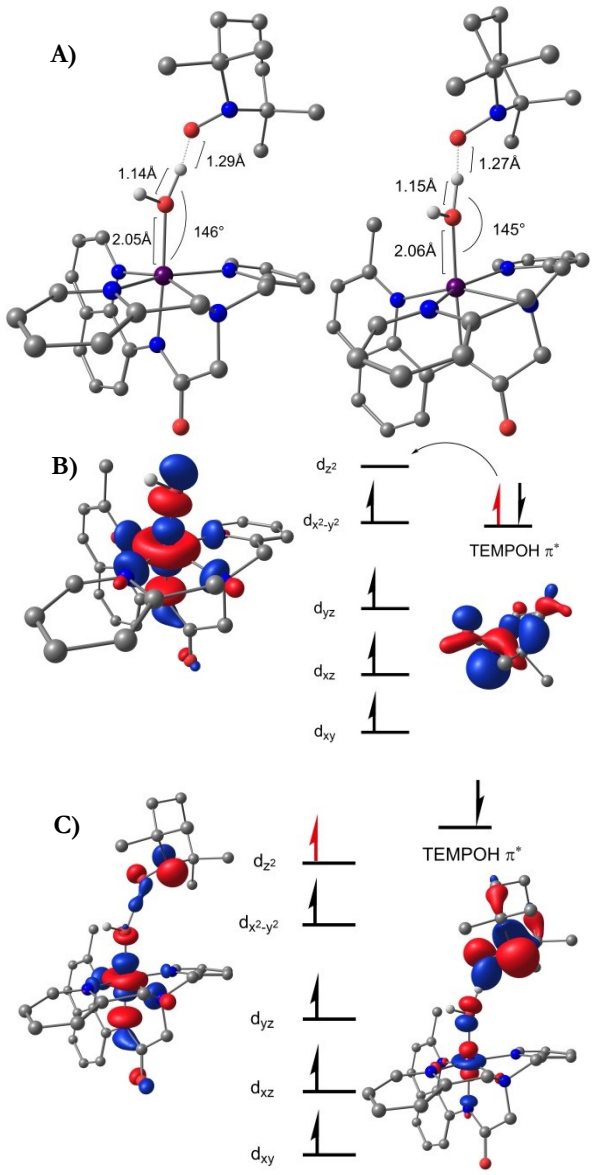

Figure 2.8. A) Structural comparison of 2-H (left) and 2-Me (right) transition states. B) Qualitative MO diagram of 2-Me and TEMPOH reactants showing the TEMPOH HOMO and manganese 3d-manifold. Surface contour plots of the 2-Me α-spin LUMO (Mn^{III} d_z^2 MO) and the α-spin TEMPOH HOMO are shown on the left- and right-hand sides, respectively. C) Corresponding transition-state MO diagram for 2-Me and TEMPOH, with surface countour plots of the α-spin HOMO (left) and LUMO (right). The transition state MO plots depict the strong interaction between Mn-hydroxo and substrate orbitals.

For the CPET reaction, the electron-accepting orbital of both **2-H** and **2-Me** is the α-spin LUMO, which consists of the Mn $3d_{z^2}$ orbital that is strongly σ-antibonding with the hydroxide $2p_z$

orbital (Figure 2.8B). In the transition state, this MO is strongly mixing with the nitrogen and oxygen orbitals of TEMPOH (Figure 2.8C), which forms a superexchange pathway mediating electron to transfer from substrate to the metal center. A previous computational investigation of iron lipoxygenase also identified strongly interacting substrate and Fe-hydroxo orbitals in the transition state, with little or no localization of electron density on the transferring proton.[54] However, in that case the orbital accepting the electron was a β-spin, Fe-OH π-antibonding MO (*i.e.*, a t_{2g} orbital, using O_h symmetry labels). For the $S = 2$ manganese(III)-hydroxo units considered here, the electron must be added to the α-spin $3d_{z^2}$ orbital (*i.e.*, an e_g orbital), which is the LUMO for both **2-Me** and **2-H**.[54] In the transition state, the LUMO shows a similar bonding pattern to the HOMO but with a much larger percent contribution from the TEMPO nitrogen and oxygen (Figure 2.8C). The composition of the HOMO and LUMO point to a strongly interacting system, with most of the character of the transferred electron residing on the manganese center. The Loewdin spin density on the manganese center in the transition state of both **2-Me** and **2-H** is also indicative of a Mn^{II} center.

The requirement for the electron to transfer into the Mn^{III} $3d_{z^2}$ - OH $2p_z$ σ-antibonding MO means that an ideal angle of approach, maximizing overlap between the donor and acceptor orbitals, would give an angle between the manganese, oxygen, and transferring hydrogen (Mn-O-H_{TEMPOH}) of near 180°. However, the Mn–O–H_{TEMPOH} angle is ~145° in both transition-state structures. This angle represents a compromise between the electronic ideal of 180° and the steric limitations created by the hydroxyl proton, which render a 180° angle unfeasible. This places a severe steric constraint upon substrate oxidation by a Mn^{III}-hydroxo species, as exemplified experimentally by the reactivity of **2-Me** with bulkier substrates.

The products of the DFT reaction coordinate calculations are the manganese(II)-aqua complex, $[Mn^{II}(OH_2)(dpaq^{R})]^{+}$, and the TEMPO radical. The driving force for the **2-Me** reaction is calculated to be almost 4 kcal mol^{-1} larger than that of **2-H** (Figure 2.7). This driving force represents the difference in O–H BDFE between the manganese(II)-aqua complexes and TEMPOH. CPET reactions, whether for metal-hydroxo or -oxo species, commonly show correlation between the thermodynamic driving force and the activation barrier, with more exergonic reactions proceeding with lower barriers.[55] This relationship holds true for the reaction of TEMPOH with **2-Me** and **2-H**, at least in terms of the DFT results (Figure 2.7), suggesting that the rate enhancement of **2-Me** can be attributed to an increase in the BDFE of the $[Mn^{II}(OH_2)(dpaq^{2Me})]^{+}$ complex. Experimentally, the BDFE of $[Mn^{II}(OH_2)(dpaq^{2Me})]^{+}$ could be calculated from the $Mn^{III}(OH)/Mn^{II}(OH)$ reduction potential and the pK_a for the manganese(III)-aqua complex using the Bordwell relationship.[56] Thus, a complete picture of the difference in driving force for **2-H** and **2-Me** requires knowledge of the reduction potentials *and* pK_a values. Unfortunately, the pK_a values of **2-H** and **2-Me**, and their Mn^{II}-aqua analogues, are currently unobtainable experimentally. None of the complexes are soluble in water at high enough concentrations to perform CV experiments at different pH, and the Mn^{III}-hydroxo species show rapid, and complex, decay upon the addition of acid. In the absence of experimental pK_a values, we estimated the shift in pK_a for **2-H** and **2-Me** using electronic structure computations following a procedure developed by Hammes-Schiffer (further details are available in Supporting Information).[57] To account for known deficiencies in the treatment of the free energy of the electron, the potential of the electrode in the reduction calculation, as well as in the free energy of the proton in the pK_a calculation, the $[Mn^{III}(OH)(PY5)]^{2+}$ complex was utilized as a reference system, as this complex has a well-defined reduction potential and pK_a.[16] As a test of the appropriateness of this method, we first calculated $E_{1/2}$ values, which were found to be -0.83 V and -

0.60 V (versus Fc/Fc^+) for **2-H** and **2-Me**, respectively. These values agree quite well with the experimental $E_{p,c}$ values (-0.73 and -0.62 V). The calculated pK_a values were quite similar, 21 and 20 for **2-H** and **2-Me**, respectively. With these $E_{1/2}$ and pK_a parameters, the BDFEs for **2-H** and **2-Me** were calculated to be 64 and 68 kcal mol^{-1}, respectively, consistent with the 4 kcal/mol difference in driving force from the reaction coordinate calculations (Figure 2.7). Importantly, these computations demonstrate that the increased driving force for the reaction of **2-Me** with TEMPOH is due to a more favorable reduction of the Mn^{III}-OH complex, a conclusion that is reinforced by the experimental CV data.

If **2-Me** has a stronger intrinsic driving force for CPET reactions, why are the reaction rates with xanthene and tri-*tert*-butylphenol more comparable to those of **2-H**? To address this question, we performed reaction coordinate calculations to identify transition states for hydrogen-atom transfer from xanthene to **2-Me** and **2-H**. These calculations indicate a lower enthalpy of activation for **2-H** compared to **2-Me** ($\Delta H^{\ddagger}$ = 22.7 and 25.6 kcal mol^{-1}, respectively), with comparable entropies of activation at 50 °C ($\Delta S^{\ddagger}$ = -11.96 and -10.94, respectively). Consequently, **2-H** has a lower free-energy barrier for hydrogen-atom transfer with xanthene (SI, Table A1.6) and is predicted to react with xanthene faster than **2-Me**. This is consistent with the experimental rates (k_{obs} of 8.0 × 10^{-4} s^{-1} and 2.5 × 10^{-4} s^{-1} for **2-H** and **2-Me**, respectively; see Table 2.2). The transition-state structures for both systems are shown in Figure 2.9. These structures indicate partial hydrogen-atom transfer, with O–H bond distances of 1.13 and 1.12 Å for **2-Me** and **2-H** respectively. The C–H bond in xanthene is also significantly elongated in each transition state (Figure 2.9). Although the structural parameters within the Mn^{III}-hydroxo-xanthene unit are comparable, the orientation of xanthene relative to the Mn^{III} complex is different, as evident in the overlay plot of the two transition states in Figure 2.9C. In the transition state of **2-H**, one ring of xanthene is located near

the quinoline ligand. Superimposing this xanthene location on the transition state of **2-Me** results in close contact between xanthene carbons atoms and hydrogen atoms of the 2-methyl-substituent (C···H contacts of 2.08 and 2.25 Å). These contacts are illustrated in a space-filling model in Supporting Information (Figure A1.6). These DFT-derived structures provide strong evidence that xanthene must oriented differently in the **2-Me** transition state to avoid the bulky quinoline moiety. We presume that this reorientation has a destabilizing effect, leading to the higher-energy transition-state of **2-Me** as compared to **2-H**.

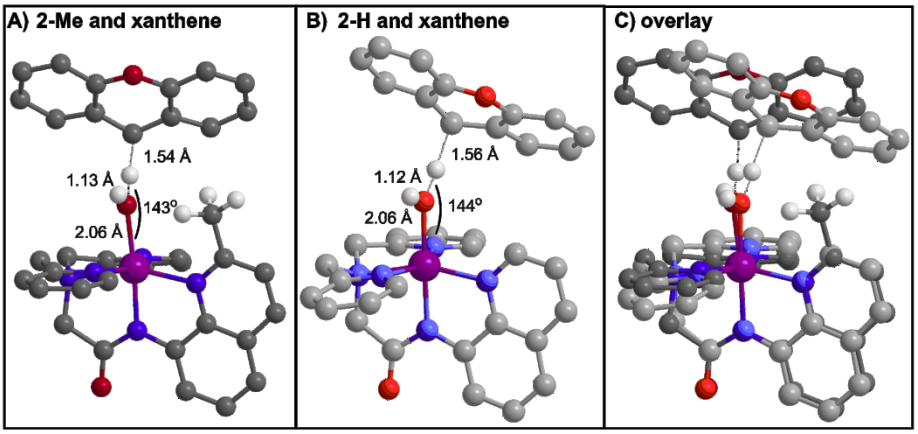

Figure 2.9. Transition-states for hydrogen-atom transfer from xanthene to 2-Me (A) and 2-H (B). Panel C shows an overlay plot, where the two transition-state structures have been superimposed.

Unfortunately, we were unable to further corrobarate this model for the tri-*tert*-butylphenol reaction, as we could not locate transition states for the reaction of this substrate with either **2-H** or **2-Me**. Surface scans of the Mn-O···H_{phenol} coordinate are endothermic and proceed uniformly uphill to products. Nonetheless, stationary points along the Mn-O···H_{phenol} coordinate show the steric restrictions of this reaction. The phenol approaches the Mn^{III}-hydroxo complex along a vector perpendicular to the quinoline moiety, similar to that observed in the transition state with TEMPOH (cf. Figures S7 and 8A). This approach trajectory places one *t*-butyl arm in close proximity with the

2-methyl substituent. An alternative approach of phenol parallel with the quinoline moiety would place the hydroxo proton in close proximity to the 2-methyl substituent, also creating steric clash. Thus, although the CPET reactivity of **2-Me** is intrinsically favored over that of **2-H** because of a larger thermodynamic driving force, we propose that steric restrictions can dampen the reactivity considerably.

Conclusions

There are few synthetic hydroxomanganese(III) complexes capable of oxidizing substrates via PCET, and, of those reported, a wide range of ligand systems are used with large differences in oxidative ability.[16-18] These differences in the ligand systems make it difficult to identify factors responsible for changes in reactivity. In order to better elucidate the nature of these reactions, small perturbations to the ligand systems can prove very useful. The work in this paper is the first to explore how such a change can affect the CPET reactivity of a hydroxomanganese(III) species. A small change to the second coordination sphere, by incorporating a 2-methyl-quinoline group in the (dpaq) ligand, leads to a dramatic increase in the rate of reaction with TEMPOH, which is related to an increased thermodynamic driving force reflected in a lower reduction potential. With the substrates tri-*tert*-butylphenol and xanthene, however, there are modest changes in reaction rate, likely due to steric clash caused by the combined effect of both the 2-methyl substituent and the hydroxo proton. Such interactions could lead to steric-controlled oxidation of substrates. Further investigation is needed to explore the oxidative limits of **2-Me** and related Mn^{III}-hydroxo complexes.

Acknowledgements

This work was supported by the U.S. National Science Foundation (CHE-1056470 to T.A.J.). The U.S. NSF is also acknowledged for funds used for the purchase of X-ray instruments (CHE-0079282) and the EPR spectrometer (CHE-0946883). Support for the NMR instrumentation was provided by NIH Shared Instrumentation Grant S10OD016360, NSF Major Research Instrumentation Grant 9977422, and NIH Center Grant P20 GM103418.

References

(1) Su, C.; Oliw, E. H. *Journal of Biological Chemistry* **1998**, *273*, 13072.
(2) Su, C.; Sahlin, M.; Oliw, E. H. *Journal of Biological Chemistry* **2000**, *275*, 18830.
(3) Wennman, A.; Karkehabadi, S.; Oliw, E. H. *Archives of Biochemistry and Biophysics* **2014**, *555–556*, 9.
(4) Gaffney, B. J.; Su, C.; Oliw, E. H. *Applied Magnetic Resonance*, *21*, 411.
(5) Wennman, A.; Oliw, E. H.; Karkehabadi, S.; Chen, Y. *J Biol Chem* **2016**.
(6) Gilchrist, M. L.; Ball, J. A.; Randall, D. W.; Britt, R. D. *Proceedings of the National Academy of Sciences of the United States of America* **1995**, *92*, 9545.
(7) Hoganson, C. W.; Lydakis-Simantiris, N.; Tang, X.-S.; Tommos, C.; Warncke, K.; Babcock, G. T.; Diner, B. A.; McCracken, J.; Styring, S. *Photosynth Res* **1995**, *46*, 177.
(8) Borovik, A. S. *Chemical Society Reviews* **2011**, *40*, 1870.
(9) Lansky, D. E.; Goldberg, D. P. *Inorg. Chem.* **2006**, *45*, 5119.
(10) Leto, D. F.; Ingram, R.; Day, V. W.; Jackson, T. A. *Chemical Communications* **2013**, *49*, 5378.
(11) Chen, J.; Lee, Y.-M.; Davis, K. M.; Wu, X.; Seo, M. S.; Cho, K.-B.; Yoon, H.; Park, Y. J.; Fukuzumi, S.; Pushkar, Y. N.; Nam, W. *Journal of the American Chemical Society* **2013**, *135*, 6388.
(12) Leeladee, P.; Baglia, R. A.; Prokop, K. A.; Latifi, R.; de Visser, S. P.; Goldberg, D. P. *Journal of the American Chemical Society* **2012**, *134*, 10397.
(13) Baglia, R. A.; Dürr, M.; Ivanović-Burmazović, I.; Goldberg, D. P. *Inorganic Chemistry* **2014**, *53*, 5893.
(14) Parsell, T. H.; Yang, M.-Y.; Borovik, A. S. *Journal of the American Chemical Society* **2009**, *131*, 2762.
(15) Wu, X.; Seo, M. S.; Davis, K. M.; Lee, Y.-M.; Chen, J.; Cho, K.-B.; Pushkar, Y. N.; Nam, W. *Journal of the American Chemical Society* **2011**, *133*, 20088.
(16) Goldsmith, C. R.; Cole, A. P.; Stack, T. D. P. *Journal of the American Chemical Society* **2005**, *127*, 9904.
(17) Coggins, M. K.; Brines, L. M.; Kovacs, J. A. *Inorg Chem* **2013**, *52*, 12383.
(18) Wijeratne, G. B.; Corzine, B.; Day, V. W.; Jackson, T. A. *Inorg Chem* **2014**, *53*, 7622.
(19) Sankaralingam, M.; Jeon, S. H.; Lee, Y.-M.; Seo, M. S.; Ohkubo, K.; Fukuzumi, S.; Nam, W. *Dalton Transactions* **2016**, *45*, 376.
(20) Hitomi, Y.; Arakawa, K.; Funabiki, T.; Kodera, M. *Angewandte Chemie International Edition* **2012**, *51*, 3448.
(21) Hitomi, Y.; Arakawa, K.; Kodera, M. *Chemistry – A European Journal* **2013**, *19*, 14697.
(22) Hitomi, Y.; Arakawa, K.; Kodera, M. *Chemical Communications* **2014**, *50*, 7485.
(23) Hitomi, Y.; Iwamoto, Y.; Kodera, M. *Dalton Transactions* **2014**, *43*, 2161.

(24) Iwamoto, Y.; Kodera, M.; Hitomi, Y. *Chemical Communications* **2015**, *51*, 9539.
(25) Zang, Y.; Kim, J.; Dong, Y.; Wilkinson, E. C.; Appelman, E. H.; Que, L. *Journal of the American Chemical Society* **1997**, *119*, 4197.
(26) Chiou, Y.-M.; Que, L. *Journal of the American Chemical Society* **1995**, *117*, 3999.
(27) Kim, J.; Zang, Y.; Costas, M.; Harrison, G. R.; Wilkinson, C. E.; Que Jr, L. *JBIC Journal of Biological Inorganic Chemistry* **2001**, *6*, 275.
(28) Mader, E. A.; Davidson, E. R.; Mayer, J. M. *Journal of the American Chemical Society* **2007**, *129*, 5153.
(29) Riedel, P. J.; Arulsamy, N.; Mehn, M. P. *Inorganic chemistry communications* **2011**, *14*, 734.
(30) *Data Collection: SMART Software in APEX2 v2010.3–0 Suite.*
(31) *Data Reduction: SAINT Software in APEX2 v2010.3–0 Suite.*
(32) *International Tables for Crystallography*, 1996; Vol. A.
(33) *Refinement: SHELXTL v2010.3–0.*
(34) Neese, F. *Wiley Interdiscip. Rev.* **2012**, *2*, 73.
(35) Becke, A. D. *Journal of Chemical Physics* **1986**, *84*, 4524.
(36) Perdew, J. P. *Phys. Rev. B* **1986**, *33*, 8822.
(37) Schäfer, A.; Horn, H.; Ahlrichs, R. *J. Chem. Phys.* **1992**, *97*, 2571.
(38) Schäfer, A.; Huber, C.; Ahlrichs, R. *J. Chem. Phys.* **1994**, *100*, 5829.
(39) Neese, F. *Journal of Computational Chemistry* **2003**, *24*, 1740.
(40) Sinnecker, S.; Rajendran, A.; Klamt, A.; Diedenhofen, M.; Neese, F. *Journal of Physical Chemistry A* **2006**, *110*, 2235.
(41) Staroverov, V. N.; Scuseria, G. E.; Tao, J.; Perdew, J. P. *The Journal of Chemical Physics* **2003**, *119*, 12129.
(42) Izsák, R.; Neese, F. *The Journal of Chemical Physics* **2011**, *135*, 144105.
(43) Neese, F.; Wennmohs, F.; Hansen, A.; Becker, U. *Chemical Physics* **2009**, *356*, 98.
(44) Mammen, M.; Shakhnovich, E. I.; Deutch, J. M.; Whitesides, G. M. *The Journal of Organic Chemistry* **1998**, *63*, 3821.
(45) Telser, J.; Krzystek, J.; Ozarowski, A. *JBIC, J. Biol. Inorg. Chem.* **2014**, *19*, 297.
(46) Ghachtouli, S. E.; Guillot, R.; Aukauloo, A.; Dorlet, P.; Anxolabéhère-Mallart, E.; Costentin, C. *Inorganic Chemistry* **2012**, *51*, 3603.
(47) El Ghachtouli, S.; Lassalle-Kaiser, B.; Dorlet, P.; Guillot, R.; Anxolabehere-Mallart, E.; Costentin, C.; Aukauloo, A. *Energy & Environmental Science* **2011**, *4*, 2041.
(48) Wang, D.; Ray, K.; Collins, M. J.; Farquhar, E. R.; Frisch, J. R.; Gomez, L.; Jackson, T. A.; Kerscher, M.; Waleska, A.; Comba, P.; Costas, M.; Que, L. *Chemical Science* **2013**, *4*, 282.
(49) Warren, J. J.; Tronic, T. A.; Mayer, J. M. *Chemical Reviews* **2010**, *110*, 6961.
(50) Porter, T. R.; Mayer, J. M. *Chemical Science* **2014**, *5*, 372.
(51) Wijeratne, G. B.; Day, V. W.; Jackson, T. A. *Dalton Transactions* **2015**, *44*, 3295.
(52) Manner, V. W.; Markle, T. F.; Freudenthal, J. H.; Roth, J. P.; Mayer, J. M. *Chemical Communications* **2008**, 256.
(53) We attempted to assess the hydrogen-atom transfer kinetics of **2-H** and **2-Me** using the less bulky 2,4-di-tert-butylphenol as a substate. However, treatment of either complex with this substrate in MeCN at 50 °C results in immediate changes in the electronic absorption spectra, showing the formation of a new chromophore (Supporting Information, Figure A1.10). This chromophore then rapidly decays. We speculate that the less bulky 2,4-di-tert-butylphenol is able to rapidly displace the hydroxide ligand and coordinate directly to the Mn^{III} center. The newly formed Mn^{III}-phenolate species would be expected to be colored, accounting for the new chromophore.

Presumably the Mn^{III}-phenolate species is unstable, and undergoes rapid decay. This proposed chemistry is consistent with an ESI-MS analysis of the resulting reaction mixture, which shows Mn^{II} products, and a peak attributed to $[Mn^{III}(phenolate)(dpaq)]^+$ (Figure A1.11). Thus, the reactions of the Mn^{III}-hydroxo species with 2,4-di-tert-butylphenol are not well behaved, and fundamentally different from the reaction with 2,4,6-tri-tert-butylphenol.

(54) Lehnert, N.; Solomon, E. I. *J Biol Inorg Chem* **2003**, *8*, 294.

(55) Mayer, J. M. *Accounts of Chemical Research* **2011**, *44*, 36.

(56) Bordwell, F. G.; Cheng, J.; Ji, G. Z.; Satish, A. V.; Zhang, X. *Journal of the American Chemical Society* **1991**, *113*, 9790.

(57) Solis, B. H.; Hammes-Schiffer, S. *Inorganic Chemistry* **2014**, *53*, 6427.

Chapter 3

Mn K-edge X-ray absorption studies of mononuclear Mn(III)-hydroxo complexes

3.1 Introduction

Monomeric Mn^{III}-OH adducts are invoked as intermediates in enzymes such as manganese superoxide dismutase (MnSOD) and manganese lipoxygenase (MnLOX). In MnSOD, an active site Mn^{III}-OH unit is proposed to facilitate the oxidation of superoxide leading to the formation of O_2.[1-2] In MnLOX an active site Mn^{III}-OH center is proposed to perform a proton-coupled electron transfer (PCET) reaction that initiates the dioxygenation of poly-unsaturated fatty acids.[3-7] While critical to the function of their respective enzymes, these Mn^{III}-OH motifs have not been characterized crystallographically. Mn K-edge X-ray absorption spectroscopy (XAS) has proven to be a valuable technique in the characterization of Mn enzymes and synthetic complexes and allows for determination of structural parameters in the absence of crystal structures. One prominent example where XAS has given valuable structural insight is the oxygen-evolving complex in photosystem II, which contains a Mn_4O_5Ca cluster at its core and is involved in the oxidation of H_2O to O_2 and protons.[8-11] To aid in characterizing these systems, benchmarking of XAS data on small, structurally well-defined model systems is necessary to understand the features and trends expected for various structural motifs. For Mn^{III}-OH model complexes, numerous models have been reported in the literature,[12-15] but there remains a lack of XAS characterization of Mn^{III}-OH adducts and their corresponding Mn^{II} complexes.

K-edge XAS is often discussed in terms of two separate regions, the X-ray absorption near edge structure (XANES) and the higher energy extended X-ray absorption fine structure (EXAFS) region. The EXAFS region gains intensity largely from the excitation of core Mn 1s electron into the continuum of electronic states. This oscillatory region is often able to be fit utilizing a single scatterer equation, which allows for extraction of the number of scatterers (atoms) and the element of the corresponding atom within a certain radial distance from the metal center. One caveat of this

method, however, is that atoms of the same element at similar distances (determined by resolution) cannot be distinguished, and instead an average distance of all degenerate pathways will be obtained. Another limitation is the inability to accurately distinguish between small atoms close in atomic number, such as O and N. Despite these shortcoming, the accuracy of distances determined by analysis of EXAFS data (~0.02 Å) allows for refinement of crystallographically characterized structures, and offers the ability to obtain accurate structural information for the first coordination sphere as well as short metal-metal distances.[16] Additionally, because EXAFS experiments can be performed for solution-phase samples, it can provide structural insight into metastable intermediates for which crystals are not able to be grown.

The XANES region provides complementary information about the electronic structure of the metal and has shown to be very sensitive to coordination environment.[17-18] Through empirical comparison with model complexes, the relative position of the edge can give insight into the oxidation state of the metal, with a shift to higher edge energy often coinciding with a change to higher oxidation state. The lower energy pre-edge region corresponds predominately to excitations from the core Mn 1s to the Mn 3d orbitals. These excitations are formally parity forbidden, but have been shown to gain intensity via mixing with Mn 4p orbitals induced by distortions to lower symmetry as well as via mixing with covalent ligand orbitals.[19-21] Combined experimental and theoretical analysis of the pre-edge region has been shown to give extensive insight into the electronic structure of the metal.[22-27] In these studies, time-dependent density-functional theory (TD-DFT) is often-utilized in tandem with experimental fitting to understand the basis for differences in pre-edge properties and can provide a quantitative description of the pre-edge region. Such quantitative descriptions are capable with thorough benchmarking using model complexes. One such study was performed on a series of Mn^{II} and Mn^{III} complexes, where the edge energy and

intensity of the experimental values were reproduced through the use of a systematic offset for the energy and a linear equation for the area.[28]

Our group has previously reported the formation of a mononuclear Mn^{III}-OH complex of the anionic N5 ligands dpaq (dpaq = 2-[bis(pyridine-2-ylmethyl)]amino-N-quinolin-8-yl-acetamidate) by dissolution of the corresponding [Mn^{II}(dpaq)](OTf) complex in MeCN in the presence of O_2 (Scheme 3.1).[13] We have also more recently reported a modified dpaq ligand using a 2-methylquinoline unit ($dpaq^{2Me}$ = 2-[bis(pyridine-2-ylemthyl)]amino-N-2-methyl-quinolin-8-yl-acetamidate), which provided steric bulk near the hydroxo ligand but still resulted in the formation of a Mn^{III}-OH complex (Scheme 3.1).[12] The crystal structures of the Mn^{II} and Mn^{III}-OH complexes were obtained for both dpaq ligand systems. The crystal structures of [Mn^{II}(dpaq)](OTf) and [Mn^{II}($dpaq^{Me}$)](OTf) (**1-H** and **1-Me**, respectively) both display polymeric structures; in each case the manganese center of one complex contains a sixth ligand from the amide O of another complex (Scheme 3.1).[12-13] In MeCN solution the Mn^{II} complexes are known to react with O_2 to form the Mn^{III}-hydroxo complexes. This reactivity suggests the dissociation of this polymer, likely into monomeric structures, in solution. EXAFS analysis of these complexes should allow for a comparison between the solid and frozen-solution states of the Mn^{II} complexes. For [Mn^{III}(OH)(dpaq)](OTf) and [Mn^{III}(OH)($dpaq^{2Me}$)](OTf) (**2-H** and **2-Me**, respectively), the crystal structures for both complexes featured a short Mn-OH bond distance of 1.806(13) Å and 1.819(3) Å, respectively.

Scheme 3.1. Structures of $[Mn^{II}(dpaq^{R})]^{+}$ in the solid-state polymeric form (left), proposed dissociation and solvation in solution (center) and $[Mn^{III}(OH)(dpaq^{R})]^{+}$ formed after exposure to O_2 (right).

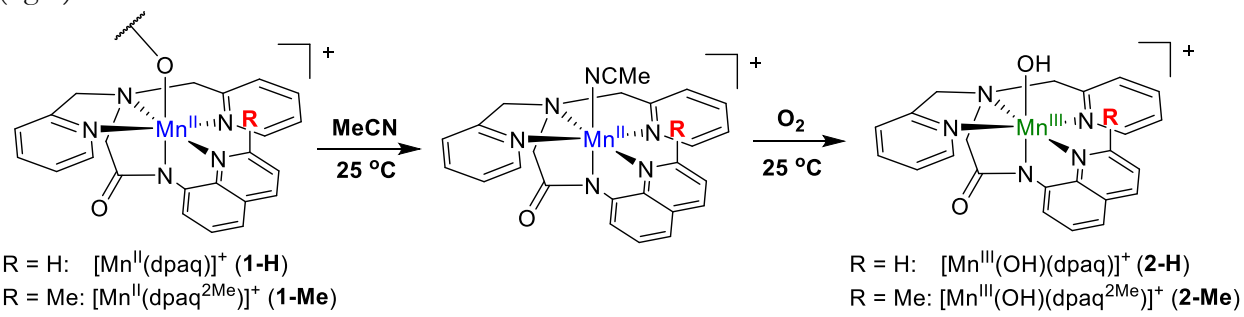

In this work, Mn K-edge XAS data were collected for **1-Me** and **1-H** in both frozen solution and solid-state samples. Corresponding data were also collected for the Mn^{III}-hydroxo complexes **2-H** and **2-Me** in both frozen-solution and solid-state. Although these Mn^{II} and Mn^{III}-hydroxo complexes have been structurally characterized in the solid-state using X-ray crystallography, structural parameters obtained from solution-phase EXAFS data can, in principle, provide confirmation (or correction) of the presumed solution structures. Analysis of the XANES region offers additional information about electronic properties of the Mn^{II} and Mn^{III}-hydroxo centers. XANES parameters (*i.e.*, edge and pre-edge energies and areas of pre-edge features) for the structurally well-defined complexes described here provide useful benchmarks for understanding corresponding data for enzymatic or unstable intermediates. Below, we first discuss structural parameters from EXAFS data analysis. Next, we examine the edge and pre-edge properties of these complexes, using TD-DFT methods to determine the electronic states that contribute most prominently to the pre-edge transitions.

3.2 Methods

Materials. All chemicals and solvents were obtained from commercial vendors at ACS grade or better and were used as received. The acetonitrile for O_2-sensitive samples was dried and degassed using a Pure Solv (2010) solvent purification system in air-tight solvent reservoirs by passing Ar gas at room temperature for 20 minutes. All complexes were synthesized and purified as previously described.[12-13]

XAS Sample Preparation. For solid samples, a 2% (w/w) dispersion was generated by grinding 4 mg of the respective crystalized complex with 196 mg of boron nitride into a fine powder with mortar and pestle. Solid samples were .0625 inches thick with 0.001 inch thick Kapton tape on each side. Frozen solution samples of **1-Me**(MeCN) and **1-H**(MeCN) were generated by preparing a 10 mM solution in an argon dry-box, bringing the sample out in a sealed, air-tight syringe and injecting approximately 300 μL of solution into the XAS container while under a nitrogen-flushed environment. The samples were then quickly frozen in liquid nitrogen. Frozen solution samples of **2-H**(H_2O) at 3.5 mM and **2-Me**(MeCN) at 10 mM were prepared by dissolving crystals of the respective complex into either deionized H_2O or dry MeCN. Approximately 300 μL of the resulting solution was added to a sample holder and carefully frozen.

XAS Data Collection. The Mn K-edge XAS data were collected over an energy range of 6300 to 7250 eV for all samples. A manganese foil was used as reference for each scan under all conditions. Internal calibration was performed by taking the zero crossing of the second derivative of the K-edge energy of the foil and assigning the value to 6539.0 eV. All XAS spectra were obtained via fluorescence excitation. XAS data for **1-Me**(solid), **1-Me**(MeCN), and **1-H**(MeCN) were collected at beamline 2-2 at Stanford Synchrotron Radiation Lightsource (SSRL) at 15 K using a Si(111) monochromator and a 13-element Ge array detector. Data for **1-H**(solid) and **2-Me**(solid)

were collected at beamline 9-3 at SSRL at 7 K using a Si(220) monochromator and a 100-element Ge array detector. Data for **2-H**(solid), **2-H**(H_2O), and **2-Me**(MeCN) were collected at beamline X3B at the National Synchrotron Light Source (NSLS) using a Si(111) monochromator and a 31-element Ge array detector.

EXAFS Data Analysis. EXAFS data analysis was performed using the *DEMETER* software package.[29] Background was removed using the *AUTOBK* algorithm as implemented in *ATHENA*. Each data set was normalized using the edge-step normalization procedure. EXAFS fitting in *ARTEMIS* was carried out on $k^3\chi(k)$ data, using *FEFF6* [30] for the phase and amplitude functions. To generate the functions, crystal structures were used for the solid samples; DFT-optimized structures were used for the solution phase samples. For each fit, the parameters R (average scattering pathway distance) and σ^2 (Debye-Waller factor) were optimized individually for each path and E_0 (k = 0) was a common variable for all paths. The n (degeneracy) parameter was fixed for each fit and systematically varied between fits in order to achieve better goodness of fit. The goodness of fit was evaluated using the R-factor:

$$R = \sum_{i=1}^{N}(\chi_i^{data} - \chi_i^{fit})^2 \,/\, \sum_{i=1}^{N}(\chi_i^{data})^2$$

XANES Data Analysis. Manganese K-edge pre-edge data were fit using Fityk.[31] The pre-edge was fit using pseudo-Voigt line shapes with a fixed 1:1: ratio of Lorentzian to Gaussian functions and varied full width at half-maximum, energy position, and peak height. The rising edge and background contribution were also fit using a pseudo-Voigt function. Fits were carried out to reproduce the features using an appropriate number of peaks, as determined by inspection of the second derivative of the pre-edge region. Manganese K-edge energy values were taken as the inflection point of the rising edge by analysis of the first derivative of the edge region.

Density Functional Theory. All DFT calculations were performed using the *ORCA* 3.0.3 software package[32] at the spin unrestricted level. Geometry optimizations were performed using the BP86 functional,[33-34] with the Ahlrichs TZVP basis set with the TZVP/J auxiliary basis set for Mn, N, and O and the smaller SVP basis set with the SVP/J auxiliary basis set for C and H.[35-36] The resolution of identity approximation was used for all optimizations.[37] Solvent was implicitly accounted for in all calculations using the COSMO continuum solvent model with the default parameters for acetonitrile as found in *ORCA*.[38] The crystal structures for **2-H** and **2-Me** were used as the initial geometry for their respective optimizations and were converged to the optimized $S = 2$ geometry.[12-13] Models for **1-H** and **1-Me** in MeCN solution were built by starting with the Mn^{II} crystal structure and truncating the polymeric chain by replacing the amide donor from an adjacent Mn^{II} complex with an acetonitrile bound to the metal center and converging to the high spin $S = 5/2$ geometry.

XAS Pre-Edge Calculations. The manganese pre-K-edge spectra were calculated using time-dependent density functional theory (TD-DFT) within the Tamm-Dancoff approximation.[39-40] Calculations were performed using the B3LYP[41-42] functional with the Ahlrichs def2-TZVP(-f) basis set for Mn, N, and O and the def2-SVP basis set for C and H.[35-36, 43] Scalar relativistic effects were accounted for at the ZORA level.[44-45] The pre-edge area (A) was calculated using a method calibrated with a series of monomeric Mn^{II} and Mn^{III} complexes, where the origin adjusted intensity (I) is calculated from the sum of the electric dipole, electric quadrupole, and magnetic dipole contributions (see SI) and used in the empirically derived equation $A = 6.01I + 1.79$ for B3LYP.[28] Spectral simulations were performed using a linewidth of 1 eV.

3.3 Results and Discussion.

EXAFS Analysis of Mn^{II} Complexes. The phase-shifted Fourier transforms (FT) and the raw EXAFS data for **1-Me**(solid) and **1-Me**(MeCN) are shown in Figure 3.1 (C and D). The Fourier transforms of the EXAFS spectra show similar features, with one large peak at R´ = 1.7 Å, and two smaller, overlapping peaks near R´ = 2.2 and 2.6 Å. To obtain metric parameters from these data, we first used phase and amplitude functions from *FEFF* calculations on the **1-Me** X-ray crystal structure. Data sets for both **1-Me**(solid) and **1-Me**(MeCN) were fit with 6 atoms (O/N) in the first coordination sphere, which are the major contributors to the feature at 1.7 Å (Table 3.1). The **1-Me**(solid) data are best fit with an O/N path at 2.23 Å (n = 6, where n is the number of scatterers in a shell). The fit is further improved by including a second coordination sphere of C scatterers at 3.09 Å (Table 3.1), which contribute to the peak near R´ = 2.6 Å. The Mn-ligand distance from this fit agrees well with the average Mn-ligand distance from X-ray crystallography (2.24 Å; see Table 3.2). Fits of the EXAFS data of **1-Me**(solid) that split the O/N shell into two smaller shells gave a smaller *R*-factor, but this small reduction in *R*-factor is likely due to an increase in the number of fitted parameters and does not reflect an increase in the actual quality of fit (Table A2.4).

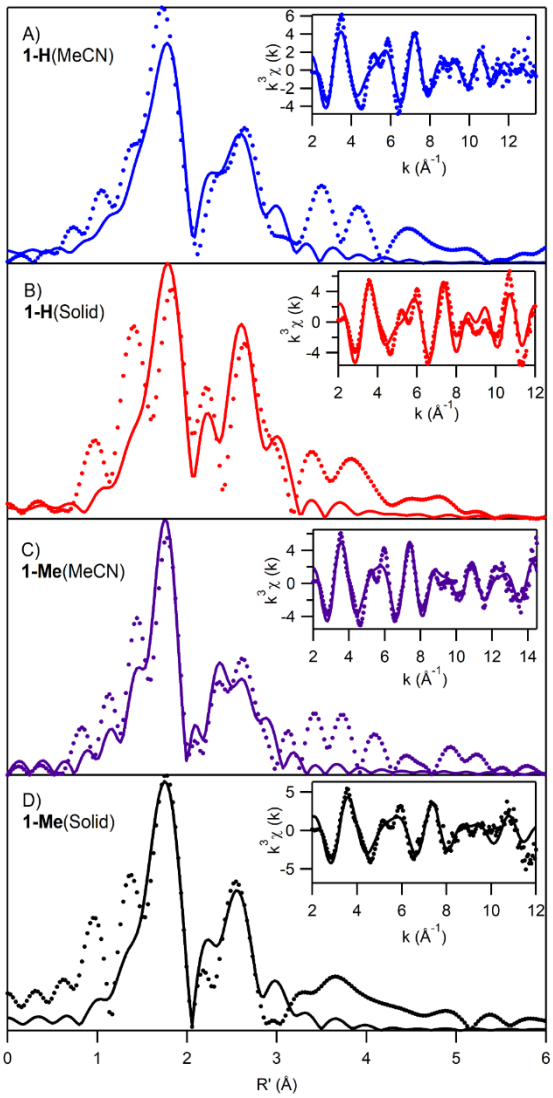

Figure 3.1. Fourier transforms of Mn-K edge EXAFS data and raw EXAFS curves (insets), experimental (•••) and fits (—) for 1-H(MeCN) (A), 1-H(solid) (B), and 1-Me(MeCN) (C) and 1-Me(solid) (D). Parameters for fits are in Table 3.1.

Table 3.1. Edge energy and parameters derived from the best EXAFS fit for each Mn^{II} and Mn^{III}-hydroxo complex.

Complex	Medium	Edge Energy (eV)	Δk ($Å^{-1}$)	Path	*n*	R_{EXAFS} (Å)	$\sigma^2 x10^3$
1-H	MeCN	6547.9	12.5	N	6	2.27	7.73
				C	8	3.15	6.30
	Solid	6547.9	10.0	O/N	6	2.24	4.95
				C	8	3.12	1.42
1-Me	MeCN	6548.6	12.9	N	6	2.21	5.19
				C	8	3.07	4.71
	Solid	6548.5	10.0	O/N	6	2.23	7.23
				C	7	3.09	5.81
2-H	H_2O	6550.6	9.0	O/N	2	1.87	4.81
				N	4	2.14	5.21
				C	6	2.91	8.89
	Solid[a]	6550.4	11.0	O	1	1.79	0.54
				N	2	1.98	1.32
				N	3	2.17	3.02
				C	5	2.92	5.22
2-Me	MeCN	6550.0	12.5	O/N	2	1.89	8.68
				N	4	2.17	2.79
				C	5	2.93	4.09
	Solid	6549.9	10.0	O/N	2	1.87	8.07
				N	4	2.16	5.61
				C	7	2.93	8.96

[a] **An alternate fit for** 2-H**(solid) that lacks the small Debye-Waller factor shown here is described in the main text and Supporting Information (**

Table A2.6).

Table 3.2. Comparison of the distances derived from EXAFS fitting of the Mn^{II} and Mn^{III}-hydroxo complexes to the average distances determined from the corresponding atoms in the crystal structures and the DFT-optimized structures.[a]

Complex	Medium	Path	*n*	R_{EXAFS} (Å)	R_{XRD} (Å)	R_{DFT} (Å)
1-H	MeCN	N	6	2.27	2.22	2.25
		C	8	3.15	3.08	3.09
	Solid	O/N	6	2.24	2.22	2.25
		C	8	3.12	3.08	3.09
1-Me	MeCN	O/N	6	2.21	2.24	2.26
		C	8	3.07	3.08	3.08
	Solid	O/N	6	2.23	2.24	2.26
		C	7	3.09	3.07	3.08
2-H	H_2O	O/N	2	1.87	1.890	1.92
		N	4	2.14	2.18	2.20
		C	6	2.91	2.95	2.97
	Solid	O	1	1.79	1.806	1.85
		N	2	1.98	2.02	2.03
		N	3	2.17	2.22	2.24
		C	5	2.92	2.92	2.95
2-Me	MeCN	O/N	2	1.89	1.90	1.92
		N	4	2.17	2.17	2.21
		C	5	2.92	2.94	2.96
	Solid	O/N	2	1.87	1.90	1.92
		N	4	2.17	2.17	2.21
		C	7	2.93	2.95	2.98

[a] For the Mn^{II} complexes 1-H and 1-Me, the XRD values pertain to those obtained from the polymeric crystal structures, while the DFT values are for DFT-optimized models of $[Mn^{II}(dpaq)(MeCN)]^+$ and $[Mn^{II}(dpaq^{Me})(MeCN)]^+$, respectively.

Fits of the EXAFS data of **1-Me**(MeCN) using *FEFF* functions from the crystal structure yield an O/N shell (n = 6) at 2.21 Å and a C shell (n = 8) at 3.07 Å (Table A2.9). This average N distance is in good agreement with those observed in the crystal structure of **1-Me** (Table 3.2). The axial amide N and O ligands in the X-ray structure of **1-Me** given an average distance of 2.14 Å and the average $Mn–N_{equatorial}$ distance is 2.29 Å which gives an overall average of 2.24. The carbons from the pyridine and quinoline moieties are near 3.1 Å (Table 3.2), accounting for the outer shell of C atoms. Fits separating the N shell into two distinct shells (Table A2.9) show modest agreement with the crystal structure but have smaller than typical Debye-Waller factors.

The EXAFS data collected for the **1-Me**(MeCN) sample were also fit using *FEFF* phase and amplitude functions generated using the DFT structure of $[Mn^{II}(dpaq^{2Me})(MeCN)]^{+}$, which is potentially a more appropriate model of the solution-phase structure. In this case, the first coordination sphere is still best fit with an N/O shell at 2.21 Å (n = 6) and the second-sphere is well accounted for with a C shell (n = 8) at 3.06 Å (Table A2.3). Both fits are of similar quality, as evaluated using the *R*-factor, with R = 0.221 and 0.223 for the DFT and crystal-structure *FEFF* functions, respectively. The inability to distinguish between O/N scatterers and the similar distance of the DFT optimized acetonitrile and of the crystallographic amide O from another metal complex, lead to these two distinct models giving nearly identical fits. Consequently, the EXAFS data do not allow a definitive statement to be made regarding the solution structure of **1-Me** compared to that observed crystallographically.

The FT of the EXAFS data for **1-H**(solid) and **1-H**(MeCN) are quite similar to those of **1-Me**, consisting of a dominant peak at R´ = 1.7 Å and a broader, less intense envelope at R´ = 2.4 Å (Figure 3.1, A and B). The **1-H**(solid) EXAFS data, fit using *FEFF* function from the X-ray

structure of $[Mn^{II}(dpaq)](OTf)$, are well-accommodated using a shell of N scatterers (n = 6) at 2.24 Å and a shell of C atoms (n = 8) at 3.12 Å. Any attempts to resolve the N shell into separate scattering paths led to a shell with physically unrealistic Debye-Waller parameters (Supporting Information, Table A2.2). Nonetheless, the distance of the N shell is in reasonable agreement with the average Mn–ligand distances in the crystal structure of $[Mn^{II}(dpaq)](OTf)$ (2.22 Å; see Table 3.2). EXAFS data for **1-H**(MeCN) were fit using *FEFF* functions from a DFT-derived model of $[Mn^{III}(dpaq)(MeCN)]^+$. In this case, the data were best fit with a nitrogen shell at 2.27 Å (n = 6) and a C shell at 3.1 Å (n = 8). This N shell agrees well with the average Mn–N distance in the DFT structure (2.25 Å; see Table 3.2). As also shown in Table 3.2, these shells are elongated slightly when compared to the distances observed in the crystal structure of $[Mn^{II}(dpaq)](OTf)$.

Overall, the EXAFS distances obtained for the Mn^{II} complexes, in both solid-state and frozen solution, are compatible with the distances observed by X-ray crystallography for the polymeric Mn^{II} structures and those predicted for the DFT-derived structures with axial MeCN ligands. As shown in Table 3.2, the X-ray and DFT distances are quite similar, and amount to minor bond length changes and substitution of an N for an O scatterer. Neither of these structural perturbations can be adequately resolved in the EXAFS fits. Consequently, the EXAFS distances provide insufficient evidence to either confirm or correct the prediction that the polymeric motif observed in the X-ray crystal structures of these Mn^{II} complexes dissociates in MeCN solution.

EXAFS Analysis of Mn^{III}-hydroxo Complexes. The raw EXAFS data and corresponding FT spectra for **2-H** (solid and H_2O) and **2-Me** (solid and MeCN) are shown in Figure 3.2. H_2O was used instead of MeCN for the solution-phase sample of **2-H** due to the possibility of dimerization of **2-H** in MeCN at the high concentrations required for XAS data collection. Previous studies of Mn^{III}-OH species have shown equilibria between Mn^{III}-OH and oxo-bridged-diamanganese(III,III)

dimers in non-hydroxylic solvents [14, 46]. Dimerization of this type is not a concern for **2-Me** because the steric bulk of the 2-Me-quinoline moiety should disfavor dimerization (Scheme 3.1). The solubility of **2-H**, however, is poor in H_2O and led to data collection at a relatively low concentration (3.5 mM). Consequently, the EXAFS analysis for **2-H**(H_2O) was performed using a small k-window of 2 – 11 $Å^{-1}$ which gives a resolution of approximately 0.17 Å.

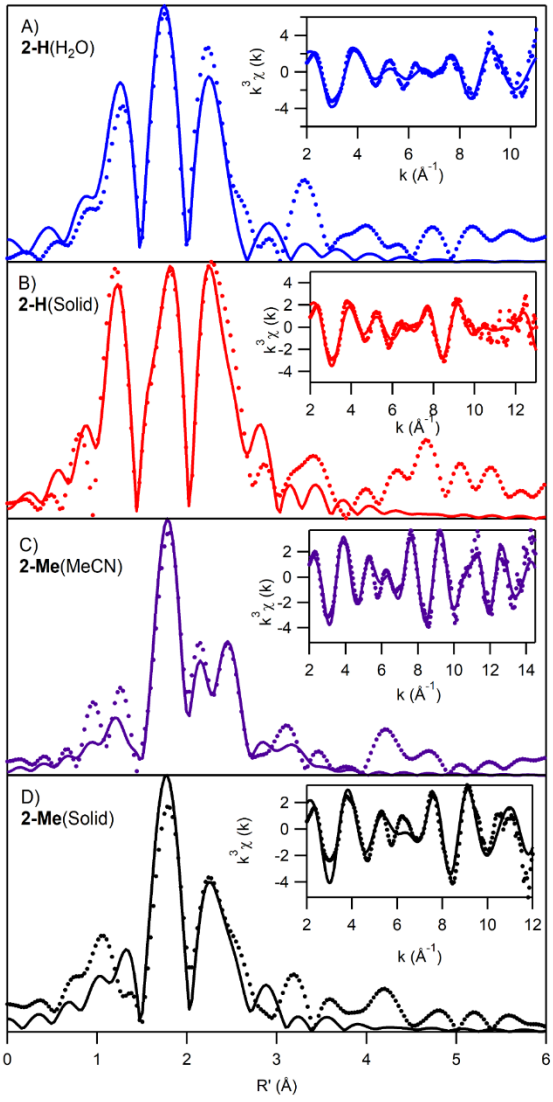

Figure 3.2. Fourier transforms of Mn-Kedge EXAFS data and raw EXAFS curves (insets), experimental (···) and fits (—) for 2-H (H_2O) (A), 2-H (solid) (B), and 2-Me (MeCN) (C) and 2-Me (solid) (D). Parameters for fits are in Table 3.1.

The Fourier-transforms of the EXAFS spectra of **2-H**(solid) and **2-H**(H_2O) appear remarkably similar (Figure 3.2, A and B), both consisting of a set of three prominent peaks around R´ of 1.2, 1.8, and 2.3 Å. There are some slight perturbations in the FT spectrum of **2-H**(H_2O); the side peaks are less intense, and the outer-peak has contracted to R´ = 2.2 Å. These slight changes in the FT spectra lead to some differences in the EXAFS fits. For example, the best fit for the EXAFS data of **2-H**(solid) includes an O shell at 1.79 Å (n = 1), which is in excellent agreement with the Mn^{III}-OH distance of 1.806(13) Å determined from the crystal structure [13]. The resolution of this shell confirms the unusually short Mn−OH bond distance in the crystal structure of **2-H**, which had a relatively large uncertainty. The EXAFS fit for **2-H**(solid) also includes two N shells at 1.98 Å (n = 2) and 2.17 Å (n = 3), which correspond well to average crystallographic distances for the amide and quinoline ligands and pyridine and amine ligands (2.02 and 2.22 Å, respectively). These three shells interfere to give the major contribution to the two sharp features at 1.3 and 1.8 Å in the FT spectrum (Figure 3.2). The EXAFS fit was further improved with the addition of a C shell at 2.92 Å (n = 5), contributing to the feature at 2.2 Å in the FT spectrum.

It is important to note that the Mn–O scattering shell in the best fit for 2-H(solid) has a Debye-Waller factor (0.5×10^{-3}) that is lower than generally expected, even for a scatterer at a short distance (values of ~2×10^{-3} are most common at such distances). Although a similarly low Debye-Waller factor of 0.7×10^{-3} was recently reported for a Fe^{III}-hydroxo complex [47], it is reasonable to question the validity of a fit with such a low σ^2 value. An alternate fit, with an (n = 2) O/N scattering shell that includes the O and trans-amide N in the same shell is shown in the Supporting Information (Table A2.6). This fit contains an N/O shell at 1.88 Å (n = 2), an N shell at 2.18 Å (n = 4), and a C shell at 2.94 Å (n = 5). The distance of the N/O shell of 1.88 Å is in agreement with an

average of the Mn–OH and Mn–N(amide) distances observed in the X-ray crystal structure of 2-H. However, this alternative fit shows a much larger R factor (0.295 compared with 0.191 for the best fit presented in Table 3.1), and the two-scatterer O/N shell displays a σ^2 value of 10.6×10^{-3}, which is relatively large for a short, two-scatterer shell. Because neither of these fits seem ideal, additional fits were performed on the single scattering model where the Mn–O σ^2 value was held constant and the other parameters were allowed to float as normal (

Table A2.6 and Figure A2.1). The Mn–scatterer distances are largely unchanged (within 0.02 Å) as the σ^2 is increased, and the fitted spectra show very modest changes (Figure A2.1). More importantly, the R-factor suffers an increase of only ~5% at $\sigma^2 = 2.0 \times 10^{-3}$ as compared to the best fit in Table 3.1. The σ^2 value for the N shells do increase as the O σ^2 is increased, even though these parameters were not found to be strongly correlated within an individual fit. Collectively, these fits suggest that the EXAFS data for **2-H**(solid) can accommodated a short Mn–O distance with a reasonable Debye-Waller factor.

In contrast, to our fit of **2-H**(solid), where the presence of a short Mn–OH distance could be supported by the data analysis, we were unable to resolve a short Mn–OH bond distance in our fits of the EXAFS data of **2-H**(H_2O). In this case, the best fit included an O/N shell (n = 2) at 1.87 Å, an N shell (n = 4) at 2.14 Å, and a C shell (n = 7) at 2.91 Å. Any attempts to include a short Mn–OH path led to fits with negative Debye-Waller factors. Thus, in this fit the hydroxide and amide ligands contribute to one shell, whereas the remaining N donors of dpaq contribute to a second shell. Crystallographically, the average distances for these ligands are observed at 1.89 and 2.18 Å, in reasonable agreement with the EXAFS distances (Table 3.2). The ability to resolve the

Mn–OH pathway in the **2-H**(solid) but not in **2-H**(H_2O) is likely due to the increased quality of data for the solid-state sample.

The FT spectra for **2-Me**(solid and MeCN) are quite different in appearance than that of **2-H** (Figure 3.2), with spectra for **2-Me** showing one intense peak at 1.8 Å, and two weaker peaks near 2.3 Å. The raw EXAFS spectra for the **2-Me** samples is also quite distinct, consisting of strong modulations throughout the k-space window (Figure 3.2, insets). Despite the difference in appearance between these spectra, the best EXAFS fits for the **2-Me** samples are quite similar to those of **2-H** (Table 3.1). For example, the best fit for **2-Me**(solid) includes an O/N shell (n = 2) at 1.87 Å, which represents the hydroxide and the amide ligands. The limited k-range of 10 A^{-1} for **2-Me**(solid) does not allow for the resolution of these two atoms into separate shells; however, the shell is close to the average distance in the crystal structure (1.90 Å) [12]. The fit also includes an N shell (n = 4) at 2.17 Å, corresponding to the equatorial nitrogens, and a carbon shell (n = 7) at 2.93 Å (Table 3.1). Although the EXAFS data for **2-Me**(MeCN) are of higher quality (permitting a fit in the k-range of 2 – 14.5 $Å^{-1}$, giving a resolution of 0.13 Å), the best fit yields Mn–scatterer distances essentially identical to those obtained for **2-Me**(solid), as summarized in Table 3.1.

Collectively, our analysis of the EXAFS data for solution- and solid-phase samples of **2-H** and **2-Me** confirms that the solid-state structures of these Mn^{III}-hydroxo complexes are retained in solution. Any differences between the fits of the solution- and solid-phase data sets can be accounted for by differences in resolution based on the quality of the EXAFS data. In addition, the EXAFS fit for **2-H**(solid) confirms the unusually short Mn–OH distance observed crystallographically.

Edge Energy. Edge energies for all Mn^{II} and Mn^{III} samples examined in this study are summarized in Table 3.1. The edge energies for the Mn^{II} complexes all lie near 6548 eV,

approximately 2 eV lower in energy than that observed for the corresponding Mn^{III}-hydroxo complexes. Some modest shifting of edge energies is also observed as a function of the supporting ligand, though this could be attributed to the way in which the edge energy is defined. For example, the edges for the **1-H** samples are ~0.7 eV lower than those of both the solid and solution (MeCN) phase edge of **1-Me**. However, upon inspection of the XANES region (Figure 3.3), both the edge positions of **1-H**(MeCN) and **1-Me**(MeCN) appear similar. Using the approximate halfway point of the rising edge, instead of the maximum of the first derivative, gives edge values of approximately 6548 eV for both samples. This result suggests that the apparent shift in edge energies in Table 3.1 is likely due to subtle changes in the shape of the rising edge between the two complexes. The solid and solution (H_2O) phase **2-H** samples display an edge 0.4 eV higher than that of the **2-Me**(MeCN) sample (Table 3.1). The XANES for the Mn^{III}(OH) samples show very minor changes in the shape of the rising edge and post-edge regions.

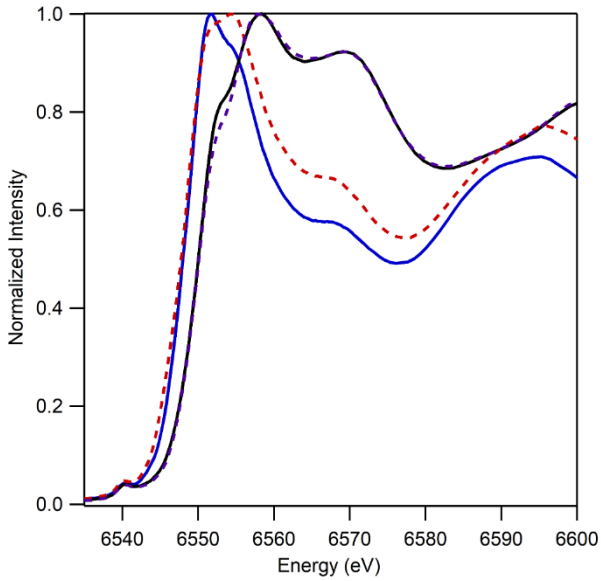

Figure 3.3. Experimental XANES of 1-H(MeCN)(—), 1-Me(MeCN)(---), 2-H(H_2O) (—), and 2-Me(MeCN) (---).

Experimental Pre-edge Areas. Pre-edge features in manganese K-edge XAS typically arise from formally forbidden manganese 1s-to-3d excitations that gain intensity from Mn 3d-4p mixing, allowed by distortions from idealized octahedral geometry. The extent of mixing reflects both the local Mn coordination geometry and Mn–ligand bonding interactions. Thus, the energies and areas of pre-edge features can serve as powerful probes of 3d orbital composition and splitting [22]. The pre-edge areas for all complexes are summarized in Table 3.3, and the individual fits of the pre-edge regions are shown in the SI (Figure A2.4).

The pre-edge spectra of the Mn^{II} complexes **1-H** and **1-Me** show a weak feature near 6540 eV (Figure 3.4), which is well-fit for all samples with one function at 6540.2 ± 0.1 eV (Table 3.3). The pre-edge areas fall into the relatively narrow range of 4.3 – 5.6 units (Table 3.3). These areas are comparable to those previously reported for mononuclear Mn^{II} centers [22, 48]. Among **1-H** and **1-Me**, the solution phase data are similar; however, there is an increase in pre-edge area for the solid-state samples. This increase could arise from self-absorption due to data collection for the concentrated solid-state samples being performed by fluorescence detection. To test this, the pre-edge data for **1-Me**(solid) were collected in transmission mode. (This sample was the only sample that showed sufficient signal-to-noise for the transmission-mode data to allow analysis of the small pre-edge region.) Data collected for **1-Me**(solid) in transmission mode showed a pre-edge area of 4.4 units (Figure A2.4), which is nearly identical to that determined for **1-Me**(MeCN). Therefore, the increase in pre-edge area for the solid-state samples is likely due to self-absorption and is not reflective of structural perturbations between the solution- and solid-state samples.

Table 3.3. Experimental manganese K-edge and pre-edge properties for Mn^{II} and Mn^{III}-hydroxo complexes, with DFT-calculated pre-edge properties and Mn 4p character in acceptor MOs.

		experimental			calculated		
complex	solvent	edge energy (eV)	pre-edge energy (eV)	area	pre-energy (eV)	area	Mn 4p (%)
1-H	MeCN	6547.9	6540.2	4.9	6539.8 6540.8	4.9	1.7
	Solid[a]	6547.9	6540.2	5.6			
1-Me	MeCN	6548.6	6540.2	4.3	6539.8 6540.8	4.7	1.4
	Solid[a]	6548.5	6540.2	5.4			
2-H	H2O	6550.6	6540.2 6541.8	4.3	6540.3 6541.7	4.1	1.2
	Solid[a]	6550.4	6540.2 6542.0	5.8	6540.3 6541.8	4.3	1.2
2-Me	MeCN	6550	6540.2 6541.6	4.1	6540.3 6541.7	3.8	1.2
	Solid[a]	6549.9	6540.3 6542.3	5.7			

[a]The pre-edge areas for the solid-state samples are likely over-estimated due to self-absorption. For example, analysis of transmission-mode pre-edge data for 1-Me(solid) showed smaller pre-edge area of 4.4 units. See main text for further details.

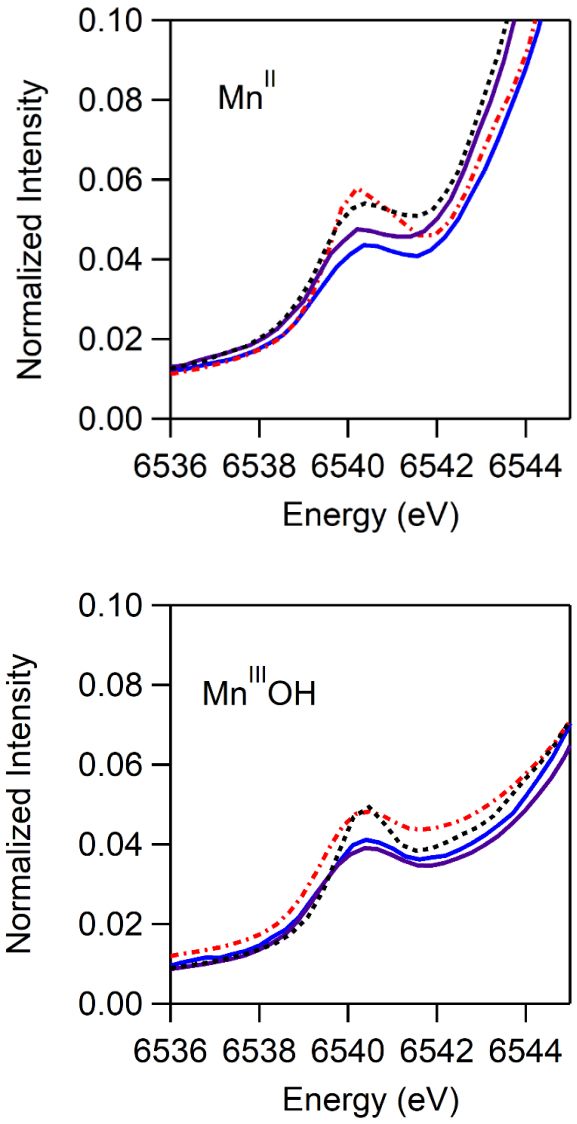

Figure 3.4. Pre-edge areas for Mn^{II} solid and solution samples (top) and Mn^{III}-OH solid and solution samples (bottom). Top: 1-H(MeCN) (blue), 1-H(solid) (red), 1-Me(MeCN) (purple), 1-Me(solid) (black). Bottom: 2-H(H_2O) (blue), 2-H(solid) (red), 2-Me(MeCN) (purple), 2-Me(solid) (black). All solid phase samples are shown in dashed lines and solution phase samples shown in solid lines.

The pre-edge spectra of the Mn^{III}-hydroxo complexes **2-H** and **2-Me** all show a weak band at 6540 eV, but analyses of the second-derivatives of the pre-edge spectra suggest the presence of a second weak band near 6542 eV (Figure A2.4). Consequently, the pre-edge regions of the Mn^{III}-hydroxo complexes were all fit with two pre-edge bands, a more intense band at 6540.2 ± 0.1 eV

and a weaker band at 6541.8 ± 0.2 eV (Table 3.3 and Figure A2.4). The total pre-edge areas were determined to be near 5.7 units for the solid-state samples of **2-H** and **2-Me**. The solution-phase samples show lower areas of 4.3 and 4.1 units for **2-H**(H_2O) and **2-Me**(MeCN), respectively, which could simply reflect self-absorption effects in the solid-state samples that artificially increase the pre-edge areas. Overall, the pre-edge regions of these Mn^{II} and Mn^{III}-hydroxo complexes are rather similar. Both sets of complexes show a prominent peak at 6540 eV (Table 3.3 and Figure A2.4) and both show similar total pre-edge areas. In fact, the solution-phase Mn^{III}-hydroxo samples show a reduction in area relative to their solution-phase Mn^{II} counterparts (Table 3.3), while the opposite trend is observed for the solid-state samples. The only common difference observed between the Mn^{II} and Mn^{III}-hydroxo samples is the presence of a higher-energy pre-edge feature for the latter samples, which varies from 6541.6 – 6542.3 eV depending on the sample (Table 3.3).

Density Functional Theory Pre-Edge and Electronic Structure. To gain insight into the electronic transitions contributing to the pre-edge region, TD-DFT spectra were computed and compared with the experimental data. The TD-DFT calculations predict excited states that contribute to the pre-edge region, and these excited states can be analyzed to determine the composition of the relevant acceptor orbitals. For the Mn^{II} and Mn^{III}-hydroxo complexes considered here, the excited states contain contributions from a large number of Kohn-Sham acceptor orbitals, which can complicate the description of the transitions in an orbital-to-orbital fashion. Thus, our analysis and discussion are aided by the use of electron difference density maps (EDDMs), which display regions of increased electron density in the excited states (*vide infra*).

For the high-spin S = 5/2 Mn^{II} complexes **1-H** and **1-Me**, the TD-DFT-computed pre-edge regions contain contributions from five 1s-to-3d transitions, each originating from one-electron excitations from the Mn 1s β-spin MO to the five unoccupied 3d β-spin MOs. The TD-DFT-

computed spectrum for $[Mn^{II}(dpaq)(MeCN)]^+$, the computational model of **1-H**(MeCN), is shown in Figure 3.5 (top) as a representative example; spectra for the other systems are in the SI (Figure A2.5). The computed spectra all show two partially overlapping peaks with maxima near 6539.8 and 6540.8 eV. The lower energy peak contains contributions from transitions 1 through 3 (Figure 3.5, top). The EDDMs for these transitions resemble the t_{2g}-type orbitals, two of which (d_{xz} and d_{xy}) are mixed. Thus, these transitions represent Mn^{II} 1s-to-3d(t_{2g}) excitations. The higher energy feature at 6540.8 eV arises from transition 4 and 5, which the EDDMs readily identify as containing the e_g-type acceptor orbitals (Figure 3.5, top). The small, 1 eV, peak separation predicted by the TD-DFT computations could account for the fact that the experimental pre-edge region of the Mn^{II} complexes is satisfactorily fit by only a single band (Figure A2.4). The average position of the TD-DFT band (6540.3 eV) is in excellent agreement with the experimental pre-edge energies of the Mn^{II} complexes (6540.2 eV). The calculated pre-edge areas of 4.7 and 4.9 for $[Mn^{II}(dpaq^{Me})(MeCN)]^+$ and $[Mn^{II}(dpaq)(MeCN)]^+$ are also in excellent agreement with the experimental areas of the respective solution-phase samples of **1-Me** and **1-H** (4.3 and 4.9; see Table 3.3). The TD-DFT computations further show that the weak pre-edge intensity of these Mn^{II} complexes arise due to the admixture of only ~1.5% 4p character into the Mn 3d manifold. For comparison, similar TD-DFT computations for the Mn^{II} complex $[Mn^{II}(Cl_2)(Me_2EBC)]$ (where Me_2EBC is the cross-clamped macrocyclic ligand 4,11-dimethyl-1,4,8,11-tetraazabicyclo[6.6.2]hexadecane) gave an pre-edge area of 2.5 units, arising from only 0.7% of 4p mixing into the 3d manifold.[22]

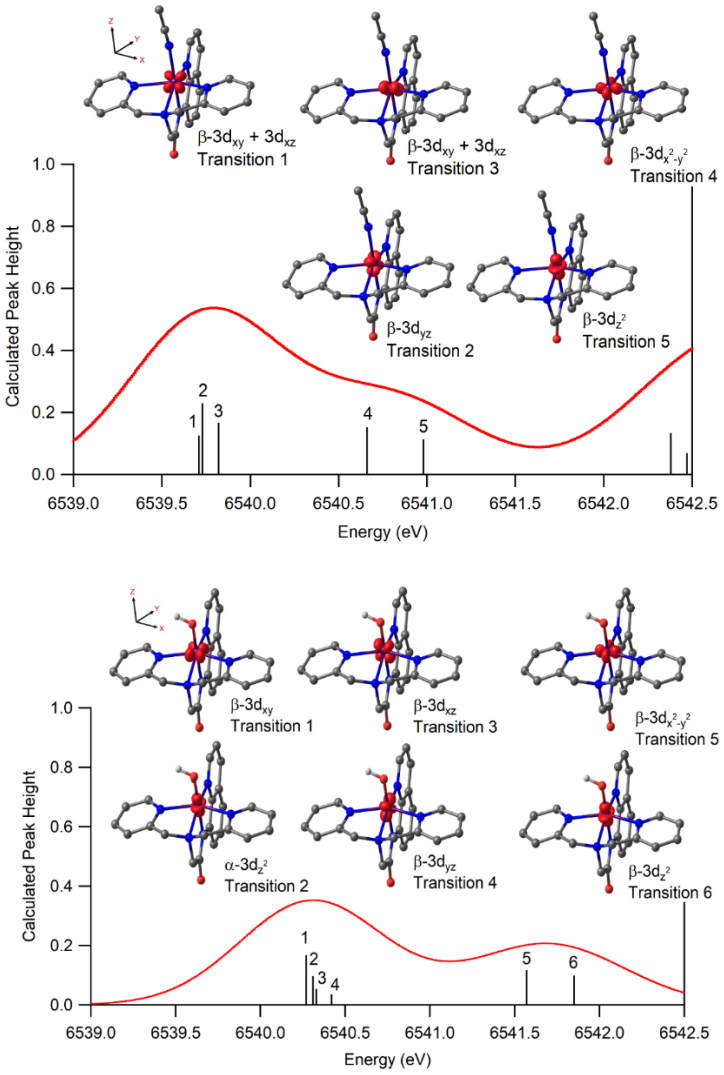

Figure 3.5. TD-DFT simulated pre-edge spectra with vertical lines showing transitions for 1-H(MeCN) (top) and 2-H(H_2O) (bottom). Electron density difference maps (EDDM) for the specified transitions are depicted and labeled by their primary acceptor orbital. The simulated spectra employed Gaussian functions with a 1 eV bandwidth.

The pre-edge regions of the Mn^{III}-hydroxo complexes **2-H** and **2-Me** are also expected to contain five 1s-to-3d transitions, from one-electron excitations from the Mn 1s β-spin MO to the five unoccupied 3d β-spin MOs, but these complexes will also contain an additional transition from the Mn 1s α-spin MO to the unoccupied $3d_z^2$ α-spin MO. In the TD-DFT spectra (see Figure 3.5, bottom for the TD-DFT spectrum computed for a DFT-geometry optimized model of **2-H**), these

six transitions give rise to two features centered at 6540.3 and 6541.7 eV, which are in good agreement with the experimental energies (Table 3.3). The lower-energy feature contains contributions from excitations terminating in the α-spin $3d_{z^2}$ and the β-spin t_{2g}-type orbitals, while the higher energy peak arises from excitations to the β-spin e_g-type orbitals (Figure 3.5, bottom). The larger splitting between the two sets of transitions for the Mn^{III} complexes reflects the increased ligand-field splitting (10*Dq*) of the Mn^{III} centers compared to their Mn^{II} counterparts. This is most likely the reason why the pre-edge spectra of complexes **2-H** and **2-Me** could be resolved into two bands (SI; Figure A2.4).

The total TD-DFT-computed area for these two pre-edge features are also very close to those observed for the **2-H**(H_2O) and **2-Me**(MeCN) samples, but lower than that observed for **2-H**(solid) (Table 3.3). Because of this slight increase in pre-edge area for **2-H**(solid) compared to **2-H**(H_2O), we evaluated the effects of minor geometric differences between the crystal-structure coordinates of **2-H** versus those obtained from DFT computations (see Table 3.2). The most notable difference between these two models is an elongation in the Mn^{III}–OH distance of ~0.04 Å in the DFT structure. For this comparison, a TD-DFT calculation was performed using the crystal structure coordinates of **2-H**, with only the positions of the hydrogen atoms optimized. The area of this structure was calculated to be 4.3 units, showing a modest increase over the 4.0 units obtained when using the DFT-optimized structure. The increase in pre-edge area can be attributed to a 35% and 40% increase in intensity of the transitions into the α- and β-spin $3d_{z^2}$ orbitals, respectively, which are strongly Mn–OH □-antibonding. This relatively large increase in the 1s-to-$3d_{z^2}$ transition intensities shows that minor differences in Mn–OH bond length could have appreciable impacts on the pre-edge features.

We compare the collective set of experimental pre-edge areas and energies with their TD-DFT counterparts in Figure 3.6. For this comparison, we expanded on our small set of data from previously reported Mn^{II}, Mn^{III}, and Mn^{IV} complexes, where the same pre-edge fitting and computational routines were employed.[22, 49] In both cases there is good agreement between experiment and theory. The graph of pre-edge area highlights the very small range of areas observed for the Mn^{II} and Mn^{III}-hydroxo complexes described in this study, which explains the difficulty in ascertaining any definitive trends among these complexes. For both the Mn^{II} and the Mn^{III}-hydroxo complexes in this work, modest 3d-4p mixing leads to relatively weak pre-edge features (Table 3.3), consistent with the experimental data. The good agreement observed here between experiment and theory is not entirely unsurprising, because the method for determining pre-edge areas was calibrated with Mn^{II} and Mn^{III} complexes, although no Mn^{III}-hydroxo complexes were included in the test set.

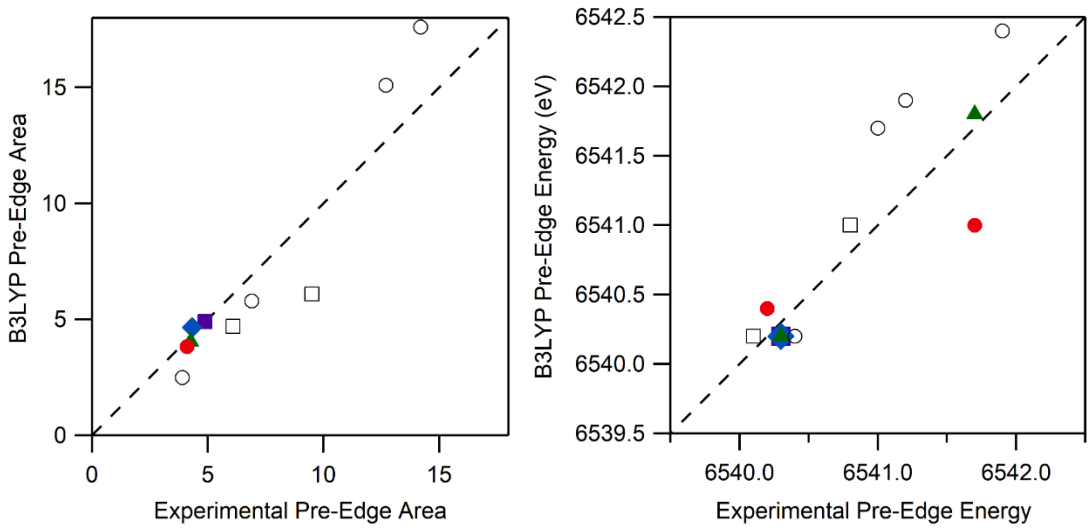

Figure 3.6. Comparison between experimental and DFT calculated pre-edge area (left) and pre-edge energies (right) for 1-H (violet rectangle), 1-Me (blue diamond), 2-H (green triangle), and 2-Me(red circle). Additional points for $[Mn^{II}(Cl_2)(Me_2EBC)]$, $[Mn^{IV}(OH)_2)(Me_2EBC)]^{2+}$, $[Mn^{IV}(O)(OH)(Me_2EBC)]^{+}$ and $[Mn^{IV}(O)(N4py)]^{2+}$ (open circles) from reference [22]. Points for $[Mn^{III}(O_2)(Me_2EBC)]^{+}$ and $[Mn^{III}(OH)(Cl)(Me_2EBC)]^{+}$ (open squares) from reference [49]. Dashed lines represent a slope of unity.

Conclusions.

Mn K-edge XAS is a prominent tool in the study of catalytic Mn centers, whether those in biological enzymes or synthetic species [8, 11, 22, 27]. The analysis of XAS data has long benefitted from benchmark studies on well-defined model systems. In such cases, it is ideal to perform such benchmarks using complexes with structural motifs found, or proposed for, the catalytic systems. Biological Mn centers often feature hydroxide ligation, with prominent examples including the Mn^{III} forms of MnSOD and MnLOX. Despite the importance of the Mn^{III}-hydroxo motif in biology, XAS studies of Mn^{III}-hydroxo complexes are quite limited. Our examination of a set of two Mn^{III}-hydroxo complexes, and their corresponding Mn^{II} species, using Mn XAS has offered new insights into the properties of these biologically-important species.

Our analysis of XAS data collected for solid- and solution-phase samples of Mn^{II} and Mn^{III}-hydroxo complexes shows that the pre-edge regions of these complexes are remarkable similar.

Despite the change in oxidation state and geometric structure, these species gave comparable total pre-edge areas (4.1 – 5.7 unites) and similar energies (6540.2 eV) for the most prominent pre-edge features. The only marked difference between the pre-edge regions is the presence of an additional pre-edge band in the Mn^{III}-hydroxo samples; although, the influence of this band on the overall pre-edge lineshape is subtle (Figure A2.4). Nonetheless, the Mn^{II} and Mn^{III}-hydroxo species considered here can be readily distinguished on the basis of their edge energies, which blue-shift by approximately 2 eV upon the increase in oxidation state (Figure 3.3). In addition, the FT EXAFS data are remarkably different, with fits of the EXAFS data for the Mn^{III}-hydroxo complexes showing the influence of the hydroxo ligand. Specifically, all EXAFS fits for the Mn^{III}-hydroxo complexes yielded a short Mn-N/O scattering shell with contributions from the hydroxo ligand as well as the *trans* amide nitrogen. However, only under very ideal circumstances could the Mn–OH distance be resolved into a separate shell. For example, the best fit to the solid-state sample of **1-H** did reveal a single O atom shell at 1.79 Å, confirming the short Mn^{III}-OH distance observed crystallographically for this complex. The resolution of this shell likely resulted from a combination of high-quality EXAFS data and an unusually short Mn^{III}-OH distance.

Collectively, our combined experimental and computational work suggests that it would be quite challenging to identify mononuclear Mn^{III}-hydroxo motifs in Mn enzymes solely on the basis of pre-edge data. This finding echoes our previous conclusions that one should always be cautious in inferring structural motifs on the basis of pre-edge data alone [22]. Nonetheless, analysis of EXAFS data for samples of good homogeneity should yield evidence of the short O atom shell expected for Mn^{III}-hydroxo centers. Only in ideal cases, however, should one expect to be able to determine the Mn^{III}-OH distance from EXAFS data analysis.

Acknowledgements.

This work was supported by NSF grant 1565661. Use of the Stanford Synchrotron Radiation Lightsource, SLAC National Accelerator Laboratory, is supported by the U.S. Department of Energy, Office of Science, Office of Basic Energy Sciences under Contract No. DE-AC02-76SF00515. The SSRL Structural Molecular Biology Program is supported by the DOE Office of Biological and Environmental Research, and by the National Institutes of Health, National Institute of General Medical Sciences (including P41GM103393). The contents of this publication are solely the responsibility of the authors and do not necessarily represent the official views of NIGMS or NIH. Use of Beamline 2-2 at SSRL was partially supported by the National Synchrotron Light Source II, Brookhaven National Laboratory, under U.S. Department of Energy Contract No. DE-SC0012704. XAS experiments were supported by the Case Western Reserve University Center for Synchrotron Biosciences NIH grant, P30-EB-009998, from the National Institute of Biomedical Imaging and Bioengineering (NIBIB). We thank Dr. Erik Farquhar at NSLS for outstanding support of our XAS experiments and for helpful conversations.

References.

1. Bull, C.; Niederhoffer, E. C.; Yoshida, T.; Fee, J. A., Kinetic-Studies of Superoxide Dismutases - Properties of the Manganese-Containing Protein from Thermus-Thermophilus. *Journal of the American Chemical Society* **1991,** *113* (11), 4069-4076.
2. Rulíšek, L.; Ryde, U., Structure of Reduced and Oxidized Manganese Superoxide Dismutase: A Combined Computational and Experimental Approach. *The Journal of Physical Chemistry B* **2006,** *110* (23), 11511-11518.
3. Wennman, A.; Oliw, E. H.; Karkehabadi, S.; Chen, Y., Crystal Structure of Manganese Lipoxygenase of the Rice Blast Fungus Magnaporthe oryzae. *J Biol Chem* **2016,** *291* (15), 8130-9.
4. Wennman, A.; Karkehabadi, S.; Oliw, E. H., Kinetic investigation of the rate-limiting step of manganese- and iron-lipoxygenases. *Archives of Biochemistry and Biophysics* **2014,** *555–556*, 9-15.
5. Su, C.; Oliw, E. H., *J. Biol. Chem.* **1998,** *273*, 13072.
6. Su, C.; Sahlin, M.; Oliw, E. H., Kinetics of Manganese Lipoxygenase with a Catalytic Mononuclear Redox Center. *Journal of Biological Chemistry* **2000,** *275* (25), 18830-18835.

7. Gaffney, B. J.; Su, C.; Oliw, E. H., Assignment of EPR Transitions in a Manganese-Containing Lipoxygenase and Prediction of Local Structure. *Appl Magn Reson* **2001,** *21* (3-4), 413-424.
8. Pecoraro, V. L.; Hsieh, W. Y., In search of elusive high-valent manganese species that evaluate mechanisms of photosynthetic water oxidation. *Inorg Chem* **2008,** *47* (6), 1765-78.
9. McEvoy, J. P.; Brudvig, G. W., Water-splitting chemistry of photosystem II. *Chem Rev* **2006,** *106* (11), 4455-83.
10. Glockner, C.; Kern, J.; Broser, M.; Zouni, A.; Yachandra, V.; Yano, J., Structural changes of the oxygen-evolving complex in photosystem II during the catalytic cycle. *J Biol Chem* **2013,** *288* (31), 22607-20.
11. Yano, J.; Yachandra, V., Mn4Ca Cluster in Photosynthesis: Where and How Water is Oxidized to Dioxygen. *Chemical Reviews* **2014,** *114* (8), 4175-4205.
12. Rice, D. B.; Wijeratne, G. B.; Burr, A. D.; Parham, J. D.; Day, V. W.; Jackson, T. A., Steric and Electronic Influence on Proton-Coupled Electron-Transfer Reactivity of a Mononuclear Mn(III)-Hydroxo Complex. *Inorg Chem* **2016,** *55* (16), 8110-20.
13. Wijeratne, G. B.; Corzine, B.; Day, V. W.; Jackson, T. A., Saturation kinetics in phenolic O-H bond oxidation by a mononuclear Mn(III)-OH complex derived from dioxygen. *Inorg Chem* **2014,** *53* (14), 7622-34.
14. Coggins, M. K.; Brines, L. M.; Kovacs, J. A., Synthesis and structural characterization of a series of Mn(III)OR complexes, including a water-soluble Mn(III)OH that promotes aerobic hydrogen-atom transfer. *Inorg Chem* **2013,** *52* (21), 12383-93.
15. Goldsmith, C. R.; Cole, A. P.; Stack, T. D. P., C−H Activation by a Mononuclear Manganese(III) Hydroxide Complex: Synthesis and Characterization of a Manganese-Lipoxygenase Mimic? *Journal of the American Chemical Society* **2005,** *127* (27), 9904-9912.
16. Yano, J.; Kern, J.; Irrgang, K. D.; Latimer, M. J.; Bergmann, U.; Glatzel, P.; Pushkar, Y.; Biesiadka, J.; Loll, B.; Sauer, K.; Messinger, J.; Zouni, A.; Yachandra, V. K., X-ray damage to the Mn4Ca complex in single crystals of photosystem II: a case study for metalloprotein crystallography. *Proc Natl Acad Sci U S A* **2005,** *102* (34), 12047-52.
17. Frank, P.; Benfatto, M.; Qayyam, M.; Hedman, B.; Hodgson, K. O., A high-resolution XAS study of aqueous Cu(II) in liquid and frozen solutions: pyramidal, polymorphic, and non-centrosymmetric. *J Chem Phys* **2015,** *142* (8), 084310.
18. Kau, L. S.; Spira-Solomon, D. J.; Penner-Hahn, J. E.; Hodgson, K. O.; Solomon, E. I., X-ray absorption edge determination of the oxidation state and coordination number of copper. Application to the type 3 site in Rhus vernicifera laccase and its reaction with oxygen. *Journal of the American Chemical Society* **1987,** *109* (21), 6433-6442.
19. Westre, T. E.; Kennepohl, P.; DeWitt, J. G.; Hedman, B.; Hodgson, K. O.; Solomon, E. I., A multiplet analysis of Fe K-edge 1s->3d pre-edge features of iron complexes. *Journal of the American Chemical Society* **1997,** *119* (27), 6297-6314.
20. DeBeer George, S.; Petrenko, T.; Neese, F., Prediction of iron K-edge absorption spectra using time-dependent density functional theory. *J Phys Chem A* **2008,** *112* (50), 12936-43.
21. DeBeer George, S.; Brant, P.; Solomon, E. I., Metal and Ligand K-Edge XAS of Organotitanium Complexes: Metal 4p and 3d Contributions to Pre-edge Intensity and Their Contributions to Bonding. *Journal of the American Chemical Society* **2005,** *127* (2), 667-674.
22. Leto, D. F.; Jackson, T. A., Mn K-Edge X-ray Absorption Studies of Oxo- and Hydroxomanganese(IV) Complexes: Experimental and Theoretical Insights into Pre-Edge Properties. *Inorg. Chem.* **2014,** *53*, 6179-6194.

23. England, J.; Martinho, M.; Farquhar, E. R.; Frisch, J. R.; Bominaar, E. L.; Munck, E.; Que, L., Jr., A synthetic high-spin oxoiron(IV) complex: generation, spectroscopic characterization, and reactivity. *Angew Chem Int Ed Engl* **2009,** *48* (20), 3622-6.
24. Jackson, T. A.; Rohde, J. U.; Seo, M. S.; Sastri, C. V.; DeHont, R.; Stubna, A.; Ohta, T.; Kitagawa, T.; Munck, E.; Nam, W.; Que, L., Jr., Axial ligand effects on the geometric and electronic structures of nonheme oxoiron(IV) complexes. *J Am Chem Soc* **2008,** *130* (37), 12394-407.
25. Rohde, J. U.; Torelli, S.; Shan, X. P.; Lim, M. H.; Klinker, E. J.; Kaizer, J.; Chen, K.; Nam, W. W.; Que, L., Structural insights into nonheme alkylperoxoiron(III) and oxoiron(IV) intermediates by x-ray absorption spectroscopy. *Journal of the American Chemical Society* **2004,** *126* (51), 16750-16761.
26. Krewald, V.; Lassalle-Kaiser, B.; Boron, T. T., 3rd; Pollock, C. J.; Kern, J.; Beckwith, M. A.; Yachandra, V. K.; Pecoraro, V. L.; Yano, J.; Neese, F.; DeBeer, S., The protonation states of oxo-bridged Mn(IV) dimers resolved by experimental and computational Mn K pre-edge X-ray absorption spectroscopy. *Inorg Chem* **2013,** *52* (22), 12904-14.
27. Rees, J. A.; Martin-Diaconescu, V.; Kovacs, J. A.; DeBeer, S., X-ray Absorption and Emission Study of Dioxygen Activation by a Small-Molecule Manganese Complex. *Inorg Chem* **2015,** *54* (13), 6410-22.
28. Roemelt, M.; Beckwith, M. A.; Duboc, C.; Collomb, M. N.; Neese, F.; DeBeer, S., Manganese K-edge X-ray absorption spectroscopy as a probe of the metal-ligand interactions in coordination compounds. *Inorg Chem* **2012,** *51* (1), 680-7.
29. Ravel, B.; Newville, M., ATHENA, ARTEMIS, HEPHAESTUS: data analysis for X-ray absorption spectroscopy using IFEFFIT. *Journal of Synchrotron Radiation* **2005,** *12* (4), 537-541.
30. Rehr, J. J.; Mustre de Leon, J.; Zabinsky, S. I.; Albers, R. C., Theoretical x-ray absorption fine structure standards. *Journal of the American Chemical Society* **1991,** *113* (14), 5135-5140.
31. Wojdyr, M., Fityk: a general-purpose peak fitting program. *Journal of Applied Crystallography* **2010,** *43* (5 Part 1), 1126-1128.
32. Neese, F., The ORCA program system. *Wires Comput Mol Sci* **2012,** *2* (1), 73-78.
33. Becke, A. D., Density Functional Calculations of Molecular Bond Energies. *Journal of Chemical Physics* **1986,** *84* (8), 4524-4529.
34. Perdew, J. P., Density Functional Approximation for the Correlation Energy of the Inhomogeneous Electron Gas. *Phys. Rev. B* **1986,** *33* (12), 8822-8824.
35. Schäfer, A.; Horn, H.; Ahlrichs, R., Fully Optimized Contracted Gaussian Basis Sets for Atoms Lithium to Krypton. *J. Chem. Phys.* **1992,** *97* (4), 2571-2577.
36. Schäfer, A.; Huber, C.; Ahlrichs, R., Fully Optimized Contracted Gaussian Basis Sets of Triple Zeta Valence Quality for Atoms Li to Kr. *J. Chem. Phys.* **1994,** *100*, 5829-5835.
37. Neese, F., An Improvement of the Resolution of the Identity Approximation for the Calculation of the Coulomb Matrix. *Journal of Computational Chemistry* **2003,** *24*, 1740-1747.
38. Sinnecker, S.; Rajendran, A.; Klamt, A.; Diedenhofen, M.; Neese, F., Calculation of Solvent Shifts on Electronic g-Tensors with the Conductor-Like Screening Model (COSMO) and Its Self-Consistent Generalization to Real Solvents (Direct COSMO-RS). *Journal of Physical Chemistry A* **2006,** *110* (6), 2235-2245.
39. Hirata, S.; Head-Gordon, M., Time-dependent Density Functional Theory for Radicals: An Improved Description of Excited States with Substantial Double Excitation Character. *Chem. Phys. Lett.* **1999,** *302*, 375-382.
40. Hirata, S.; Head-Gordon, M., Time-dependent Density Functional Theory within the Tamm–Dancoff Approximation. *Chem. Phys. Lett.* **1999,** *314*, 291-299.

41. Becke, A. D., Density-functional Thermochemistry. III. The Role of Exact Exchange. *J. Chem. Phys.* **1993,** *98* (7), 5648-5652.
42. Lee, C.; Yang, W.; Parr, R. G., Development of the Colle-Salvetti Correlation-energy Formula into a Functional of the Electron Density. *Phys. Rev. B* **1988,** *37* (2), 785-789.
43. Weigend, F.; Ahlrichs, R., Balanced basis sets of split valence, triple zeta valence and quadruple zeta valence quality for H to Rn: Design and assessment of accuracy. *Physical Chemistry Chemical Physics* **2005,** *7* (18), 3297-3305.
44. Lenthe, E. v.; Baerends, E. J.; Snijders, J. G., Relativistic regular two-component Hamiltonians. *Journal of Chemical Physics* **1993,** *99* (6), 4597-4610.
45. van Wüllen, C., Molecular density functional calculations in the regular relativistic approximation: Method, application to coinage metal diatomics, hydrides, fluorides and chlorides, and comparison with first-order relativistic calculations. *Journal of Chemical Physics* **1998,** *109* (2), 392-399.
46. Ciringh, Y.; Gordon-Wylie, S. W.; Norman, R. E.; Clark, G. R.; Weintraub, S. T.; Horwitz, C. P., Multinuclear Paramagnetic NMR Spectra and Solid State X-ray Crystallographic Characterization of Manganese(III) Schiff-Base Complexes. *Inorganic Chemistry* **1997,** *36* (22), 4968-4982.
47. Ching, W. M.; Zhou, A.; Klein, J.; Fan, R.; Knizia, G.; Cramer, C. J.; Guo, Y.; Que, L., Jr., Characterization of the Fleeting Hydroxoiron(III) Complex of the Pentadentate TMC-py Ligand. *Inorg Chem* **2017,** *56* (18), 11129-11140.
48. Leto, D. F.; Ingram, R.; Day, V. W.; Jackson, T. A., Spectroscopic properties and reactivity of a mononuclear oxomanganese(iv) complex. *Chemical Communications* **2013,** *49* (47), 5378-5380.
49. Colmer, H. E.; Howcroft, A. W.; Jackson, T. A., Formation, Characterization, and O-O Bond Activation of a Peroxomanganese(III) Complex Supported by a Cross-Clamped Cyclam Ligand. *Inorg Chem* **2016,** *55* (5), 2055-69.

Chapter 4

NMR Studies of Mn^{III}-hydroxo Adduct Reveal an Equilibrium between Mn^{III}-hydroxo and μ-Oxodimanganese(III,III) Species

4.1 Introduction

Manganese-hydroxo units play critical roles in a number of manganese-dependent enzymes.[1] For example, the manganese(III) forms of both manganese superoxide dismutase (MnSOD)[2-4] and manganese lipoxygenase (MnLOX)[5-7] have been proposed to contain mononuclear Mn^{III}-hydroxo adducts that are critical to the functions of these enzymes. In MnSOD, the Mn^{III}-hydroxo unit mediates the oxidation of superoxide to dioxygen,[4] which constitutes half of the superoxide disproportionation reaction. In MnLOX, an active-site Mn^{III}-hydroxo center abstracts a hydrogen atom from an unsaturated fatty acid, initiating C–H bond peroxidation.[6-7] Manganese-hydroxo motifs might also serve as intermediates in the stepwise oxidation of the oxygen-evolving complex of photosystem II.[8] In each of these processes, an oxidation-reduction event is coupled (to varying degrees) with a proton transfer. Because of the importance of Mn^{III}-hydroxo species in proton-coupled electron-transfer processes in biology, there has been much interest in understanding the properties and chemical reactivity of synthetic complexes bearing the Mn^{III}-hydroxo unit.[9-18]

In recent years, a number of Mn^{III}-hydroxo complexes have highlighted the chemical reactivity of these complexes and raised intriguing questions concerning the structural and electronic factors that influence reactivity. In 2005, Goldsmith and Stack reported a mononuclear Mn^{III}-hydroxo complex supported by a pentadentate, pyridine-containing ligand, PY5 (PY5 = 2,6-bis(bis(2-pyridyl)methoxymethane)pyridine).[9] This complex was capable of attacking C–H bonds of moderate strength, such as those of toluene (C–H bond dissociation energy, BDE, of ca. 88 kcal/mol), by a hydrogen-atom transfer (HAT) mechanism. The relatively high reactivity of this complex was attributed to the moderate strength of the O–H bond formed in the Mn^{II}-aqua product (BDE of 82 ± 2 kcal/mol).[9] More recently, Coggins, Kovacs, and co-workers described a series of Mn^{III}–OR complexes (where R = H, Ph, Me, and *p*-NO_2-C_6H_4) supported by the pentadentate,

thiolate-containing, N_4S^- ligand ($S^{Me2}N_4$(tren)).[10] These complexes were generated by treatment of the oxo-bridged dimanganese(III,III) complex $[Mn^{III}_2(\mu\text{-}O)(S^{Me2}N_4(tren))_2]^{2+}$ with an excess of ROH. In this system, the Mn^{III}-hydroxo complex $[Mn^{III}(OH)(S^{Me2}N_4(tren))_2]^+$ could only attack the highly activated O–H bond of TEMPOH (2,2',6,6'-tetramethylpiperidine-1-ol; O–H BDE of 66.5 kcal/mol),[10] showing more limited reactivity than $[Mn^{III}(OH)(PY5)]^+$. The muted reactivity of $[Mn^{III}(OH)(S^{Me2}N_4(tren))]^+$ likely derives from the weaker O–H bond formed in the $[Mn^{II}(OH_2)(S^{Me2}N_4(tren))]^+$ product (bond dissociation free energy, BDFE, of 70 kcal/mol in CH_3CN).[10]

Our lab has recently reported a pair of Mn^{III}-hydroxo complexes supported by monoanionic, pentadentate ligands with an amide function *trans* to the hydroxo moiety (dpaq and $dpaq^{2Me}$; 2-[bis(pyridin-2-ylmethyl)]amino-N-quinolin-8-yl-acetamidate and 2-[bis(pyridin-2-ylmethyl)]amino-N-2-methyl-quinolin-8-yl-acetamidate, respectively).[11-12, 18] The molecular structures of these complexes, which were determined by X-ray crystallography, are shown in Figure 4.1. The originally reported $[Mn^{III}(OH)(dpaq)]^+$ complex showed HAT reactivity intermediate between that of $[Mn^{III}(OH)(PY5)]^+$ and $[Mn^{III}(OH)(S^{Me2}N_4(tren))]^+$.[18] For example, $[Mn^{III}(OH)(dpaq)]^+$ was capable of oxidizing phenolic O–H bonds with BDEs up to 79 kcal/mol.[18] In spite of the greater range of reactivity compared to $[Mn^{III}(OH)(S^{Me2}N_4(tren))]^+$, the $[Mn^{III}(OH)(dpaq)]^+$ complex oxidized TEMPOH with a second order rate constant (k_2) roughly 10^4-fold smaller than that of $[Mn^{III}(OH)(S^{Me2}N_4(tren))]^+$.[10, 18] To understand the factors affecting the HAT reaction rate, both the Mn^{III}-methoxy analogue, $[Mn^{III}(OMe)(dpaq)]^+$, and the $[Mn^{III}(OH)(dpaq^{2Me})]^+$ derivative were generated and investigated (Figure 4.1).[11, 19] While $[Mn^{III}(OMe)(dpaq)]^+$ showed HAT rates with TEMPOH nearly identical to those observed for $[Mn^{III}(OH)(dpaq)]^+$,[19] the $[Mn^{III}(OH)(dpaq^{2Me})]^+$ complex displayed a dramatic rate enhancement for TEMPOH oxidation of 240-fold compared to

$[Mn^{III}(OH)(dpaq)]^{+}$.[11] In $[Mn^{III}(OH)(dpaq^{2Me})]^{+}$, the quinoline moiety is appended with a methyl group adjacent to the nitrogen donor atom (Figure 4.1, center). This methyl group causes an elongation in the Mn–N(quinoline) distance that results in the $dpaq^{2Me}$ ligand being a weaker donor than dpaq. The dramatic rate increase for $[Mn^{III}(OH)(dpaq^{2Me})]^{+}$ was attributed in part to the 0.09 V more positive Mn^{III}/Mn^{II} reduction potential of this complex, which derives from the weaker Mn–N(quinoline) interaction (increase in Mn–N(quinoline) distance of 0.11 Å for $[Mn^{III}(OH)(dpaq^{2Me})]^{+}$).[11]

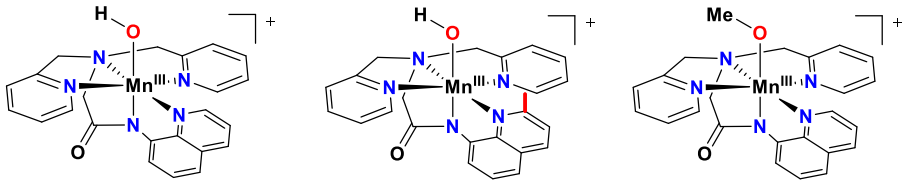

[Mn^{III}(OH)(dpaq)]$^{+}$ **[Mn^{III}(OH)(dpaq^{2Me})]$^{+}$** **[Mn^{III}(OMe)(dpaq)]$^{+}$**

Figure 4.1. Molecular structures of $[Mn^{III}(OH)(dpaq)]^{+}$ (left), $[Mn^{III}(OH)(dpaq^{2Me})]^{+}$ (center), and $[Mn^{III}(OMe)(dpaq)]^{+}$ (right). The methylquinoline group of the dpaq2Me ligand is shown in bold-red for emphasis.

One challenge in understanding how the structural and electronic properties of these mononuclear Mn^{III}-hydroxo and Mn^{III}-methoxy species influence their reactivity is the lack of spectroscopic methods available for solution-phase characterization at temperatures relevant to the kinetic experiments. While electronic absorption spectroscopy is an outstanding tool for following reaction kinetics, this method can provide only limited insight into structural properties of the Mn^{III} center. We have recently reported Mn K-edge X-ray absorption experiments of solution- and solid-state samples of the $[Mn^{III}(OH)(dpaq)]^{+}$ and $[Mn^{III}(OH)(dpaq^{2Me})]^{+}$ complexes.[12] Analyses of EXAFS data revealed very similar structures for the solution- and solid-state samples; however, these experiments were performed for samples at low-temperatures (10 K).[12] A potentially attractive

method for gaining further insight into the properties of these Mn^{III} units in solution is ^{1}H-NMR spectroscopy. Although hyperfine interactions involving unpaired electrons on the Mn^{III} centers cause the ^{1}H-NMR signals of these complexes to be broad and extend over a wide chemical shift range, several groups have had success in characterizing Mn^{III}-Schiff base complexes using ^{1}H-NMR spectroscopy.[20-22]

In this present work, we describe ^{1}H-NMR experiments to investigate the properties of the $[Mn^{III}(OH)(dpaq)]^+$ and $[Mn^{III}(OH)(dpaq^{2Me})]^+$ complexes in CD_3CN solution at room temperature. The ^{1}H-NMR spectrum of $[Mn^{III}(OH)(dpaq^{2Me})]^+$ shows hyperfine-shifted resonances spanning the 128 to -53 ppm range, as expected for this mononuclear S = 2 Mn^{III} species. In contrast, the ^{1}H-NMR spectrum of $[Mn^{III}(OH)(dpaq)]^+$ in CD_3CN shows hyperfine-shifted resonances associated with the Mn^{III}-hydroxo complex, as well as resonances in the diamagnetic region that arise from a separate, spin-coupled Mn species. Mn K-edge X-ray absorption data, along with other physical methods, support the formulation of this diamagnetic species as $[Mn^{III}_2(\mu\text{-}O)(dpaq)_2]^{2+}$. The addition of small amounts of water to this mixture of complexes in acetonitrile results in near-complete formation of the mononuclear $[Mn^{III}(OH)(dpaq)]^+$ complex. These new findings prompted us to re-evaluate the HAT reactivity of $[Mn^{III}(OH)(dpaq)]^+$ towards TEMPOH. Prior kinetics experiments, which were performed in CH_3CN in the absence of any added water, were reflective not only of the reactivity of the Mn^{III}-hydroxo species, but also the water-dependent equilibrium between the $[Mn^{III}(OH)(dpaq)]^+$ and $[Mn^{III}_2(\mu\text{-}O)(dpaq)_2]^{2+}$ complexes. Kinetics experiments performed for $[Mn^{III}(OH)(dpaq)]^+$ in the presence of added water show that the rate of TEMPOH oxidation is more similar to that of $[Mn^{III}(OH)(dpaq^{2Me})]^+$ than previously reported.

4.2 Materials and Methods

Materials and Instrumentation. All chemical and solvents were obtained from commercial vendors at, or better than, ACS grade, unless otherwise described. CH_3CN, CH_3OH, and ether were dried and degassed using a Pure Solv purification system, as previously described.[11] Deuterated acetonitrile (CD_3CN) and methanol (CD_3OD) were purchased from Acros Organics, dried over 3 Å sieves, and degassed using the freeze-pump-thaw method. The $[Mn^{III}(OH)(dpaq)](OTf)$,[18] $[Mn^{III}(OMe)(dpaq)](OTf)$,[19] and $[Mn^{III}(OH)(dpaq^{2Me})](OTf)$[11] complexes, and TEMPOH,[23] were prepared as described previously. The water content in dried acetonitrile was determined to be 64(8) ppm by Karl-Fischer titration with a Mettler Toledo DL39 coulometric titrator. This quantity of water corresponds to a concentration of 2.8 mM.

Acquisition of ^{1}H NMR Data. Samples were collected on a 400 MHz Bruker AVIIIHD NMR with an acquisition time of 0.27 s and a D1 of 0 seconds with a spectral width of 150 to -100 ppm. Multiple acquisitions, scanning a total width of 1 000 to -500 ppm, showed no peaks outside 150 to -100 ppm. At least 1000 scans were collected to provide sufficient S/N. Spectra were baseline subtracted with the multipoint fitting procedure using spline functions as available in MestReNova. Quantification of diamagnetic species was performed in CD_3CN using equimolar (per Mn) 1,2,4,5-tetrachloro-3-nitrobenzene, with a delay, *D1*, of 50 s, and 128 scans were averaged to provide a sufficient signal-to-noise ratio.

Measurement of ^{1}H Longitudinal Relaxation Time Constants (T_1) for $[Mn^{III}(OMe)(dpaq)]^+$. ^{1}H-NMR spectra for a 80 mM sample of $[Mn^{III}(OMe)(dpaq)]^+$ in CD_3OD were acquired on a 500 MHz Bruker DRX spectrometer equipped with an X-channel broadband observe probe. Data were processed and visualized using Bruker Topspin and Mestrelabs MestReNova software. The required spectral width to sample all resonances of the paramagnetic

complex $[Mn^{III}(OMe)(dpaq)]^+$ is greater than 200 ppm. To enable digitally oversampled data acquisition with high resolution and sensitivity, we took a 'divide-and-conquer' approach and collected five separate spectra with spectral widths ca. 20 ppm to sample the entire chemical shift range. The pseudo-2D "inversion recovery" pulse sequence was used to measure the T_1 relaxation time constant.[24] Equation 1 was fit to the results of this experiment,

$$I^{raw}(\tau) = I_0^{raw}(1 - 2 \times A \times e^{\frac{-\tau}{T_1}}) \quad (1)$$

where $I^{raw}(\tau)$, I_0^{raw}, A, τ and T_1 are the raw integral value at time *t*, the equilibrium raw integral value (*i.e.*, $I^{raw}(\tau = \infty)$), flip angle factor, delay between pulses, and longitudinal relaxation time constant, respectively. The flip angle factor (which equals 1 when T_1 >> 180° pulse width) is included to account for relaxation during pulses. To facilitate comparison between experiments, the inversion recovery experimental data are presented as normalized peak integral values according to equation 2,

$$I^{norm}(\tau) = 1 - 2 \times e^{\frac{-\tau}{T_1}} \quad (2)$$

where $I^{norm}(\tau)$ is related to $I^{raw}(\tau)$ by equation 3,

$$I^{norm}(\tau) = 1 - \frac{(1 - \frac{I^{raw}(\tau)}{I_0^{raw}})}{A} \quad (3)$$

The longitudinal relaxation time constant (T_1) of nine peaks (labeled 1 - 9 in Figure A3.1) were measured using the inversion recovery pulse sequence. Table A3.1 summarizes the results from the inversion recovery experiments. Figures S2, S4, S8, S10 and S14 show the truncated 1D ^{1}H spectra of the selected peaks. Figure A3.3, A3.5, A3.6, A3.7, A3.9, A3.11, A3.12, A3.13 and A3.15 show the

normalized peak integral versus *t* for peaks 1 - 9, respectively. Figure A3.16 shows the inverted diamagnetic peaks surrounding the peak at 2.3 ppm at a τ of 0.01 s.

Kinetic Studies of the H_2O Addition to CH_3CN Solutions of $[Mn^{III}(OH)(dpaq)](OTf)$. Solutions of $[Mn^{III}(OH)(dpaq)](OTf)$ dissolved in CH_3CN consist of a mixture of a dimeric species and a mononuclear Mn^{III}-hydroxo adduct. The rate of conversion of the dimer to the Mn^{III}-hydroxo monomer in CH_3CN was investigated as a function of water concentration at -15 °C and 25 °C. For these experiments, a 1.25 mM solution of $[Mn^{III}(OH)(dpaq)](OTf)$ dissolved in CH_3CN was prepared in an argon-filled glovebox. A 2 mL aliquot of this solution was placed in a gastight cuvette and sealed with a septum. The cuvette was removed from the glovebox and placed in a Unisoku cryostat, interfaced with an Agilent 8453 spectrophotometer. The cuvette was allowed to equilibrate in the cryostat for 10 minutes before the reaction was initiated. A separate solution of CH_3CN with varying amounts of added H_2O was prepared and sparged with N_2 gas for 10 minutes. A 100 μL aliquot of this CH_3CN:H_2O solution (containing variable amounts of H_2O; 22 to 2200 equivalents of H_2O per Mn), or 200 μL neat H_2O for the delivery of 4400 equivalents, was added to the cuvette and the ensuing reaction was monitored by electronic absorption spectroscopy. After the addition of water, the decrease in absorbance at 620 nm versus time followed first-order behavior for 5 half-lives, which permitted the determination of a first-order rate constant at different concentrations of added water.

Kinetic Studies of the Reaction of $[Mn^{III}(OH)(dpaq)](OTf)$ with TEMPOH in a CH_3CN:H_2O mixture. A 1.25 mM solution of $[Mn^{III}(OH)(dpaq)](OTf)$ in CH_3CN was prepared in an argon-filled glovebox, and 2 mL of this solution were placed in a gastight cuvette and sealed with a septum. The cuvette was removed from the glovebox and placed in a Unisoku cryostat, held at -35 °C, interfaced with an Agilent 8453 spectrophotometer or a Cary 50 Bio spectrophotometer. The

cuvette was allowed to equilibrate to -35 °C for 10 minutes before initiating the reaction. A 100 μL aliquot of a 60:40 (vol:vol) CH_3CN:H_2O solution, which had been sparged with N_2 gas, was added to the cuvette. This corresponds to an addition of 880 equivalents of H_2O per Mn. On the basis of ^{1}H-NMR experiments, this H_2O:Mn ratio leads to over 95% formation of the mononuclear Mn^{III}-hydroxo species. After the reaction with H_2O was judged complete using electronic absorption spectroscopy, 100 μL of a solution of TEMPOH in CH_3CN was added to the cuvette. The disappearance of the Mn^{III}-hydroxo signal was monitored by electronic absorption spectroscopy, and the decrease in the signal at 770 nm versus time was fit to determine a pseudo-first order rate constant. Stock solutions of TEMPOH were used to deliver between 10 and 100 equivalents relative to the total Mn, and pseudo-first order rates collected at different equivalents of TEMPOH were used to determine a second-order rate constant. The temperature-dependence of the reaction with TEMPOH was determined by carrying out the above procedure at temperatures between -35 and 11.5 °C for 10 equivalents TEMPOH per Mn.

XAS Experiments for $[Mn^{III}_2(\mu\text{-}O)(dpaq)_2]^{2+}$. A frozen solution sample of $[Mn^{III}_2(\mu\text{-}O)(dpaq)_2]^{2+}$ was generated by preparing a 10 mM solution of $[Mn^{III}(OH)(dpaq)](OTf)$ in CH_3CN, transferring this solution to an XAS sample cup, and rapidly freezing the sample in liquid nitrogen. The Mn K-edge XAS data were collected over an energy range from 6300 – 7250 eV. A manganese foil was used as a reference and internal calibration was performed by assigning the edge energy of the foil to 6539.0 eV. Spectra were obtained via fluorescence excitation at beamline 2-2 at Stanford Synchrotron Radiation Lightsource (SSRL) at 10 K using a Si(111) monochromator and 13-element Ge array detector.

EXAFS data analysis was performed using the *DEMETER* software package and fitting was carried out in *ARTEMIS* on the $k^3\chi$(k) data.[25] *FEFF6* was used to generate the phase and amplitude

functions from the DFT-optimized antiferromagnetically coupled (*i.e.*, broken symmetry $S = 0$) $[Mn^{III}_2(\mu\text{-}O)(dpaq)_2]^{2+}$ structure.[26] For the fits, the parameters R (average scattering pathway distance) were optimized individually and the E_0 parameter was a common variable for all paths. The *n* (degeneracy) parameter was fixed for each fit and varied between fits. The σ^2 (Debye-Waller factor) was optimized individually for all single-scattering O, N, and C pathways but was optimized as a single variable for both the O-Mn and O-Mn-O collinear multiple-scattering pathways ($\sigma^2_{OMn} = \sigma^2_{OMnO}$).

Electronic Structure Calculations. DFT calculations were performed using the *ORCA 4.0.1* software package.[27-28] The broken symmetry ($S = 0$) $[Mn^{III}_2(\mu\text{-}O)(dpaq)_2]^{2+}$ and $[Mn^{III}_2(\mu\text{-}OH)(dpaq)_2]^{3+}$ complexes were optimized using the BP86 functional and the RI approximation.[29-30] The def2-TZVP basis set was used for Mn, O, and N and the def2-SVP basis set was used for all C and H atoms and the respective auxiliary basis sets were used for the RI approximation.[31]

4.3 Results and Discussion

Summary of Previous Characterization of $[Mn^{III}(OH)(dpaq)]^+$. Previous investigations of $[Mn^{III}(OH)(dpaq)]^+$ had established the molecular structure of this complex through X-ray crystallography.[18] The X-ray structure revealed a mononuclear Mn^{III} center in a distorted octahedral environment, with the hydroxo *trans* to the amide function of the dpaq ligand (Figure 4.1, left). The properties of $[Mn^{III}(OH)(dpaq)]^+$ in CH_3CN solution were probed by electrospray ionization mass spectrometry (ESI-MS), which showed an ion peak associated with $[Mn^{III}(OH)(dpaq)]^+$ (all other ion peak intensities were <5% that of the $[Mn^{III}(OH)(dpaq)]^+$ peak).[18] In addition, the solution magnetic moment of $[Mn^{III}(OH)(dpaq)]^+$ was in excellent agreement with that expected for a high-spin d^4

system (4.88 and 4.89 μ_B, respectively).[18] Collectively, these data provided reasonable evidence to presume that the mononuclear structure of $[Mn^{III}(OH)(dpaq)]^+$ was retained in CH_3CN solution.

^{1}H-NMR investigations of $[Mn^{III}(OH)(dpaq)]^+$ in CD_3CN reveal a water-dependent equilibrium. The ^{1}H-NMR spectrum of $[Mn^{III}(OH)(dpaq)](OTf)$ dissolved in CD_3CN reveals at least twenty-eight peaks that span the chemical shift range of 130 to -60 ppm (Figure 4.2A). Because this number of peaks is greater than the number of protons in the $[Mn^{III}(OH)(dpaq)]^+$ complex, additional species must be present in solution. Moreover, only seventeen of the twenty-eight peaks are outside the chemical shift window of 14 to 0 ppm (Figure 4.2A). The majority of peaks observed within this diamagnetic region show relatively sharp linewidths (Figure A3.17). Previously reported ^{1}H-NMR spectra of Mn^{III} complexes with Schiff base ligands showed that hyperfine-shifted ligand protons typically displayed signals outside the chemical shift window of 20 to -3 ppm.[20-21] Any signals observed from 20 to -3 ppm that were associated with the mononuclear Mn^{III} complexes were quite broad relative to solvent-derived peaks. We therefore conclude that many of the signals observed in the ^{1}H-NMR spectrum of $[Mn^{III}(OH)dpaq)]^+$ in CD_3CN arise from one or more diamagnetic species.

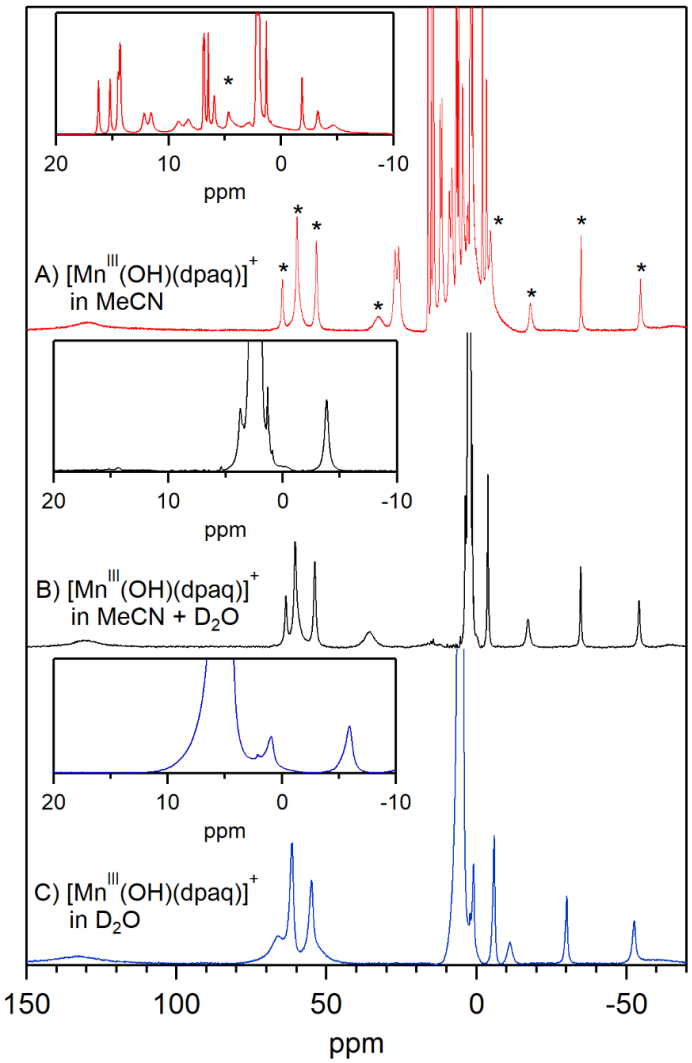

Figure 4.2. ^{1}H-NMR spectra of 15 mM [Mn^{III}(OH)(dpaq)](OTf) dissolved in A) CD_3CN, B) CD3CN and 45 µL added D_2O, and C) pure D_2O (4 mM). The insets show an expanded view of the 20 to -10 ppm region. The asterisks in A) mark resonances that show a Curie temperature dependence, as expected for signals associated with a paramagnetic species.

To further explore the large number of ^{1}H-NMR peaks observed when [Mn^{III}(OH)(dpaq)](OTf) is dissolved in CD_3CN, we determined the temperature dependence of the chemical shifts from 25 to -35 °C (Figure 4.3, Figure A3.18). From this analysis, we observe two types of peaks. There are nine peaks that shift towards the diamagnetic region and sharpen with increasing temperature (Figure 4.3, left). These peaks are marked with asterisks in Figure 4.2A. (We

were unable to collect temperature-dependent shifts for the peaks at 130 and -65 ppm, as these peaks were too broad and weak to reliably observe at temperatures below 25 °C.) Prior NMR studies on copper systems have shown that paramagnetic, or weakly antiferromagnetically-coupled, systems will follow Curie behavior, and as temperature is increased, the isotropically-shifted peaks shift towards the diamagnetic region and sharpen.[20, 32-34] Thus, the temperature-dependence of these chemical shifts support our assignment that these peaks are associated with the $S = 2$ $[Mn^{III}(OH)(dpaq)]^+$ complex.

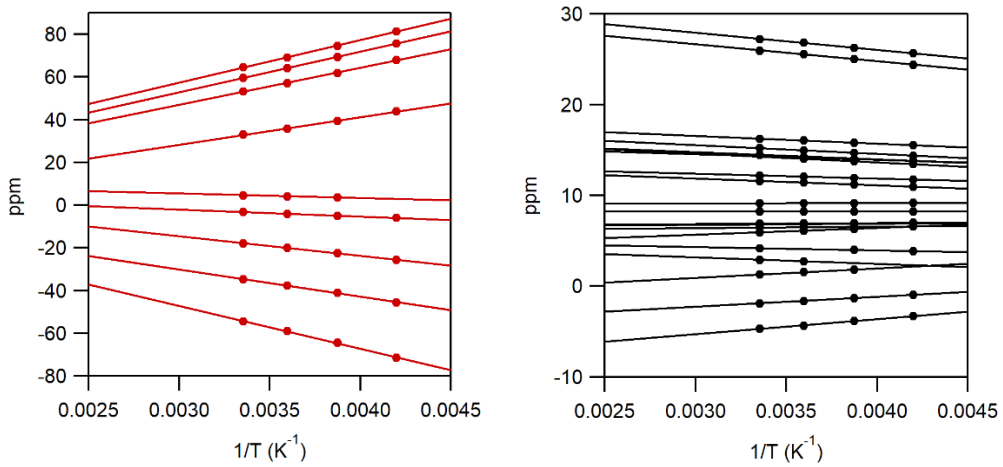

Figure 4.3. Chemical shifts vs. inverse temperature (K^{-1}) for ^{1}H-NMR resonances of 16 mM $[Mn^{III}(OH)(dpaq)](OTf)$ in CD_3CN. Resonances corresponding to $[Mn^{III}(OH)(dpaq)]^+$ and the diamagnetic species are shown on the left and right plots, respectively. A linear dependence is shown over the temperature range studied.

The variable-temperature ^{1}H-NMR experiments reveal a large number of resonances that display anti-Curie behavior, shifting further from the diamagnetic region and broadening as temperature is increased (Figure 4.3, right). This behavior is associated with strongly antiferromagnetically coupled systems.[32-34] The remaining resonances do not show a strong temperature dependence (Figure 4.3, right). Collectively, these data suggest that the diamagnetic

signals observed in the ^{1}H-NMR spectrum of $[Mn^{III}(OH)(dpaq)](OTf)$ dissolved in CD_3CN arise from an $S = 0$, spin-coupled species.

The addition of a small amount of D_2O to CD_3CN solutions of $[Mn^{III}(OH)(dpaq)]^+$ (45 μL D_2O; 880 equivalents per Mn^{III}) causes the near complete loss of the majority of signals in the diamagnetic region of the ^{1}H-NMR spectrum (Figure 4.2B). A set of eleven signals remains. The remaining signals are the broad peaks at 130 and -65 ppm, and the nine signals that showed the Curie temperature dependence (Figure 4.3, left), further confirming that these signals arise from $[Mn^{III}(OH)(dpaq)]^+$. The positions of these signals are only slightly perturbed by the addition of D_2O (Table A3.2). A ^{1}H-NMR spectrum was also collected for $[Mn^{III}(OH)(dpaq)](OTf)$ dissolved in pure D_2O. The resulting spectrum (Figure 4.2C) is quite similar to that observed for $[Mn^{III}(OH)(dpaq)]^+$ dissolved in CD_3CN in the presence of 45 μL D_2O. However, the precise peak positions of the hyperfine-shifted resonances are sensitive to the CD_3CN:D_2O ratio.

On the basis of these ^{1}H-NMR data, we postulate that the dissolution of $[Mn^{III}(OH)(dpaq)](OTf)$ in CD_3CN in the absence of added water results in an equilibrium mixture of $[Mn^{III}(OH)(dpaq)]^+$ and a spin-coupled, diamagnetic complex. Given previous observations that Mn^{III}-hydroxo species can be formed by hydrolysis of μ-oxo-dimanganese(III,III) complexes,[10] we propose that the diamagnetic species is $[Mn^{III}_2(\mu\text{-}O)(dpaq)_2]^{2+}$ (equation 4).

$$[Mn^{III}_2(\mu\text{-}O)(dpaq)_2]^{2+} + H_2O \leftrightarrows 2\,[Mn^{III}(OH)(dpaq)]^+ \qquad (4)$$

The addition of water shifts the equilibrium in favor of $[Mn^{III}(OH)(dpaq)]^+$. To test this model, samples of $[Mn^{III}(OH)(dpaq)]^+$ in CD_3CN and D_2O, which lack ^{1}H-NMR signals from the diamagnetic species, were dried under vacuum to remove CD_3CN and D_2O. The ^{1}H-NMR spectrum of the resultant solid dissolved in CD_3CN showed signals associated with both $[Mn^{III}(OH)(dpaq)]^+$

and the diamagnetic species (Figure A3.19). These results demonstrate that the diamagnetic species (presumably $[Mn^{III}_2(\mu\text{-}O)(dpaq)_2]^{2+}$) can be reformed from $[Mn^{III}(OH)(dpaq)]^{+}$ upon the removal of CD_3CN and D_2O. Experiments aimed at generating only the diamagnetic species by excluding water were unsuccessful. ^{1}H-NMR signals due to the paramagnetic $[Mn^{III}(OH)(dpaq)]^{+}$ complex were observed even when using dried CD_3CN. This result is consistent with a Karl-Fischer analysis of the water content of our dried acetonitrile, which revealed the persistent of 64±8 ppm water.

The ratio of paramagnetic and diamagnetic species present in dried CH_3CN was investigated by two separate methods. First, we measured the magnetic moment of a 23.5 mM $[Mn^{III}(OH)(dpaq)](OTf)$ solution in dried CH_3CN using the NMR method of Evans. This concentration is similar to that employed for the collection of ^{1}H-NMR spectra. At 25 °C, we determined a magnetic moment of 0.97 μ_B. As this value is considerably lower than that observed in wet CH_3CN (4.88 μ_B), this measurement suggests that the diamagnetic species is dominant in dried CH_3CN at 25 °C. The addition of 5 μL H_2O to the solution of $[Mn^{III}(OH)(dpaq)](OTf)$ in dried CH_3CN caused a large increase in the magnetic moment to 3.47 μ_B, consistent with a shift in equilibrium to favor the paramagnetic Mn^{III}-hydroxo species.

Second, we used a standard (1,2,4,5-tetrachloro-3-nitrobenzene) to determine the concentration of the diamagnetic species in a 1.25 mM $[Mn^{III}(OH)(dpaq)](OTf)$ solution of dried CD_3CN. This lower concentration is the same as that employed in kinetic experiments (*vide infra*). From this analysis, the concentration of the diamagnetic species under these conditions is 1 mM in Mn, also giving a 20:80 (mol:mol in Mn) ratio of paramagnetic:diamagnetic components. Collectively, these independent methods provide strong support that the diamagnetic species is dominant when $[Mn^{III}(OH)(dpaq)](OTf)$ is dissolved in dried acetonitrile.

The proposed equilibrium between the paramagnetic Mn^{III}-hydroxo adduct and a diamagnetic species allows us to reconcile the present observations with our previous solution-phase characterization of $[Mn^{III}(OH)(dpaq)]^+$.[18] In the previous experiments, the $[Mn^{III}(OH)(dpaq)](OTf)$ complex was recrystallized under ambient atmosphere, using solvents exposed to atmosphere. Thus, the magnetic moment determined for $[Mn^{III}(OH)(dpaq)](OTf)$ was for a sample in wet CH_3CN, where the mononuclear Mn^{III}-hydroxo species is the dominant component in solution. However, kinetic experiments were performed using $[Mn^{III}(OH)(dpaq)](OTf)$ dissolved in dried CH_3CN and reflect the presence of both components (*vide infra*).

Electronic absorption experiments for $[Mn^{III}(OH)(dpaq)]^+$ in CH_3CN also reveal the influence of added water. The effect of water on the composition of CH_3CN solutions of $[Mn^{III}(OH)(dpaq)](OTf)$ can also be monitored using electronic absorption spectroscopy. In the absence of added water, the electronic absorption spectrum of $[Mn^{III}(OH)(dpaq)](OTf)$ dissolved in CH_3CN at 25 °C shows broad signals at 550 and 780 nm (Figure 4.4, red trace), as previously reported.[18] However, in light of the ^{1}H-NMR experiments, this electronic absorption spectrum is actually a composite spectrum of $[Mn^{III}(OH)(dpaq)]^+$ and one or more diamagnetic species. The addition of 20 μL (440 equivalents per equivalent Mn^{III}) of water to this solution causes the electronic absorption bands to sharpen (Figure 4.4, black trace). In particular, the higher-energy band becomes much better defined, displaying a maximum closer to 500 nm. The more resolved low-energy feature now shows a maximum at 770 nm (ε_{770} = 114 M^{-1} cm^{-1} at 25 °C). Thus, the electronic absorption spectrum observed in the absence of added water is a composite spectrum of at least two species.

For comparison, we note that the previously reported $[Mn^{III}_2(\mu\text{-}O)(S^{Me2}N_4(tren))_2]^{2+}$ complex of Kovacs and co-workers showed an electronic absorption band at 520 nm, with a weaker shoulder

at 575 nm.[10] The corresponding $[Mn^{III}(OH)(S^{Me2}N_4(tren))]^+$ complex showed bands at 500 and 411 nm. Thus, in that system, a mixture of $[Mn^{III}_2(\mu\text{-}O)(S^{Me2}N_4(tren))_2]^{2+}$ and $[Mn^{III}(OH)(S^{Me2}N_4(tren))]^+$ species would give rise to a band maximum near ~510 nm, with a weak shoulder at lower energy. This is consistent with the changes in the electronic absorption spectrum observed when water is added to an CH_3CN solution of $[Mn^{III}(OH)(dpaq)]^+$ (Figure 4.4). There is a loss of absorption intensity near 600 nm and a shift in the band near 500 nm.

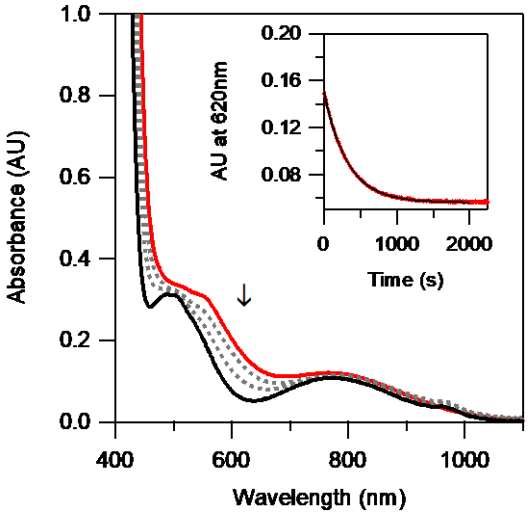

Figure 4.4. Electronic absorption spectrum of 1.25 mM $[Mn^{III}(OH)(dpaq)]^+$ in 2 mL CH_3CN before (red trace) and after the addition of 20 μL H_2O (black trace). The inset follows the change in absorption at 620 nm over time after addition of H_2O.

Mn K-edge X-ray absorption and ^{1}H-NMR experiments provide insight into the nature of the diamagnetic species. Attempts to isolate the diamagnetic species that contributes to the ^{1}H-NMR spectrum of $[Mn^{III}(OH)(dpaq)](OTf)$ in CD_3CN were unsuccessful. These attempts included O_2 oxidation of $[Mn^{II}(dpaq)](OTf)$ in dried CD_3CN. In this case, paramagnetically-shifted signals, associated with the mononuclear $[Mn^{III}(OH)(dpaq)]^+$ species, were diminished but still persisted in ^{1}H-NMR experiments of the dissolved solids (Figure A3.20).

In contrast, low-temperature (~10 K) Mn K-edge X-ray absorption (XAS) experiments performed for concentrated (10 mM) samples of $[Mn^{III}(OH)(dpaq)](OTf)$ dissolved in dried CH_3CN provided significant insight into the nature of the diamagnetic species. Figure 4.5 shows the edge and pre-edge region for the 10 mM sample of $[Mn^{III}(OH)(dpaq)](OTf)$ dissolved in dry CH_3CN compared with corresponding data collected for a dilute (3.5 mM) sample prepared in water.[12] A solid-state sample of $[Mn^{III}(OH)(dpaq)](OTf)$ dispersed in boron nitride provided data essentially identical to the sample in H_2O, as previously described.[12] The edge energies of the CH_3CN, H_2O and solid-state samples are quite similar (Figure 4.5 and Table 1), each occurring near 6550.5 eV. Because the K-edge energy is strongly influence by metal oxidation state,[35-36] the common edge energies suggest that Mn^{III} is the predominant form of Mn in each of these samples. Additionally, previous X-band EPR experiments for $[Mn^{III}(OH)(dpaq)]^+$ under similar conditions as the XAS sample (dried MeCN, 2.5 mM) revealed this system to be EPR silent, also suggestive of a mononuclear Mn(III) and/ or spin-coupled species.[18]

The pre-edge peaks show more variation than the edge position (Figure 4.5, inset). While each sample shows a prominent pre-edge feature centered near 6540 eV, the 10 mM sample of $[Mn^{III}(OH)(dpaq)](OTf)$ dissolved in CH_3CN shows a shoulder at higher energy. This large shoulder results in a significantly increased pre-edge area for this sample compared to the samples of $[Mn^{III}(OH)(dpaq)](OTf)$ dissolved in water and in the solid state (Table 1). The perturbation in the pre-edge region is consistent with a difference in composition for the sample in CH_3CN, corroborating the ^{1}H-NMR data (Figure 4.2).

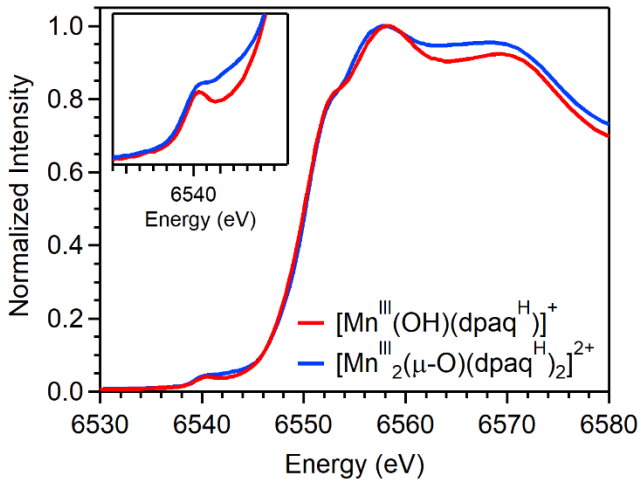

Figure 4.5. Near-edge regions of the 10 K Mn K-edge XAS spectra of 10 mM [Mn^{III}(OH)(dpaq)](OTf) dissolved in CH_3CN (blue trace) and 3.5 mM [Mn^{III}(OH)(dpaq)](OTf) dissolved in H_2O (red trace). Analysis of EXAFS data suggests that dominant species present in the former sample is $[Mn^{III}_2(\mu\text{-}O)(dpaq)_2]^{2+}$.

Table 4.1. X-ray Absorption Near-Edge Properties of $[Mn^{III}(OH)(dpaq)]^+$ and $[Mn^{III}_2(\mu\text{-}O)(dpaq)_2]^{2+}$ samples.

complex	media	edge energy (eV)	pre-edge	
			energy (eV)	area
$[Mn^{III}_2(\mu\text{-}O)(dpaq)_2]^{2+}$ [a]	10 mM in dried CH_3CN	6550.4	6540.3 6542.5	11.0
$[Mn^{III}(OH)(dpaq)]^+$ [b]	H_2O	6550.6	6540.2 6541.8	4.3
$[Mn^{III}(OH)(dpaq)]^+$ [b]	solid[c]	6550.4	6540.2 6542.0	5.8

[a] This sample was prepared by dissolving [Mn^{III}(OH)(dpaq)](OTf) in dried CH_3CN and flash freezing. On the basis of the EXAFS data, we propose that $[Mn^{III}_2(\mu\text{-}O)(dpaq)_2]^{2+}$ is the dominant species under these conditions (*i.e.*, at 10 K). [b] From reference 12. [c] Solid crystals of [Mn^{III}(OH)(dpaq)](OTf) dispersed in boron nitride.

While the edge and pre-edge properties of the CH_3CN and water samples of [Mn^{III}(OH)(dpaq)](OTf) have notable similarities, the appearance of the extended X-ray absorption fine structure (EXAFS) data are remarkably different (Figure 4.6). For example, the Fourier transform (FT) of the EXAFS data for the 10 mM sample dissolved in CH_3CN shows peaks at 1.75, 2.15, 2.49, and 3.25 Å, with the peak at 3.25 Å being the most prominent. In contrast, the sample of

[Mn^{III}(OH)(dpaq)](OTf) prepared in water shows three peaks at 1.2, 1.8, and 2.3 Å. A weak feature is observed at 3.25 Å, but this peak carries roughly a third the intensity of the peak at 2.3 Å (Figure 4.6, bottom). A previously published analysis of the EXAFS data for [Mn^{III}(OH)(dpaq)](OTf) prepared in water revealed manganese-atom scatterer distances of 1.87 (2 N/O scatterers), 2.14 (4 N scatterers), and 2.91 (6 C scatterers) Å (see Table 4.2 and Figure 4.6).[12] These distances are consistent with those observed in the crystal structure of [Mn^{III}(OH)(dpaq)](OTf) (Table 4.2),[11-12] confirming that the mononuclear Mn^{III}-hydroxo adduct is the dominant species in water solution.

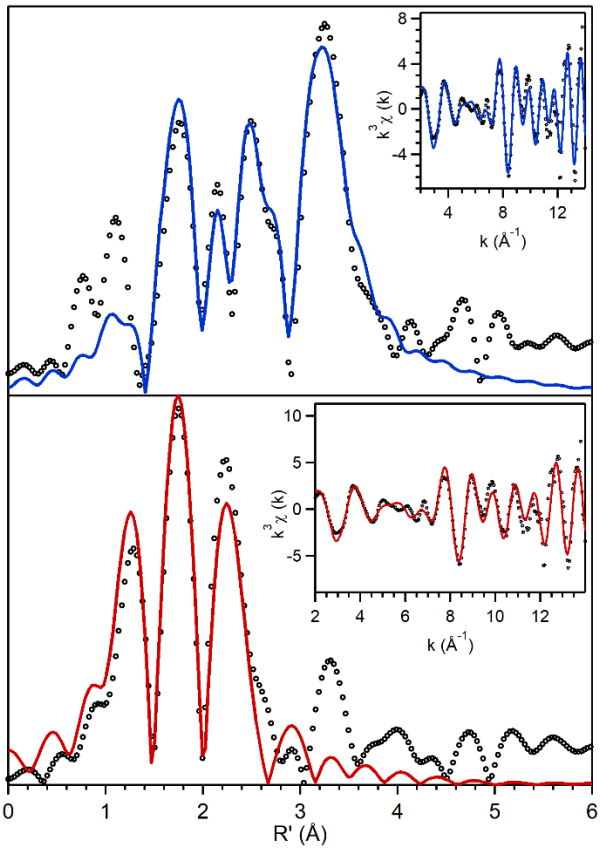

Figure 4.6. Fourier transforms of Mn K-edge EXAFS data [$k^3\chi(k)$] and raw EXAFS spectra (insets), experimental data (open circles) and fits (solid traces), for [Mn^{III}(OH)(dpaq)](OTf) dissolved in dried CH_3CN (top) and H_2O (bottom; from reference 12). In both cases, data were collected at 10 K.

Table 4.2. Comparison of Metric Parameters (Å) from EXAFS, DFT computations, and X-ray diffraction (XRD) for $[Mn^{III}_2(\mu\text{-O})(dpaq)_2]^{2+}$ and $[Mn^{III}(OH)(dpaq)]^{+}$.

	Mn–O/N[a]	Mn–N(equatorial)[b]	Mn···Mn	Mn···C
$[Mn^{III}_2(\mu\text{-O})(dpaq)_2]^{2+}$				
EXAFS	1.87	2.17	3.55	2.95
DFT	1.90[c]	2.24	3.64	2.99[d]
$[Mn^{III}(OH)(dpaq)]^{+}$				
EXAFS[e]	1.87	2.14		2.91
DFT[f]	1.92	2.20		2.97
X-ray crystallography[f]	1.89	2.18		2.95

[a] The average of the Mn–oxo/hydroxo and Mn–N(amide) distances. [b] The average of the Mn–N distances for the equatorial pyridine, quinoline, and amine donors of the dpaq ligand. [c] Average of Mn–O(μ-oxo) and Mn–N(amide) distances of 1.817 and 1.986 Å, respectively. [d] Average distance of six-closest C atoms. [e] Distances from analysis of EXAFS data of a solution sample of $[Mn^{III}(OH)(dpaq)]^{+}$ in H_2O; from reference [12]. [f] DFT and X-ray crystallographic distances from reference 11.

Analysis of the EXAFS data collected for the 10 mM sample in CH_3CN reveal metric parameters for the light-atom scatterers that are very similar to those of $[Mn^{III}(OH)(dpaq)](OTf)$ in water (Tables 2 and 3). For example, the data for the 10 mM sample in CH_3CN are well fit with 2 N/O atoms at 1.87 Å, 4 N atoms at 2.17 Å, and 5 C atoms at 2.95 Å. Thus, for these shells, the only difference between the CH_3CN and H_2O samples is a slight elongation in the Mn–distances for the N and C shells in the former sample. However, the inclusion of these three shells cannot account for the peak at 3.25 Å in the FT EXAFS spectrum of $[Mn^{III}(OH)(dpaq)](OTf)$ dissolved in CH_3CN. Successful modeling of this peak requires two colinear multiple scattering pathways consisting of O–Mn double scatterer and O–Mn–O triple scatterer pathways at 3.55 Å (Table 4.3). The single scatterer Mn···Mn shell could not be resolved, as all fits including this shell showed negative σ^2 values. Moreover, with the DFT-optimized Mn–O–Mn angle of 179°, this pathway was predicted to have low contribution to the EXAFS. The 3.55 Å Mn···Mn separation is in good agreement corresponding Mn···Mn distances observed for crystallographically characterized μ-oxo-dimanganese(III,III) complexes (3.4 to 3.6 Å).[10, 37-39] On the basis of this result, we can also postulate

that the weaker peak observed at 3.25 Å in the FT EXAFS spectrum of $[Mn^{III}(OH)(dpaq)]^+$ in H_2O (Figure 4.6, bottom) could be due to some fraction of $[Mn^{III}_2(\mu\text{-}O)(dpaq)_2]^{2+}$ present at low temperature (10 K) even in H_2O. Although room-temperature ^{1}H-NMR experiments for $[Mn^{III}(OH)(dpaq)]^+$ in D_2O show no evidence of a species other than the Mn^{III}-hydroxo, simple entropic considerations would suggest that the $[Mn^{III}_2(\mu\text{-}O)(dpaq)_2]^{2+}$ dimer is favored over Mn^{III}-hydroxo monomers at lower temperatures, such as those used for the EXAFS experiments.

Table 4.3. EXAFS Fitting Results for [MnIII(OH)(dpaq)](OTf) Dissolved in Dried CH3CN

Mn—O/N			Mn—N			Mn•••C			Mn••O••Mn			Mn••O••Mn••O			
n	R (Å)	σ^2 (x10^{-3})	*n*	R (Å)	σ^2 (x10^{-3})	*n*	R (Å)	σ^2 (x10^{-3})	*n*	R (Å)	σ^2 (x10^{-3})	*n*	R (Å)	σ^2 (x10^{-3})	R
2	1.86	11.1	4	2.17	6.4										0.86
2	1.85	11.3	4	2.29	5.6	5	2.95	0.69							0.76
2	1.86	10.8	4	2.30	5.3	5	2.97	2.3							0.58
2	1.87	11.1	4	2.17	5.5	5	2.95	2.1	1	3.580	-0.8				0.18
2	1.87	9.8	4	2.17	5.6	5	2.95	1.7	1	3.550	1.5	1	3.55	1.5	0.26

The metric parameters obtained for the 10 mM sample prepared in CH_3CN are also in good agreement with distances determined from a DFT-optimized structure of $[Mn^{III}_2(\mu\text{-}O)(dpaq)_2]^{2+}$ (Figure 4.7). This structure was obtained for a species converged to an $S = 0$ broken-symmetry state. The optimized structure shows a Mn−O distance of 1.817 Å and a Mn···Mn separation of 3.63 Å. The average Mn–ligand distances from DFT also agree reasonably well with their counterparts from the EXAFS analysis (Table 4.2). Both the Mn−O and Mn···Mn distances for our DFT-optimized

model of $[Mn^{III}_2(\mu\text{-}O)(dpaq)_2]^{2+}$ are longer than those determined by X-ray crystallography for a series of μ-oxodimanganese(III,III) centers supported by N_4S^- ligands (Mn–O and of 1.750 - 1.794 Å and 3.433 – 3.520 Å, respectively).[37] However, unlike for $[Mn^{III}_2(\mu\text{-}O)(dpaq)_2]^{2+}$, those complexes lacked a strongly-donating *trans* ligand and had two weakly-donating *cis* ligand. Both of these differences could account for the longer Mn–O and Mn···Mn separations in the DFT structure of $[Mn^{III}_2(\mu\text{-}O)(dpaq)_2]^{2+}$. We also used DFT computations to determine metric parameters for the hydroxo-bridged $[Mn^{III}_2(\mu\text{-}OH)(dpaq)_2]^{3+}$ species (Figure A3.21). The computed Mn–O and Mn···Mn distances for this structure are 2.05 and 4.05 Å, respectively, and the Mn–O(H)–Mn unit is no longer linear (angle of 163°). These metric parameters are in poorer agreement with the EXAFS data (Table 4.2), leading us to discount the $[Mn^{III}_2(\mu\text{-}OH)(dpaq)_2]^{3+}$ structure.

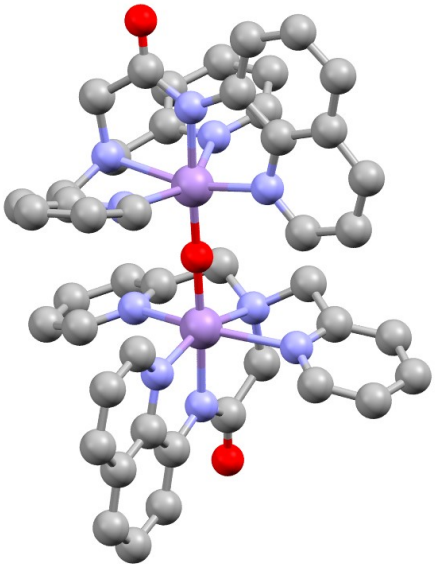

Figure 4.7. Molecular structure of $[Mn^{III}_2(\mu\text{-}O)(dpaq)_2]^{2+}$ from broken-symmetry DFT geometry optimization.

In the DFT structure of $[Mn^{III}_2(\mu\text{-}O)(dpaq)_2]^{2+}$, all 20 protons of an individual ligand are in unique chemical environments. Even if rotation around the Mn−O−Mn axis is hindered in solution, the two Mn^{III}(dpaq) subunits are still related by a C_2-axis perpendicular to the Mn-O-Mn axis. This symmetry gives rise to twenty distinct signals, each with an integration of two. To determine if this prediction is in accordance with the ^{1}H-NMR data, we performed peak integrations and a COSY NMR analysis for the diamagnetic signals of $[Mn^{III}(OH)(dpaq)](OTf)$ in CD_3CN. Fitted parameters for these ^{1}H-NMR signals at 25 °C are collected in Table A3.3. One of these signals, at 4.33 ppm, is obscured by overlapping resonances from the Mn^{III}-hydroxo monomer, and integration was not possible. Integration was also challenging for the broad resonances at 2.95 and -4.7 ppm (see Figure A3.18 and Table A3.3). In these cases, these peaks integrated to ca. 1 proton, but this value should be viewed with considerable uncertainty. All other peaks, with the exception of the resonance at 14.31 ppm, integrated to 2 protons. Integration of the peak at 14.31 ppm gave 4 protons, which would be inconsistent with the DFT structure of $[Mn^{III}_2(\mu\text{-}O)(dpaq)_2]^{2+}$. However, both the variable-temperature ^{1}H-NMR data and the COSY NMR data show that this peak actually contains two peaks, with chemical shifts of 14.29 and 14.33 ppm, in distinct chemical environments (see Supporting Information, Figures S18 and S20). For example, the COSY NMR data reveal peaks at 14.29 and 14.33 ppm, which display unique couplings (see Supporting Information). Thus, the collective analysis of the ^{1}H-NMR data for the diamagnetic signals of $[Mn^{III}(OH)(dpaq)](OTf)$ in CD_3CN is consistent with the DFT structure of $[Mn^{III}_2(\mu\text{-}O)(dpaq)_2]^{2+}$, revealing 20 proton resonances, each with a unique chemical environment and an integration of 2 (or close to it). The COSY NMR data reveals couplings only for the resonances with narrow linewidths (Figure A3.22), and these couplings are discussed in the Supporting Information.

Collectively, the analysis of the EXAFS data, coupled with a DFT structure of $[Mn^{III}_2(\mu\text{-}O)(dpaq)_2]^{2+}$, corroborates our proposal, based on the ^{1}H-NMR data described above, that the diamagnetic species present in solution samples of $[Mn^{III}(OH)(dpaq)]^+$ can be reasonably formulated as the oxo-bridged $[Mn^{III}_2(\mu\text{-}O)(dpaq)_2]^{2+}$ complex. In addition, several of the reported μ-oxo-dimanganese(III,III) complexes show strong antiferromagnetic coupling,[39] consistent with the proposed diamagnetism of $[Mn^{III}_2(\mu\text{-}O)(dpaq)_2]^{2+}$. This assignment is also compatible with the ^{1}H-NMR data collected for $[Mn^{III}(OH)(dpaq)](OTf)$ in CD_3CN.

^{1}H-NMR experiments for $[Mn^{III}(OMe)(dpaq)]^+$ and $[Mn^{III}(OH)(dpaq^{2Me})]^+$ only reveal signals from the Mn^{III}-methoxy and Mn^{III}-hydroxo species. ^{1}H-NMR spectra were also collected for $[Mn^{III}(OH)(dpaq^{2Me})]^+$ in CD_3CN and $[Mn^{III}(OMe)(dpaq)]^+$ in CD_3OD (Figure 4.8, center and bottom, respectively). Neither of these spectra show a large number of prominent signals in the diamagnetic region, suggesting that the mononuclear Mn^{III}-hydroxo and Mn^{III}-methoxy adducts are the dominant species in solution. The lack of signals due to a diamagnetic μ-oxodimanganese(III,III) species can be readily rationalized for both of these samples. For $[Mn^{III}(OMe)(dpaq)]^+$ in CD_3OD, the large excess of CD_3OD solvent greatly favors the mononuclear Mn^{III}-methoxy adduct over the μ-oxodimanganese(III,III) species. This parallels the behavior of $[Mn^{III}(OH)(dpaq)](OTf)$ in H_2O. For $[Mn^{III}(OH)(dpaq^{2Me})]^+$, we propose that the 2-methyl-quinoline moiety is sufficiently bulky so as to favor the mononuclear Mn^{III}-hydroxo adduct over the oxo-bridged dimer.

The positions of the hyperfine-shifted proton resonances observed for $[Mn^{III}(OH)(dpaq^{2Me})]^+$ and $[Mn^{III}(OMe)(dpaq)]^+$ are qualitatively similar to those observed for $[Mn^{III}(OH)(dpaq)]^+$ in D_2O (Figure 4.8 and Table A3.2). In each case, there is a set of five signals upfield from the diamagnetic region, a cluster of four to five resonances from 64 to 36 ppm, and a

broad signal near 120 - 130 ppm. The gross similarities between the ^{1}H-NMR resonances of these complexes is anticipated given their similar molecular structures (Figure 4.1), while perturbations in positions of particular resonances can be readily attributed to ligand variations (dpaq versus dpaq^{2Me} and hydroxo versus methoxy) and solvent-dependent shifts.

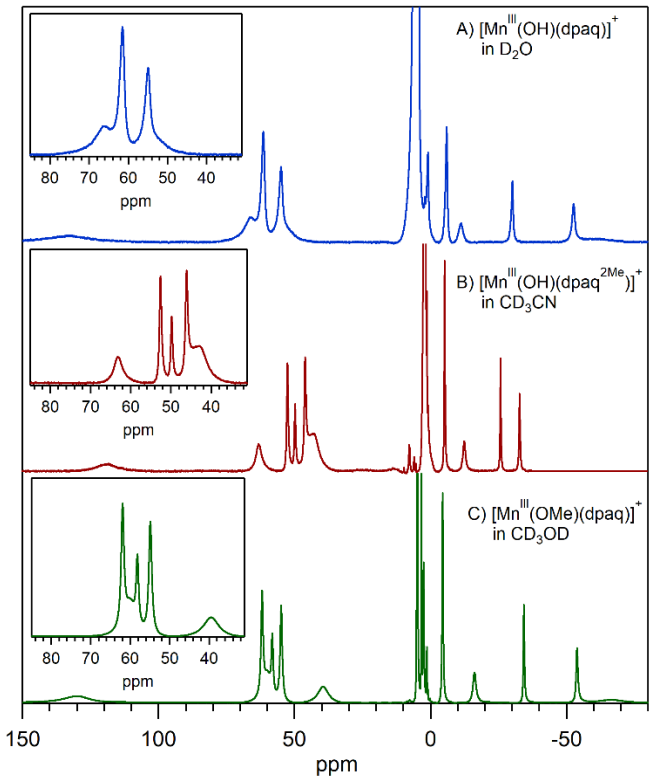

Figure 4.8. 1H-NMR spectra of A) 4 mM [MnIII(OH)(dpaq)](OTf) in pure D2O, B) 15 mM [MnIII(OH)(dpaq2Me)](OTf) in CD3CN, and C) 80 mM [MnIII(OMe)(dpaq)](OTf) in CD3OD. The insets show an expanded view of the 85 to 30 ppm region.

Assignments of ^{1}H-NMR signals for the Mn^{III}-methoxy complex. Assignments for a number of the hyperfine-shifted ^{1}H-NMR signals of [Mn^{III}(OMe)(dpaq)]$^{+}$ in CD_3OD were developed by determining T_1 relaxation times and estimating peak integrations (Tables 4, S1 and S4). This combination of complex and solvent gives the highest solubility (80 mM in CD_3OD), permitting the collection of ^{1}H-NMR data with the highest signal-to-noise ratios. Unfortunately, the

lower solubility of $[Mn^{III}(OH)(dpaq)](OTf)$ and $[Mn^{III}(OH)(dpaq^{2Me})](OTf)$ in CD_3CN resulted in ^{1}H-NMR spectra with higher signal-to-noise ratios that precluded the collection of accurate T_1 relaxation times and peak integrations. Thus, the assignments described here strictly pertain only to $[Mn^{III}(OMe)(dpaq)]^+$ in CD_3OD.

Table 4.4. ^{1}H-NMR Chemical Shifts, T_1 Relaxation Times, and Peak Integrations for $[Mn^{III}(OMe)(dpaq)]^+$ in CD_3OD.

assignment[a]	$[Mn^{III}(OMe)(dpaq)]^+$		
	δ (ppm)	T_1 (ms)	integration
α-H (py)	127.5	0.09 ± 0.02	2
H (py)	60.8	1.12 ± 0.02	2
H (qn)	59.9[b]	ND	1
H (qn)	57.2	0.89 ± 0.02	1
H (py)	53.9	1.22 ± 0.02	2
CH_2[c]	38.5	0.07 ± 0.02	2
ND[d]	2.54	ND	ND[d]
H (py)	-4.2	3.55 ± 0.15	2
H (qn)	-15.7	0.87 ± 0.04	1
H (qn)	-33.6	3.21 ± 0.05	1
H (qn)	-52.7	1.69 ± 0.04	1
α-H (qn)	-66.3	ND	1

[a] Proton labeling scheme is shown in Figure 4.9. [b] This peak overlaps with the adjacent, and sharper, resonances at 60.8 and 57.2 ppm (Figure A3.23). While peak fitting allowed us to determine the position and area of this peak, we were unable to determine a relaxation time. [c] This signal is attributed to either the –CH_2– group linking the amide and tertiary amine or two protons from the –CH_2– groups linking the pyridines and tertiary amine. [d] This resonance shows overlap with adjacent signals from methanol, precluding an accurate peak integration and tentative assignment.

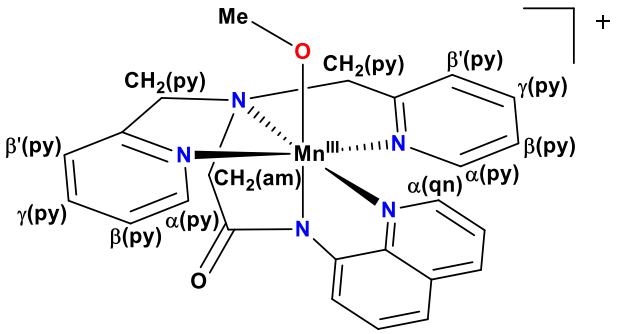

$[Mn^{III}(OMe)(dpaq)]^+$

Figure 4.9. Proton labeling scheme used in ^{1}H-NMR peak assignments (**Table 4.4**).

The broad resonances of $[Mn^{III}(OMe)(dpaq)]^+$ at 127.5 and 38.5 ppm showed the smallest T_1 values of 0.09 and 0.07 ms, respectively (Table 4.4). Presumably, the extremely broad resonance at -66.3 ppm (Figure 4.8) also has a small T_1 value; however, the poor signal-to-noise ratio for this resonance precluded the measurement of its T_1 value. Integration of the signals at 127.5 and 38.5 ppm were consistent with two protons for each of these resonances. In contrast, the resonance at -66.3 ppm integrated to give a single proton. Considering this information, we assign the resonances at 127.5 and -66.3 ppm to the α-H protons of the pyridine and quinoline moieties, respectively. The resonance at 38.5 ppm is tentatively attributed to the $–CH_2–$ group linking the amide and tertiary amine (Figure 4.9). Previous studies of Fe^{II} complexes containing aminopyridyl ligands have shown signals from α-H(pyridine) and $–CH_2–$ groups in the chemical shift ranges of 141 - 111 and 75 - 33 ppm, respectively,[40-41] which is consistent with our assignments. $[Mn^{III}(OMe)(dpaq)]^+$ is also expected to display two additional broad signals, each with an integration of two, due to the protons of the $–CH_2–$ groups linking the pyridine moieties to the tertiary amine (the protons of the individual pyridine $–CH_2–$ groups are inequivalent). As the peak at 38.5 ppm could alternatively be attributed to one of these sets of protons, we attribute this peak to a $–CH_2–$ group in Table 4.4. ^{1}H-NMR studies of Mn^{III}-Schiff base complexes by Pecoraro and co-workers failed to observe signals due to $–CH_2–$ groups in a propylene backbone.[20] Thus, the resonances for the four unobserved $–CH_2–$ protons in $[Mn^{III}(OMe)(dpaq)]^+$ are either too rapidly relaxing to observe in our ^{1}H-NMR experiment or are obscured by peaks from solvent (see Supporting Information for additional discussion of the point).

The ^{1}H-NMR resonances for $[Mn^{III}(OMe)(dpaq)]^+$ at 60.8, 53.9, and -4.2 ppm each integrate to two protons and show T_1 relaxation times from 1.1 to 3.55 ms, with the resonance at -4.2 ppm

showing the longest T_1 relaxation time (Table 4.4). Based on their integrations and longer relaxation times, these resonances are attributed to the remaining protons of the pyridine rings (β, γ, and β′; see Figure 4.9). In aminopyridyl-Fe^{II} complexes, the β-H(pyridine) protons are typically shifted downfield (~64 – 36 ppm) and display T_1 values intermediate between those of α- and γ-protons.[40-41] These prior studies suggest that the resonances for $[Mn^{III}(OMe)(dpaq)]^+$ at 60.8 and 53.9 ppm arise from the β- and β′-H(pyridine) protons, while the resonance at -4.2 ppm is from the γ-H(pyridine) proton.

Five of the remaining ^{1}H-NMR resonances for $[Mn^{III}(OMe)(dpaq)]^+$ (59.9, 57.2, -15.7, -33.6, and -52.7 ppm; see Table 4.4) each integrate to a single proton. These five resonances are tentatively attributed to the five remaining protons (excluding the α-proton) on the quinoline moiety of the dpaq ligand. Collection of ^{1}H-NMR data for $[Mn^{III}(OMe)(dpaq)]^+$ using the inversion recovery pulse sequence also identified a fast-relaxing peak at 2.54 ppm (Figure A3.16), which is most likely associated with the mononuclear Mn^{III}-methoxy complex. Because this peak overlaps with an adjacent peak from methanol, we were unable to obtain an accurate integration and, in light of this, cannot offer a tentative peak assignment.

Influence of the Equilibrium Between $[Mn^{III}_2(\mu\text{-O})(dpaq)_2]^{2+}$ and $[Mn^{III}(OH)(dpaq)]^+$ on TEMPOH Oxidation. On the basis of the observations described above, our previous investigations of the HAT reactivity of $[Mn^{III}(OH)(dpaq)]^+$ were actually performed for an equilibrium mixture of $[Mn^{III}_2(\mu\text{-O})(dpaq)_2]^{2+}$ and $[Mn^{III}(OH)(dpaq)]^+$ in CH_3CN, with the bulk of the Mn^{III} in the dimeric form. To determine the influence of this equilibrium on these oxidation reactions, we first investigated the rate of conversion of $[Mn^{III}_2(\mu\text{-O})(dpaq)_2]^{2+}$ to $[Mn^{III}(OH)(dpaq)]^+$ as a function of added water. For these experiments, we added different

amounts of water (22 – 4400 equivalents per Mn^{III}) to solutions of $[Mn^{III}(OH)(dpaq)](OTf)$ dissolved in dried CH_3CN and monitored the conversion of $[Mn^{III}_2(\mu\text{-}O)(dpaq)_2]^{2+}$ to $[Mn^{III}(OH)(dpaq)]^+$ using the change in absorbance at 620 nm (see Figure 4.4). Experiments were performed at both 25 and -15 °C. Electronic absorption and ^{1}H-NMR data indicate near complete formation of the $[Mn^{III}(OH)(dpaq)]^+$ complex following the addition of water in excess of 440 equivalents at room temperature. In these cases, the changes in the electronic absorption signals following the addition of water showed pseudo-first-order behavior (Figure 4.10, top), allowing us to determine rate constants as a function of water concentration. These experiments reveal that, with at least 440 equivalents of H_2O, the rate of $[Mn^{III}(OH)(dpaq)]^+$ formation shows only a weak dependent on the water concentration, with k_{obs} = 2.3(2) × 10^{-1} s^{-1} at 25 °C and 2.7(3) × 10^{-3} s^{-1} at -15 °C (Figure 4.10).

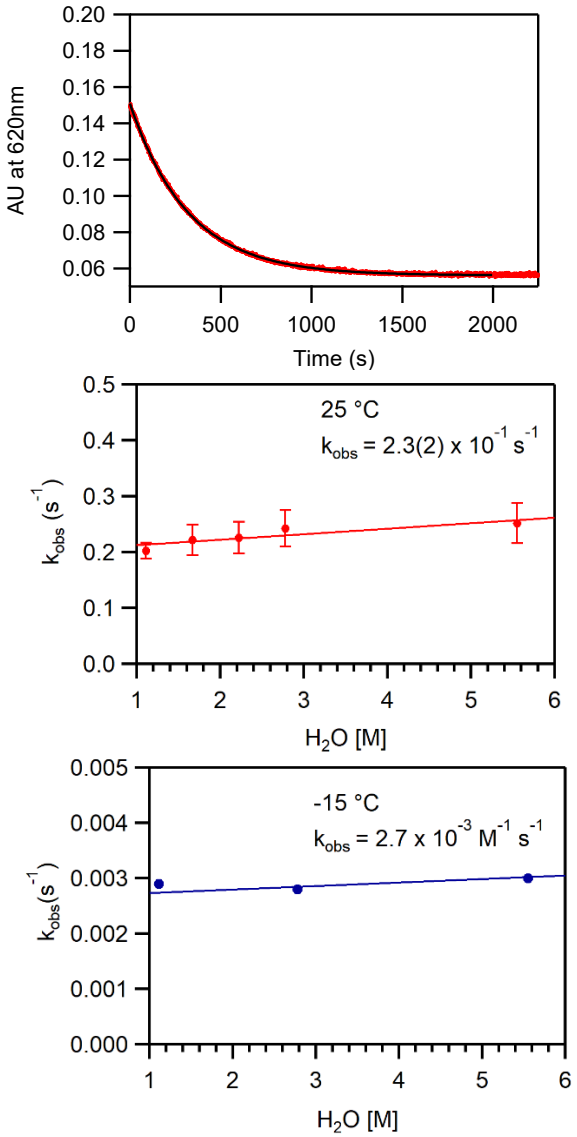

Figure 4.10. Top: Electronic absorption signal of [Mn^{III}(OH)(dpaq)](OTf) dissolved in CH_3CN at 620 nm following the addition of 440 equivalents H_2O at -15 °C (red dots) and fit to pseudo-first-order kinetic model (solid black trace). Center and Bottom: Rate constant for the reaction of [Mn^{III}(OH)(dpaq)](OTf) dissolved in CH_3CN with H_2O as a function of H_2O concentration at 25 (center) and -15 °C (bottom).

To decouple the dimer-monomer equilibrium from TEMPOH oxidation, we investigated TEMPOH oxidation rates for [Mn^{III}(OH)(dpaq)](OTf) in CH_3CN in the presence of added H_2O. First, we determined rates for the reaction of 40 equivalents of TEMPOH with 1.25 mM [Mn^{III}(OH)(dpaq)](OTf) at -15 °C for samples with 440 and 880 equivalents of added water. Both

reactions followed pseudo-first-order behavior, giving similar k_{obs} values of 0.29 and 0.20 s^{-1}, respectively. These data suggest that the *amount* of added water has a minor effect on the rate of TEMPOH oxidation. Moreover, these rates for TEMPOH at -15 °C are roughly 100-fold greater than the rate observed for the dimer-to-monomer conversion at -15 °C (Figure 4.10, bottom). Therefore, our previous analysis of TEMPOH oxidation by $[Mn^{III}(OH)(dpaq)](OTf)$ was complicated by multiple processes.

We next investigated the reaction of TEMPOH and $[Mn^{III}(OH)(dpaq)]^+$ at -35 °C using a fixed water concentration of 880 equivalents relative to Mn^{III}, but with the TEMPOH concentration varied between 10 – 100 equivalents relative to Mn^{III}. For these reactions, we first added water and monitored the dimer to monomer conversion by electronic absorption spectroscopy. Once the $[Mn^{III}(OH)(dpaq)]^+$ had fully formed, we added TEMPOH. At all concentrations of TEMPOH examined, we observed pseudo-first-order kinetic behavior (Figure A3.24). We also observed a linear increase in k_{obs} as a function of increasing TEMPOH concentration (Figure 4.11), giving a k_2 value of 1.1 $M^{-1}s^{-1}$ at -35 °C. This new k_2 for TEMPOH oxidation is substantially faster than that previously reported for $[Mn^{III}(OH)(dpaq)]^+$ at 25 °C (1.3×10^{-1} $M^{-1}s^{-1}$)[18] and only a factor of four slower than that reported for $[Mn^{III}(OH)(dpaq^{2Me})]^+$ (Figure 4.11).[11]

To rule out that the observed rate enhancement is simply a solvent effect, caused by the greater concentration of H_2O in CH_3CN solution, we determined the k_{obs} value for the oxidation of 40 equivalents TEMPOH by $[Mn^{III}(OH)(dpaq^{2Me})]^+$ in the presence of 440 equivalents H_2O. Because $[Mn^{III}(OH)(dpaq^{2Me})]^+$ only shows signals associated with the Mn^{III}-hydroxo adduct even in the absence of added water, the added water in this case does not serve to perturb the equilibrium position between the dimer and the monomer. In support, the addition of water to a CH_3CN solution of $[Mn^{III}(OH)(dpaq^{2Me})]^+$ at -35 °C did not perturb the electronic absorption signals beyond

that expected for dilution (Figure A3.25). Following the addition of 40 equivalents TEMPOH to this solution, we observed a decay of a the Mn^{III}-hydroxo with a k_{obs} of 0.174 s^{-1} at -35 °C (Figure A3.25), which is essentially identical to that previously report for a reaction lacking added water (k_{obs} = 0.173 s^{-1} at -35 °C).[11]

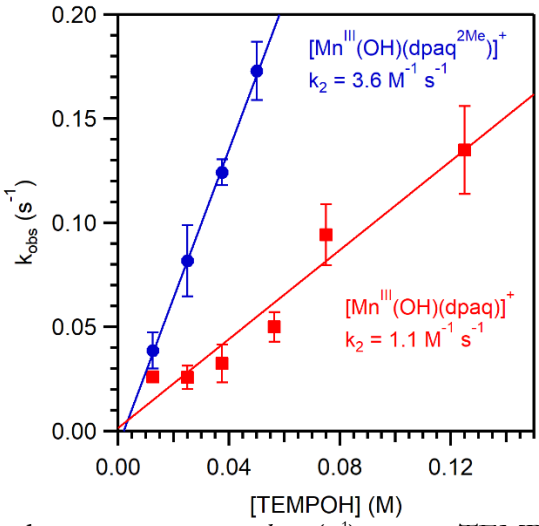

Figure 4.11. Pseudo-first-order rate constants, k_{obs} (s^{-1}) versus TEMPOH concentration for a 1.25 mM solution of $[Mn^{III}(OH)(dpaq)](OTf)$ in CH_3CN in the presence of 440 equivalents H_2O. The second-order rate constants were determined from the best-fit lines. Corresponding data previously reported for $[Mn^{III}(OH)(dpaq^{2Me})]^+$ (ref 11) are included for comparison.

A more detailed comparison of the reactivity of $[Mn^{III}(OH)(dpaq)]^+$ and $[Mn^{III}(OH)(dpaq^{2Me})]^+$ was obtained by determining the temperature dependence of the oxidation of 10 equivalents of TEMPOH by $[Mn^{III}(OH)(dpaq)](OTf)$ in the presence of 880 equivalents water from -35 to 11.5 °C. An Eyring analysis of the rate data gave activation parameters $\Delta H^{\ddagger}$ and $\Delta S^{\ddagger}$ of 5.3(9) kcal/mol and -43(4) cal/(mol K), respectively (Figure 4.12). The $\Delta H^{\ddagger}$ is nearly half that previously reported for TEMPOH oxidation by $[Mn^{III}(OH)(dpaq)]^+$ (9.9 kcal/mol), while the $\Delta S^{\ddagger}$ is slightly larger (-35 cal/(mol K)).[18] The new activation parameters are essentially identical to those reported for TEMPOH oxidation by $[Mn^{III}(OH)(dpaq^{2Me})]^+$ ($\Delta H^{\ddagger}$ = 5.7(3) kcal/mol and $\Delta S^{\ddagger}$ = -

41(1) cal/(mol K)).[11] Thus, the reactivity of the $[Mn^{III}(OH)(dpaq)]^+$ and $[Mn^{III}(OH)(dpaq^{2Me})]^+$ in TEMPOH oxidation are actually quite similar.

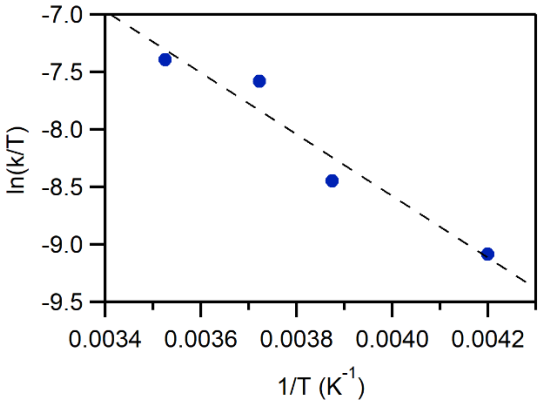

Figure 4.12. Eyring plot showing $\ln(k/T)$ versus $1/T$ (K^{-1}) for the reaction of TEMPOH with 1.25 mM $[Mn^{III}(OH)(dpaq)](OTf)$ in CH_3CN with 880 equivalents of water from -35 to 12 °C (238 – 285 K).

A key question that remains is why the previous kinetic data for TEMPOH oxidation by the equilibrium mixture of $[Mn^{III}(OH)(dpaq)]^+$ and $[Mn^{III}_2(\mu\text{-}O)(dpaq)_2]^{2+}$ were well behaved (*i.e.*, the reactions followed pseudo-first order behavior to five half-lives and k_{obs} values increased linearly with TEMPOH concentration).[18] The method of TEMPOH preparation that we employ generates a hydrated form, with a 3:1 TEMPOH:H_2O ratio.[23] Thus, in the previously reported experiments, the addition of TEMPOH was accompanied by the addition of small amounts of H_2O (roughly 3 – 80 equivalents relative to total Mn^{III} concentration). To investigate the dependence of the dimer to monomer conversion using similar amounts of water, we monitored the conversion kinetics by adding smaller amounts of water (22 to 330 equivalents per Mn^{III}) to CH_3CN solutions of $[Mn^{III}(OH)(dpaq)](OTf)$ at 25 °C. Under these reaction conditions, the conversion of $[Mn^{III}_2(\mu\text{-}O)(dpaq)_2]^{2+}$ to $[Mn^{III}(OH)(dpaq)]^+$ does not go to completion, and a proper treatment of the kinetics requires an opposing second-order model.[42]

However, the loss of absorbance at 620 nm can be well fit to a pseudo-first order model (Figure 4.10). For reactions involving these smaller equivalents of water, where the dimer to monomer conversion is not pushed to completion, the k_{obs} values obtained from the pseudo-first fits increase linearly with increasing amounts of H_2O (Figure 4.11). The apparent second-order rate constant obtained from this analysis is 2.5(1) × 10^{-1} $M^{-1}s^{-1}$ (at 25 °C; see Figure 4.11), which is remarkably similar to that previously reported for TEMPOH oxidation by the equilibrium mixture of $[Mn^{III}(OH)(dpaq)]^+$ and $[Mn^{III}_2(\mu\text{-}O)(dpaq)_2]^{2+}$ (1.3(1) × 10^{-1} $M^{-1}s^{-1}$ at 25 °C).[18] Thus, we conclude that for the previously reported kinetic experiments, the rate-limiting step of the reaction was the rate of $[Mn^{III}(OH)(dpaq)]^+$ formation from $[Mn^{III}_2(\mu\text{-}O)(dpaq)_2]^{2+}$ that was initiated by the addition of water in the TEMPOH hydrate. Once formed, the $[Mn^{III}(OH)(dpaq)]^+$ species reacted rapidly with TEMPOH (Figure 4.11) by a hydrogen atom abstraction step.

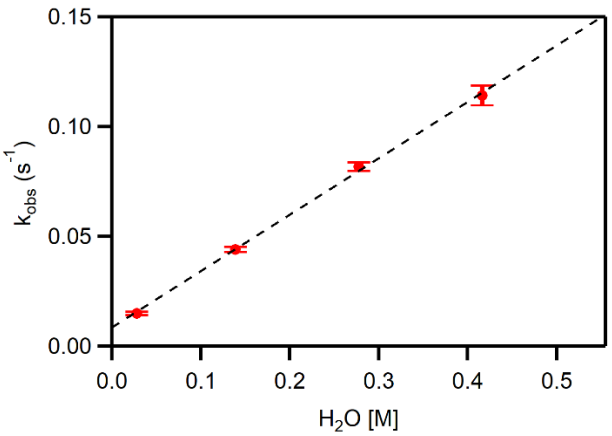

Figure 4.13. Pseudo-first-order rate constants, k_{obs} (s^{-1}) versus H_2O concentration when 22 to 330 equivalents of H_2O are added to a 1.25 mM solution of $[Mn^{III}(OH)(dpaq)](OTf)$ in CH_3CN at 25 °C.

While our proposed model for reactivity is consistent with the present observations, there are alternative explanations that cannot be ruled out at present. For example, it is possible that the rate observed when TEMPOH is added to the equilibrium mixture of $[Mn^{III}(OH)(dpaq)]^+$ and

$[Mn^{III}_2(\mu\text{-}O)(dpaq)_2]^{2+}$ reflects the slow reaction of the μ-oxodimanganese(III,III) complex with TEMPOH.

Conclusions

Given the role of Mn^{III}-hydroxo motifs in facilitating biologically important proton-coupled electron transfer reactions, there is significant current interest in understanding the interplay between chemical reactivity and structural and electronic properties. As part of our on-going efforts to understand the HAT reactivity of Mn^{III}-hydroxo adducts, we applied ^{1}H-NMR spectroscopy to study the $[Mn^{III}(OH)(dpaq)]^+$, $[Mn^{III}(OH)(dpaq^{2Me})]^+$, and $[Mn^{III}(OMe)(dpaq)]^+$ complexes. Unexpectedly, ^{1}H-NMR spectra of $[Mn^{III}(OH)(dpaq)](OTf)$ dissolved in CD_3CN showed both hyperfine-shifted signals associated with the mononuclear, $S = 2$ $[Mn^{III}(OH)(dpaq)]^+$ complex and signals in the diamagnetic region attributed to the dimeric $[Mn^{III}_2(\mu\text{-}O)(dpaq)_2]^{2+}$ complex. We propose that these species exist in an equilibrium, whose position is influenced by added water (equation 3). These proposals are based on the following observations: (i) the addition of water to CD_3CN solutions of $[Mn^{III}(OH)(dpaq)](OTf)$ leads to the disappearance of the diamagnetic signals; (ii) removal of solvent from the CD_3CN:D_2O solution of $[Mn^{III}(OH)(dpaq)](OTf)$ and dissolution of the resulting solid in dried CD_3CN leads to re-appearance of the diamagnetic signals; and (iii) Mn K-edge X-ray absorption data collected for a concentrated sample of $[Mn^{III}(OH)(dpaq)](OTf)$ in dried CD_3CN yields EXAFS distances consistent with a DFT-derived model of $[Mn^{III}_2(\mu\text{-}O)(dpaq)_2]^{2+}$. Kinetic investigation of the conversion of μ-oxodimanganese(III,III) species to the corresponding Mn^{III}-hydroxo adduct revealed that this process is slow compared to TEMPOH oxidation by $[Mn^{III}(OH)(dpaq)]^+$. Consequently, our previously reported rate from TEMPOH oxidation by $[Mn^{III}(OH)(dpaq)]^+$ is in error. Experiments performed for bona fide samples of

$[Mn^{III}(OH)(dpaq)]^+$, forced to favor the Mn^{III}-hydroxo adduct using added water, show this complex to be nearly 100-fold more reactive than previously reported. This re-evaluation of rates also means that the $[Mn^{III}(OH)(dpaq)]^+$ and $[Mn^{III}(OH)(dpaq^{2Me})]^+$ complexes actually display similar rates for HAT with TEMPOH. Collectively, this work highlights the complexity in the solution-phase chemistry of a Mn^{III}-hydroxo adduct. This work also demonstrates the power of ^{1}H-NMR spectroscopy to characterize Mn^{III}-hydroxo systems.

Supporting Information Available: Listings of inversion recovery experiments, chemical shifts, additional NMR spectra including temperature dependent NMR, $[Mn^{III}_2(\mu\text{-}OH)(dpaq)_2]^{3+}$ structure, proton integrations, COSY, kinetic traces, and DFT optimized coordinates.

Acknowledgements. This work was supported by NSF grant 1565661 to T.A.J. We heartily thank Dr. Davide Lionetti (University of Kansas), Prof. Misha Barybin (University of Kansas), and Prof. Matt Liptak (University of Vermont) for helpful conversations regarding the ^{1}H NMR data. We thank Dr. Erik Farquhar at NSLS for superb support of our XAS experiments. The SSRL Structural Molecular Biology Program is supported by the DOE Office of Biological and Environmental Research, and by the National Institutes of Health, National Institute of General Medical Sciences (including P41GM103393). The contents of this publication are solely the responsibility of the authors and do not necessarily represent the official views of NIGMS or NIH. Use of Beamline 2-2 at SSRL was partially supported by the National Synchrotron Light Source II, Brookhaven National Laboratory, under U.S. Department of Energy Contract No. DE-SC0012704. XAS experiments were supported by the Case Western Reserve University Center for Synchrotron Biosciences NIH grant, P30-EB-009998, from the National Institute of Biomedical Imaging and Bioengineering

(NIBIB). Support for NMR instrumentation was provided by NIH grants P20 GM103418, S10 OD016360, S10 RR024664 and NSF grants 1625923 and 9977422.

References

1. Rice, D. B.; Massie, A. A.; Jackson, T. A., Manganese–Oxygen Intermediates in O–O Bond Activation and Hydrogen-Atom Transfer Reactions. *Acc. Chem. Res.* 2017, *50* (11), 2706-2717.
2. Jackson, T. A.; Gutman, C. T.; Maliekal, J.; Miller, A.-F.; Brunold, T. C., Geometric and Electronic Structures of Manganese-Substituted Iron Superoxide Dismutase. *Inorg. Chem.* 2013, *52* (6), 3356-3367.
3. Grove, L. E.; Brunold, T. C., Second-sphere Tuning of the Metal Ion Reduction Potentials in Iron and Manganese Superoxide Dismutases. *Comments Inorg. Chem.* 2008, *29* (5/6), 134-168.
4. Sheng, Y.; Abreu, I. A.; Cabelli, D. E.; Maroney, M. J.; Miller, A.-F.; Teixeira, M.; Valentine, J. S., Superoxide Dismutases and Superoxide Reductases. *Chem. Rev.* 2014, *114* (7), 3854-3918.
5. Wennman, A.; Oliw, E. H.; Karkehabadi, S.; Chen, Y., Crystal Structure of Manganese Lipoxygenase of the Rice Blast Fungus Magnaporthe oryzae. *J. Biol. Chem.* 2016.
6. Wennman, A.; Karkehabadi, S.; Oliw, E. H., Kinetic investigation of the rate-limiting step of manganese- and iron-lipoxygenases. *Arch. Biochem. Biophys.* 2014, *555–556* (0), 9-15.
7. Su, C.; Sahlin, M.; Oliw, E. H., Kinetics of Manganese Lipoxygenase with a Catalytic Mononuclear Redox Center. *J. Biol. Chem.* 2000, *275* (25), 18830-18835.
8. Yano, J.; Yachandra, V., Mn4Ca Cluster in Photosynthesis: Where and How Water is Oxidized to Dioxygen. *Chem. Rev.* 2014, *114* (8), 4175-4205.
9. Goldsmith, C. R.; Cole, A. P.; Stack, T. D. P., C−H Activation by a Mononuclear Manganese(III) Hydroxide Complex: Synthesis and Characterization of a Manganese-Lipoxygenase Mimic? *J. Am. Chem. Soc.* 2005, *127* (27), 9904-9912.
10. Coggins, M. K.; Brines, L. M.; Kovacs, J. A., Synthesis and Structural Characterization of a Series of MnIIIOR Complexes, Including a Water-Soluble MnIIIOH That Promotes Aerobic Hydrogen-Atom Transfer. *Inorg. Chem.* 2013, *52* (21), 12383-12393.
11. Rice, D. B.; Wijeratne, G. B.; Burr, A. D.; Parham, J. D.; Day, V. W.; Jackson, T. A., Steric and Electronic Influence on Proton-Coupled Electron-Transfer Reactivity of a Mononuclear Mn(III)-Hydroxo Complex. *Inorg. Chem.* 2016, *55* (16), 8110-8120.
12. Rice, D. B.; Wijeratne, G. B.; Jackson, T. A., Mn K-edge X-ray absorption studies of mononuclear Mn(III)–hydroxo complexes. *J. Biol. Inorg. Chem.* 2017, *22* (8), 1281-1293.
13. Gupta, R.; MacBeth, C. E.; Young, V. G.; Borovik, A. S., Isolation of Monomeric MnIII/II−OH and MnIII−O Complexes from Water: Evaluation of O−H Bond Dissociation Energies. *J. Am. Chem. Soc.* 2002, *124* (7), 1136-1137.
14. Gupta, R.; Taguchi, T.; Borovik, A. S.; Hendrich, M. P., Characterization of Monomeric MnII/III/IV–Hydroxo Complexes from X- and Q-Band Dual Mode Electron Paramagnetic Resonance (EPR) Spectroscopy. *Inorg. Chem.* 2013, *52* (21), 12568-12575.
15. Shirin, Z.; Hammes, B. S.; Young, V. G.; Borovik, A. S., Hydrogen Bonding in Metal Oxo Complexes: Synthesis and Structure of a Monomeric Manganese(III)−Oxo Complex and Its Hydroxo Analogue. *J. Am. Chem. Soc.* 2000, *122* (8), 1836-1837.
16. Shirin, Z.; S. Borovik, A.; G. Young Jr, V., Synthesis and structure of a MnIII(OH) complex generated from dioxygen. *Chem. Commun.* 1997, (20), 1967-1968.

17. Shook, R. L.; Peterson, S. M.; Greaves, J.; Moore, C.; Rheingold, A. L.; Borovik, A. S., Catalytic Reduction of Dioxygen to Water with a Monomeric Manganese Complex at Room Temperature. *J. Am. Chem. Soc.* 2011, *133* (15), 5810-5817.
18. Wijeratne, G. B.; Corzine, B.; Day, V. W.; Jackson, T. A., Saturation Kinetics in Phenolic O–H Bond Oxidation by a Mononuclear Mn(III)–OH Complex Derived from Dioxygen. *Inorg. Chem.* 2014, *53* (14), 7622-7634.
19. Wijeratne, G. B.; Day, V. W.; Jackson, T. A., O-H bond oxidation by a monomeric MnIII-OMe complex. *Dalton Trans.* 2015, *44* (7), 3295-3306.
20. Bonadies, J. A.; Maroney, M. J.; Pecoraro, V. L., Structurally diverse manganese(III) Schiff base complexes: solution speciation via paramagnetic proton NMR spectroscopy and electrochemistry. *Inorg. Chem.* 1989, *28* (11), 2044-2051.
21. Ciringh, Y.; Gordon-Wylie, S. W.; Norman, R. E.; Clark, G. R.; Weintraub, S. T.; Horwitz, C. P., Multinuclear Paramagnetic NMR Spectra and Solid State X-ray Crystallographic Characterization of Manganese(III) Schiff-Base Complexes. *Inorg. Chem.* 1997, *36* (22), 4968-4982.
22. Sheats, J. E.; Czernuszewicz, R. S.; Dismukes, G. C.; Rheingold, A. L.; Petrouleas, V.; Stubbe, J.; Armstrong, W. H.; Beer, R. H.; Lippard, S. J., Binuclear manganese(III) complexes of potential biological significance. *J. Am. Chem. Soc.* 1987, *109* (5), 1435-1444.
23. Mader, E. A.; Davidson, E. R.; Mayer, J. M., Large Ground-State Entropy Changes for Hydrogen Atom Transfer Reactions of Iron Complexes. *J. Am. Chem. Soc.* 2007, *129* (16), 5153-5166.
24. Braun, S.; Kalinowski, H.-O.; Berger, S., *150 and More Basic NMR Experiments*. Wiley-VCH: Weinheim, 1998; p 520.
25. Ravel, B.; Newville, M., ATHENA, ARTEMIS, HEPHAESTUS: data analysis for X-ray absorption spectroscopy using IFEFFIT. *J. Synchrotron Radiat.* 2005, *12* (4), 537-541.
26. Rehr, J. J.; Mustre de Leon, J.; Zabinsky, S. I.; Albers, R. C., Theoretical X-ray Absorption Fine Structure Standards. *J. Am. Chem. Soc.* 1991, *113*, 5135-5140.
27. Neese, F., The ORCA program system. *Wiley Interdisciplinary Reviews: Computational Molecular Science* 2012, *2* (1), 73-78.
28. Neese, F., Software update: the ORCA program system, version 4.0. *Wiley Interdisciplinary Reviews: Computational Molecular Science* 2018, *8* (1), e1327.
29. Becke, A. D., Density Functional Calculations of Molecular Bond Energies. *J. Chem. Phys.* 1986, *84* (8), 4524-4529.
30. Perdew, J. P., Density Functional Approximation for the Correlation Energy of the Inhomogeneous Electron Gas. *Phys. Rev. B* 1986, *33* (12), 8822-8824.
31. Weigend, F.; Ahlrichs, R., Balanced basis sets of split valence, triple zeta valence and quadruple zeta valence quality for H to Rn: Design and assessment of accuracy. *PCCP* 2005, *7* (18), 3297-3305.
32. Holz, R. C.; Brink, J. M.; Rose, R. A., J-Dependent Curie or Anti-Curie Behavior of Proton NMR Resonances for Antiferromagnetically Coupled Dinuclear Copper(II) Complexes. *J. Magn. Reson., Ser. A* 1996, *119* (1), 125-128.
33. Holz, R. C.; Bradshaw, J. M.; Bennett, B., Synthesis, Molecular Structure, and Reactivity of Dinuclear Copper(II) Complexes with Carboxylate-Rich Coordination Environments. *Inorg. Chem.* 1998, *37* (6), 1219-1225.
34. Asokan, A.; Manoharan, P. T., 1H NMR Studies on Strongly Antiferromagnetically Coupled Dicopper(II) Systems. *Inorg. Chem.* 1999, *38* (25), 5642-5654.

35. Leto, D. F.; Jackson, T. A., Mn K-Edge X-ray Absorption Studies of Oxo- and Hydroxo-manganese(IV) Complexes: Experimental and Theoretical Insights into Pre-Edge Properties. *Inorg. Chem.* 2014, *53* (12), 6179-6194.
36. Colmer, H. E.; Howcroft, A. W.; Jackson, T. A., Formation, Characterization, and O–O Bond Activation of a Peroxomanganese(III) Complex Supported by a Cross-Clamped Cyclam Ligand. *Inorg. Chem.* 2016, *55* (5), 2055-2069.
37. Coggins, M. K.; Toledo, S.; Shaffer, E.; Kaminsky, W.; Shearer, J.; Kovacs, J. A., Characterization and Dioxygen Reactivity of a New Series of Coordinatively Unsaturated Thiolate-Ligated Manganese(II) Complexes. *Inorg. Chem.* 2012, *51* (12), 6633-6644.
38. Lee, C.-M.; Wu, W.-Y.; Chiang, M.-H.; Bohle, D. S.; Lee, G.-H., Generation of a Mn(IV)–Peroxo or Mn(III)–Oxo–Mn(III) Species upon Oxygenation of Mono- and Binuclear Thiolate-Ligated Mn(II) Complexes. *Inorg. Chem.* 2017, *56* (17), 10559-10569.
39. Mukhopadhyay, S.; Mandal, S. K.; Bhaduri, S.; Armstrong, W. H., Manganese Clusters with Relevance to Photosystem II. *Chem. Rev.* 2004, *104* (9), 3981-4026.
40. Chiou, Y.-M.; Que, L. J., Models for a-Keto Acid-Dependent Non-heme Iron Enzymes: Structures and Reactivity of $[Fe^{II}(L)(O_2CCOPh)](ClO_4)$ Complexes. *J. Am. Chem. Soc.* 1995, *117*, 3999-4013.
41. Zang, Y.; Que, L., Structure and Reactivity of Fe(II)-SAr Complexes: Relevance to the Active Site of Isopenicillin N Synthase. *Inorg. Chem.* 1995, *34* (5), 1030-1035.
42. Pladziewicz, J. R.; Lesniak, J. S.; Abrahamson, A. J., Treatment of kinetic data for opposing second-order and mixed first and second-order reactions. *J. Chem. Educ.* 1986, *63* (10), 850.

Chapter 5

Structure and Reactivity of (μ-oxo)dimanganese(III,III) and Mononuclear Hydroxomanganese(III) Adducts Supported by Derivatives of an Amide-containing Pentadentate Ligand

All X-ray diffraction data collection and analysis were carried out by Dr. Victor W. Day. All other experiments for the $[Mn^{III}(OH)(dpaq^{5Cl})]^{+}$ and $[Mn^{III}Mn^{III}(\mu{-}O)(dpaq^{5Cl})_2]^{2+}$ were performed by Aruna Munasinghe. TEMPOH kinetics and crystalline material for the $[Mn^{III}(OH)(dpaq^{5NO2})]^{+}$ were obtained by Elizabeth N. Grotemeyer.

5.1 Introduction

Hydrogen atom transfer (HAT) reactions, where a proton and electron are transferred in the same kinetic step,[1] are ubiquitous in biological systems and synthetic chemistry. While high-valent metal-oxo species are among the most common hydrogen-atom abstraction agents, there is increasing interest in understanding the HAT reactivity of both high- and mid-valent metal-hydroxo species.[2] In nature, mid-valent metal-hydroxo motifs are involved in a variety of redox transformations, including the oxidation of substrate C–H bonds of weaker bond strength. For example, the Fe and Mn lipoxygenase (LOX) enzymes respectively employ active-site Fe^{III}-hydroxo and Mn^{III}-hydroxo units to attack a C–H bond of a cis, cis-1,4-pentadiene-containing polyunsaturated fatty acid, which has a low bond dissociation free energy (BDFE) of 77 kcal/mol.[3-9] For both the Fe and Mn forms of LOX, the reaction between the metal-hydroxo adduct and substrate proceeds with a large substrate H/D kinetic isotope effect (> 21)[5] supporting a HAT pathway with a significant tunneling contribution.

The chemistry of Fe- and Mn-LOX has inspired a number of Fe^{III}-hydroxo and Mn^{III}-hydroxo model systems. Using both heme and nonheme supporting ligands, a variety of groups have described the ability of mononuclear Fe^{III}-hydroxo complexes to perform HAT reactions with hydrocarbons.[10-14] Some of these complexes are excellent oxidants. For example, the recently reported $[Fe^{III}(OH)(OH_2)(PyPz)]^{4+}$ (PyPz = tetramethyl-2,3-pyridino porphyrazine) complex displayed a second-order rate constant for DHA oxidation that far exceeds that of many high-valent Fe-oxo species.[11] In contrast, the number of Mn^{III}-hydroxo units known to attack C–H bonds of any strength is extremely limited. The $[Mn^{III}(OH)(PY5)]^{+}$ complex of Stack and Goldberg (Figure 5.1, top left) remains the most impressive synthetic Mn^{III}-hydroxo unit for HAT reactions.[15] This complex is capable of oxidizing the relatively strong C–H bond of toluene (BDFE of 87 kcal/mol in

CH_3CN[16]), albeit slowly. In contrast, the $[Mn^{III}(OH)(S^{Me2}N_4(tren))]^+$ complex of Kovacs and co-workers (Figure 5.1, top right) was limited in the scope of its reactivity, being only capable of attacking the activated O–H bond of TEMPOH (O–H BDFE in CH_3CN of 66.5 kcal/mol[16]) but doing so with a rapid rate.[17]

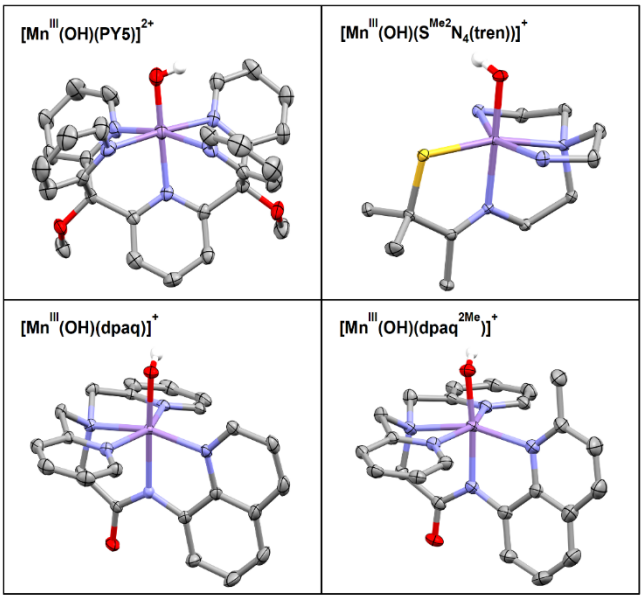

Figure 5.1. Comparison of ORTEP diagrams of $[Mn^{III}(OH)(PY5)]^{2+}$ (top left)[15], $[Mn^{III}(OH)(S^{Me2}N_4(tren))]^+$ (top right),[17] $[Mn^{III}(OH)(dpaq)]^+$ (bottom left)[18] and $[Mn^{III}(OH)(dpaq^{2Me})]^+$ (bottom right).[19]

Our lab has reported a pair of Mn^{III}-hydroxo complexes, supported by amide-containing pentadentate ligands (Figure 5.1, bottom), with HAT abilities intermediate between those of the $[Mn^{III}(OH)(PY5)]^+$ and $[Mn^{III}(OH)(S^{Me2}N_4(tren))]^+$ complexes.[18] Although the rates of TEMPOH oxidation by $[Mn^{III}(OH)(dpaq)]^+$ and $[Mn^{III}(OH)(dpaq^{2Me})]^+$ are ca. 100-fold slower than that of $[Mn^{III}(OH)(S^{Me2}N_4(tren))]^+$, the former complexes are capable of attacking substrates with stronger O–H and C–H bonds. For example, both $[Mn^{III}(OH)(dpaq)]^+$ and $[Mn^{III}(OH)(dpaq^{2Me})]^+$ oxidize xanthene (C–H BDFE of 73.3 kcal/mol in DMSO[16]), with rates only ca. 10 to 30-fold slower than

that of $[Mn^{III}(OH)(PY5)]^{+}$. Among the $[Mn^{III}(OH)(dpaq)]^{+}$ and $[Mn^{III}(OH)(dpaq^{2Me})]^{+}$ complexes, we originally reported that the latter was a significantly more reactive HAT agent towards sterically unencumbered substrates.[19] However, our initial kinetic investigations of $[Mn^{III}(OH)(dpaq)]^{+}$ were complicated by an equilibrium between this complex and a spin-coupled diamagnetic species.[20] Analysis of the ^{1}H-NMR signals of this species, along with low-temperature Mn K-edge X-ray absorption experiments, suggest that the diamagnetic species is the dimeric $[Mn^{III}Mn^{III}(\mu\text{-}O)(dpaq)_2]^{2+}$ complex. A subsequent kinetic investigation of $[Mn^{III}(OH)(dpaq)]^{+}$ in a CH_3CN:H_2O mixture, where the mononuclear Mn^{III}-hydroxo adduct is the dominant species, revealed a TEMPOH oxidation rate nearly identical to that of $[Mn^{III}(OH)(dpaq^{2Me})]^{+}$.[20]

To better understand the factors affecting the HAT reactivity of Mn^{III}-hydroxo complexes, we report here a series of mononuclear Mn^{III}-hydroxo adducts using dpaq derivatives with chloro, methoxy, and nitro substituents placed at the 5 position of the quinolinyl moiety (referred to as $[Mn^{III}(OH)(dpaq^{5R})]^{+}$). Hitomi and co-workers have previously shown that these $dpaq^{5R}$ ligands, which place substituents *para* to the amide nitrogen, can exert a significant influence over the Mn reduction potential for the $[Mn(dpaq^{5R})(NO)]ClO_4$ (R = OMe, H, Cl and NO_2) complexes.[21] In this present study, we show how these ligand perturbations influence the HAT reactivity and thermodynamic properties (*i.e.*, $Mn^{III/II}$ peak potentials) of the Mn^{III}-hydroxo unit. In addition, ^{1}H NMR studies of the new systems reveals that, in each case, the Mn^{III}-hydroxo complex is in a water-dependent equilibrium with a diamagnetic species, which we formulate as a (μ-oxo)dimanganese(III,III) complex. This formulation is bolstered by crystallographic characterization of the three $[Mn^{III}Mn^{III}(\mu\text{-}O)(dpaq^{5R})_2](OTf)_2$ complexes.

5.2 Materials and Method

Materials and Instrumentation. All solvents and chemicals were obtained from commercial vendors at ACS grade or better and, unless described otherwise, were used without further purification. Acetonitrile and ether were dried and degassed using a Pure Solv (2010) solvent purification system, as described previously.[20] The $Hdpaq^{5Cl}$, $Hdpaq^{5OMe}$, and $Hdpaq^{5NO2}$ ligands, $[Mn^{II}(dpaq)](OTf)$ and $[Mn^{II}(dpaq^{2Me})](OTf)$ complexes, $[Mn^{II}(CH_3CN)_2(OTf)_2]_n$ salt, and TEMPOH were generated by previously reported methods.[18-19, 22-24] Elemental analysis was performed on solid samples by Micro-Analysis, Inc. All ^1H NMR spectra were collected on a 400 MHz Bruker AVIIIHD NMR with an acquisition time of 0.27 s and a spectral width of 150 to – 100 ppm. At least 1000 scan were collected to provide sufficient S/N. Spectra were baseline-subtracted with the multipoint fitting procedure using spline functions as available in MestReNova. Mass spectrometry and EPR experiments were collected on previously described instrumentation.[20]

Preparation and Characterization of $[Mn^{II}(dpaq^{5R})](OTf)$. All syntheses and manipulations of Mn^{II} complexes were performed in an Ar-filled glovebox. The $[Mn^{II}(dpaq^{5R})](OTf)$ complexes were prepared by analogy to methods reported for the perchlorate salts,[21] with the change that metalation reactions were performed using $[Mn^{II}(CH_3CN)_2(OTf)_2]_n$. The $[Mn^{II}(dpaq^{5R})](OTf)$ complexes were purified by recrystallization in CH_3CN:Et_2O and then oxidized to form their Mn^{III} analogues by the procedures described below. ESI-MS: $\{[Mn^{II}(dpaq^{5NO2})]^+\}$ m/z = 482.0884 (calculated m/z = 482.0899); $\{[Mn^{II}(dpaq^{5Cl})]^+\}$ m/z = 471.0514 (calculated m/z = 471.0659); $\{[Mn^{II}(dpaq^{5OMe})]^+\}$ m/z = 467.1141 (calculated m/z = 467.1154).

Preparation and Characterization of (μ-oxo)dimanganese(III,III) and hydroxomanganese(III) Complexes. *$[Mn^{III}Mn^{III}(\mu\text{-}O)(dpaq^{5Cl})_2](OTf)_2$.* A solution of 55 mg (88 μmol) crystalline $[Mn^{II}(dpaq^{5Cl})](OTf)$ was prepared in 2 mL dried CH_3CN in a glove box. Solid

iodosobenzene (9.7 mg; 44 μmol) was added to this solution, and the reaction mixture was stirred for 12 hours. The resulting solution was evaporated to dryness under vacuum. This solid was dissolved in a minimum amount of CH_3CN and subjected to repeated recrystallizations by vapor diffusion with Et_2O. The procedure yielded needle-like, dark-brown crystals of $[Mn^{III}Mn^{III}(\mu\text{-}O)(dpaq^{5Cl})_2](OTf)_2$ (30 mg; 55% yield), suitable for X-ray diffraction analysis. The solid-phase composition of this complex was also supported by elemental analysis: calculated (%): C 45.84, H 3.05, N 11.14; found (%): C 45.51, H 3.36, N 11.00. The solution-phase composition of $[Mn^{III}Mn^{III}(\mu\text{-}O)(dpaq^{5Cl})_2](OTf)_2$ was analyzed by ^1H NMR spectroscopy and the Evan's NMR method, both in acetonitrile. The ^1H NMR spectrum of $[Mn^{III}Mn^{III}(\mu\text{-}O)(dpaq^{5Cl})_2](OTf)_2$ dissolved in dried CD_3CN showed chemical shifts in the diamagnetic range (0 to 30 ppm), which we attribute to $[Mn^{III}Mn^{III}(\mu\text{-}O)(dpaq^{5Cl})_2](OTf)_2$. A set of nine signals observed outside this chemical shift range are attributed to $[Mn^{III}(OH)(dpaq^{5Cl})]^+$, which is generated from the reaction of $[Mn^{III}Mn^{III}(\mu\text{-}O)(dpaq^{5Cl})_2](OTf)_2$ with water. In support, the effective magnetic moment of a CD_3CN solution $[Mn^{III}Mn^{III}(\mu\text{-}O)(dpaq^{5Cl})](OTf)_2$ was determined to be 1.88 μ_B per Mn.

$[Mn^{III}(OH)dpaq^{5Cl}](OTf)$. A 2.5 mM $[Mn^{II}(dpaq^{5Cl})](OTf)$ solution was prepared in 2 mL of CH_3CN in a glove box. This solution was transferred to a cuvette that was sealed with a rubber septum and then removed from the glove box. This solution was stirred and monitored by electronic absorption spectroscopy, during which $O_2(g)$ was bubbled through the solution. A dark-brown solution was formed, with optical changes completed in ca. 5 hours. On the basis of ^1H NMR and electronic absorption data (*vide infra*), this solution contains a mixture of $[Mn^{III}Mn^{III}(\mu\text{-}O)(dpaq^{5Cl})_2]^{2+}$ and $[Mn^{III}(OH)(dpaq^{5Cl})]^+$. To isolate the $[Mn^{III}(OH)(dpaq^{5Cl})]^+$ species, 560 equivalents of water were added to the solution of $[Mn^{III}Mn^{III}(\mu\text{-}O)(dpaq^{5Cl})_2]^{2+}$ and

$[Mn^{III}(OH)(dpaq^{5Cl})]^+$, and the color of the solution changed from dark-brown to orange. Electronic absorption and ^1H NMR data (*vide infra*) show that the $[Mn^{III}(OH)(dpaq^{5Cl})]^+$ species is the dominant species in solution under these conditions. To obtain quantities of $[Mn^{III}(OH)(dpaq^{5Cl})](OTf)$ suitable for bulk characterization, the above synthesis was carried out on a larger scale. A stirred solution of 50 mg (78 μmol) of crystalline $[Mn^{II}(dpaq^{5Cl})](OTf)$ in 2 mL of CH_3CN was prepared and stirred overnight under an $O_2(g)$ atmosphere. The resulting solution was evaporated to dryness and then dissolved in a minimum amount of 90:10 $CH_3CN:H_2O$ (vol:vol). Brown-orange crystalline plates of $[Mn^{III}(OH)(dpaq^{5Cl})](OTf)$, suitable for X-ray diffraction analysis, were obtained with good yield (90%) after three re-crystallizations by vapor diffusion of Et_2O into the concentrated 90:10 $CH_3CN:H_2O$ (vol:vol) solution. The composition of $[Mn^{III}(OH)(dpaq^{5Cl})](OTf)$ was further determined by a variety of methods. ESI-MS: m/z = 488.0683 (calculated m/z = 488.0686 for $\{[Mn^{III}(OH)(dpaq^{5Cl})]^+\}$); elemental analysis $[Mn^{III}(OH)(dpaq^{5Cl})](OTf)(MeCN)(H_2O)$: calculated (%): C 44.81, H 3.62, N 12.06; found (%): C 44.72, H 3.50, N 12.23; μ_{eff} (Evan's NMR) = 4.91 μ_B (calculated μ_{eff} = 4.90 μ_B for a high-spin S = 2 Mn^{III} center).

$[Mn^{III}Mn^{III}(\mu\text{-}O)(dpaq^{5OMe})_2](OTf)_2$ and $[Mn^{III}(OH)(dpaq^{5OMe})]^+$. A solution of 50 mg $[Mn^{II}(dpaq^{5OMe})](OTf)$ was prepared in CH_3CN and O_2 was bubbled through the solution for 30 minutes, during which the solution changed from orange to dark brown. The resulting solution was dried and recrystallized through vapor diffusion of CH_3CN with Et_2O. This recrystallization yielded dark-brown, needle-like crystals of $[Mn^{III}Mn^{III}(\mu\text{-}O)(dpaq^{5OMe})_2](OTf)_2$ suitable for X-ray diffraction. The solid-phase composition of $[Mn^{III}Mn^{III}(\mu\text{-}O)(dpaq^{5OMe})_2](OTf)_2(H_2O)$ was also supported by elemental analysis: $[Mn^{III}Mn^{III}(\mu\text{-}O)(dpaq^{5OMe})_2](OTf)_2(H_2O)$ calculated (%): C 47.40, H 3.66, N 11.06; found (%): C 46.73, H 3.82, N 11.11. The ^1H NMR spectrum of $[Mn^{III}Mn^{III}(\mu\text{-}O)(dpaq^{5OMe})_2](OTf)_2$ dissolved in dried CD_3CN showed chemical shifts in the diamagnetic range (0

to 30 ppm), which we attribute predominantly to $[Mn^{III}Mn^{III}(\mu\text{-}O)(dpaq^{5OMe})_2](OTf)_2$. Two of the signals in the diamagnetic region, as well as the ten signals outside of that chemical shift range are attributed to $[Mn^{III}(OH)(dpaq^{5OMe})]^+$, formed from the reaction of $[Mn^{III}Mn^{III}(\mu\text{-}O)(dpaq^{5OMe})_2](OTf)_2$ with water. The addition of 880 equiv. of D_2O to this ^1H NMR sample resulted in the disappearance of the majority of the peaks in the diamagnetic region, leaving only the peaks attributed to $[Mn^{III}(OH)(dpaq^{5OMe})]^+$. The solution properties of $[Mn^{III}(OH)(dpaq^{5OMe})]^+$ were further determined by a variety of methods. ESI-MS: m/z = 484.0881 (calculated m/z = 484.1181 for $\{[Mn^{III}(OH)(dpaq^{5OMe})]\}$; μ_{eff} (Evan's NMR) = 4.9 μ_B (calculated μ_{eff} = 4.9 μ_B for a high-spin S = 2 Mn^{III} center).

$[Mn^{III}Mn^{III}(\mu\text{-}O)(dpaq^{5NO2})_2](OTf)_2$ and $[Mn^{III}(OH)(dpaq^{5NO2})]^+$. A solution of 40 mg $[Mn^{II}(dpaq^{5NO2})](OTf)$ was prepared in CH_3CN and 0.5 equiv. iodosobenzene were added to this solution. The reaction slurry was sonicated for 20 minutes, during which time the solution changed from orange to dark brown. The resulting solution was dried under vacuum, and the solid residue was recrystallized through vapor diffusion of CH_3CN with Et_2O. This recrystallization yielded dark-brown, needle-like crystals of $[Mn^{III}Mn^{III}(\mu\text{-}O)(dpaq^{5NO2})_2](OTf)_2$ suitable for X-ray diffraction. The solid-phase composition of $[Mn^{III}Mn^{III}(\mu\text{-}O)(dpaq^{5NO2})_2](OTf)_2(H_2O)$ was also supported by elemental analysis: calculated (%): C 44.45 H 3.11, N 12.96; found (%): C 43.80, H 3.50, N 13.09. The ^1H NMR spectrum of $[Mn^{III}Mn^{III}(\mu\text{-}O)(dpaq^{5NO2})_2](OTf)_2$ dissolved in dried CD_3CN showed chemical shifts in the diamagnetic range (0 to 30 ppm), which we attribute predominantly to $[Mn^{III}Mn^{III}(\mu\text{-}O)(dpaq^{5NO2})_2](OTf)_2$. One signal in the diamagnetic region, as well as ten signals outside of that chemical shift range are attributed to $[Mn^{III}(OH)(dpaq^{5NO2})]^+$, which is formed from the reaction of $[Mn^{III}Mn^{III}(\mu\text{-}O)(dpaq^{5NO2})_2](OTf)_2$ with water. The addition of 880 equiv. of D_2O to

this ^{1}H NMR sample, resulted in the disappearance of the majority of the peaks in the diamagnetic region, leaving only the peaks attributed to $[Mn^{III}(OH)(dpaq^{5NO2})]^+$. The solution properties of $[Mn^{III}(OH)(dpaq^{5NO2})]^+$ were further determined by a variety of methods. ESI-MS: m/z = 499.0915 (calculated m/z = 499.0927 for $\{[Mn^{III}(OH)(dpaq^{5NO2})]\}$; μ_{eff} (Evan's NMR) = 4.8 μ_B (calculated μ_{eff} = 4.9 μ_B for a high-spin S = 2 Mn^{III} center).

X-ray Crystallographic Studies for $[Mn^{III}Mn^{III}(\mu\text{-}O)(dpaq^{5Cl})_2](OTf)_2$, $[Mn^{III}(OH)(dpaq^{5Cl})](OTf)$, $[Mn^{III}Mn^{III}(\mu\text{-}O)(dpaq^{5OMe})_2](OTf)_2$ and $[Mn^{III}Mn^{III}(\mu\text{-}O)(dpaq^{5NO2})_2](OTf)_2$. Complete sets of unique reflections were collected with monochromated CuKα radiation for single-domain crystals of all four compounds. Totals of 3930 ($[Mn^{III}Mn^{III}(\mu\text{-}O)(dpaq^{5Cl})_2](OTf)_2$), 3142 ($[Mn^{III}(OH)(dpaq^{5Cl})](OTf)$), 2221 ($[Mn^{III}Mn^{III}(\mu\text{-}O)(dpaq^{5OMe})_2](OTf)_2$) and 2779 ($[Mn^{III}Mn^{III}(\mu\text{-}O)(dpaq^{5NO2})_2](OTf)_2$) 1.0°-wide ω- or ϕ-scan frames with counting times of 6-30 seconds ($[Mn^{III}Mn^{III}(\mu\text{-}O)(dpaq^{5Cl})_2](OTf)_2$) or 4-6 seconds ($[Mn^{III}(OH)(dpaq^{5Cl})](OTf)$, $[Mn^{III}Mn^{III}(\mu\text{-}O)(dpaq^{5OMe})_2](OTf)_2$, and $[Mn^{III}Mn^{III}(\mu\text{-}O)(dpaq^{5NO2})_2](OTf)_2$) were collected on a Bruker APEX II ($[Mn^{III}Mn^{III}(\mu\text{-}O)(dpaq^{5Cl})_2](OTf)_2$ and $[Mn^{III}(OH)(dpaq^{5Cl})](OTf)$) or Platinum 135 ($[Mn^{III}Mn^{III}(\mu\text{-}O)(dpaq^{5OMe})_2](OTf)_2$ and $[Mn^{III}Mn^{III}(\mu\text{-}O)(dpaq^{5NO2})_2](OTf)_2$) CCD area detector. X-rays were provided by a Bruker MicroStar microfocus rotating anode operating at 45kV and 60 mA and equipped with Helios high-brilliance multilayer x-ray optics. Preliminary lattice constants were obtained with the Bruker program SMART.[25] Integrated reflection intensities for all four compounds were produced using the Bruker program SAINT.[26] Each data set was corrected empirically for variable absorption effects using equivalent reflections. The Bruker software package SHELXTL was used to solve each structure using "direct methods" techniques. All stages of weighted full-matrix least-squares refinement were conducted using Fo^2 data with the SHELXTL

v2014 software package.[27]

The final structural model for each compound incorporated anisotropic thermal parameters for all ordered nonhydrogen atoms; isotropic thermal parameters were used for all included hydrogen atoms and disordered nonhydrogen atoms that were not modeled with anisotropic thermal parameters. The cationic Mn(III) complexes in all four crystals were ordered and their nonhydrogen atoms were incorporated into the structural models with anisotropic thermal parameters. Hydrogen atoms in each complex (except the hydroxyl hydrogen in $[Mn^{III}(OH)(dpaq^{5Cl})](OTf)$) were fixed at idealized riding model sp^2- or sp^3-hybridized positions with C-H bond lengths of 0.95 - 0.99 Å. The acetonitrile methyl of $[Mn^{III}(OH)(dpaq^{5Cl})](OTf)$ and the methoxy methyl group of $[Mn^{III}Mn^{III}(\mu\text{-}O)(dpaq^{5OMe})_2](OTf)_2$ were both refined as idealized rigid rotors (with a C-H bond length of 0.98 Å) that were allowed to rotate freely about their C-C or O-C bonds in least-squares refinement cycles. No other acetonitrile hydrogen atoms were included in the structural models. The isotropic thermal parameters of idealized hydrogen atoms in all four structures were fixed at values 1.2 (non-methyl) or 1.5 (methyl) times the equivalent isotropic thermal parameter of the carbon atom to which they are covalently bonded. The relevant crystallographic and structure refinement data for all four compounds are given in Tables S1 to S4.

The asymmetric unit of $[Mn^{III}Mn^{III}(\mu\text{-}O)(dpaq^{5Cl})_2](OTf)_2$ contains one dimeric dication, one ordered triflate anion, one 69%/31% disordered triflate anion, one ordered full-occupancy acetonitrile molecule of crystallization and one partially-occupied (40%) disordered acetonitrile. The two orientations for the disordered triflate anion and the partial-occupancy acetontitrile were incorporated into the structural model with isotropic thermal parameters. The bond lengths and angles for both orientations of the disordered triflate were restrained to have bond lengths and angles similar to those of the ordered triflate. The nonhydrogen atoms of the partial-occupancy

(40%) acetonitrile were restrained to have bond lengths and angles similar to those of the ordered acetonitrile. This disorder for $[Mn^{III}Mn^{III}(\mu\text{-}O)(dpaq^{5Cl})_2](OTf)_2$ introduced on A-level alert with checkCIF.

The asymmetric unit of $[Mn^{III}(OH)(dpaq^{5Cl})](OTf)$ contains one monomeric monocation and a 91%/9% disordered triflate anion. The minor-occupancy (9%) triflate anion was incorporated into the structural model with isotropic thermal parameters and its bond lengths and angles were restrained to have values similar to those of the major-occupancy (91%) triflate. The hydroxyl hydrogen was located from a difference Fourier and refined as an independent isotropic atom.

The asymmetric unit of $[Mn^{III}Mn^{III}(\mu\text{-}O)(dpaq^{5OMe})_2](OTf)_2$ contains half of a dimeric dication, one ordered triflate anion and half of a water molecule of crystallization. The water hydrogen was located from a difference Fourier and refined as an independent isotropic atom with the O-H bond length restrained to be 0.84 Å.

The asymmetric unit of $[Mn^{III}Mn^{III}(\mu\text{-}O)(dpaq^{5NO2})_2](OTf)_2$ contains half of a dimeric dication, a 54%/46% disordered triflate anion and a 53%/47% disordered acetonitrile solvent molecule of crystallization. Both orientations for the disordered triflate anion and acetonitrile solvent molecule of crystallization were restrained to have nearly idealized geometries by using free variables for the triflate S-O, triflate C-F and nitrile C-N bond lengths. The remaining bond lengths and angles in the anions and solvent of $[Mn^{III}Mn^{III}(\mu\text{-}O)(dpaq^{5NO2})_2](OTf)_2$ were restrained to be multiples of these three free variables that were consistent with sp- or sp^3-hybridization. Mild restraints were applied to the anisotropic thermal parameters of O3. This disorder for $[Mn^{III}Mn^{III}(\mu\text{-}O)(dpaq^{5NO2})_2](OTf)_2$ introduced one A-level alert with checkCIF.

Kinetic Studies of TEMPOH oxidation by $[Mn^{III}(OH)(dpaq^{5Cl})]^+$, $[Mn^{III}(OH)(dpaq^{5OMe})]^+$, and $[Mn^{III}(OH)(dpaq^{5NO2})]^+$. All kinetic experiments were performed using an Agilent 8453

spectrometer. As common procedures were used for each $[Mn^{III}(OH)(dpaq^{5R})]^+$ complex, we describe our kinetic experiments with reference to $[Mn^{III}(OH)(dpaq^{5R})]^+$, where R = Cl, OMe, and NO_2. In a glovebox, a 1.25 mM $[Mn^{III}(OH)(dpaq^{5R})]^+$ solution was prepared in 2 mL of acetonitrile and transferred to a cuvette that was sealed with a rubber septum. The cuvette was removed from the glovebox, at which point a 100 μL aliquot of a 60:40 $CH_3CN:H_2O$ (vol:vol) solution, purged with nitrogen, were added using a gastight syringe that had been purged with Ar(g) before use. This addition delivers 880 equivalents of water per Mn, ensuring that the Mn^{III}-hydroxo species is dominant in solution. This solution was equilibrated at -35 °C for at least 10 minutes using a Unisoku cryostat. Stock solutions of TEMPOH were prepared in 500 μL of CH_3CN in a glove box. The concentrations of these solutions were such that the addition of a 100 μL aliquot to the 2 mL solution of 1.25 mM $[Mn^{III}(OH)(dpaq^{5R})]^+$ delivers 10 – 40 equivalents of TEMPOH per Mn. The 100 μL aliquots of TEMPOH solution were contained in gastight syringes with the needles sealed by a rubber septum. These syringes were removed from the glovebox, at which point they were immediately added to the solution of $[Mn^{III}(OH)(dpaq^{5R})]^+$ maintained at -35 °C. The addition of TEMPOH led to the rapid disappearance of the electronic absorption signatures of $[Mn^{III}(OH)(dpaq^{5R})]^+$. A pseudo-first-order decay rate (k_{obs}) for this process was determined by fitting the change in absorbance at approximately 770 nm as a function of time. The final reaction mixture for TEMPOH oxidation by $[Mn^{III}(OH)(dpaq^{5Cl})]^+$ was analyzed by perpendicular-mode X-band EPR spectroscopy at 10 K; the EPR spectrum showed a characteristic signal consistent with a TEMPO radical (Figure A4.1).

Cyclic Voltammetry for $[Mn^{III}(OH)(dpaq^{5Cl})]+$, $[Mn^{III}(OH)(dpaq^{5OMe})]^+$, and $[Mn^{III}(OH)(dpaq^{5NO2})]^+$. Cyclic voltammetry (CV) data were collected for a 1.85 mM solution of each $[Mn^{III}(OH)(dpaq^{5R})]^+$ derivative in 10.8 mL of 92.5:7.5 (vol:vol) $CH_3CN:H_2O$. A larger amount

of H_2O was needed than used in the kinetic experiments (98:02 CH_3CN:H_2O; vol:vol) in order to eliminate the presence of multiple reduction events that were observed for solvent mixtures with higher CH_3CN:H_2O ratios. All CV experiments were performed under an inert atmosphere. Solvents were purged with nitrogen to remove O_2 until no redox peaks related to O_2 were observed. A Ag/AgCl quasi-reference electrode, a platinum auxiliary electrode, and a glassy carbon electrode were used as the three electrode system, with 0.1 M $Bu_4N(PF_6)$ as the supporting electrolyte. Peak positions were referenced to the Fc^+/Fc couple used as an internal standard.

Electronic Structure Calculations. All density functional theory (DFT) calculations were performed using the *ORCA* 4.0 software package.[28] Geometry optimizations were performed using the B3LYP[29-30] functional with the def2-TZVP basis set for Mn, N and O and the def2-SVP basis set with C and H.[31-32] Analytical frequency calculations were performed at the same level of theory as the geometry optimizations. The frequency calculations provided the zero point and thermal corrections to energy as well as the entropy. Single-point energy calculations were performed on all structures using the larger def2-TZVPP basis set on all atoms with the large integration grid (Grid7 in *ORCA*) and exchange grid (GridX7 in *ORCA*). Solvation was accounted for using the SMD solvent model with the default parameters for acetonitrile.[33] The RIJCOSX approximation was used for all calculations with the def2/J auxiliary basis sets.

For determination of pK_a, reduction potential, and BDFE values, a relatively accurate method has been outlined by Solis et al.[34] For this method, a reference complex, which is chemically similar to the complexes being studied, bypasses the need to rely upon calculated proton free energies and electrode potentials. The use of this reference complex also allows for cancelation of systematic errors in the theoretical treatment. We used $[Mn^{III}(OH)(PY5)]^{2+}$ as the reference complex in this work, as i) experimental pK_a and $E_{1/2}$ values are available for this complex, and ii) the use of

this complex as a reference has previously proven to give good agreement between experimental and calculated reduction potentials for Mn^{III}-hydroxo complexes.[19] The pK_a values and reduction potentials calculated here rely on the DFT-optimized structures of the Mn^{III}-hydroxo, Mn^{II}-hydroxo, and Mn^{II}-aqua adducts of all $dpaq^{5R}$ ligands. The free energy difference between the Mn^{III}-hydroxo and Mn^{II}-hydroxo complexes were used to determine the $E_{1/2}$ vs. Fc^+/Fc, and the free energy difference between the Mn^{II}-hydroxo and Mn^{II}-aqua complexes were used to determine the pK_a. These values were then used to calculated the O–H BDFE for the Mn^{II}-aqua complexes using the Bordwell relationship.[35]

5.3 Results and Discussion

Dioxygen Oxidation of [Mn^{II}($dpaq^{5Cl}$)](OTf) and [Mn^{II}($dpaq^{5OMe}$)](OTf) Complexes. Acetonitrile solutions of the [Mn^{II}($dpaq^{5R}$)](OTf) complexes show only very weak bands in the visible region (Figure 5.2, black traces), consistent with the previous report of Hitomi and co-workers. Oxidation of [Mn^{II}($dpaq^{5R}$)](OTf) (R = 5Cl and 5OMe) complexes in CH_3CN leads to the appearance of new electronic absorption features in the visible region (Figure 5.2, red traces). For each complex, a broad shoulder is observed near 770 nm, with the broadness of the features differing significantly from complex to complex. The relative broadness of the features is sensitive to small changes in the amounts of water in solution. The addition of 80 μL water to the solutions causes the electronic absorption bands to sharpen, revealing maxima near 770 nm (Figure 5.2, blue traces).

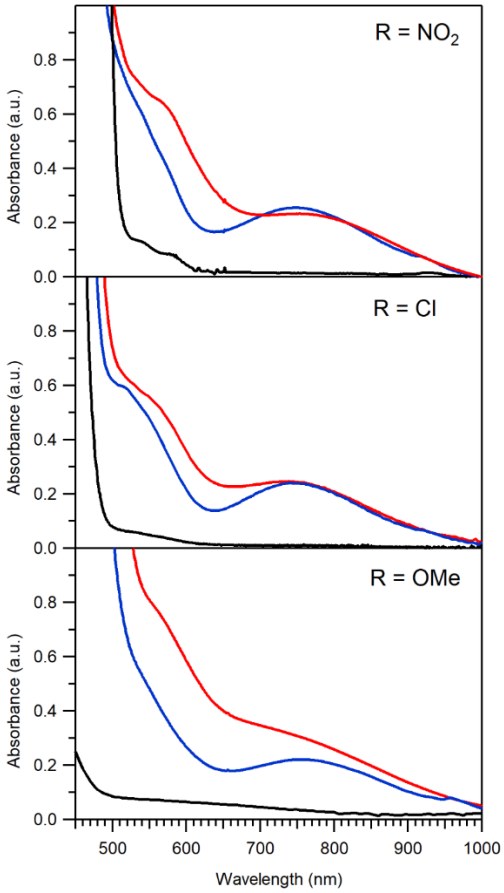

Figure 5.2. Electronic absorption spectra of [Mn^{II}($dpaq^{5NO2}$)](OTf) (top), [Mn^{II}($dpaq^{5Cl}$)](OTf) (center), and [Mn^{II}($dpaq^{5OMe}$)](OTf) (bottom), before oxidation (black), after oxidation (red) and after the addition of 880 equiv. H_2O to the oxidized solutions (blue). All reactions were performed for 2.5 mM CH_3CN solutions at 25 °C.

The nature of the oxidized products, and the influence of water, can be understood on the basis of ^1H NMR experiments (*vide infra*) and by analogy to a recent investigation of the oxygenation products of [Mn^{II}(dpaq)](OTf).[20] The electronic absorption features initially observed upon reaction of [Mn^{II}($dpaq^{5Cl}$)](OTf) and [Mn^{II}($dpaq^{5OMe}$)](OTf) with O_2 are similar in energy and intensity to those observed when [Mn^{II}(dpaq)](OTf) is reacted with O_2 in CH_3CN (λ_{max} = 550 and 780 nm).[18] In that case, the electronic absorption spectrum was revealed to contain contributions from both the mononuclear [Mn^{III}(OH)(dpaq)]$^+$ species, as well as a diamagnetic species, which we formulated as

$[Mn^{III}Mn^{III}(\mu\text{-}O)(dpaq)_2]^{2+}$.[20] The addition of water caused a shift in the equilibrium between these components to favor the Mn^{III}-hydroxo complex. We likewise propose that oxygenation of $[Mn^{II}(dpaq^{5Cl})](OTf)$ and $[Mn^{II}(dpaq^{5OMe})](OTf)$ initially forms a mixture of (μ-oxo)dimanganese(III,III) and Mn^{III}-hydroxo species, with the latter being favored by the addition of water. In support, the energies and intensities for the electronic absorption signals for the putative $[Mn^{III}(OH)(dpaq^{5Cl})]^+$ and $[Mn^{III}(OH)(dpaq^{5OMe})]^+$ species (observed upon water addition) are essentially identical to those of $[Mn^{III}(OH)(dpaq)]^+$ (Table 1).

Table 5.1. Electronic Absorption Properties of Mn^{III}-hydroxo Complexes Supported by the $dpaq^R$ Ligands.

	λ_{max} (nm)	ε_{max} ($M^{-1}cm^{-1}$)
$[Mn^{III}(OH)(dpaq)]^+$	770	114
$[Mn^{III}(OH)(dpaq^{2Me})]^+$	780	130
$[Mn^{III}(OH)(dpaq^{5NO2})]^+$	770	102
$[Mn^{III}(OH)(dpaq^{5Cl})]^+$	765	96
$[Mn^{III}(OH)(dpaq^{5OMe})]^+$	760	89

[a] Collected in a 98:2 CH_3CN:H_2O (vol:vol) solution.

Iodosobenzene Oxidation of $[Mn^{II}(dpaq^{5NO2})](OTf)$. The $[Mn^{II}(dpaq^{5NO2})](OTf)$ complex showed limited reactivity with O_2, showing only partial oxidation after 24 hours of exposure to air. Presumably, the weakened donation of the amide group caused by the 5-nitroquinolinyl moiety leads to a $Mn^{III/II}$ reduction potential too high to support reactivity with O_2. Consequently, oxidation of $[Mn^{II}(dpaq^{5NO2})](OTf)$ was achieved by reacting this complex with iodosobenzene (PhIO). This approach was previously employed to generate the $[Mn^{III}(OH)(PY5)]^{2+}$ complex from its Mn^{II} precursor.[15] Following the addition of 0.5 equivalents PhIO to an CH_3CN solution of

$[Mn^{II}(dpaq^{5NO2})](OTf)$ at 25 °C, we observe the appearance of new optical signal at 550 and 770 nm, which are quite similar to those observed upon oxygenation of the other $[Mn^{II}(dpaq^{5R})](OTf)$ complexes (R = OMe and Cl; see Figure 5.2). Addition of water to the solution of $[Mn^{II}(dpaq^{5NO2})](OTf)$ after PhIO oxidation also leads to a sharpening and slight shifting of the electronic absorption bands to give features that resemble those of the other Mn^{III}-hydroxo species (Table 2). Overall the Mn^{III}-hydroxo complexes show only small shifts in the λ_{max} of the low energy transition of approximately 10 nm and very similar intensities for the 5-substituted complexes. This behavior differs significantly from the $\{MnNO\}^6$ $[Mn(NO)(dpaq^{5R})]^+$ complexes, where the R = NO_2 derivative showed significant shifts relative to the other derivatives in the electronic absorption features at wavelengths longer than 500 nm.

^{1}H NMR Characterization of the Mn^{III} Oxidation Products. Further insight into the products of the reactions of $[Mn^{II}(dpaq^{5Cl})](OTf)$ and $[Mn^{II}(dpaq^{5OMe})](OTf)$ with O_2, and of $[Mn^{II}(dpaq^{5NO2})](OTf)$ with PhIO, were obtained through ^{1}H NMR experiments. The ^{1}H-NMR samples were prepared by first oxidizing the $[Mn^{II}(dpaq^{5R})](OTf)$ complexes (with O_2 or PhIO) and then removing solvent under vacuum to obtain a solid residue. This residue was then dissolved in CD_3CN and analyzed by the ^{1}H NMR method. The resulting ^{1}H NMR spectra are shown in Figure 5.3. The previously reported ^{1}H NMR spectrum of $[Mn^{III}(OH)(dpaq)](OTf)$ dissolved in dried CD_3CN is included for comparison.[20] In that spectrum, we have marked peaks associated with the $[Mn^{III}(OH)(dpaq)]^+$ species with asterisks. The remaining peaks, which are observed in the diamagnetic region (0 to 30 ppm), were attributed to the spin-coupled $[Mn^{III}Mn^{III}(\mu\text{-}O)(dpaq)_2]^+$ species.

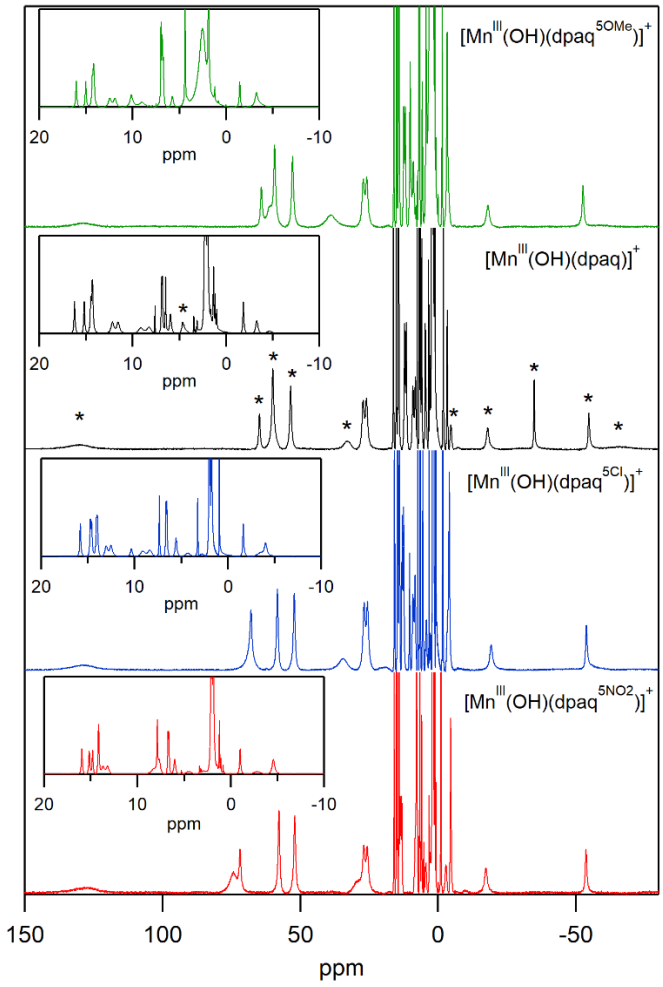

Figure 5.3. ^{1}H NMR spectra of 15 mM solutions of O_2 (for $[Mn^{II}(dpaq^{5OMe})](OTf)$ and $[Mn^{II}(dpaq^{5Cl})](OTf)$) or PhIO (for $[Mn^{III}(OH)(dpaq^{5NO2})](OTf)$) oxidation products of $[Mn^{II}(dpaq^{5R})](OTf)$ complexes dissolved in CD_3CN. The ^{1}H NMR spectrum of $[Mn^{III}(OH)(dpaq)](OTf)$ dissolved in CD_3CN is included for comparison (data taken from reference [20]). Asterisks indicate peaks previously assigned to the paramagnetic species, $[Mn^{III}(OH)(dpaq)]^+$.

Each of the oxidized $[Mn^{II}(dpaq^{5R})](OTf)$ complexes shows nine or ten hyperfine-shifted peaks with chemical shifts similar to those of $[Mn^{III}(OH)(dpaq)]^+$ (Figure 5.3). (We will discussion the variations in the chemical shifts of these hyperfine-shifted resonances among the Mn^{III}-hydroxo complexes in the next paragraph.) Each of these spectra also contains a large number of proton resonances in the diamagnetic region (Figure 3, insets). These signals disappear upon addition of

D_2O to these solutions (cf. Figure 5.3 and Figure 5.4), leaving just the hyperfine-shifted peaks (and solvent peaks). (For $[Mn^{III}(OH)(dpaq^{5NO2})]^+$, the added D_2O also gives rise to weak peaks associated with the $dpaq^{5NO2}$ free ligand. The observation of these peaks suggests some demetallation; however, the intensities of the signals associated with free ligand are so small as to preclude reliable peak integration. Therefore, we assume that the amount of free ligand in these samples is minor.) These observations reinforce our conclusion, based on electronic absorption spectroscopy, that oxidation of the $[Mn^{II}(dpaq^{5R})](OTf)$ complexes results in an equilibrium mixture of $[Mn^{III}(OH)(dpaq^{5R})]^+$ and $[Mn^{III}Mn^{III}(\mu\text{-}O)(dpaq^{5R})]^+$ species, with the Mn^{III}-hydroxo becoming the dominant species in solution upon the addition of water.

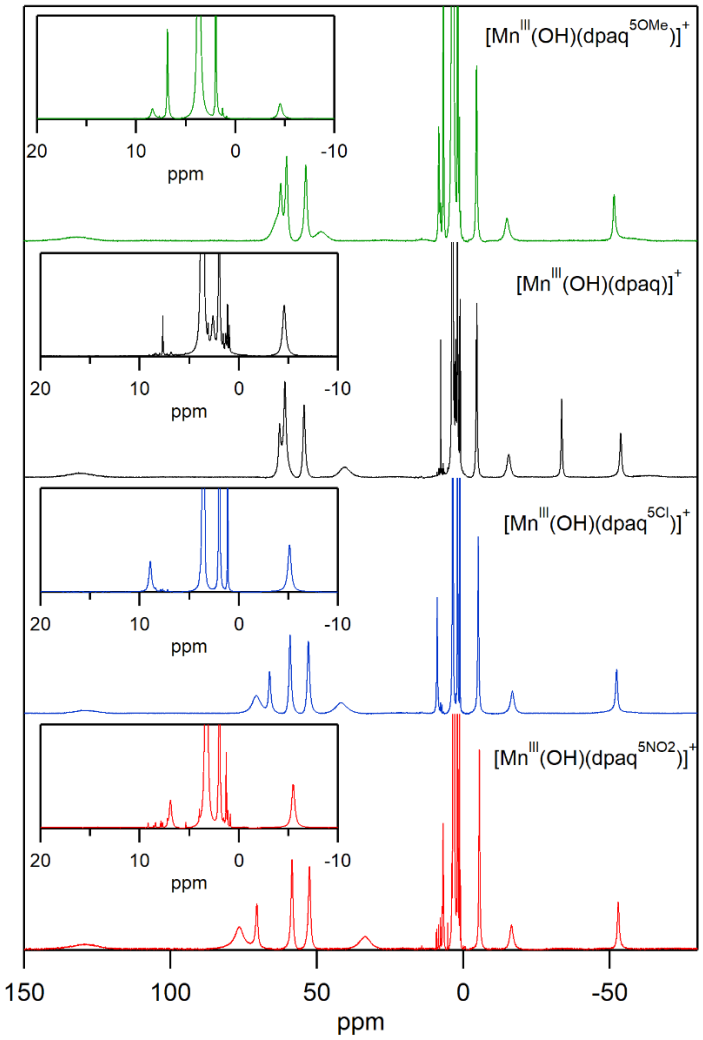

Figure 5.4. ^{1}H NMR spectra of 15 mM solutions of $[Mn^{III}(OH)(dpaq^{5OMe})]^+$, $[Mn^{III}(OH)(dpaq)]^+$, $[Mn^{III}(OH)(dpaq^{5Cl})]^+$, and $[Mn^{III}(OH)(dpaq^{5NO2})]^+$ in CD_3CN after addition of 880 equiv. D_2O.

Before discussing the variations in the ^{1}H NMR peak positions of the Mn^{III}-hydroxo species, we will first summarize the tentative assignments previously developed on the basis of peak integrations and T_1 relaxation times for $[Mn^{III}(OMe)(dpaq)]^+$.[20] The downfield resonances at 130, 60, and 54 ppm, as well as the slightly upfield resonance at -4 ppm, were attributed to the pyridine protons. We also proposed that the quinoline protons give rise to the four upfield resonances, at -16, -34, -54, and -65 ppm, as well as two downfield resonances, one at 62 ppm and the other a broad

feature partially obscured by the pyridine signals at 60 and 54 ppm. In the absence of 2D NMR to aid in assigning the resonances, the ^{1}H NMR spectra for the $[Mn^{III}(OH)(dpaq^{5R})]^+$ complexes can be used to assess these assignments.

A summary of the signals from the $[Mn^{III}(OH)(dpaq^{5R})]^+$ complexes are shown in Table 2. It is immediately obvious that the -34 ppm resonance observed for $[Mn^{III}(OH)(dpaq)]^+$ is not present in the spectra of any of the $[Mn^{III}(OH)(dpaq^{5R})]^+$ complexes (Figure 5.4). The disappearance of this peak confirms its initial assignment as a quinoline resonance, and further establishes this peak as arising from the 5-position of the quinoline. The resonance observed at -63 for $[Mn^{III}(OH)(dpaq)]^+$ is only observed for $[Mn^{III}(OH)(dpaq^{5OMe})]^+$ and $[Mn^{III}(OH)(dpaq^{5NO2})]^+$ (Figure A4.2). This weak, broad feature could be obscured in the $[Mn^{III}(OH)(dpaq^{5Cl})]^+$ spectrum by the feature at -52.4 or unable to be resolved from the baseline. ^{1}H NMR signals that were assigned as pyridine resonances (at 130, 60, 54, and -4 ppm) show only minor shifts (less than 3 ppm) for the $[Mn^{III}(OH)(dpaq^{5R})]^+$ complexes. Because the pyridine protons are far from the 5-quinolinyl substituent, it would be expected that their chemical shift values are only weakly dependent on the properties of this substituent.

In contrast, the 62 ppm resonance of $[Mn^{III}(OH)(dpaq)]^+$ shifts downfield for the $[Mn^{III}(OH)(dpaq^{5Cl})]^+$ and $[Mn^{III}(OH)(dpaq^{5NO2})]^+$ complexes by ca. 3.5 and 8 ppm, repsectively. The peak position of this resonance is largely unaffected in $[Mn^{III}(OH)(dpaq^{5OMe})]^+$ (Table 2), indicating a far greater sensitivity in the position of this resonance to the presence of electron-withdrawing groups. The broad resonance obscured between the 60 and 54 ppm pyridine signals for $[Mn^{III}(OH)(dpaq)]^+$ becomes readily apparent in the ^{1}H NMR spectra of $[Mn^{III}(OH)(dpaq^{5Cl})]^+$ and $[Mn^{III}(OH)(dpaq^{5NO2})]^+$, as this resonance shows a pronounced shift further downfield (to 70.6 and 76.5 ppm, respectively). The other broad resonance at 40.5 ppm in $[Mn^{III}(OH)(dpaq)]^+$ shows large

shifts downfield for $[Mn^{III}(OH)(dpaq^{5OMe})]^+$ (to 48.4) and shifts upfield for $[Mn^{III}(OH)(dpaq^{5Cl})]^+$ and $[Mn^{III}(OH)(dpaq^{5NO2})]^+$ (to 41.8 and 33.5 ppm, respectively). Figures showing the shifts of all resonances as a function of the Hammet σ_{para} parameter are in the Supporting Information (Figure A4.3). The chemical shift variations for several resonances, such as the resonance of $[Mn^{III}(OH)(dpaq)]^+$ at 130.5, 62, 40.5, and -4.6 ppm, show a linear correlation with the Hammet σ_{para} parameter. The other resonances show greater scatter but still demonstrate the general trend that an increase in the strength of the electron withdrawing group on the quinolinyl moiety causes an upfield shift for the resonances assigned to the pyridine ligand, and a shift away from the diamagnetic region for resonances assigned to the quinoline (Figure A4.3).

Table 5.2. ^{1}H NMR Chemical Shifts (ppm) for $[Mn^{III}(OH)(dpaq^{5R})]^+$ Complexes in CD_3CN with 880 equiv. D_2O.

	$[Mn^{III}(OH)(dpaq^{5R})]^+$			
tentative assignment	R = OMe	R = H	R = Cl	R = NO_2
H-py	131.9	130.5	129.5	129.0
H-qn			70.6	76.5
H-qn	62.3	62.7	66.1	70.5
H-py	60.3	60.9	59.1	58.4
H-py	53.7	54.3	52.9	52.5
	48.4	40.5	41.8	33.5
	8.3		8.9	6.8
	6.8			
H-py	-4.5	-4.6	-5.1	-5.5
H-qn	-15	-15.5	-16.8	-16.5
H-qn		-33.7		
H-qn	-51.6	-53.8	-52.4	-53.0
H-qn	-58	-63.4		-49

Following the assignments of pyridine and quinoline protons in Table 2, the hyperfine-shift pattern of the pyridine peaks of these Mn^{III}-hydroxo complexes leads to three downfield resonances

and one upfield resonance. This pattern is indicative of a predominant spin-delocalization mechanism, where the spin of a singly occupied orbital on the metal is delocalized over a ligand via a strongly interacting orbital and induces positive spin-density on the ligand.[36] This mechanism matches that reported for a series of $S = 1$ Fe^{IV}-oxo complexes with aminopyridyl ligands.[37] In that case, the effects of spin-delocalization were seen to drop off dramatically with increasing distance from the metal center, leading to polarization effects serving as the dominate spin propagation mechanism at the β′ position of the pyridines. Thus, in those systems, the α-, β-, and γ-pyridine protons appear downfield, while the β′-proton is upfield. (In our previous study, we had tentatively attributed the upfield-shifted pyridine resonance of $[Mn^{III}(OH)(dpaq)]^+$ to the γ-pyridine proton, which was based on analogy to ^1H NMR assignments for $S = 2$ Fe^{II} complexes with aminopyridyl ligands. A spin density analysis from DFT computations, see below, supports our initial assignment.) In contrast, the observation of three upfield and two downfield quinoline resonances for the $[Mn^{III}(OH)(dpaq^{5R})]^+$ complexes is in keeping with an alternating upfield-downfield pattern, indicative of spin polarization as the primary mechanism for spin propagation.[36] The spin-polarization mechanism places positive spin density on the C atoms at the 2, 4, 5 and 7 positions and negative spin density on the C atoms at the 3 and 6 positions. This C spin density will then induce oppositely-signed spin density on the bound protons, accounting for the upfield-downfield pattern observed in the ^1H NMR spectrum (Figure 5.4). These different spin propagation mechanisms for the pyridine and quinoline rings of the $[Mn^{III}(OH)(dpaq^{R})]^+$ complexes is similar to that reported for $[Fe^{IV}(O)(BnTPEN)]^+$, where different mechanisms were observed for pyridine rings depending on whether the ring was oriented perpendicular or parallel to the Fe=O vector.[37]

A DFT Mulliken spin density plot for $[Mn^{III}(OH)(dpaq^{5OMe})]^+$ nicely illustrates the different spin propagation mechanisms for the pyridine and quinoline rings (Figure 5.5). Spin polarization, with

alternating C atom spin density, is shown to propagate throughout the π system of the quinoline. From the Mulliken spin density, the protons at the 3 and 6 positions of the quinoline should be shifted downfield. In support, the chemical shift of the sharper quinoline resonance (at 62 ppm in $[Mn^{III}(OH)(dpaq)]^{+}$) shows a linear correlation with the Hammet σ_{para} parameter (Figure A4.3). Although the chemical shift of the broader downfield quinoline resonance (between 60 and 54 ppm for $[Mn^{III}(OH)(dpaq)]^{+}$) does not show the same degree of correlation, its position is still strongly modulated by functionalization at the 5-position. In contrast to the quinoline spin propagation mechanism, the spin density at the pyridine carbon atoms shows no such alternating positive-negative pattern (Figure 5). Instead, a delocalization mechanism, which places positive spin density on both the carbon and bound proton is observed, with the spin decreasing dramatically with distance from the metal center. Consequently, the γ-pyridine proton shows little spin-density (Figure 5).

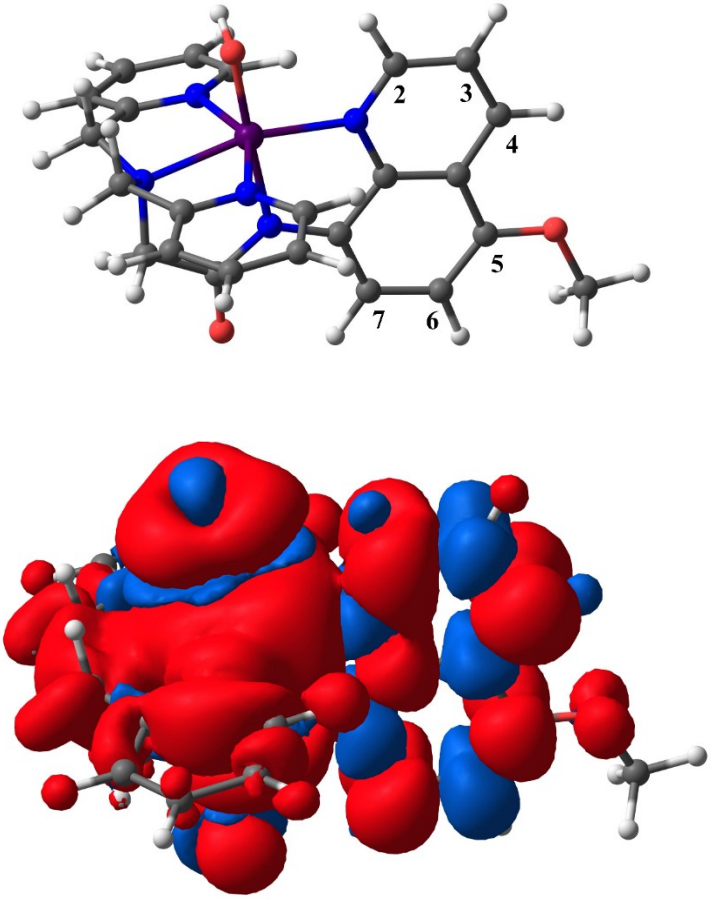

Figure 5.5. DFT optimized structure for $[Mn^{III}(OH)(dpaq^{5OMe})]^{+}$ with quinolinyl positions labeled (top). Visualization of the spin density for $[Mn^{III}(OH)(dpaq^{5OMe})]^{+}$ with an isovalue of 0.0001 (bottom). Red and blue denote positive and negative spin density, respectively.

Structural Properties of $[Mn^{III}Mn^{III}(\mu\text{-}O)(dpaq^{5NO2})](OTf)_2$, $[Mn^{III}Mn^{III}(\mu\text{-}O)(dpaq^{5Cl})](OTf)_2$, and $[Mn^{III}Mn^{III}(\mu\text{-}O)(dpaq^{5OMe})](OTf)_2$ from X-ray crystallography. On the basis of ^{1}H NMR and Mn K-edge X-ray absorption data, we had previously assigned the paramagnetic species observed in the ^{1}H NMR spectrum of $[Mn^{III}(OH)(dpaq)](OTf)$ dissolved in dried CH_3CN to the oxo-bridged $[Mn^{III}Mn^{III}(\mu\text{-}O)(dpaq)_2]^{2+}$ complex.[20] Here we have reported that, upon oxidation with O_2 or PhIO, the ^{1}H NMR spectra of the $[Mn^{II}(dpaq^{5Cl})](OTf)$,

$[Mn^{II}(dpaq^{5OMe})](OTf)$, and $[Mn^{II}(dpaq^{5NO2})](OTf)$ complexes also show resonances in the diamagnetic chemical shift region that can analogously be attributed to spin-coupled (μ-oxo)dimanganese(III,III) species (Figure 3). To provide further evidence for these assignments, we isolated and examined crystals obtained from the reactions of $[Mn^{II}(dpaq^{5Cl})](OTf)$ and $[Mn^{II}(dpaq^{5NO2})](OTf)$ with PhIO oxidation and the reaction of $[Mn^{II}(dpaq^{5OMe})](OTf)$ with O_2 in CH_3CN. (PhIO oxidation of $[Mn^{II}(dpaq^{5Cl})](OTf)$ and $[Mn^{II}(dpaq^{5OMe})](OTf)$ in CH_3CN leads to optical signals essentially identical to those observed for the corresponding O_2 oxidation reactions.) For $[Mn^{II}(dpaq^{5Cl})](OTf)$ and $[Mn^{II}(dpaq^{5NO2})](OTf)$, oxidation by 0.5 equivalents PhIO in CH_3CN, followed by vapor diffusion of Et_2O into this solution, procedure dark brown needles. XRD analysis of these crystals revealed them to contain the (μ-oxo)dimanganese(III,III) complexes $[Mn^{III}Mn^{III}(\mu\text{-}O)(dpaq^{5Cl})_2](OTf)_2$ and $[Mn^{III}Mn^{III}(\mu\text{-}O)(dpaq^{5NO2})_2](OTf)_2$ (Figure 6). Similarly, when $[Mn^{II}(dpaq^{5OMe})](OTf)$ was subjected to O_2 oxidation in CH_3CN, we were able to obtain dark brown crystals of $[Mn^{III}Mn^{III}(\mu\text{-}O)(dpaq^{5OMe})_2](OTf)_2$, the structure of which is shown in Figure 5.6. The metric parameters for these complexes, along with those predicted from previously-reported DFT computations for $[Mn^{III}Mn^{III}(\mu\text{-}O)(dpaq)_2]^{2+}$, are collected in Table 3.[20]

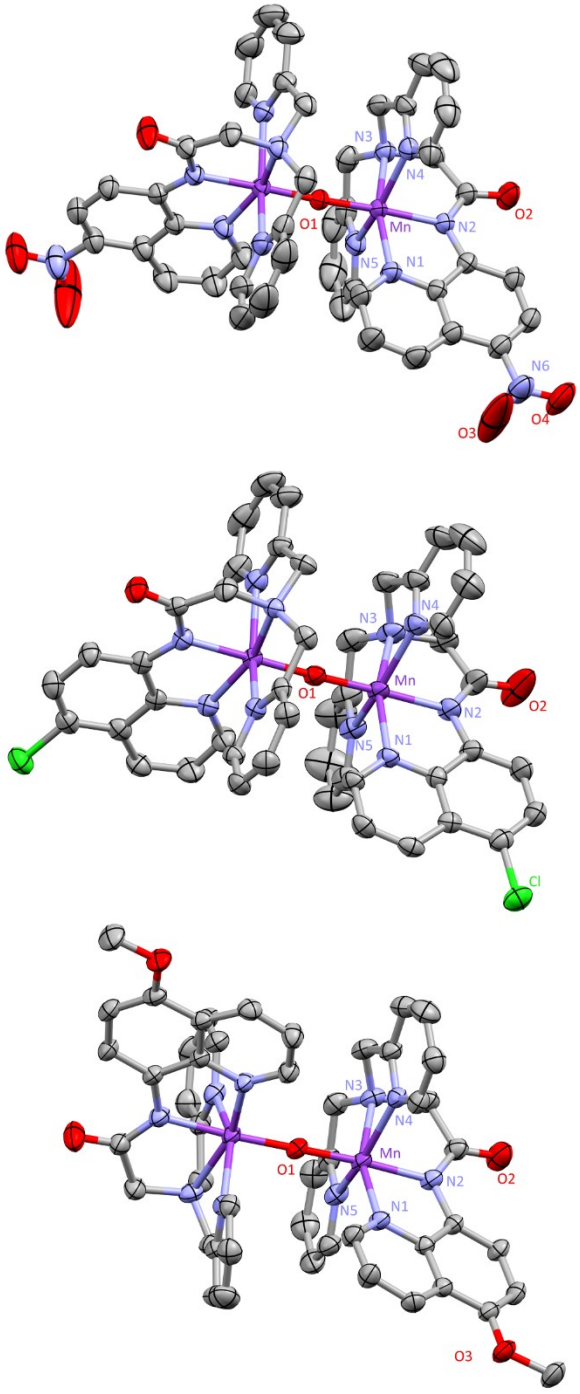

Figure 5.6. ORTEP diagrams of $[Mn^{III}Mn^{III}(\mu\text{-}O)(dpaq^{5NO2})_2](OTf)_2$ (top), $[Mn^{III}Mn^{III}(\mu\text{-}O)(dpaq^{5Cl})_2](OTf)_2$ (middle) and $[Mn^{III}Mn^{III}(\mu\text{-}O)(dpaq^{5OMe})_2](OTf)_2$ (bottom). Protons, solvent and triflate counter anions have been removed for clarity.

Table 5.3. Selected Manganese-Ligand Bond Lengths (Å), Manganese-Manganese Separation (Å), and Manganese-Oxo-Manganese Angle (°) from the Crystal Structures of $[Mn^{III}Mn^{III}(\mu\text{-}O)(dpaq^{5NO2})_2](OTf)_2$, $[Mn^{III}Mn^{III}(\mu\text{-}O)(dpaq^{5Cl})_2](OTf)_2$ and $[Mn^{III}Mn^{III}(\mu\text{-}O)(dpaq^{5OMe})_2](OTf)_2$ and the DFT Structure of $[Mn^{III}Mn^{III}(\mu\text{-}O)(dpaq)_2]^{2+}$.

	$[Mn^{III}Mn^{III}(\mu\text{-}O)(dpaq^{5R})_2](OTf)_2$			$[Mn^{III}Mn^{III}(\mu\text{-}O)(dpaq)_2]^{+a}$
	R = NO_2	R = Cl	R = OMe	DFT
Mn–O1	1.7918(4)	1.797(3)	1.7937(7)	1.81
		1.796(3)		
Mn–N1	2.054(2)	2.092(4)	2.069(4)	2.06
		2.090(4)		
Mn–N2	1.973(2)	1.985(4)	1.981(4)	1.98
		1.982(4)		
Mn–N3	2.199(2)	2.185(4)	2.194(4)	2.23
		2.183(4)		
Mn–N4	2.186(2)	2.221(4)	2.247(4)	2.35
		2.242(4)		
Mn–N5	2.288(3)	2.230(4)	2.217(4)	2.33
		2.260(5)		
Mn···Mn	3.5827(8)	3.5914(9)	3.5854(14)	3.64
Mn–O1–Mn	177.45(15)	177.6(2)	176.1(3)	179.16

[a] From reference [20].

For $[Mn^{III}Mn^{III}(\mu\text{-}O)(dpaq^{5NO2})_2](OTf)_2$ and $[Mn^{III}Mn^{III}(\mu\text{-}O)(dpaq^{5OMe})_2](OTf)_2$, the two Mn^{III} centers are equivalent. The two metal centers for $[Mn^{III}Mn^{III}(\mu\text{-}O)(dpaq^{5Cl})_2](OTf)_2$ are independent, but variations in metric parameters between the Mn^{III} centers are minor (Table 3). Each of the (μ-oxo)dimanganese(III,III) complexes displays Mn–O–Mn cores that are nearly linear (angles of 176 - 177°), with Mn–O bond lengths of 1.792 – 1.797 Å and a Mn···Mn separate just under 3.6 Å (Table 3). The Mn···Mn separations is in excellent agreement with that determined for

$[Mn^{III}Mn^{III}(\mu\text{-}O)(dpaq)_2]^{2+}$ from frozen solution EXAFS data (3.55 Å). In general, these metric parameters comparable favorably to a series of (μ-oxo)dimanganese(III,III) complexes supported by thiolate-containing N_4S^- ligands reported by Kovacs and co-workers.[17]

For the present series of complexes, the shortest Mn–N bond length in each complex comes from the amide nitrogen (N2). This Mn–N2 distances ranges from 1.973(2) Å for $[Mn^{III}Mn^{III}(\mu\text{-}O)(dpaq^{5NO2})_2](OTf)_2$ to 1.985(4) Å for $[Mn^{III}Mn^{III}(\mu\text{-}O)(dpaq^{5Cl})_2](OTf)_2$ (the Mn–N2 bond lengths for $[Mn^{III}Mn^{III}(\mu\text{-}O)(dpaq^{5Cl})_2](OTf)_2$ and $[Mn^{III}Mn^{III}(\mu\text{-}O)(dpaq^{5OMe})_2](OTf)_2$ are identical within experimental error; see Table 3). This minor variation in Mn–N(amide) bond length contrasts with observations of Hitomi *et al.* for the corresponding $[Mn(NO)(dpaq^{5R})]^+$ complexes, where the Mn–N(amide) distances showed a steady, and more pronounced, elongation in the order $[Mn(NO)(dpaq^{5OMe})]^+$ (1.923(7) Å) < $[Mn(NO)(dpaq^{5Cl})]^+$ (1.941(3) Å) > $[Mn(NO)(dpaq^{5NO2})]^+$ (1.957 Å).[21] This latter trend for the $\{MnNO\}^6$ series is accordant with that anticipated on the basis of the electron-donating and -withdrawing properties of the 5-quinolinyl substituents. However, the $[Mn(NO)(dpaq^{5R})]^+$ complexes also showed a large variation in Mn–NO distances inverse to that of the Mn–N(amide) bond lengths (from 1.742(8) Å for $[Mn(NO)(dpaq^{5OMe})]^+$ to 1.660(5) Å for $[Mn(NO)(dpaq^{5NO2})]^+$), which is evidence of a *trans* influence between the NO and amide donors. No such influence is apparent from the structures of the (μ-oxo)dimanganese(III,III) complexes, as the Mn–O distance hardly changes (Table 3). With regard to the remaining Mn–N distances from the quinolinyl, pyridyl, and amine ligands, these values all fall within the range of 2.054(2) – 2.288(3) Å, consistent with Mn–N distances observed for high-spin Mn^{III} centers. The experimental bond lengths of these complexes are all in reasonable agreement with that predicted for $[Mn^{III}Mn^{III}(\mu\text{-}$

O)(dpaq)$_2$]$^{2+}$ from DFT computations; although, in general, the DFT distances are slightly longer than their experimental counterparts (Table 3).

DFT Structures of the Mononuclear Mn^{III}-hydroxo Complexes. In the absence of crystal structures for the other monomeric [Mn^{III}(OH)(dpaq^{5R})]$^+$ complexes, DFT computations were employed to examine any structural variations within this series. The Mn-ligand bond lengths from DFT geometry optimized structures of these complexes are shown in Table 5. Overall there is little structural variation in the DFT-optimized structures, with all Mn-ligand distances changing by less than 0.02 Å. The largest change in bond-length is in the Mn–N(quinolinyl) distance (Mn–N1) where [Mn^{III}(OH)(dpaq^{5Cl})]$^+$ shows a bond ca. 0.02 Å shorter than those of the other complexes (Table 5). There is also a trend showing a minor decrease in the Mn–OH (Mn–O1) distance with the increasing electron-withdrawing ability of the 5R groups (Table 5). However, the predicted variation in Mn–OH distance of 0.006 Å would be difficult to detect by experimental means. Overall, the variations in Mn-ligand metric parameters for these DFT-optimized Mn^{III}-hydroxo complexes are quite minor, similar to that observed experimentally for the [Mn^{III}Mn^{III}(μ-O)(dpaq^{5R})$_2$](OTf)$_2$ complexes (Table 3).

Table 5.4. Selected Manganese–Ligand Bond Lengths (Å) from DFT Optimized Structures of $[Mn^{III}(OH)(dpaq^{5R})]^+$ Complexes.

	$[Mn^{III}(OH)(dpaq^{5R})]^+$			
	R = OMe	R = H	R = Cl	R = NO_2
Mn–O1	1.828	1.827	1.826	1.822
Mn–N1	2.083	2.083	2.067	2.086
Mn–N2	1.964	1.968	1.967	1.972
Mn–N3	2.221	2.224	2.221	2.221
Mn–N4	2.299	2.294	2.293	2.287
Mn–N5	2.279	2.277	2.275	2.271

Reduction Potentials of Mn^{III}-hydroxo Complexes. Cyclic voltammetry (CV) experiments were performed for each $[Mn^{III}(OH)(dpaq^{5R})]^+$ complex. In each case, irreversible reduction responses were observed that are attributed to the $Mn^{III/II}$ couple (Figure A4.4), and the peak potentials for these responses are collected in Table 1. The potentials become more positive in the order $[Mn^{III}(OH)(dpaq^{5OMe})]^+$ (-0.72 V) < $[Mn^{III}(OH)(dpaq)]^+$ (-0.70 V) < $[Mn^{III}(OH)(dpaq^{5Cl})]^+$ (-0.66 V) < $[Mn^{III}(OH)(dpaq^{2Me})]^+$ (-0.62 V) < $[Mn^{III}(OH)(dpaq^{5NO2})$ (-0.57 V) (Figure A4.4). The potential for $[Mn^{III}(OH)(dpaq)]^+$ and shows a minor decreases compared to previous reports,[18] which is attributed to the slight change in CH_3CN:H_2O ratio in the present and prior experiments. Among the $[Mn^{III}(OH)(dpaq^{5R})]^+$ series, the peak potentials show a linear correlation with the σ_{para} parameter for the 5-quinolinyl substituent (Figure 8), indicating that the variation in this substituent is responsible for the trend in reduction potentials. The difference in peak potentials between $[Mn^{III}(OH)(dpaq^{5OMe})]^+$ and $[Mn^{III}(OH)(dpaq^{5NO2})]^+$ is 150 mV, which is similar to the 140 mV difference in reduction potentials observed for the corresponding $[Mn(NO)(dpaq^{5R})]^+$ complexes.[22]

The previously reported trend between reduction potentials and σ_{para} parameter reported for the $[Mn(NO)(dpaq^{5R})]^+$ complexes is included in Figure 8 for comparison.[22]

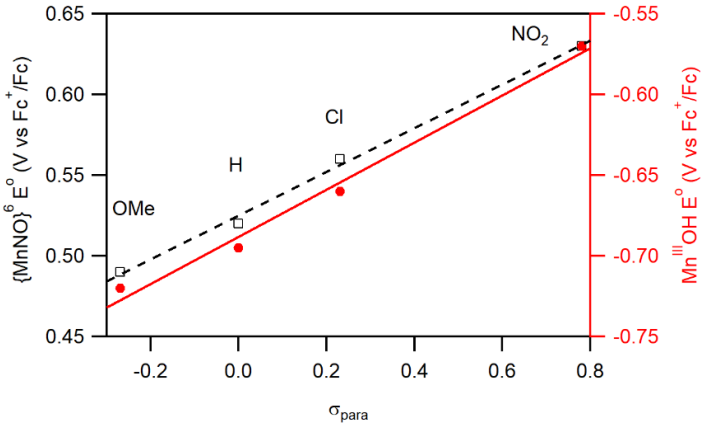

Figure 5.7. Hammet plot showing the correlation between the respective peak and reduction potentials of $[Mn^{III}(OH)(dpaq^{5R})]^+$ (red circles, right axis) and $[Mn(NO)(dpaq^{5R})]^+$ (black open squares, left axis) with the σ_{para} parameter for the 5-quinolinyl substituent. The reduction potentials for $[Mn(NO)(dpaq^{5R})]^+$ are from reference 21.

TEMPOH Oxidation by the Mn^{III}-hydroxo Complexes. The HAT reactivity of the $[Mn^{III}(OH)(dpaq^{5R})]^+$ (R = NO_2, Cl, and OMe) complexes was assessed using TEMPOH as a common substrate. These experiments were performed in a solvent mixture of 98:2 CH_3CN:H_2O, which ensures that the Mn^{III}-hydroxo species is dominant in solution. In these experiments, an excess of TEMPOH (10 – 40 equivalents) was added to the $[Mn^{III}(OH)(dpaq^{5R})]^+$ complex at -35 °C, which resulted in the disappearance of the characteristic optical bands of the Mn^{III}-hydroxo species (Figure 5.8). Under these conditions, each decay followed first order behavior to at least 5 half-lives, permitting the determination of pseudo-first order rate constants (k_{obs}). Second-order rate constants (k_2) for these reactions were obtained by fitting the increase in k_{obs} vs TEMPOH concentration to a linear function (Figure 5.9). The second-order rate constants obtained for TEMPOH oxidation by the $[Mn^{III}(OH)(dpaq^{5R})]^+$ (R = NO2, Cl, and OMe) complexes are collected in Table 6. We have also included values for $[Mn^{III}(OH)(dpaq)]^+$ and $[Mn^{III}(OH)(dpaq^{2Me})]^+$ in Table 6 for comparison. These

data show an increase in k_2 in the following order: $[Mn^{III}(OH)(dpaq^{5NO2})]^+$ > $[Mn^{III}(OH)(dpaq^{2Me})]+$ > $[Mn^{III}(OH)(dpaq^{5Cl})]+$ > $[Mn^{III}(OH)(dpaq)]+$ > $[Mn^{III}(OH)(dpaq^{5OMe})]+$. However, of this series, the range of k_2 values only spans a factor of ~9.

Table 5.5. Second-order Rate Constants (k_2) for TEMPOH Oxidation by Mn^{III}-hydroxo Complexes Supported by the $dpaq^R$ Ligands and Experimental and DFT-Calculated Thermodynamic Parameters.

	Experimental		DFT-Calculated		
Ligand	$E_{p,c}$ (V)[a]	TEMPOH k_2 ($M^{-1}s^{-1}$)	Mn^{III}/Mn^{II} $E_{1/2}$[b]	$Mn^{II}–OH_2$ pK_a	BDFE[c]
$dpaq^{5OMe}$	-0.72	0.8(1)	-0.66	19.5	66.3
dpaq	-0.7	1.1(1)[d]	-0.62	19.3	67.0
$dpaq^{5Cl}$	-0.66	2.8(2)	-0.56	18.8	67.7
$dpaq^{2Me}$	-0.62[e,f]	3.9(3)[e]	-0.52	18.7	68.5
$dpaq^{5NO2}$	-0.57	7(1)	-0.44	17.9	69.2

[a] vs. Fc^+/Fc. [b] Values based on the experimental PY5 Mn^{III}/Mn^{II} potential of 0.17 V vs Fc^+/Fc in MeCN. [c] in kcal mol^{-1}. [d] From ref. 20. [e] From ref. 19. [f] In MeCN:H_2O 94:6.

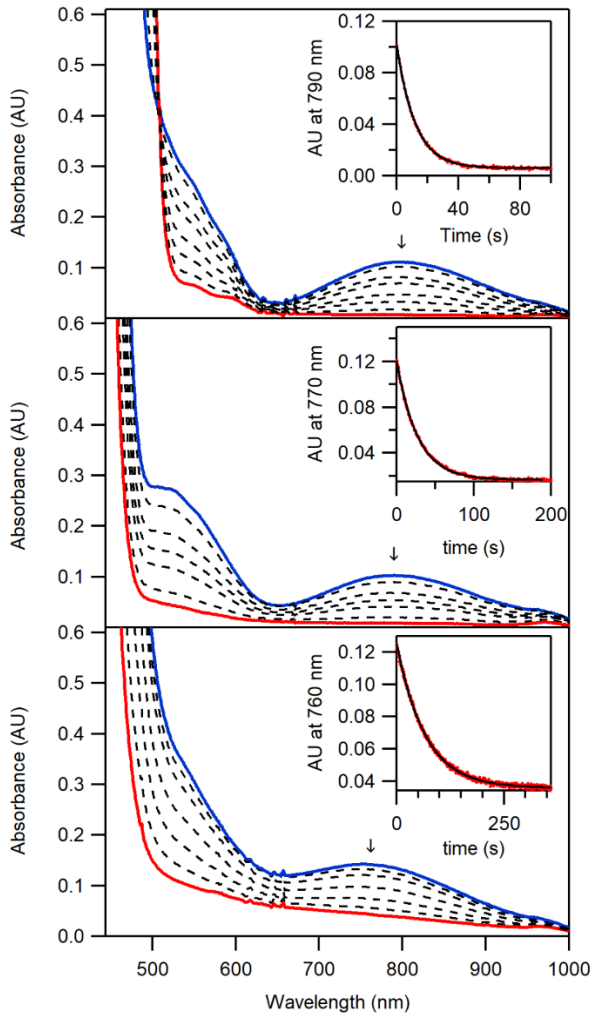

Figure 5.8. Electronic absorption spectra of 1.25 mM $[Mn^{III}(OH)(dpaq^{5NO2})]^+$ (top), $[Mn^{III}(OH)(dpaq^{5NCl})]^+$ (middle), and $[Mn^{III}(OH)(dpaq^{5OMe})]^+$ (bottom) upon the addition of 10 equiv TEMPOH at -35 °C in 98:2 MeCN:H_2O (vol:vol) solvent mixture (initial and final spectra are blue and red traces, respectively). The insets show the decay of the low-energy bands over time.

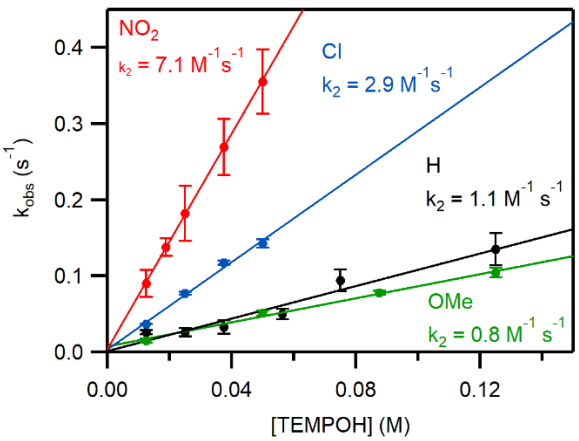

Figure 5.9. Pseudo-first-order rate constants, k_{obs} (s^{-1}), versus TEMPOH concentration for a 1.25 mM solutions of $[Mn^{III}(OH)(dpaq^{5R})]^+$ in CH_3CN in the presence of 440 equiv. H_2O. The second order rate constants were determined from the best-fit lines. Corresponding data for $[Mn^{III}(OH)(dpaq)]^+$ (from reference 20) are included for comparison.

Thermodynamic Driving Force and PCET Reactivity. Variations in PCET reactivity are often understood through the use of a free-energy relationship, where the rate is dependent on the reaction driving force.[1, 16] In the transfer of a hydrogen atom between TEMPOH and the Mn^{III}-hydroxo complexes described above, the reaction driving force is the difference in the bond-dissociation free energies (BDFE) of the $Mn^{II}O(H)$–H bond being formed and the TEMPO–H bond being broken. The BDFEs in these reactions can be further deconstructed into the stepwise addition/removal of a proton and an electron to/from the molecule of interest. This deconstruction is often represented as a square diagram (Scheme 5.1), where, in this instance, the vertical lines represent single electron transfers and horizontal lines represent single proton transfers. The diagonal line is the concerted hydrogen atom transfer.

Scheme 5.1. Thermodynamic scheme for PCET with a Mn^{III}–OH / Mn^{II}–OH_2 complex.

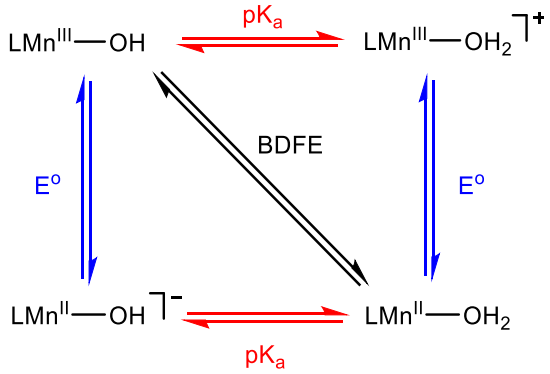

For our system, the BDFE (in kcal mol^{-1}) of the Mn^{II}–OH_2 product complex can be determined via the one-electron reduction of Mn^{III}–OH to Mn^{II}–OH and the protonation of Mn^{II}–OH to give Mn^{II}–OH_2 using the equation:

$$BDFE_{sol}(O–H) = 1.37pK_a + 23.06E° + C_{G,sol}$$

where $C_{G,sol}$ is a constant dependent on the solvent in which the reactions are performed.[16, 35] At present, we have been unable to determine experimental pK_a values for the $[Mn^{II}(OH_2)(dpaq^{5R})]^+$ complexes, so we cannot obtain experimental Mn^{II}-OH_2 BDFE values for use in a linear free energy plots. Nonetheless, a comparison of log(k_2) for TEMPOH oxidation by the $[Mn^{III}(OH)(dpaq^{5R})]^+$ complexes versus the experimental $Mn^{III/II}$ peak potentials for the Mn^{III}-hydroxo complexes reveals a linear correlation between these parameters, with a slope of 6.02 V (Figure 5.10). This correlation suggests that the rate variations for TEMPOH oxidation among this series are caused by the changes in $Mn^{III/II}$ potential induced by the electronic properties of the 5-substituents of the $dpaq^{5R}$ ligands. However, this dependence is weak, as the observed rates change by only a factor of 9 (Table 6). This weak dependence suggests that variations in Mn^{II}–OH_2 pK_a values oppose the contributions reflected in the $Mn^{III/II}$ peak potentials.

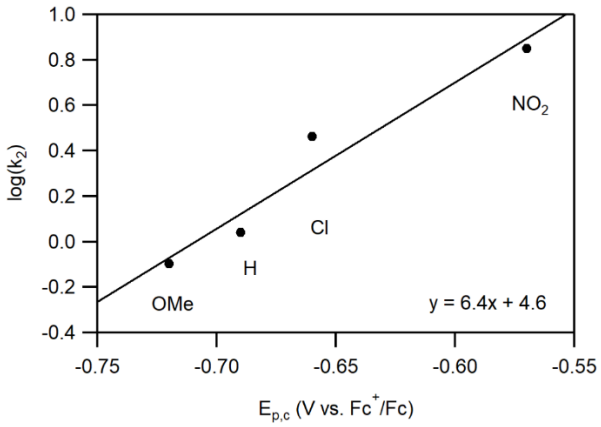

Figure 5.10. Comparison of second-order rate constants (as $\log(k_2)$) for the $[Mn^{III}(OH)(dpaq^{5R})]^+$ with $Mn^{III/II}$ peak potentials from CV measurements.

While we have been unable to obtain the experimental pK_a values necessary to validate this claim, we can estimate the pK_a values, and their influence on the Mn^{II}–OH_2 BDFE values, using DFT computations. The precise calculation of absolute pK_a values is still rather challenging, but here we have taken the approach suggested by Hammes-Schiffer and co-workers,[34] where the calculated pK_a values and redox potentials are referenced to a related complex, for which experimental values are known (we have chosen $[Mn^{II}(OH_2)(PY5)]^{2+}$ as a reference; pK_a = 13, $E_{1/2}$ = 0.17 vs Fc^+/Fc.).[15] These calculations benefit from the fact that the experimental conditions are already accounted for in the experimentally determined reference values. In addition, any intrinsic errors in the calculations should be comparable, and largely cancel, among this series of similar complexes.

The reduction potentials, pK_a and corresponding BDFE values determined by this approach are shown in Table 6. The values calculated for the reduction potential are $E_{1/2}$ rather than the $E_{p,c}$ values determined experimentally. This difference will cause some variability between the two approaches, but the intrinsic error associated with the calculated $E_{1/2}$ values is potentially larger than the expected difference between the experimental $E_{p,c}$ and $E_{1/2}$ values. The calculations predict a

potential range of 0.22 V between the extremes of $[Mn^{III}(OH)(dpaq^{5OMe})]^+$ and $[Mn^{III}(OH)(dpaq^{5NO2})]^+$, which is somewhat larger than the experimental range of 0.15 V. However, the relative ordering of the calculated $E_{1/2}$ values matches the $E_{p,c}$ ordering exactly (Table 6). Thus, the DFT method slightly overestimates the influence of the electron-donating and -withdrawing properties of the 5R groups of the $dpaq^{5R}$ ligands on the reduction potential, but the trend in potentials is perfectly reproduced. The calculated pK_a values fall into a narrow range of 19.5 – 17.9 units, with the $[Mn^{III}(OH)(dpaq^{OMe})]^+$ and $[Mn^{III}(OH)(dpaq^{5NO2})]^+$ having these respective extremes. It is notable that the complex with the most positive reduction potential ($[Mn^{III}(OH)(dpaq^{5NO2})]^+$), and thus the highest affinity for adding an electron, is also the complex which is the most acidic (*i.e.*, has the lowest propensity for adding a proton).

To illustrate the compensatory relationship between the $E_{1/2}$ and pK_a values and the electronic properties of the $dpaq^{5R}$ ligands, we have plotted the contributions from the DFT-derived $E_{1/2}$ and pK_a values to the total BDFE (in kcal mol^{-1}) as a function of the σ_{para} parameter of the 5-substituent of the $dpaq^{5R}$ ligand (Figure 12). This plot illustrates that an increase in σ_{para} causes the $E_{1/2}$ contribution to the BDFE to become less negative (*i.e.*, increases the magnitude of the Mn^{II}–OH_2 BDFE; Figure 12, black line). At the same time, the increase in σ_{para} causes a decrease in the pK_a contribution to the BDFE (Figure 12, red line). It is also evident from this plot that variations in the reduction potential as a function of σ_{para} more strongly modulate the overall BDFE than variations in the pK_a value. This effect is apparent from the magnitudes of the slopes in Figure 12, and gives rise to an overall increase in BDFE by the more electron-withdrawing $dpaq^{5R}$ groups (Table 6). The result is an overall change in Mn^{II}–OH_2 BDFE of 2.9 kcal mol^{-1} between $[Mn^{II}(OH_2)(dpaq^{5OMe})]^+$ and $[Mn^{II}(OH_2)(dpaq^{5NO2})]^+$ (Table 6). This net change is minor in part because of the opposing influences of changes in $E_{1/2}$ and pK_a. However, it is also important to note

that if one considers only the change in the experimental $E_{p,c}$, and assumes no counterbalance from the pK_a (an unrealistically optimal tuning), then the overall change in $Mn^{II}–OH_2$ BDFE between $[Mn^{III}(OH)(dpaq^{5OMe})]^+$ and $[Mn^{III}(OH)(dpaq^{5NO2})]^+$ only increases to 3.6 kcal mol^{-1}. Thus, while the pK_a reduces the effect of the change in $Mn^{III/II}$ reduction potential, the intrinsic contribution from the reduction potential on the $Mn^{II}–OH_2$ BDFE is small in the $[Mn^{III}(OH)(dpaq^{5R})]^+$ series.

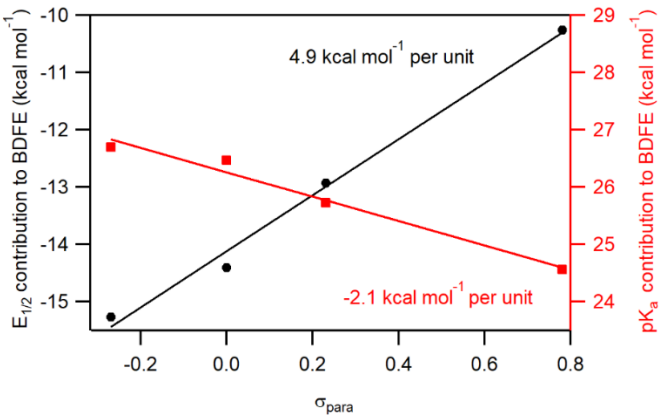

Figure 5.11. The $E_{1/2}$ (left axis) and pK_a (right axis) respective contributions to the Mn^{II}-aqua O–H BDFE in kcal mol^{-1} as determined by the Bordwell equation (eqn. 1). The slopes of the lines indicate the modulation to the BDFE as a function of the Hammett σ_{para} parameter.

It is illustrative to compare these present results for the $[Mn^{III}(OH)(dpaq^{5R})]^+$ series with those recently reported by Tolman and co-workers for a series of Cu^{III}-hydroxo complexes supported by ligands with varying electron donating ability.[38] In that series, the range of $Cu^{III/II}$ reduction potentials was almost 0.4 V, which resulted in a respective decrease in pK_a of 4 units. This opposite behavior for $E_{1/2}$ and pK_a creates a trend similar to the one seen here for the $[Mn^{III}(OH)(dpaq^{5R})]^+$ complexes (Figure 12). For the Cu^{III}-hydroxo complexes, it was also observed that the increase in reduction potential was greater than the decrease in pK_a, giving an overall increase in BDFE. Therefore, the rates of HAT reactions for the Cu^{III}-hydroxo complexes increased

as the reduction potential increased. In that study, this effect was shown using a plot of $E_{1/2}$ vs pK_a, which gave a slope of -0.94 V per pK_a unit. A slope of -0.59 V per pK_a unit is expected for perfect pK_a compensation of reduction potential change (*i.e.*, under perfect compensation a change in $E_{1/2}$ would be exactly balanced by a change in pK_a to give no net change in BDFE). Construction of a similar plot using the DFT-calculated pK_a values and experimental $E_{p,c}$ potentials for our Mn^{III}-hydroxo complexes gives a straight line with a slope of -0.92 V per pK_a unit (Figure 13). It should be noted that the pK_a range for our complexes is smaller than in the Cu^{III}-hydroxo system, which can give greater uncertainty in our slope from errors in the pK_a calculations. Nonetheless, the observation that potential versus pK_a plots for dissimilar Cu^{III}-hydroxo and Mn^{III}-hydroxo complexes should give such remarkably similar slopes is, to us, unexpected, and might be indicative of a general potential-pK_a compensation relationship.

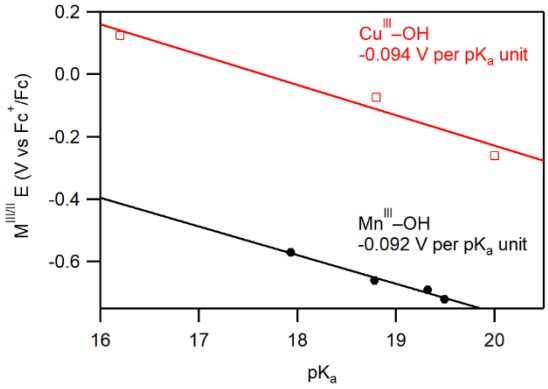

Figure 5.12. Plot of the $M^{III/II}$ potential as a function of pK_a for the $[Mn^{III}(OH)(dpaq^{5R})]^+$ system (black) and the Cu^{III}–OH system (from reference 38). Experimental $E_{p,c}$ vs DFT pK_a values are used for Mn^{III}–OH and the experimental $E_{1/2}$ and pK_a values are used for Cu^{III}–OH.

A final note of comparison for the present trends in reactivity of the $[Mn^{III}(OH)(dpaq^{5R})]^+$ complexes comes from a series of Mn^{III}–OR complexes of Kovacs and co-workers, which have the general formula $[Mn^{III}(OR)(S^{Me2}N4(tren))]^+$, with R = H, $^-$OMe, $^-$OPh, and $^-OC_6H_4{}^pNO_2$.[17] This variation in the function appended directly to the oxygen ligand led to tuning of the properties and

reactivity of these complexes. In this series, the $Mn^{III/II}$ potentials ranged from -0.6 to -0.22 V (vs Fc^+/Fc) for the Mn^{III}–OH and Mn^{III}–$O_6H_4{}^pNO_2$ complexes, respectively. Even though the Mn^{III}–$OC_6H_4{}^pNO_2$ complex showed a significantly more positive reduction potential, this complex was unable to oxidize TEMPOH. The corresponding Mn^{III}–OH complex, with the much lower potential, reacted with TEMPOH quite rapidly.[17] Although pK_a values could only be measured for the $[Mn^{II}(OH_2)(S^{Me2}N4(tren))]^+$ complex, it was proposed that the pK_a values of the $[Mn^{II}(OHR)(S^{Me2}N4(tren))]^+$ complexes (R = $^-$OMe, $^-$OPh, and $^-OC_6H_4{}^pNO_2$) must decrease substantially to overcome any increase in reduction potential. These observations provide an interesting contrast to the Mn^{III}-hydroxo and Cu^{III}-hydroxo series mentioned above, as they illustrate a case where shifts in the pK_a are apparently dominant over shifts in the reduction potential. Whether this change in pK_a and $E_{1/2}$ compensation is a general trend for metal-OR species is unclear at present.

Conclusions

In order to probe the effects of electronic perturbations on the HAT reactions of mononuclear Mn^{III}-hydroxo complexes, we prepared a series of complexes substituted with electron-donating and -withdrawing groups at the 5-position of the quinoline moiety of the $dpaq^{5R}$ ligand. For each system, O_2 or PhIO oxidation of the $[Mn^{II}(dpaq^{5R})](OTf)$ complex resulted in an equilibrium mixture of mononuclear Mn^{III}-hydroxo and spin-coupled dinuclear species in MeCN solution. This mixture, which was confirmed by both ^{1}H NMR and electronic absorption methods, could be converted to give a majority of the Mn^{III}-hydroxo species upon the addition of water. XRD experiments provide confirmation that the spin-coupled species observed by ^{1}H NMR spectroscopy is the $[Mn^{III}Mn^{III}(\mu\text{-}O)(dpaq^{5R})_2]^{2+}$ complex. Kinetic experiments for the oxidation of TEMPOH by the Mn^{III}-hydroxo

complexes revealed only slight (ca. 9-fold) variation in second-order rate constants, showing only a modest increase in reactivity between $[Mn^{III}(OH)(dpaq^{5OMe})]^+$ and $[Mn^{III}(OH)(dpaq^{5NO2})]^+$, which showed the extreme rates in this series. This small change in reactivity can be understood through thermodynamic parameters obtained through experimental measurements of the $1e^-$ reduction of Mn^{III}-hydroxo adducts, as well as theoretically calculated $E_{1/2}$ and pK_a values. From this analysis it was seen that changes in $E_{1/2}$ are compensated, albeit incompletely, by opposing changes in pK_a values. These competing effects give rise to only a small increase in the BDFE of the Mn^{II}-aqua products as a function of changes in the $dpaq^{5R}$ ligands, which is in agreement with the small variations in the second-order rate constants for TEMPOH oxidation.

Acknowledgements

This work was supported by NSF grant 1565661 to T.A.J. Support for the NMR instrumentation was provided by NIH Shared Instrumentation Grant S10OD016360.

References.

1. Mayer, J. M., Understanding Hydrogen Atom Transfer: From Bond Strengths to Marcus Theory. *Accounts of Chemical Research* **2011,** *44* (1), 36-46.
2. Pirovano, P.; McDonald, A. R., Synthetic High-Valent M-O-X Oxidants: Synthetic High-Valent M-O-X Oxidants. *European Journal of Inorganic Chemistry* **2018**.
3. Wennman, A.; Oliw, E. H.; Karkehabadi, S.; Chen, Y., Crystal Structure of Manganese Lipoxygenase of the Rice Blast Fungus Magnaporthe oryzae. *J Biol Chem* **2016,** *291* (15), 8130-9.
4. Wennman, A.; Karkehabadi, S.; Oliw, E. H., Kinetic investigation of the rate-limiting step of manganese- and iron-lipoxygenases. *Archives of Biochemistry and Biophysics* **2014,** *555–556*, 9-15.
5. Su, C.; Sahlin, M.; Oliw, E. H., Kinetics of Manganese Lipoxygenase with a Catalytic Mononuclear Redox Center. *Journal of Biological Chemistry* **2000,** *275* (25), 18830-18835.
6. Su, C.; Oliw, E. H., Manganese Lipoxygenase: PURIFICATION AND CHARACTERIZATION. *Journal of Biological Chemistry* **1998,** *273* (21), 13072-13079.

7. Glickman, M. H.; Klinman, J. P., Lipoxygenase Reaction Mechanism: Demonstration That Hydrogen Abstraction from Substrate Precedes Dioxygen Binding during Catalytic Turnover. *Biochemistry* **1996,** *35* (39), 12882-12892.
8. Pavlosky, M. A.; Solomon, E. I., Near-IR CD/MCD Spectral Elucidation of Two Forms of the Non-Heme Active Site in Native Ferrous Soybean Lipoxygenase-1: Correlation to Crystal Structures and Reactivity. *Journal of the American Chemical Society* **1994,** *116* (25), 11610-11611.
9. Boyington, J.; Gaffney, B.; Amzel, L., The three-dimensional structure of an arachidonic acid 15-lipoxygenase. *Science* **1993,** *260* (5113), 1482-1486.
10. Porter, T. R.; Mayer, J. M., Radical reactivity of the Fe(iii)/(ii) tetramesitylporphyrin couple: hydrogen atom transfer, oxyl radical dissociation, and catalytic disproportionation of a hydroxylamine. *Chem. Sci.* **2014,** *5* (1), 372-380.
11. Gao, H.; Groves, J. T., Fast Hydrogen Atom Abstraction by a Hydroxo Iron(III) Porphyrazine. *Journal of the American Chemical Society* **2017,** *139* (11), 3938-3941.
12. Ching, W.-M.; Zhou, A.; Klein, J. E. M. N.; Fan, R.; Knizia, G.; Cramer, C. J.; Guo, Y.; Que, L., Characterization of the Fleeting Hydroxoiron(III) Complex of the Pentadentate TMC-py Ligand. *Inorganic Chemistry* **2017,** *56* (18), 11129-11140.
13. Goldsmith, C. R.; Stack, T. D. P., Hydrogen Atom Abstraction by a Mononuclear Ferric Hydroxide Complex: Insights into the Reactivity of Lipoxygenase. *Inorganic Chemistry* **2006,** *45* (15), 6048-6055.
14. Gupta, R.; Borovik, A. S., Monomeric Mn ^{III/II} and Fe ^{III/II} Complexes with Terminal Hydroxo and Oxo Ligands: Probing Reactivity via O−H Bond Dissociation Energies. *Journal of the American Chemical Society* **2003,** *125* (43), 13234-13242.
15. Goldsmith, C. R.; Cole, A. P.; Stack, T. D. P., C−H Activation by a Mononuclear Manganese(III) Hydroxide Complex: Synthesis and Characterization of a Manganese-Lipoxygenase Mimic? *Journal of the American Chemical Society* **2005,** *127* (27), 9904-9912.
16. Warren, J. J.; Tronic, T. A.; Mayer, J. M., Thermochemistry of Proton-Coupled Electron Transfer Reagents and its Implications. *Chemical Reviews* **2010,** *110* (12), 6961-7001.
17. Coggins, M. K.; Brines, L. M.; Kovacs, J. A., Synthesis and structural characterization of a series of Mn(III)OR complexes, including a water-soluble Mn(III)OH that promotes aerobic hydrogen-atom transfer. *Inorg Chem* **2013,** *52* (21), 12383-93.
18. Wijeratne, G. B.; Corzine, B.; Day, V. W.; Jackson, T. A., Saturation Kinetics in Phenolic O–H Bond Oxidation by a Mononuclear Mn(III)–OH Complex Derived from Dioxygen. *Inorg. Chem.* **2014,** *53* (14), 7622-7634.
19. Rice, D. B.; Wijeratne, G. B.; Burr, A. D.; Parham, J. D.; Day, V. W.; Jackson, T. A., Steric and Electronic Influence on Proton-Coupled Electron-Transfer Reactivity of a Mononuclear Mn(III)-Hydroxo Complex. *Inorg Chem* **2016,** *55* (16), 8110-20.
20. Rice, D. B.; Jones, S. D.; Douglas, J. T.; Jackson, T. A., NMR Studies of a Mn(III)-hydroxo Adduct Reveal an Equilibrium between Mn(III)-hydroxo and mu-Oxodimanganese(III,III) Species. *Inorg Chem* **2018,** *57* (13), 7825-7837.
21. Hitomi, Y.; Iwamoto, Y.; Kodera, M., Electronic tuning of nitric oxide release from manganese nitrosyl complexes by visible light irradiation: enhancement of nitric oxide release efficiency by the nitro-substituted quinoline ligand. *Dalton Transactions* **2014,** *43* (5), 2161-2167.

22. Hitomi, Y.; Arakawa, K.; Kodera, M., Electronic Tuning of Iron-Oxo-Mediated C□H Activation: Effect of Electron-Donating Ligand on Selectivity. *Chemistry - A European Journal* **2013,** *19* (43), 14697-14701.
23. Riedel, P. J.; Arulsamy, N.; Mehn, M. P., Facile Routes to Manganese(II) Triflate Complexes. *Inorganic chemistry communications* **2011,** *14* (5), 734-737.
24. Mader, E. A.; Davidson, E. R.; Mayer, J. M., Large Ground-State Entropy Changes for Hydrogen Atom Transfer Reactions of Iron Complexes. *Journal of the American Chemical Society* **2007,** *129* (16), 5153-5166.
25. *Data Collection: SMART Software in APEX2 v2014.11-0 Suite. Bruker-AXS, 5465 E. Cheryl Parkway, Madison, WI 53711-5373 USA.* .
26. *Data Reduction: SAINT Software in APEX2 v2014.11-0 Suite. Bruker-AXS, 5465 E. Cheryl Parkway, Madison, WI 53711-5373 USA.* .
27. *Refinement: SHELXTL Software in APEX2 v2014.11-0 Suite. Bruker-AXS, 5465 E. Cheryl Parkway, Madison, WI 53711-5373 USA.*
28. Neese, F., Software update: the ORCA program system, version 4.0. *Wiley Interdisciplinary Reviews: Computational Molecular Science* **2018,** *8* (1), e1327.
29. Becke, A. D., Density-functional Thermochemistry. III. The Role of Exact Exchange. *J. Chem. Phys.* **1993,** *98* (7), 5648-5652.
30. Lee, C.; Yang, W.; Parr, R. G., Development of the Colle-Salvetti Correlation-energy Formula into a Functional of the Electron Density. *Phys. Rev. B* **1988,** *37* (2), 785-789.
31. Weigend, F., Accurate Coulomb-fitting basis sets for H to Rn. *Physical Chemistry Chemical Physics* **2006,** *8* (9), 1057-1065.
32. Weigend, F.; Ahlrichs, R., Balanced basis sets of split valence, triple zeta valence and quadruple zeta valence quality for H to Rn: Design and assessment of accuracy. *Physical Chemistry Chemical Physics* **2005,** *7* (18), 3297-3305.
33. Marenich, A. V.; Cramer, C. J.; Truhlar, D. G., Universal Solvation Model Based on Solute Electron Density and on a Continuum Model of the Solvent Defined by the Bulk Dielectric Constant and Atomic Surface Tensions. *The Journal of Physical Chemistry B* **2009,** *113* (18), 6378-6396.
34. Solis, B. H.; Hammes-Schiffer, S., Proton-Coupled Electron Transfer in Molecular Electrocatalysis: Theoretical Methods and Design Principles. *Inorganic Chemistry* **2014,** *53* (13), 6427-6443.
35. Bordwell, F. G.; Cheng, J.; Ji, G. Z.; Satish, A. V.; Zhang, X., Bond dissociation energies in DMSO related to the gas phase values. *Journal of the American Chemical Society* **1991,** *113* (26), 9790-9795.
36. Novotny, J.; Sojka, M.; Komorovsky, S.; Necas, M.; Marek, R., Interpreting the Paramagnetic NMR Spectra of Potential Ru(III) Metallodrugs: Synergy between Experiment and Relativistic DFT Calculations. *J Am Chem Soc* **2016,** *138* (27), 8432-45.
37. Klinker, E. J.; Kaizer, J.; Brennessel, W. W.; Woodrum, N. L.; Cramer, C. J.; Que, L., Structures of Nonheme Oxoiron(IV) Complexes from X-ray Crystallography, NMR Spectroscopy, and DFT Calculations. *Angewandte Chemie International Edition* **2005,** *44* (24), 3690-3694.
38. Dhar, D.; Yee, G. M.; Spaeth, A. D.; Boyce, D. W.; Zhang, H.; Dereli, B.; Cramer, C. J.; Tolman, W. B., Perturbing the Copper(III)-Hydroxide Unit through Ligand Structural Variation. *J Am Chem Soc* **2016,** *138* (1), 356-68.

Chapter 6

Enhancement of the Proton-Coupled Electron Transfer Reactivity of a Mn^{III}-hydroxo Complex via Scandium Triflate

6.1 Introduction

Mononuclear manganese-hydroxo adducts have been proposed to be vital intermediates in manganese-dependent enzymes such as manganese lipoxygenase (MnLOX).[1-4] In this enzyme, a Mn^{III}–OH is proposed to perform a PCET reaction with polyunsaturated fatty acids to initiate substrate dioxygenation. One way of further understanding the reactivity of complicated biological systems comes through the use of model complexes. With such complexes, small perturbations can be made to the ligand and their effects on structure and reactivity more easily characterized. A current challenge with Mn^{III}–OH model complexes lies in the inability to oxidize C–H bonds near strengths seen in MnLOX. The only Mn^{III}–OH complexes with reported C–H activation are $[Mn^{III}(OH)(PY5)]^{2+}$ from Goldsmith and $[Mn^{III}(OH)(dpaq^{2R})]^{+}$ (R = H, Me) from our group.[5-6] The $[Mn^{III}(OH)(PY5)]^{2+}$ complex is capable of reacting with substrates such as toluene (BDE = 88 kcal mol^{-1}, k_{2corr} = 2.2 x 10^{-3}) while $[Mn^{III}(OH)(dpaq^{2R})]^{+}$ is shown only capable of abstracting from the weak C–H bond of xanthene (BDE = 75 kcal mol^{-1}, k_{obs} = ~8 x 10^{-4} s^{-1}).

We have recently synthesized a series of complexes that modify the reactivity of $[Mn^{III}(OH)(dpaq)]^{+}$ (**1**) through a series of substitutions at the 5-position of the quinoline, but the modifications only provide limited enhancement of PCET reactivity. Another avenue for modulating reactivity has been shown for iron[7-9] and high-valent manganese[10-15] oxidants through the use of redox-inactive Lewis acids. The use of Lewis acids is of interest not only for their ability to significantly alter reactivity, but also to aid in understanding the role that the Ca^{2+} center has in photosystem II. It is known that Ca^{2+} is required for enzyme activity, and, in one proposed mechanism, the O–O bond formation step proceeds through a nucleophilic attack from a Ca-bound water or hydroxide.[16-17]

In this work, the redox-inactive Lewis acid, $Sc(OTf)_3$, is added to $[Mn^{III}(OH)(dpaq)]^+$ (**1**) in order to evaluate the effects on structure and reactivity. Two intermediates can be formed, with one being formed in dry MeCN (intermediate **2**) and the other in MeCN in the presence of H_2O (intermediate **3**). UV-Vis absorption, NMR, X-ray absorption (XAS) and kinetic studies are performed to probe changes in reactivity and to begin to understand what role the Lewis acid plays in modulating properties of the Mn^{III}–OH unit.

6.2 Experimental

Formation of Intermediates. A 1.25 mM solution of **1** was prepared in an argon-filled glovebox in 2 mL of MeCN, placed in a gastight cuvette and sealed with a septum. A solution of 2 equiv. $Sc(OTf)_3$ was prepared in 100 μL MeCN and stored in a gas-tight syringe. For formation of intermediate **2**, the solution was brought out of the glovebox and the $Sc(OTf)_3$ solution was added at 25 °C. For formation of intermediate **3**, a 100 μL, aliquot of a 90:10 (v/v) CH_3CN:H_2O solution, which had been sparged with N_2 gas, was added to the cuvette first followed by the addition of the $Sc(OTf)_3$ solution at 25 °C.

Kinetic Studies of $[Mn^{III}(OH)(dpaq](OTf)•Sc(OTf)_3$. For kinetic experiments, **3** was generated as described above, with the exception that the solution was first heated to 50 °C in a Unisoku crystat interfaced with an Agilent 8453 spectrophotometer. The $Sc(OTf)_3$ solution was then added to the cuvette, and **3** was allowed to form maximally as determined by following the absorbance at 700 nm. Substrate was added at maximal formation, and the reaction was monitored by disappearance of the signal at 700 nm. Pseudo first-order rates collected at different equivalents of substrate were used to determine a second-order rate constant.

Acquisition of ^{1}H NMR Data. 2.5 mM solutions of **2** were prepared in MeCN-d_3 and the addition of 20 μL D_2O followed by 2 equiv. $Sc(OTf)_3$ dissolved in MeCN-d_3. 2.5 mM solutions of **3** were

prepared in MeCN-d_3 and the addition of 20 μL D_2O followed by 2 equiv. $Sc(OTf)_3$ dissolved in MeCN-d_3. Samples were collected on a 400 MHz Bruker AVIIIHD NMR with an acquisition time of 0.27 s and a D1 of 0 s with a spectral width of 150 to -100 ppm. At least 1000 scans were collected to provide sufficient S/N. Spectra were baseline-subtracted with the multipoint fitting procedure using spline functions as available in MestReNova.

XAS Experiments for $[Mn^{III}(OH)(dpaq)](OTf)•Sc(OTf)_3$. A frozen solution sample of **3** was generated by preparing a 2.5 mM solution of **1** and adding 20 μL H_2O and 2 equiv. $Sc(OTf)_3$ and the resulting solution was monitored by UV-Vis. Once **3** was maximally formed, the solution was transferred to an XAS sample cup and rapidly frozen in liquid nitrogen. The Mn K-edge XAS data were collected over an energy range of 6400–7250 eV. A manganese foil was used as a reference and internal calibration was performed by assigning the edge energy of the foil to 6539.0 eV. Spectra were obtained via fluorescence excitation at beamline 9-3 at Stanford Synchrotron Radiation Lightsource (SSRL) at 7 K using a Si(220) monochromator and a 100-element Ge array detector.

EXAFS data analysis was performed using the *DEMETER* software package and fitting was carried out in *ARTEMIS* on the $k_3\chi(k)$ data.[18] *FEFF6*[19] was used to generate the phase and amplitude functions from the crystal structure of $[Mn^{III}(OH)(dpaq)](OTf)$. For the fits, the parameters R (average scattering pathway distance) and σ^2 (Debye-Waller factor) were optimized individually, and the E_0 parameters was a common variable for all paths. The *n* (degeneracy) parameter was fixed for each fit and varied between fits.

6.3 Results

Formation of Intermediates 2 and 3. Addition of $Sc(OTf)_3$ to **1** in dry MeCN at 25°C leads to the formation of a new species (**2**) over several hours, which has UV-Vis bands at 500 and 595 nm and a broad band at 925 nm as shown in Figure 6.1 (left). The formation of **2** is rapidly accelerated at

50°C, showing maximal formation after approximately 1000 seconds. Adding the same equivalents of $Sc(OTf)_3$ to **1** in a $MeCN/H_2O$ solution at 25°C shows a change in the UV-Vis absorption spectra over the course of several hours leading to a new species (**3**) as shown in Figure 6.1. **3** shows a significant shift in absorption features, showing a near-IR (NIR) band at ca. 1150 nm and a higher energy peak at 700 nm. Due to the slow formation of **3** at room temperature, the intermediate was also formed at 50°C, where the reaction reaches a maximum at approximately 1500 seconds. This significantly enhanced rate of formation facilitated the kinetic studies below.

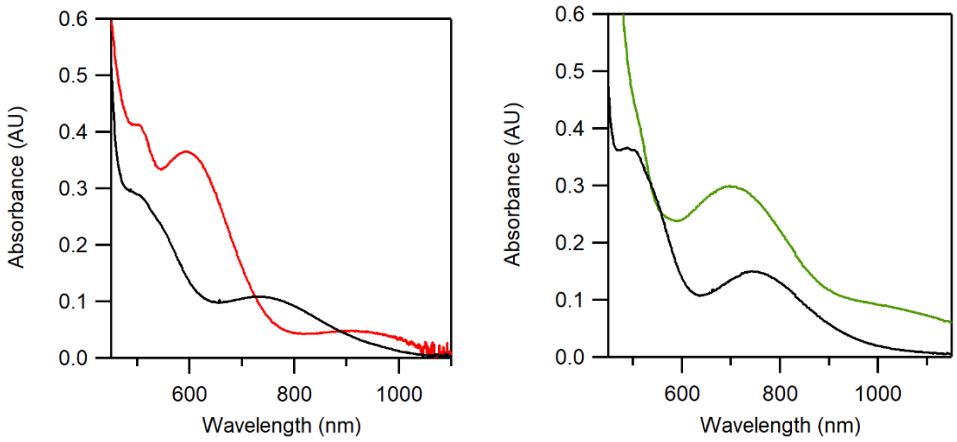

Figure 6.1. Electronic absorption spectrum of 2 mM $[Mn^{III}(OH)(dpaq)]^+$ in 2 mL CH_3CN (left) and $CH_3CN:H_2O$ 99:1 (right) before (black trace) and after the addition of 2 equiv. of $Sc(OTf)_3$ (red and green trace) at room temperature.

^{1}H NMR Characterization of 2 and 3. The ^{1}H NMR samples were prepared at room temperature as above but using deuterated solvents. The ^{1}H spectrum for **2** appears significantly changed from the spectra of **1** (Figure 6.2). A majority of the peaks of the paramagnetic species span a similar spectral window but have a significant difference in peak shape. There are now six or seven small, sharper peaks shifted downfield beyond 20 ppm and at least three peaks shifted upfield beyond -40

ppm. The resonance near 130 ppm **1** is either unresolved in **2**, or present as one of the sharper peaks less downfield-shifted.

In contrast, the ^{1}H NMR spectra for **3** shows many similarities to that of **1**, including similar lineshapes (Figure 6.2). All resonances see some degree of shifting, but there are a similar number of features in both spectra, showing that the symmetry of the molecule is not altered. This type of Sc^{3+} interaction with **1** would preclude significant interaction with the pyridine rings of the ligand, as that would split the pyridine resonances into non-degenerate environments. There are significant shifts in the upfield-shifted peaks associated with the quinoline. The sharp peak at -33 ppm is shifted and could potentially be one of the two furthest upfield peaks. Efforts are currently underway to provide further characterization of these peaks in NMR so as to better understand the differences present in **3**.

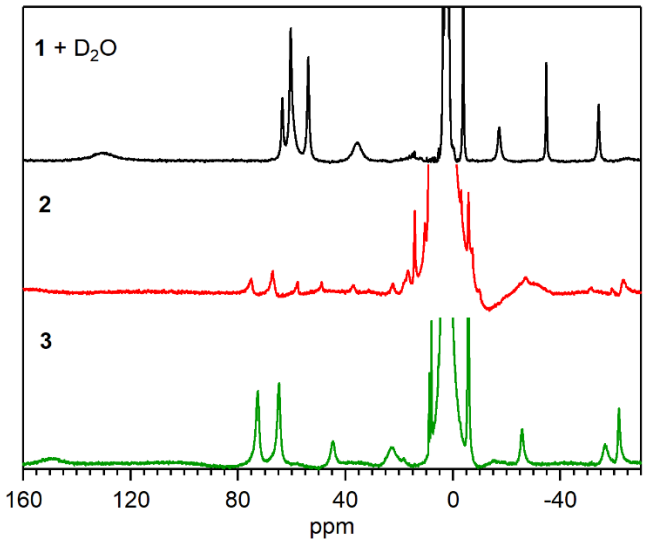

Figure 6.2. ^{1}H NMR spectra of 2 mM **1** dissolved in MeCN:H_2O 98:2 (top) and **3** dissolved in MeCN:H_2O 99:1 (bottom).

X-ray Absorption Spectroscopy of 3. The X-ray absorption near-edge spectra (XANES) for $[Mn^{II}(dpaq)]^{+}$, **1**, and **3** are shown in Figure 6.3. The K-edge energy serves as a probe for the

oxidation state of the Mn center and shifts of 1 eV or more to higher energy are indicative of an increase in oxidation state. Here, the edge energy is defined as the inflection point of the rising edge and is identified by the second derivative of the spectra. **3** has an identical edge energy to **1**, indicating that the oxidation state is likely unchanged upon addition of Sc^{3+}. The rest of the XANES region including the pre-edge and immediate post-edge also show little perturbation from **1**.

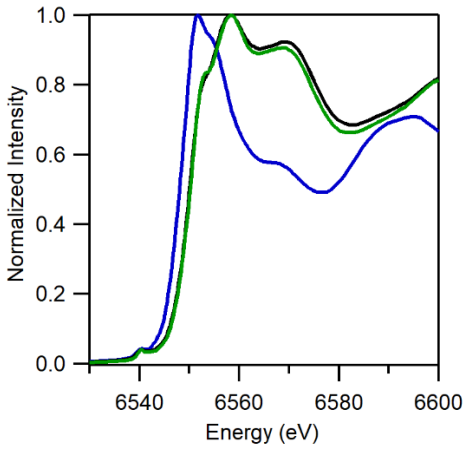

Figure 6.3. Normalized X-ray absorption spectra for $[Mn^{II}(dpaq)]^+$ (blue), **1** (black), and **3** (green) near the Mn K-edge. Data for $[Mn^{II}(dpaq)]^+$ and **1** are from ref [20].

Structural Characterization from EXAFS. Parameters obtained from fits of the $k^3\chi(k)$ data are shown in Table 6.1. The best fit, as determined by the reduced χ^2 is bolded and italicized. In this fit, the manganese is coordinated by a nearby O/N shell with a degeneracy of 2 and an average distance of R = 1.92 Å. There is a second, further coordination shell of N scatterers with a degeneracy of 4 and an average distance of R = 2.18 Å. It is also necessary to include a distant C scattering shell arising from nearby ligand carbons with an average pathlength of 2.94 Å. The parameters from this fit of 3 suggest that the coordination environment has not changed significantly from 1 upon the addition of Sc^{3+} (Table 6.2). The average distance of the nearest O/N shell has increased by 0.05 Å and the N shell increased by 0.04 Å. In a μ-oxoiron(III) scandium(III) complex, the Que group observed from a large peak in the Fourier transform beyond 3 Å the O-bound Sc^{3+} ion.[7] The lack of

such a prominent feature in the Fourier transform of 3 beyond 3 Å would suggest that the Sc^{3+} is not bound directly to the Mn-hydroxo adduct. It is important to note that there is an alternative fit that shows a similar goodness-of-fit as above if evaluated by the R-factor (Table 6.1, italicized). This fit differs from the one above by separating the O into its own shell at R = 1.85 Å. The N atoms are then split into two separate shells of n = 2 and n = 3 at 2.014 and 2.18 Å, respectively. This fit, however, has one σ^2 value that is exceptionally low, and the R-factor is shown to only be improved due to the inclusion of additional degrees of freedom. Thus, a better comparison between these fits comes from the reduced χ^2, which accounts of the degrees of freedom in the analysis. As such the original fit mentioned above (Table 6.1, bolded and italicized) is deemed the most reliable fit.

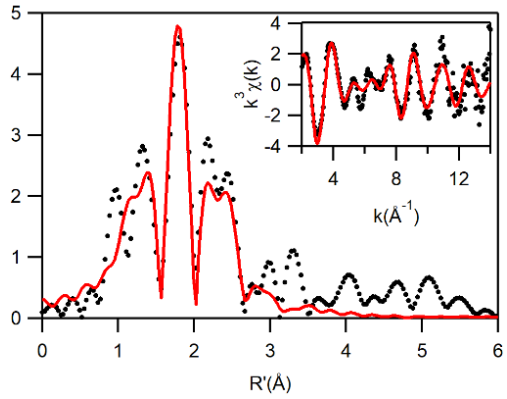

Figure 6.4. Fourier transform of Mn K-edge EXAFS data and raw EXAFS curve (inset) for **3** with experimental (dotted lines) and fit (solid lines). Parameters for the fit are bolded and italicized in Table 6.1.

Table 6.1. EXAFS Fitting Parameters for **3**

Mn—O			Mn—N			Mn—N			Mn···C				
n	R (Å)	σ^{2a}	*n*	R (Å)	σ^{2a}	*n*	R (Å)	σ^{2a}	*n*	R (Å)	σ^{2a}	R-factor	$\chi^2_{red}{}^b$
			6	2.26	22.50							0.607	8.9
1	1.90	2.43	5	2.19	9.22							0.365	6.5
1	1.86	0.80	2	2.02	1.90	3	2.22	1.61				0.325	7.2
1	2.17	-0.43	5	2.01	21.14				6	2.94	9.70	0.255	5.6
1	*1.85*	*0.95*	*2*	*2.014*	*2.1*	*3*	*2.18*	*1.91*	*6*	*2.93*	*10.5*	*0.191*	*5.7*
2	***1.92***	***6.32***	***4***	***2.18***	***5.87***				***6***	***2.94***	***4.84***	***0.216***	***4.8***

[a] Value x10^3. [b] Value x10^{-6}

Table 6.2. Comparison of the parameters derived from the best EXAFS fits for **1** and **3**.

Complex	Path	*n*	R(Å)	σ^2 x 10^3
1[a]	O/N	2	1.87	4.81
	N	4	2.14	5.21
	C	6	2.91	8.89
3	O/N	2	1.92	6.32
	N	4	2.18	5.87
	C	6	2.94	4.84

[a] values from ref [20]

C-H Oxidation by 3. While **1** and its derivatives are capable of abstracting a H-atom from substrates with weak O-H bonds, such as TEMPOH, they have not been shown competent oxidants for substrates with C–H bonds of moderate strength. **2** shows moderate reactivity with substrate oxidation, but the rate of this reaction follows neither clean pseudo-first order nor second order decay, and so further discussion of kinetics will focus on **3**. Upon addition of excess (> 10 equiv.) 9,10-dihydroanthracene (DHA, BDFE = 76 kcal mol^{-1})[21] to **3**, a pseudo-first order decay of the optical signals is observed (Figure 6.5, left). The k_{obs} of this process can be plotted as a function of DHA concentration, and a corrected second-order rate constant of 0.16 $M^{-1}s^{-1}$ is obtained. **1** is unable to react with DHA, and the only Mn^{III}–OH complex that is currently reported to react with this substrate is $[Mn^{III}(OH)(PY5)]^{2+}$, which had a corrected k_2 = 0.0055 $M^{-1}s^{-1}$.[22] The 30-fold faster

rate of **3** demonstrates the ability of a redox inactive Lewis acid to greatly increase the reactivity of the complex and allows for reactions with substrates of bond strengths that were previously inaccessible. To further probe the reactivity, **3** was reacted with a substrate with a stronger C–H, ethylbenzene (BDFE = 87 kcal mol^{-1})[21] at 50 °C. A corrected second-order rate constant of 0.043 $M^{-1}s^{-1}$ was measured and shows a weak dependence on the C–H bond strength. A KIE has not currently been obtained with **3**, as the reaction with deuterated DHA proceeds at a rate slow enough such that it is unable to be separated from a secondary decay process. While this is only weak evidence of the presence of a KIE, evaluation of a true KIE could be done with substrates of weaker C–H bonds or with significantly larger concentrations of DHA, if soluble.

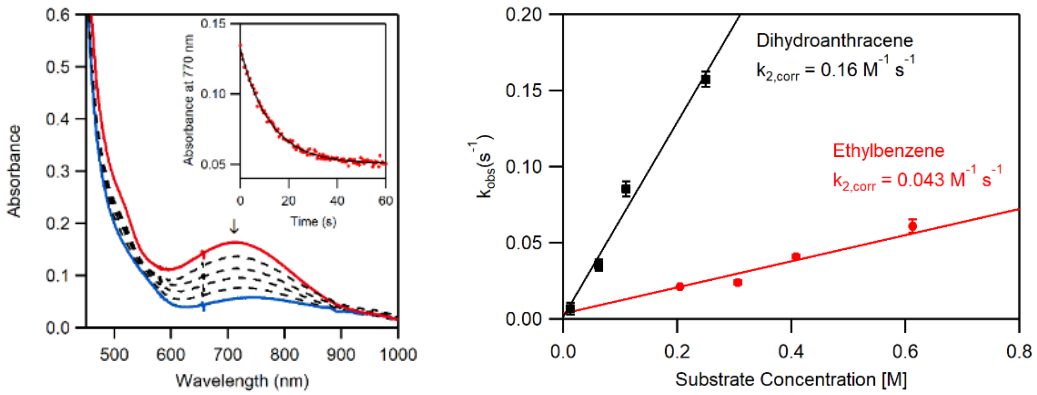

Figure 6.5. (Left) Electronic absorption spectrum of 1.25 mM **3** in 2 mL of CH_3CN before (red trace) and after (blue trace) the addition of 100 equivalents of DHA. Inset shows the decay of 700 nm as a function of time. (Right) Plot of k_{obs} as a function of substrate concentration for DHA (black) and ethylbenzene (red).

6.4 Discussion

Structure of 3. Combining the information from XAS, UV-Vis, and ^{1}H NMR methods, some comments can be made about the structure of **3**. The ^{1}H NMR, as mentioned above, provides insight into the symmetry of **3**. Maintaining the same symmetry would require an interaction either

the hydroxo moiety that could rotate in solution or the oxygen of the amide trans to the hydroxo. Binding to either location would likely result in greater elongation of the axial bonds, which is supported by the EXAFS parameters. However, the EXAFS data display a lack of a signature metal-metal scatterer peak in the Fourier transform which suggests that the Sc^{3+} is not binding to the hydroxide. However, this does not provide definitive support that the Sc^{3+} is binding to the amide O. Finally, the appearance of the NIR band for **3** tentatively supports the binding of the Sc^{3+} to the amide through a simple ligand-field analysis. Weakening the strength of the interaction of the manganese with the axial ligands greater than the equatorial ligands would result in a greater reduction in the Mn $3d_{z2}$ energy relative to the Mn $3d_{x2-y2}$ energy. This would lower the energy of the d-d transition that was originally at 770 nm in **1**.

Alternative Structure of 3. There is also an alternative proposal to consider due to the presence of significant H_2O in solution. The addition of $Sc(OTf)_3$ could result in the formation of $[Sc(OH_2)]^{3+}$ which has a pK_a of approximately 4.3.[23] This aqua complex could protonate the Mn^{III}–OH which will have an increased basicity due to negatively charged trans-amide ligand. This structure is consistent with the analysis above, as protonation of the hydroxo would not change the symmetry of the complex. The EXAFS would also not show any scattering contributions from the additional proton, but the proton would elongate the Mn–O bond. There has been a recently reported crystal structure of the $[Mn^{III}(OH_2)](dpaq)]^+$ complex. The metric parameters from the structure would give an O/N shell at 1.93 Å and a N shell at 2.16 Å which agree very well with the parameters derived from the EXAFS fit.[24] The oxidation state of the metal center would also not change. Finally, this elongated bond would still cause a decrease in the d-d transition energy, which is potentially seen in NIR. The addition of Bronsted acids of similar or greater pK_a to the Sc-aqua could help in determination of such a structure.

Reactivity Enhancement. The addition of $Sc(OTf)_3$ to **1** in the presence of H_2O allows for activation of previously unobtainable bond strengths. This new reactivity likely arises from an increase in the $Mn^{III/II}$ couple, which will create a more favorable electron transfer. There should be a corresponding increase in acidity, but we have observed in our derivatives of **1** that an increase in the reduction potential can outweigh a corresponding decrease in pK_a. The two possible structures and their likely products are shown in Scheme 6.1.

Scheme 6.1. Potential structures for **3** and predicted products for **3** and its reaction with C–H bonds.

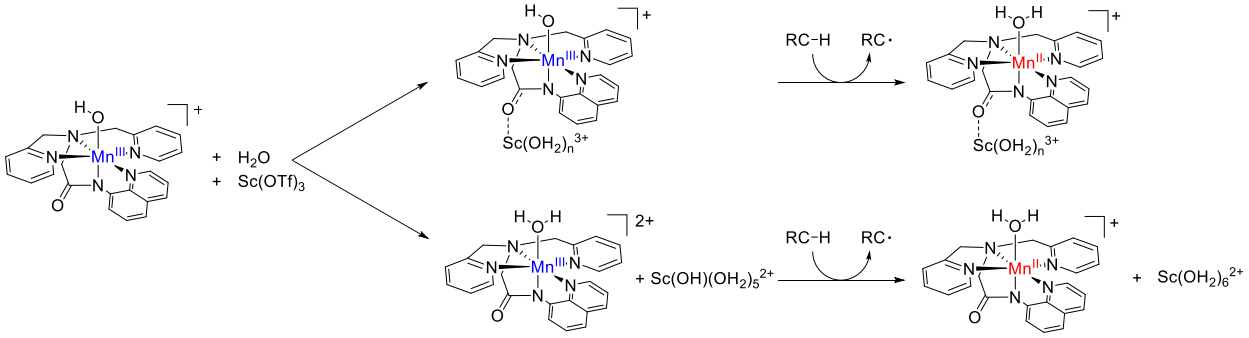

The top pathway is more straightforward and involves a hydrogen atom transfer directly to the Mn^{III}–OH moiety that would generate a Mn^{II}–OH_2 with a Sc^{3+} either still bound to the complex, or it could dissociate. The bottom pathway involves an electron transfer to the Mn^{III}–OH_2 and a proton transfer either directly to complex, generating a hydronium that would later reprotonate the $Sc(OH)(OH_2)_5^{2+}$ or directly to the $Sc(OH)(OH_2)^{2+}$. Such multisite PCET reactions have been observed before, however in one such study it was proposed that their reaction included a hydrogen-bonded substrate-base precursor that had simultaneous proton transfer and outer-sphere electron transfer.[25] Such a precursor complex is unlikely with a C–H bond, and so the most likely explanation is direct transfer to the Mn^{III}–OH_2 moiety based on the tentative KIE. Whichever

intermediate is formed through the addition of $Sc(OTf)_3$, it is apparent that the reactivity of the complex has been greatly enhanced.

Conclusion

The addition of $Sc(OTf)_3$ to **1** allows for the formation of two different intermediates depending on the presence or absence of H_2O in MeCN. **2**, which is formed in the absence of H_2O, shows significantly perturbed NMR spectra from **1** and complicated kinetics with substrate oxidation. **3**, which is formed in the presence of H_2O shows similar NMR to **1** and clean reaction kinetics are able to be monitored. Characterization suggests that complex still contains a Mn(III) center and that there are only minor structural perturbations. Further studies are needed to fully characterize the intermediate, but despite these small structural changes, **3** is capable of abstracting H-atoms from substrates with C–H BDFE of at least 87 kcal mol^{-1}.

References

1. Su, C.; Sahlin, M.; Oliw, E. H., Kinetics of Manganese Lipoxygenase with a Catalytic Mononuclear Redox Center. *Journal of Biological Chemistry* **2000,** *275* (25), 18830-18835.
2. Su, C.; Oliw, E. H., Manganese Lipoxygenase: PURIFICATION AND CHARACTERIZATION. *Journal of Biological Chemistry* **1998,** *273* (21), 13072-13079.
3. Wennman, A.; Oliw, E. H.; Karkehabadi, S.; Chen, Y., Crystal Structure of Manganese Lipoxygenase of the Rice Blast Fungus Magnaporthe oryzae. *J Biol Chem* **2016,** *291* (15), 8130-9.
4. Wennman, A.; Karkehabadi, S.; Oliw, E. H., Kinetic investigation of the rate-limiting step of manganese- and iron-lipoxygenases. *Archives of Biochemistry and Biophysics* **2014,** *555–556*, 9-15.
5. Wijeratne, G. B.; Corzine, B.; Day, V. W.; Jackson, T. A., Saturation kinetics in phenolic O-H bond oxidation by a mononuclear Mn(III)-OH complex derived from dioxygen. *Inorg Chem* **2014,** *53* (14), 7622-34.
6. Rice, D. B.; Wijeratne, G. B.; Burr, A. D.; Parham, J. D.; Day, V. W.; Jackson, T. A., Steric and Electronic Influence on Proton-Coupled Electron-Transfer Reactivity of a Mononuclear Mn(III)-Hydroxo Complex. *Inorg Chem* **2016,** *55* (16), 8110-20.
7. Prakash, J.; Rohde, G. T.; Meier, K. K.; Jasniewski, A. J.; Van Heuvelen, K. M.; Münck, E.; Que, L., Spectroscopic Identification of an FeIII Center, not FeIV, in the Crystalline Sc–O–Fe Adduct Derived from [FeIV(O)(TMC)]2+. *Journal of the American Chemical Society* **2015,** *137* (10), 3478-3481.
8. Fukuzumi, S.; Morimoto, Y.; Kotani, H.; Naumov, P.; Lee, Y.-M.; Nam, W., Crystal structure of a metal ion-bound oxoiron(IV) complex and implications for biological electron transfer. *Nat Chem* **2010,** *2* (9), 756-759.

9. Park, J.; Morimoto, Y.; Lee, Y. M.; Nam, W.; Fukuzumi, S., Unified view of oxidative C-H bond cleavage and sulfoxidation by a nonheme iron(IV)-oxo complex via Lewis acid-promoted electron transfer. *Inorg Chem* **2014,** *53* (7), 3618-28.
10. Miller, C. G.; Gordon-Wylie, S. W.; Horwitz, C. P.; Strazisar, S. A.; Peraino, D. K.; Clark, G. R.; Weintraub, S. T.; Collins, T. J., A Method for Driving O-Atom Transfer: Secondary Ion Binding to a Tetraamide Macrocyclic Ligand. *Journal of the American Chemical Society* **1998,** *120*, 11540-11541.
11. Baglia, R. A.; Dürr, M.; Ivanović-Burmazović, I.; Goldberg, D. P., Activation of a High-Valent Manganese–Oxo Complex by a Nonmetallic Lewis Acid. *Inorganic Chemistry* **2014,** *53* (12), 5893-5895.
12. Leeladee, P.; Baglia, R. A.; Prokop, K. A.; Latifi, R.; de Visser, S. P.; Goldberg, D. P., Valence Tautomerism in a High-Valent Manganese–Oxo Porphyrinoid Complex Induced by a Lewis Acid. *Journal of the American Chemical Society* **2012,** *134* (25), 10397-10400.
13. Zhang, Z.; Coats, K. L.; Chen, Z.; Hubin, T. J.; Yin, G., Influence of Calcium(II) and Chloride on the Oxidative Reactivity of a Manganese(II) Complex of a Cross-Bridged Cyclen Ligand. *Inorganic Chemistry* **2014,** *53* (22), 11937-11947.
14. Yoon, H.; Lee, Y.-M.; Wu, X.; Cho, K.-B.; Sarangi, R.; Nam, W.; Fukuzumi, S., Enhanced Electron-Transfer Reactivity of Nonheme Manganese(IV)–Oxo Complexes by Binding Scandium Ions. *Journal of the American Chemical Society* **2013,** *135* (24), 9186-9194.
15. Chen, J.; Lee, Y.-M.; Davis, K. M.; Wu, X.; Seo, M. S.; Cho, K.-B.; Yoon, H.; Park, Y. J.; Fukuzumi, S.; Pushkar, Y. N.; Nam, W., A Mononuclear Non-Heme Manganese(IV)–Oxo Complex Binding Redox-Inactive Metal Ions. *Journal of the American Chemical Society* **2013,** *135* (17), 6388-6391.
16. Yano, J.; Yachandra, V., Mn4Ca Cluster in Photosynthesis: Where and How Water is Oxidized to Dioxygen. *Chemical Reviews* **2014,** *114* (8), 4175-4205.
17. Cox, N.; Pantazis, D. A.; Neese, F.; Lubitz, W., Biological water oxidation. *Acc Chem Res* **2013,** *46* (7), 1588-96.
18. Ravel, B.; Newville, M., ATHENA, ARTEMIS, HEPHAESTUS: data analysis for X-ray absorption spectroscopy using IFEFFIT. *Journal of Synchrotron Radiation* **2005,** *12* (4), 537-541.
19. Rehr, J. J.; Mustre de Leon, J.; Zabinsky, S. I.; Albers, R. C., Theoretical x-ray absorption fine structure standards. *Journal of the American Chemical Society* **1991,** *113* (14), 5135-5140.
20. Rice, D. B.; Wijeratne, G. B.; Jackson, T. A., Mn K-edge X-ray absorption studies of mononuclear Mn(III)-hydroxo complexes. *J Biol Inorg Chem* **2017,** *22* (8), 1281-1293.
21. Warren, J. J.; Tronic, T. A.; Mayer, J. M., Thermochemistry of Proton-Coupled Electron Transfer Reagents and its Implications. *Chemical Reviews* **2010,** *110* (12), 6961-7001.
22. Goldsmith, C. R.; Cole, A. P.; Stack, T. D., C-H activation by a mononuclear manganese(III) hydroxide complex: synthesis and characterization of a manganese-lipoxygenase mimic? *J Am Chem Soc* **2005,** *127* (27), 9904-12.
23. Gilson, R.; Durrant, M. C., Estimation of the pKa values of water ligands in transition metal complexes using density functional theory with polarized continuum model solvent corrections. *Dalton Transactions* **2009,** (46), 10223-10230.
24. Sankaralingam, M.; Lee, Y. M.; Karmalkar, D. G.; Nam, W.; Fukuzumi, S., A Mononuclear Non-heme Manganese(III)-Aqua Complex as a New Active Oxidant in Hydrogen Atom Transfer Reactions. *J Am Chem Soc* **2018,** *140* (40), 12695-12699.
25. Morris, W. D.; Mayer, J. M., Separating Proton and Electron Transfer Effects in Three-Component Concerted Proton-Coupled Electron Transfer Reactions. *J Am Chem Soc* **2017,** *139* (30), 10312-10319.

Chapter 7

Theoretical Investigation into the Multistate Reactivity of C–H Activation by a Mn^{IV}–oxo complex

7.1 Introduction

High-valent metal-oxo species are often invoked as intermediates in hydrogen-atom-transfer (HAT) processes in both biological and synthetic systems.[1-15] Fe^{IV}-oxo species in particular have been shown to be highly reactive in the abstraction of hydrogen atoms from unactivated of C–H bonds, leading to hydroxylation, halogenation or desaturation. The investigation of Fe^{IV}-oxo systems has led to a wealth of kinetic, spectroscopic and theoretical investigations into the reaction pathways of these intermediates. Density functional theory (DFT) calculations have highlighted the possible role of multistate reactivity for HAT reactions of synthetic Fe^{IV}-oxo systems. In most synthetic complexes, the Fe^{IV}-oxo begins in a triplet (S = 1) ground state. It has been proposed that during the course of the HAT reaction, a low-lying quintet state (S = 2) becomes accessible that offers a lower activation barrier (Scheme 7.1, top). The multistate reactivity of Fe^{IV}-oxo complexes provides an explanation for many of the observed reactivity trends, including the generally enhanced reactivity of Fe^{IV}-oxo adducts with low-lying S = 2 excited states or S = 2 ground states. Additionally, these mechanistic models of HAT reactivity for Fe^{IV}-oxo centers has led to the recent synthesis and reactivity studies of a complex cleverly designed to avoid the multistate reactivity in order to probe characteristics of the reactivity of an individual state.

In contrast to their Fe^{IV}-oxo counterparts, there has been considerably less focus on their reactivity Mn^{IV}-oxo complexes. This is due in part to the fact that many Mn^{IV}-oxo complexes display sluggish or limited reactivity with substrates. More recent studies by Nam as well as by our group,[16-17] have shown the ability of Mn^{IV}-oxo complexes to attack C–H bonds of moderate strengths at rates comparable to those of Fe^{IV}-oxo complexes. The $[Mn^{IV}(O)(N4py)]^{2+}$ and the $[Mn^{IV}(O)(BnTPEN)]^{2+}$ complexes have been shown to react with strong C–H bonds such as toluene and cyclohexane. Our group proposed that the enhanced reactivity of these Mn^{IV}-adducts was based on thermodynamic

arguments from the $Mn^{IV/III}$ reduction potential. However, with the pK_a values for reactive Mn^{IV}-oxo complexes being unavailable, the Mn^{III}–OH BDFE is not able to be obtained.

On the basis of DFT studies, Nam and Shaik have proposed that the reactivity of the $[Mn^{IV}(O)(N4py)]^{2+}$ and the $[Mn^{IV}(O)(BnTPEN)]^{2+}$ is due to a multistate reactivity, where the complex begins in the $^4B_1$ ground state and crosses to a ^4E state during the reaction. The $^4B_1$ and ^4E states are related by a promotion of an electron from either of the singly occupied d_{xz} or d_{yz} orbitals into the unoccupied d_{x2-y2} orbital (Scheme 7.1, bottom). To test the feasibility of this mechanism, our group recently evaluated the electronic transitions of $[Mn^{IV}(O)(N4py)]^{2+}$ using magnetic circular dichroism spectroscopy and were able to show that a band at 10 500 cm^{-1} arises from the $^4B_1$ to ^4E transition. We then synthesized a set of N4py derivatives with the goal of perturbing the Mn $3d_{x2-y2}$ orbital, and therefore the ^4E energy, through axial ligand substitutions. Rates of C–H bond oxidation by Mn^{IV}-oxo adducts supported by these N4py derivatives and the BnTPEN ligand showed that there is a correlation between the rate of ethylbenzene oxidation (k_2) and the $^4B_1 \rightarrow {}^4E$ excitation energy.[16] We also noted that there is a strong correlation between the $\log(k_2)$ for ethylbenzene oxidation for $[Mn^{IV}(O)(N4py)]^{2+}$ and its derivatives and the reduction potential for these three complexes. These joint correlations still leave the question of how to explain the mechanism for C-H activation by Mn^{IV}-oxo complexes, as both the multistate and thermodynamic arguments were tentatively supported through this work.

Scheme 7.1. States and configurations relevant to the two-state reactivity of Fe^{IV}-oxo (top) and Mn^{IV}-oxo (bottom) complexes

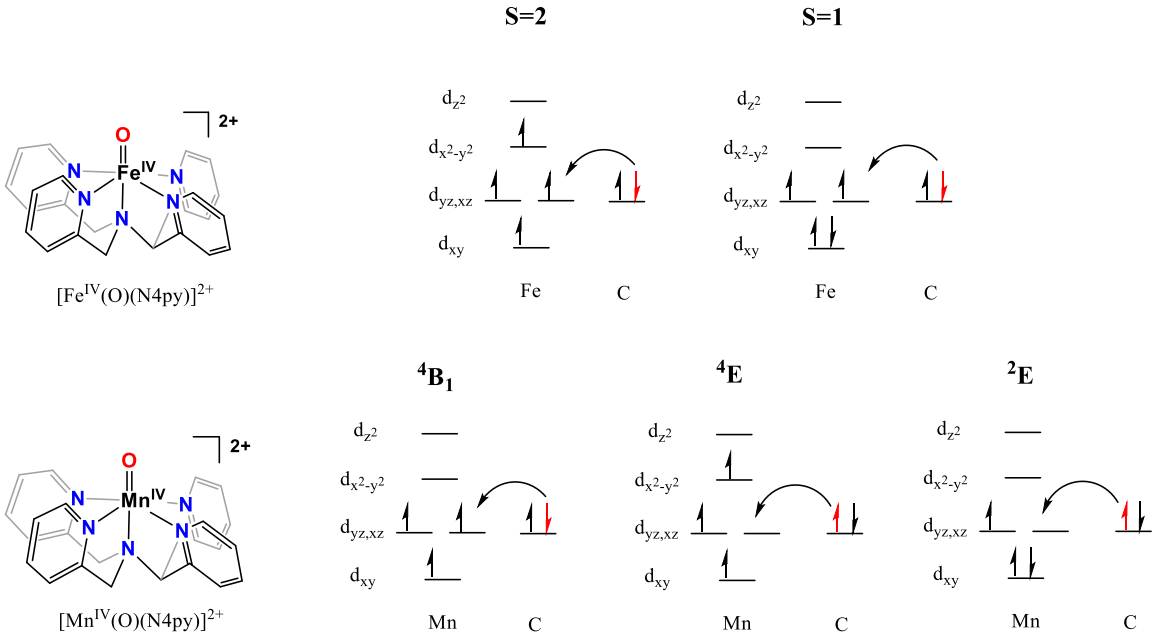

In Shaik's original paper, it was noted that in the ^4E state of $[Mn^{IV}(O)(BnTPEN)]^{2+}$ had significant Mn^{III}-oxyl character in the reactant complex as associated with the opposite (negative) spin on the oxygen atom. In the single-reference method, DFT, this spin-coupled system is described using unrestricted orbitals which manifest as spatial separation of the α and β orbitals giving more positive spin on the Mn and negative spin on the oxygen and can lead to spin contamination. A more rigorous method of describing these spin-coupled systems is through the use of multireference methods, such as complete active space self-consistent field (CASSCF) often followed by second-order perturbation theory. This methodology has been employed to study a wide range of spin-coupled systems including Fe^{IV}-oxo PCET reactivity, the dioxygen binding iron hemoglobin, the electronic structure of metal nitrosyl complexes, and the spin states of Mn^{V}-oxo complexes.[18-24]

To further evaluate the multistate reactivity model of Mn^{IV}-oxo oxidants, we present here a combined experimental and theoretical investigation into the HAT reactions of $[Mn^{IV}(O)(N4py)]^{2+}$

with ethylbenzene. Additionally, we have complemented DFT computations with the multireference method complete active space self-consistent field (CASSCF), followed by N-electron valence perturbation theory up to second order (NEVPT2) using the DFT optimized structures. This DFT/NEVPT2 methodology allows for the accurate description of the static correlation present in systems with significant multireference character. The calculations are then used to analyze the changes in electronic structure along the reaction coordinate to provide insight into the mechanism and demonstrate the strong correlation between inherent electronic structure of the complex and its reactivity with substrates.

7.2 Methods

Density Functional Theory

All DFT calculations were performed using the *ORCA* 4.0 software package.[25] Geometry optimizations were performed using the B3LYP[26-27] functional utilizing Grimme's D3[28] with Becke-Johnson damping scheme[29] for dispersion corrections. The RIJCOSX approximation was used to speed up the calculations. The def2-TZVP basis set was used for Mn, N, and O and the def2-SVP basis set was used for C and H.[30-31] Larger grid sizes for the DFT grid and exchange grid (Grid6 and GridX6 in *ORCA*) were utilized. To account for solvation, the implicit SMD solvent model was used with the default parameters for 2,2,2-trifluoroethanol, which is the solvent used for the experimental studies.[32] Numerical frequency calculations were performed at the same level of theory as geometry optimizations. Reactants, reactant complexes, products, and product complexes all were verified to be minima on the potential energy surface by having no imaginary frequencies. Transition states were optimized by starting from the highest energy structure from a constrained surface scan along the Mn^{IV}-oxo - substrate O – H distance and inputting the full Hessian matrix to start the calculation. Transition states were confirmed to contain only a single imaginary frequency

corresponding to the expected reaction coordinate. Single-point energy calculations were performed on all structures using B3LYP-D3 with the def2-TZVPP basis set on all atoms and grid sizes Grid7 and GridX7.

In order to obtain geometries for the ^{4}E surface, the structure was first optimized as a sextet with a constrained O–H distance, then reoptimized on the quartet surface, giving a broken-symmetry type structure with the oxo showing opposite sign spin density to that of the manganese. The spin density and atomic structure for $[Mn^{IV}(O)(N4py)]^{2+}$ was similar to that seen by Shaik in his initial work.

Complete Active Space Self-Consistent Field

CASSCF[33-34] calculations followed by NEVPT2[35] were performed using the def2-TZVPP basis set on Mn, N, and O and the def2-TZVP basis set on C and H. States were converged to a state-specific solution from an initial state-averaged solution including three quartet states.

For structures without a substrate, the active space was chosen to consist of the five orbitals of the Mn d-manifold, d_{xy}, d_{xz}, and d_{yz}, $d_{x^2-y^2}$, and d_{z^2} (nb, π_x*, π_y*, σ^*_{eq}, and σ_z, respectively), the two oxo pπ orbitals (π_x and π_y), one oxo σ orbital (σ_z), and the Mn^{IV}-N4py equatorial σ-bonding orbital (σ_{eq}). This gives a total of 11 electrons in 9 orbitals, written as CAS(11,9). For structures including a substrate, the active space was the same as above, except with the additional inclusion of the C-H bonding (σ_{CH}) and antibonding (σ_{CH}*) orbitals, giving a CAS(13,11), which were needed to accurately describe C-H bond cleavage and O-H bond formation. It has been shown that Mn 4d orbitals can be important in providing needed flexibility in the wavefunction in the follow perturbation step (NEVPT2). In order to approximate this effect, the active spaces were further increased by the addition of three virtual orbitals consisting of a Mn $4d_{xy}$ and two strongly

interacting Mn 4d – O 3p π-bonding orbitals. Thus, all computations including substrate were ran at a CAS(13,14) level and without substrate at a CAS(11,12) level.

Because the degeneracy of the ^{4}E state is broken upon optimization to a lower symmetry structure, we will describe the two non-degenerate states derived from the ^{4}E as $^4E_1$ and $^4E_2$, where $^4E_1$ is now the lower-energy state. In addition, the normally doubly degenerate Mn^{IV}-oxo π and π* orbitals also become non-degenerate in the presence of substrate, and are termed π_1 and π_2, with the orbitals along the O-H-C reaction coordinate labeled π_1 and π_1* and the orbitals perpendicular to the reaction coordinate π_2 and π_2*.

7.3 Results and Discussion

PCET Reactivity

Relaxed surface scans were performed starting from the weakly interacting reactant complex (RC) on the $^4B_1$ surface and scanned following the (C)H···O(Mn) distance. A fully optimized ^{4}E RC was unable to be obtained, as all optimizations relaxed to the $^4B_1$ structure. Structures from constrained O–H optimizations, however, were able to be obtained. In the presence of a substrate the $^4E_1$ state could be isolated through the use of broken-symmetry DFT. The relevant $^4B_1$ and $^4E_1$ transition states were located for the reactions of $[Mn^{IV}(O)(N4py)]^{2+}$ with ethylbenzene and cyclohexane. A direct σ-approach for the substrate (Mn-O-H angle of approximately 180°) was not found to be energetically relevant at the B3LYP level as all optimizations starting in such an orientation optimized to a narrower angle. Table 1 lists key geometric parameters for reactions with each substrate at the optimized stationary points. The TS geometry of the $^4B_1$ state of **1**-cyclohexane shows significant elongation in the Mn – O bond distance to 1.77 Å. Meanwhile, there is little change in the equatorial Mn–N_{eq} bond distances compared to the RC and the N–Mn–N angle is

163° for both sets of trans N atoms. The $^4E_1$ state has a slightly shorter Mn–O bond distance of 1.73 Å compared to the $^4B_1$ TS. The average Mn–N_{eq} bond distance has increased significantly to 2.17 Å, which is due to the elongation of two equatorial Mn – N bonds trans to one another. Additionally, the N–Mn–N angle for the elongated equatorial N atoms has contracted from 163° to 153°, while the N–Mn–N angle for the other trans pair is 160°.

Table 3. Selected geometric parameters for the transition state structures.

State	Structure	Mn - O (Å)	Mn -Neq (Å)	O - H (Å)
$^4B_1$	$[Mn^{IV}(O)(N4py)]^{2+}$	1.66	2.01	-
	TS ethylbenzene	1.75	2.01	1.25
	TS cyclohexane	1.77	2.02	1.24
$^4E_1$	TS ethylbenzene	1.71	2.17	1.58
	TS cyclohexane	1.73	2.17	1.4

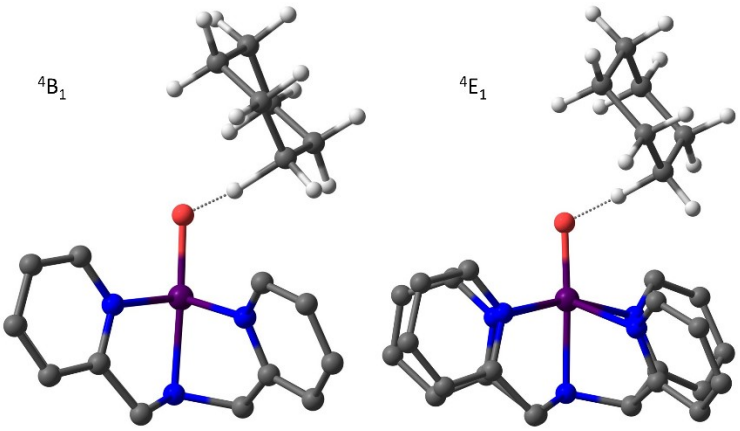

Figure 7.1. DFT optimized structure for transition state structures of $[Mn^{IV}(O)(N4py)]^{2+}$ with cyclohexane on the $^4B_1$ (left) and $^4E_1$ (right) surfaces. Hydrogens hidden on $[Mn^{IV}(O)(N4py)]^{2+}$ for clarity.

The activation parameters for the B3LYP calculations for HAT from ethylbenzene and cyclohexane to $[Mn^{IV}(O)(N4py)]^{2+}$ are shown in Table 2. These values are obtained when comparing the energy of the transition state structures of their respective state to those of the infinitely separated reactants on the $^4B_1$ surface. When comparing to the experimental values for ethylbenzene,

the $^4B_1$ structure values are very close with $\Delta H^‡$ = 13.3 kcal mol^{-1} and $-T\Delta S^‡$ = 8.5 kcal mol^{-1}. However, a comparison of the $^4B_1$ TS with the $^4E_1$ TS energies show that the latter is ca. 10 kcal mol^{-1} lower in energy (Table 2). This result would imply that the $^4E_1$ structure is the likely pathway for reactivity, but the barrier is unphysically low. B3LYP computations for cyclohexane oxidation by **1** also predicts the ^{4}E TS to lie ca. 10 kcal/mol below the $^4B_1$ TS (table 2). However, in this case there are no experimental values to benchmark these reactions. A comparison of the barriers for $[Mn^{IV}(O)(N4py)]^{2+}$ with cyclohexane with the $\Delta E^‡$ obtained from Nam and Shaik require a different initial energy, defined as the energy of the $^4B_1$ RC. With this definition, we obtain for $^4B_1$ and ^{4}E a $\Delta E^‡$ of 29.2 and 18.6 kcal mol^{-1}, respectively. This is nearly identical to the values previously reported of $\Delta E^‡$ = 28.7 and 19.5 kcal mol^{-1} for the $^4B_1$ and $^4E_1$ TS structures. While treating the RC as the initial point for the electronic energy comparison raises the barrier, it nearly eliminates the $-T\Delta S^‡$, further reducing the activation barrier. These results support the conclusion of Nam and Shaik that HAT by **1** involves crossing from the $^4B_1$ and ^{4}E states, as the latter provides a far lower TS energy. However, the error between the calculated and experimental values for ethylbenzene suggests some errors in the DFT treatment. In a follow-up study using the $\ln(k_2)$ for reaction of $[Mn^{IV}(O)(N4py)]^{2+}$ with 1,4-cyclohexadiene as an experimental benchmark, Nam also saw that the ^{4}E structure was too low in energy for what would be expected. They offered the explanation that the actual barrier to reaction was a vertical excitation from the ground state to the excited state followed by barrierless relaxation to the products. Here, to explore the nature of this error, we re-evaluated the energies of the TS for ethylbenzene and cyclohexane oxidation by $[Mn^{IV}(O)(N4py)]^{2+}$ using the CASSCF/NEVPT2 method.

Table 4. Activation parameters for $[Mn^{IV}(O)(N4py)]^{2+}$ from experiment and calculated at the B3LYP and NEVPT2 levels of theory.

substrate		State	[a]$\Delta E^{\ddagger}$	[a]$\Delta H^{\ddagger}$	[a,b]$T\Delta S^{\ddagger}$	[a]$\Delta G^{\ddagger}$
ethylbenzene	[c]Exp.			13.5	-6.9	20.4
	B3LYP	$^4B_1$	17.2	13.3	-8.5	21.7
		$^4E_1$	6.3	3.9	-8.6	12.5
	NEVPT2	$^4B_1$	30.3	26.0	-8.5	34.5
		$^4E_1$	14.9	15.5	-8.6	24.1
cyclohexane	Exp.			-	-	-
	B3LYP	$^4B_1$	24.9	22.0	-8.5	30.5
		$^4E_1$	14.3	11.8	-8.9	20.6
	NEVPT2	$^4B_1$	37.9	30.6	-8.5	36.5
		$^4E_1$	26.9	20.1	-8.9	26.3

[a]All values in kcal mol^{-1}. [b]Entropy values at 25°C [c] Massie, A. A. unpublished results.

In considering activation parameters using NEVPT2 energies, the difference in electronic energy between the free reactants and the reactant complex was obtained using the B3LYP values. Differences in energy between the infinitely separated reactants and the RC should largely be affected by dynamic correlation, of which B3LYP-D3 is able to adequately treat. Additionally, any failures of describing the multireference character in the Mn−O should remain consistent between both structures due to little change in the geometry of **1** going from reactant to RC. In contrast, CASSCF/NEVPT2 accounts for dynamic correlation at a multi-reference second-order perturbation level of theory, and therefore can be inadequate in describing changes in energy that arise from dynamic correlation. However, when the description of the static correlation becomes more important, as in going from the RC structure to the TS structure, the NEVPT2 treatment will become more accurate. Therefore, the NEVPT2 electronic energy was used to determine the energy differences of the RC to TS. Finally, the ZPE, thermal correction and entropy terms are obtained from the DFT numerical frequency calculations and so are the same for both B3LYP and NEVPT2

values. This scheme was utilized previously by Neese et al. in examination of an Fe^{IV}-oxo HAT reaction along multiple spin pathways.[20]

The NEVPT2 activation parameters determined using the above approach are shown in Table 2. In general, the NEVPT2 electronic energies (and therefore free energies) are ca. 12 kcal mol^{-1} higher than their DFT counterparts. For example, ethylbenzene oxidation by $[Mn^{IV}(O)N4py)]^{2+}$, $\Delta G^{\ddagger}$ for the $^4B_1$ reaction is now 34.5 kcal mol^{-1}, which is significantly higher than the experimental value of 20.4 kcal mol^{-1}. In contrast, the barrier on the $^4E_1$ surface is $\Delta G^{\ddagger}$ of 24.1 kcal mol^{-1}. This overestimation of the activation free energy and is due to minor overestimations of both $\Delta H^{\ddagger}$ and $\Delta S^{\ddagger}$. For cyclohexane, a similar trend is seen where the $\Delta G^{\ddagger}$ for the $^4B_1$ and $^4E_1$ states increase to 36.5 and 26.3 kcal mol^{-1}, respectively. Overall there is an increase in $\Delta E^{\ddagger}$ relative to the B3LYP energies.

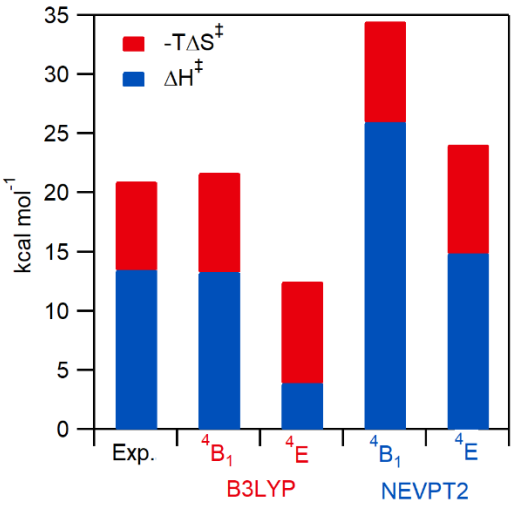

Figure 7.2. Graph showing the activation parameters for $[Mn^{IV}(O)(N4py)]^{+}$ with ethylbenzene derived from experimental and theoretical methods shown as the summed contributions to $\Delta G^{\ddagger}$ calculated at 25 °C.

Barrier Composition. In our initial work, we showed that the energy gap between the $^4E_1$ and $^4B_1$ states was still ~30 kcal mol^{-1} at the $^4B_1$ transition state structure. We noted then that geometric

rearrangements could lead to a reduction in the energy gap and possibly additional stabilization from the substrate. Here, with the optimized structures and state-specific calculations we can test these possibilities using a model to deconvolute the energetic barrier, $\Delta E^{\ddagger}$, into the sum of two components (Figure 7.3). The first is the energy to distort the reactants to their transition state geometries calculated in the absence of the any substrate-complex interaction, ΔE_{def}. The second is the energy of interaction upon bringing the distorted molecules together to the transition state distances, ΔE_{int}. ΔE_{def} will always be positive as distorted the molecules from their equilibrium geometry incurs an energetic penalty, but ΔE_{int} can positive or negative, depending on multiple factors. Steric effects induce a positive ΔE_{int} but factors such as favorable orbital mixing can decrease ΔE_{int}.

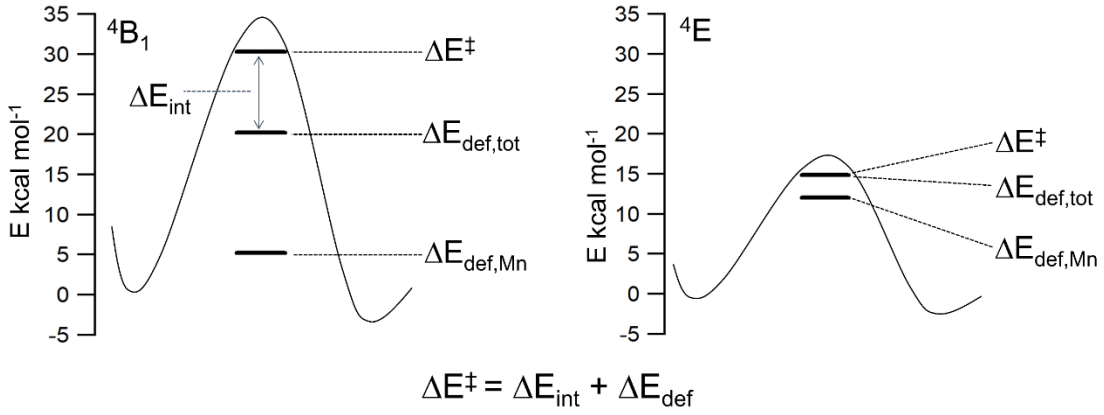

Figure 7.3. Components contributing to the activation energy barrier for $[Mn^{IV}(O)(N4py)]^{2+}$ with ethylbenzene for the $^4B_1$ state (left) and the $^4E_1$ state (right).

The energy required to distort the $^4B_1$ equilibrium structure to its ethylbenzene transition state geometry, ΔE_{def} is calculated to be 5 kcal mol^{-1}. This is similar to what our previous state averaged calculations predicted. The energy required to distort to the $^4E_1$ TS electronic structure and geometry is now only 12 kcal mol^{-1}, compared to the ca. 30 kcal mol^{-1} shown previously. This drastic

change in ΔE_{def} shows that through geometric distortions, the complex is able to access this state at a much lower energetic penalty. However, this reduction in ΔE_{def} alone is not enough to make the $^4E_1$ state relevant as it is still 7 kcal mol^{-1} higher in energy than the $^4B_1$ state. Looking at the energy penalty to distort the substrate, for the $^4B_1$ state the ΔE_{def} for the substrate is 15 kcal mol^{-1} and for the $^4E_1$ TS it is only 3 kcal mol^{-1}. This difference in ΔE_{def} arises from the C–H bond being significantly elongated in the TS for $^4B_1$. Putting these two components together, the ΔE_{def} is ca. 20 kcal mol^{-1} and 14.9 kcal mol^{-1} for the $^4B_1$ and $^4E_1$ geometries, respectively.

Finally, for the $^4B_1$ TS, there is an additional penalty for bringing the distorted structures together, as shown by the positive ΔE_{int} of 10 kcal mol^{-1}. In contrast, the $^4E_1$ TS has no additional energetic penalty for bringing the distorted structures together. A ΔE_{int} of 0 kcal mol^{-1} indicates that any unfavorable interaction of steric effects is likely countered by favorable orbital overlap, and the total energetic cost for reaction on the $^4E_1$surface arises from distorting the reactants. A further look into the electronic structure can elucidate why there are such differences in the PCET barrier.

Electronic Structure of $[Mn^{IV}(O)N4py)]^{2+}$ $^4B_1$ and ^4E States. To begin evaluating the differences of the $^4B_1$ and $^4E_1$ states, we first provide analysis of the $^4B_1$ and $^4E_1$ states of $[Mn^{IV}(O)(N4py)]^{2+}$ without substrates to look at the fundamental differences in the electronic structure. DFT calculations utilizing broken symmetry were unable to converge to the ^4E state without substrate present. Due to this, only the CASSCF description is used to analyze the structures without substrate.

The CAS wavefunction of the $^4B_1$ electronic structure has four configurations with weights above 2%, shown in equations 1a – 1d:

$$^{4B1}\varphi_1 = |(\sigma_z)^2(\pi_1)^2(\pi_2)^2(d_{xy})^1(\pi_1^*)^1(\pi_2^*)^1(\sigma^*_{eq})^0(\sigma^*_z)^0\rangle \quad 1a$$

$$^{4B1}\varphi_2 = |(\sigma_z)^1(\pi_1)^1(\pi_2)^2(d_{xy})^1(\pi_1^*)^2(\pi_2^*)^1(\sigma^*_{eq})^0(\sigma^*_z)^1\rangle \quad 1b$$

$$^{4B1}\varphi_3 = |(\sigma_z)^1(\pi_1)^2(\pi_2)^1(d_{xy})^1(\pi_1^*)^1(\pi_2^*)^2(\sigma^*_{eq})^0(\sigma^*_z)^1\rangle \quad 1c$$

$$^{4B1}\varphi_4 = |(\sigma_z)^0(\pi_1)^2(\pi_2)^2(d_{xy})^1(\pi_1^*)^1(\pi_2^*)^1(\sigma^*_{eq})^0(\sigma^*_z)^2\rangle \quad 1d$$

with $^{4B1}\varphi_1$ contributing 83% and the other three configurations contributing 2 to 3%. Two of the additional configurations arise from the promotion of two electrons by one $\pi \rightarrow \pi^*$ and one $\sigma \rightarrow \sigma^*$ one-electron excitations. The final configuration consists of a doubly occupied σ_z^* orbital at the expense of two electrons from the σ_z orbital. These configurations lead to a state that is largely Mn^{IV}-oxo. This is supported by the orbital occupation numbers (ON), which provide a way to simplify the picture presented by multiple configurations contributing to a single state. The ideal, single-reference picture would present ON values either at 0 (unoccupied), 1 (singly occupied) or 2 (doubly occupied). Deviations from these values are indicative of multi-reference character. In this structure, the σ_z MO, formally a doubly occupied orbital shows an ON of 1.83. This is compensated by an ON of 0.16 in the σ_z^* orbital, which formally an unoccupied orbital. There is only a minor decrease in the ON of π_1 and π_2 to 1.91.

In the $^4E_1$ state of **1** at the TS geometry, there are three major configurations

$$^{4E1}\varphi_{20} = |(\sigma_z)^2(\pi_1)^2(\pi_2)^2(d_{xy})^1(\pi_1^*)^0(\pi_2^*)^1(\sigma^*_{eq})^1(\sigma^*_z)^0\rangle \quad 2a$$

$$^{4E1}\varphi_{11} = |(\sigma_z)^2(\pi_1)^1(\pi_2)^2(d_{xy})^1(\pi_1^*)^1(\pi_2^*)^1(\sigma^*_{eq})^1(\sigma^*_z)^0\rangle \quad 2b$$

$$^{4E1}\varphi_{02} = |(\sigma_z)^2(\pi_1)^0(\pi_2)^2(d_{xy})^1(\pi_1^*)^2(\pi_2^*)^1(\sigma^*_{eq})^1(\sigma^*_z)^0\rangle \quad 2c$$

with $^{4E1}\varphi_{20}$ contributing 64% to the wavefunction. All other major contributing configurations can be viewed as variations from this dominant configuration. The second largest contributing configuration ($^{4E1}\varphi_{11}$, 13%) arises from a one-electron excitation from the π_1 to π_1*. The third largest configuration ($^{4E1}\varphi_{02,}$ 9%) has the π_1* orbital doubly occupied and the π_1 unoccupied. The composition of the π orbitals also differ significantly from the $^4B_1$ state (Figure 7.4). The π_1/π_1* set of orbitals maintain a nearly equal contribution from both Mn and O at the transition state geometry, with the π_1 MO showing slightly more O character (55%) and the π_1* showing slightly greater Mn character (59%). This contrasts with the π_2/π_2* set of orbitals which have become localized, with the π_2 having 83% O character and the π_2* having 89% Mn character. The ON for π_1 has decreased from ~2 to 1.59, which is compensated by an increase to the π_1* ON to 0.4. The ON for the π_2 set of orbitals π_2 (O p_y) is at 1.95 and the π_2* (d_{xy}) is 1.02.

Mulliken spin density analysis can provide a simplified way to look at how these different states alter the electronic structure of the complex. In the $^4B_1$ state, the oxo adduct has and overall positive spin density, with positive spin density in the xy-plane and a small amount of negative spin density along the z-axis. This O spin density is in contrast to the $^4E_1$ state, where the oxo adduct has a majority negative spin density, with the negative density predominately along the x-axis and positive density along the y-axis. In a fully ionic picture, the oxo would have no spin density as the oxygen orbitals are fully occupied. However, the oxo unit bonding to the manganese is highly covalent, and the oxo is able to gain spin density in two ways.[18] If the antibonding orbitals are singly occupied, then the oxo will gain spin density from delocalization of the α-spin into the oxo orbitals at the expense of spin density on the manganese center. If the antibonding orbitals are unoccupied, then the oxo will gain spin density from spin-polarization where additional α-spin will be present on

the metal and β-spin will accumulate on the oxo. In the $^4B_1$ state this explains the positive spin in the xy-plane and negative spin density along the z-axis with its singly occupied π^* orbitals and empty σ^*_z orbital. In the $^4E_1$ state, with unequal π^* occupation, the unoccupied π_1^* orbital induces a negative spin on the oxo in the direction of the unoccupied orbital.

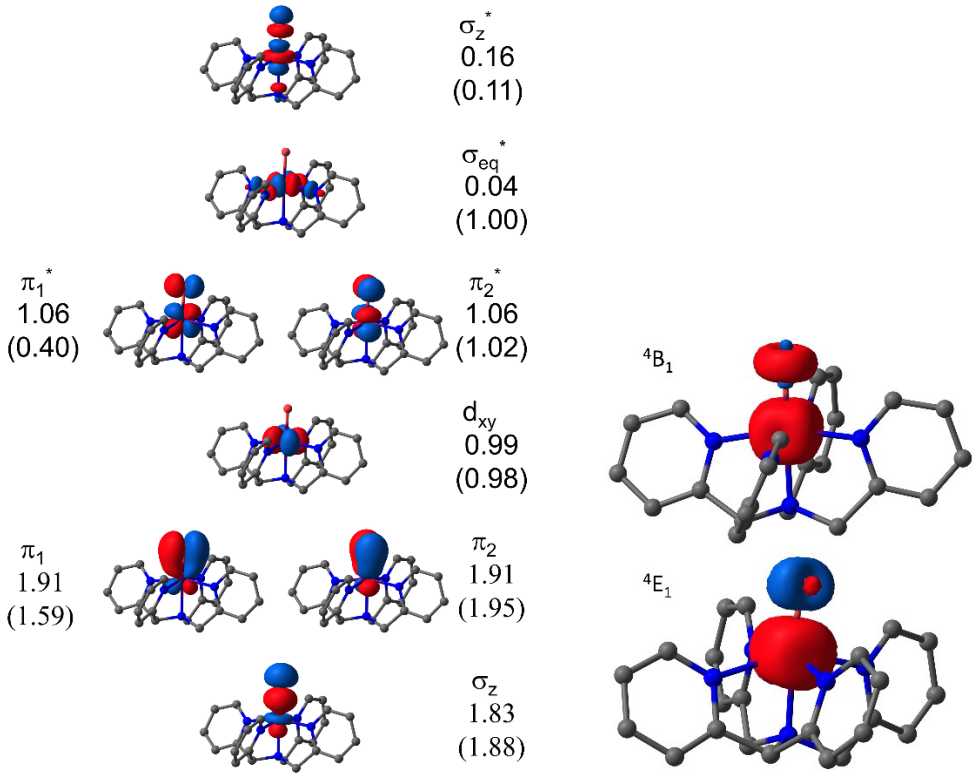

Figure 7.4. MO-diagram showing the $^4B_1$ orbitals and the occupation numbers for the $^4B_1$ state and the $^4E_1$ state (in parenthesis) in the absence of substrate (left). Spin density from CASSCF calculations at the $^4B_1$ (top right) and $^4E_1$ (bottom right) transition state geometries with substrate removed. Positive spin density is displayed in red and negative spin density in blue (right).

$^4B_1$ PCET Reactivity with Cyclohexane. The $^4B_1$ TS for $[Mn^{IV}(O)(N4py)]^{2+}$ with cyclohexane is dominated by a single configuration (90%),

$$^{4B1}\varphi'_1 = |(\sigma_z)^2(\sigma_{OHC})^2(C)^1(\pi_2)^2(d_{xy})^2(d_{xz})^1(\pi_2^*)^1(\sigma^*_{eq})^0(\sigma^*_z)^0(\sigma_{OHC}^*)^0\rangle \qquad 4$$

The occupancies of the d_{xy} (2) and π_1^* and π_2^* (1.0 each) are consistent with a Mn^{III} description. Thus, at this TS geometry, the electron transfer from the C–H σ^b and the Mn^{IV}-oxo has occurred. The accompanying O–H formation and C–H cleavage processes are accomplished by mixing of the Mn=O π_1 and π_1^* MOs with the σ_{CH} and σ_{CH}^* MOs of cyclohexane to give a set of two strongly interacting and two weakly interacting MOs. An MO diagram depicting this process is shown in Figure 7.5, left. The doubly occupied σ_{CHO} MO (53% O, 13% C, 22% H character) is formed by mixing of the doubly-occupied oxo-based π_1 MO (70% oxo character) with the singly-occupied σ_{CH} MO. The σ_{OHC} MO eventually evolves to give the σ_{OH} MO of the Mn^{III}-hydroxo product. The corresponding antibonding MO, σ_{OHC}^* is unoccupied (0.03 ON). One of the singly occupied orbitals, $-C_p$, is dominated by C character (40%), with minor admixture from Mn and O (10 and 23%, respectively). This MO evolves into the C-radical MO in the product complex. The π_1^* has little C or O character (1.9% and 6%, respectively), and is therefore essentially the Mn-based d_{xz} orbital (88.4% Mn). The π_2/π_2^* MOs have lost most of their covalent character, with the π_2 localized on the O (83% O and 13% Mn character), while the π_2^* MO is of dominant Mn character (90.3% Mn and 7.6% O character).

The electronic structure of this TS is very similar to that seen in the $[L^{NHC}Fe^{IV}(O)(MeCN)]^{2+}$ CASSCF calculations with cyclohexadiene.[20] This gives a reaction pathway analogous to that of the $^4B_1$ state of $[Mn^{IV}(O)(N4py)]^{2+}$, but with an additional electron occupying the d_{xy} orbital prior to reaction with the substrate. The change in orbital occupancy results in electron transfer to the Fe-

based π_1* orbital (π_x in their work). In that complex, the Fe^{IV}-oxo bonding is very covalent in the reactant complex but loses a majority of covalency in the TS. A similar O-H-C bonding and antibonding interaction is seen, as well as significant C character gained in the π_1 orbital (π_x* in their work). Thus, in the absence of multistate reactivity, the similar electronic structures of the two metal-oxo units give rise to very similar π-pathway HAT pathways.

$^4E_1$ PCET Reactivity with Cyclohexane. There are some general similarities in the compositions of the MOs between the $^4E_1$ and the $^4B_1$ transition states. For example, there is a doubly occupied O-H-C bonding orbital that consists of 30.6% O character, 16.5% C character and 26.9% H character (Figure 7.5). The corresponding O-H-C antibonding orbital is unoccupied and shows two distinct nodes in the reaction pathway on either side of the H-orbital. The π_2 MO is localized on the O, with 85% O character and 11% Mn character, while the π_2* MO is of dominant Mn character (91.7% Mn to 6.4% O character). However, as in the $^4E_1$ structure without a substrate, the π_1/π_1* orbitals are significantly different in their composition (Figure 7.5, right). Both orbitals have significant Mn character (51.3% and 48.7% Mn character for π_1 and π_1*, respectively) and the π_1 orbital is also composed of 24.2% O character and 13.1% C character while the π_1* orbital contains 31.4% O character and 10.8% C character. The π_1 orbital displays a strong Mn-O π-bonding interaction and a σ-antibonding interaction between the O and C. The π_1* orbital shows Mn-O π-antibonding due to a change in Mn phase but maintains the O and C σ-antibonding.

The predominant configuration (55%, labeled φ_{20}) for the state is

$$^{4E1}\varphi'_{20} = |(\sigma_z)^2(\sigma_{OHC})^2(\pi_{1\text{-}C})^2(\pi_2)^2(d_{xy})^1(\pi_{1\text{-}C}^*)^0(\pi_2^*)^1(\sigma^*_{eq})^1(\sigma^*_z)^0(\sigma_{OHC}^*)^0\rangle \quad 5a$$

$$^{4E1}\varphi'_{11} = |(\sigma_z)^2(\sigma_{OHC})^2(\pi_{1\text{-}C})^1(\pi_2)^2(d_{xy})^1(\pi_{1\text{-}C}^*)^1(\pi_2^*)^1(\sigma^*_{eq})^1(\sigma^*_z)^0(\sigma_{OHC}^*)^0\rangle \quad 5b$$

$$^{4E1}\varphi'_{02} = |(\sigma_z)^2(\sigma_{OHC})^2(\pi_{1\text{-}C})^0(\pi_2)^2(d_{xy})^1(\pi_{1\text{-}C}^*)^2(\pi_2^*)^1(\sigma^*_{eq})^1(\sigma^*_z)^0(\sigma_{OHC}^*)^0\rangle \quad 5c$$

Similar to the $^4E_1$ state without the substrate, there are two other significant configurations. The second largest configuration ($^{4E1}\varphi'_{11}$, 21%) consists of the promotion of a single electron from π_1 to π_1^* and the final significant configuration ($^{4E1}\varphi'_{02}$, 13%) again consists of the promotion of both electrons from π_1 into π_1^*. The configurations for the state as well as the ON are indicative of significant multireference character, similar to what was seen in the structure without the substrate. This gives ON in π_1 of 1.45 and π_1^* of 0.55.

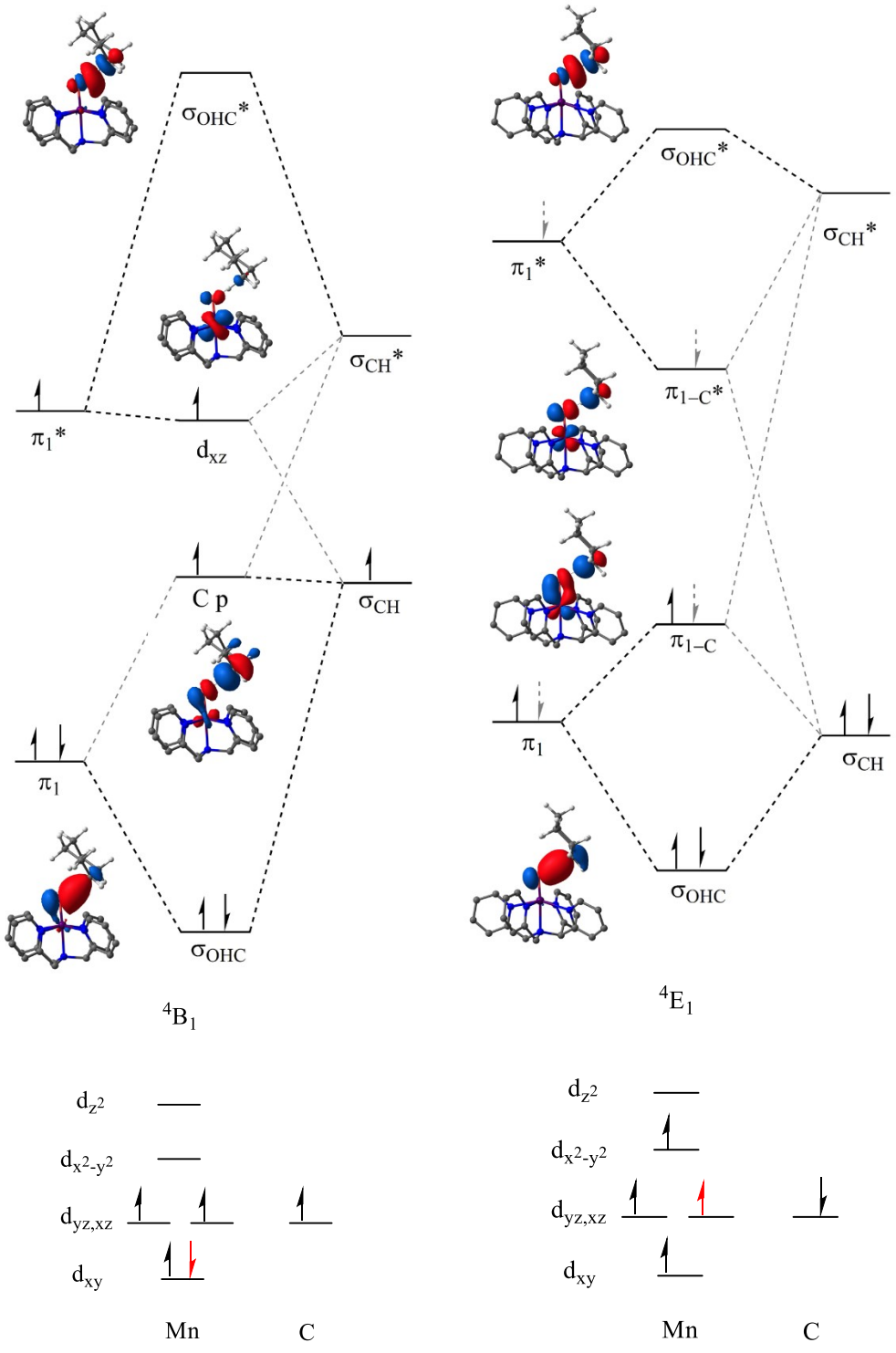

Figure 7.5. Diagram showing the π_1, π_1*, σ_{CH}, and σ_{CH}* interaction at the $^4B_1$ TS (top left) and $^4E_1$ TS (top right) with surface contour plots of the resulting transition state MOs. Diagram showing a simplified MOs with d-orbital labels for the $^4B_1$ TS (bottom left) and to the Mn d_{xz} orbital in the $^4E_1$ TS (bottom right).

By looking at the $^4E_1$ wavefunction prior to and beyond the transition state (Figure 7.6), additional insight can be gained into the nature of the MOs. The composition of the π_1 and π_1^* orbitals change significantly as the reaction progresses, with a loss of O character and an increase in substrate C character. By an O–H distance of 1.0 Å the O contribution to the orbital composition of π_1 has almost completely disappeared, as it is now involved in the localized O-H bond. The $^{4E1}\varphi'_{20}$ configuration decreases significantly in weight at the expense of $^{4E1}\varphi'_{11}$ and $^{4E1}\varphi'_{02,}$ and all three configurations are nearly equal in weight at the O-H distance of 1.0 Å. Finally, the ON of π_1 and π_1^* are nearing unity. This shows that as the hydrogen is being transferred to the complex, the increase in ON of π_1^* describes the gradual localization of the electron pairs at ends of the extended bonding network.

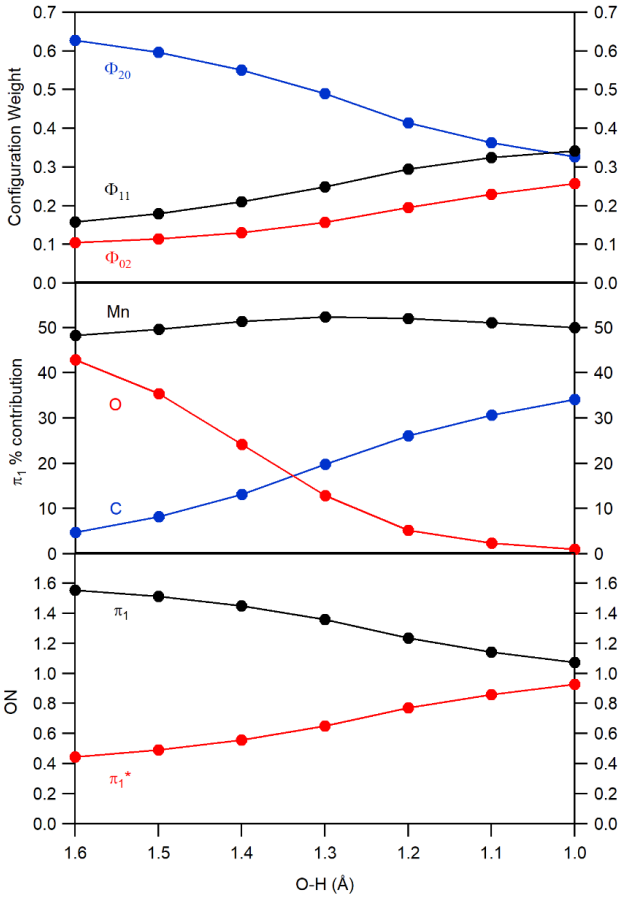

Figure 7.6. Plot of the weights for the largest configurations for the $^4E_1$ state (top), % contribution to the π_1 orbital (center) and occupation number for the π_1 and π_1* orbitals (bottom) as a function of O-H distance along a relaxed surface scan.

For the $^4B_1$ state, the configuration changes rapidly from a Mn^{IV} configuration prior to the TS to a dominant Mn^{III} configuration at the TS. This can be illustrated and compared to the ^4E state through analysis of the spin density on the $[Mn^{IV}(O)(N4py)]^{2+}$ complex as a function of O–H distance (Figure 7.7, bottom). At an O–H distance of 1.6 Å, the spin density determined from the CASSCF calculations is 3, indicative of a Mn^{IV}–oxo / Mn^{III}–oxyl complex. As the O–H distance gets smaller, the spin density of the $^4E_1$ state gradually increases which is in agreement with the analysis of the CASSCF wavefunction above. For the $^4B_1$state, there is little change in the spin

density until the transition state, where there is a sudden drop in spin density indicating the formation of the intermediate spin Mn^{III}. This is also illustrated in the Mn–O distance as a function of O–H distance. Here the $^4E_1$ state has a gradual elongation of the Mn–O as the substrate approaches the complex, but the $^4B_1$ state has a sudden elongation at the TS geometry.

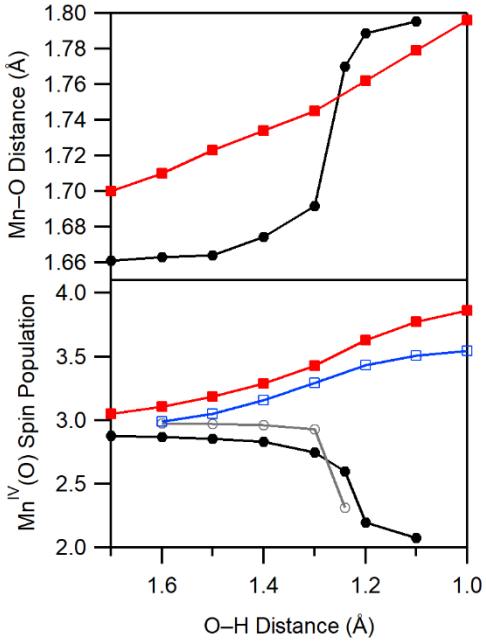

Figure 7.7. Mn–O bond length (top) and Mn^{IV}(O) spin density (bottom) as a function of O–H distance from the relaxed surface scans. ^4B values for DFT (solid circles) and CASSCF (open circles) as well as the ^4E DFT (solid squares) and CASSCF (open squares) are presented.

The analysis of the electronic structure can provide insight into the differences in ΔE_{int} and ΔE_{def} noted above. The ET on the $^4E_1$ surface takes place between the substrate C–H bond and the Mn–O π_1^* orbital. These orbitals are able to overlap and mix significantly at the transition state as seen in Figure 7.5 and create a favorable ΔE_{int}. ET on the $^4B_1$ surface involves a transfer from the substrate C–H bond to the Mn d_{xy} orbital. These orbitals are unable to interact throughout the

reaction, and instead the ET is driven by destabilization of the C–H bond via elongation. Once the C–H bond is sufficiently destabilized, the electron is transferred to the more stable Mn $3d_{xy}$ orbital to form a Mn^{III} complex. This is shown by a repulsive ΔE_{int} as well as a larger ΔE_{def} for the substrate due to the required elongation.

Conclusion

DFT and CASSCF/NEVPT2 calculations were performed to probe the PCET reactivity of $[Mn^{IV}(O)(N4py)]^{2+}$ with two substrates, cyclohexane and ethylbenzene. The activation parameters of ethylbenzene were compared to experimentally determined values, and it was found that previous discrepancies reported in activation barriers between theory and experiment could be due to and underestimation of the barriers by DFT. The CASSCF/NEVPT2 calculations were able to reproduce the barrier with reasonable accuracy utilizing the $^4E_1$. Evaluation of the electronic structure shows that the $^4E_1$ state has favorable orbital overlap with the substrate, while the $^4B_1$ state has largely repulsive interactions with the substrate. This supports our proposal form our previous work, that scans accounting only for the Mn–O elongation were overpredicting the energy of the ^4E state relative to the $^4B_1$ state due to the lack of substrate stabilization.

References

1. Borovik, A. S., Role of metal-oxo complexes in the cleavage of C-H bonds. *Chemical Society Reviews* **2011,** *40* (4), 1870-1874.
2. Mayer, J. M., Understanding Hydrogen Atom Transfer: From Bond Strengths to Marcus Theory. *Accounts of Chemical Research* **2011,** *44* (1), 36-46.
3. McDonald, A. R.; Que, L., High-valent nonheme iron-oxo complexes: Synthesis, structure, and spectroscopy. *Coordination Chemistry Reviews* **2013,** *257* (2), 414-428.
4. Nam, W., Synthetic Mononuclear Nonheme Iron–Oxygen Intermediates. *Accounts of Chemical Research* **2015,** *48* (8), 2415-2423.
5. Solomon, E. I.; Wong, S. D.; Liu, L. V.; Decker, A.; Chow, M. S., Peroxo and oxo intermediates in mononuclear nonheme iron enzymes and related active sites. *Current Opinion in Chemical Biology* **2009,** *13* (1), 99-113.
6. Srnec, M.; Wong, S. D.; Solomon, E. I., Excited state potential energy surfaces and their interactions in Fe(IV)=O active sites. *Dalton Trans* **2014,** *43* (47), 17567-77.

7. Ye, S.; Geng, C. Y.; Shaik, S.; Neese, F., Electronic structure analysis of multistate reactivity in transition metal catalyzed reactions: the case of C-H bond activation by non-heme iron(IV)-oxo cores. *Phys Chem Chem Phys* **2013,** *15* (21), 8017-30.
8. Puri, M.; Que, L., Jr., Toward the synthesis of more reactive S = 2 non-heme oxoiron(IV) complexes. *Acc Chem Res* **2015,** *48* (8), 2443-52.
9. Ye, S.; Neese, F., Quantum chemical studies of C–H activation reactions by high-valent nonheme iron centers. *Current Opinion in Chemical Biology* **2009,** *13* (1), 89-98.
10. Yin, G., Understanding the Oxidative Relationships of the Metal Oxo, Hydroxo, and Hydroperoxide Intermediates with Manganese(IV) Complexes Having Bridged Cyclams: Correlation of the Physicochemical Properties with Reactivity. *Accounts of Chemical Research* **2013,** *46* (2), 483-492.
11. Costas, M.; Mehn, M. P.; Jensen, M. P.; Que, L., Dioxygen Activation at Mononuclear Nonheme Iron Active Sites: Enzymes, Models, and Intermediates. *Chemical Reviews* **2004,** *104* (2), 939-986.
12. Ray, K.; Pfaff, F. F.; Wang, B.; Nam, W., Status of Reactive Non-Heme Metal–Oxygen Intermediates in Chemical and Enzymatic Reactions. *Journal of the American Chemical Society* **2014,** *136* (40), 13942-13958.
13. Ray, K.; Heims, F.; Schwalbe, M.; Nam, W., High-valent metal-oxo intermediates in energy demanding processes: from dioxygen reduction to water splitting. *Current Opinion in Chemical Biology* **2015,** *25* (Supplement C), 159-171.
14. Sahu, S.; Goldberg, D. P., Activation of Dioxygen by Iron and Manganese Complexes: A Heme and Nonheme Perspective. *Journal of the American Chemical Society* **2016,** *138* (36), 11410-11428.
15. Engelmann, X.; Monte-Perez, I.; Ray, K., Oxidation Reactions with Bioinspired Mononuclear Non-Heme Metal-Oxo Complexes. *Angew Chem Int Ed Engl* **2016,** *55* (27), 7632-49.
16. Massie, A. A.; Denler, M. C.; Cardoso, L. T.; Walker, A. N.; Hossain, M. K.; Day, V. W.; Nordlander, E.; Jackson, T. A., Equatorial Ligand Perturbations Influence the Reactivity of Manganese(IV)-Oxo Complexes. *Angewandte Chemie International Edition* **2017,** *56* (15), 4178-4182.
17. Leto, D. F.; Ingram, R.; Day, V. W.; Jackson, T. A., Spectroscopic properties and reactivity of a mononuclear oxomanganese(iv) complex. *Chemical Communications* **2013,** *49* (47), 5378-5380.
18. Venturinelli Jannuzzi, S. A.; Phung, Q. M.; Domingo, A.; Formiga, A. L.; Pierloot, K., Spin State Energetics and Oxyl Character of Mn-Oxo Porphyrins by Multiconfigurational ab Initio Calculations: Implications on Reactivity. *Inorg Chem* **2016,** *55* (11), 5168-79.
19. Radoń, M.; Broclawik, E.; Pierloot, K., Electronic Structure of Selected {FeNO}7 Complexes in Heme and Non-Heme Architectures: A Density Functional and Multireference ab Initio Study. *The Journal of Physical Chemistry B* **2010,** *114* (3), 1518-1528.
20. Kupper, C.; Mondal, B.; Serrano-Plana, J.; Klawitter, I.; Neese, F.; Costas, M.; Ye, S.; Meyer, F., Nonclassical Single-State Reactivity of an Oxo-Iron(IV) Complex Confined to Triplet Pathways. *J Am Chem Soc* **2017,** *139* (26), 8939-8949.
21. Shaik, S.; Chen, H., Lessons on O2 and NO bonding to heme from ab initio multireference/multiconfiguration and DFT calculations. *JBIC Journal of Biological Inorganic Chemistry* **2011,** *16* (6), 841-855.
22. Schuth, N.; Mebs, S.; Huwald, D.; Wrzolek, P.; Schwalbe, M.; Hemschemeier, A.; Haumann, M., Effective intermediate-spin iron in O₂-transporting heme proteins. *Proceedings of the National Academy of Sciences* **2017**.
23. Tomson, N. C.; Crimmin, M. R.; Petrenko, T.; Rosebrugh, L. E.; Sproules, S.; Boyd, W. C.; Bergman, R. G.; DeBeer, S.; Toste, F. D.; Wieghardt, K., A step beyond the Feltham-Enemark notation: spectroscopic and correlated ab initio computational support for an antiferromagnetically

coupled M(II)-(NO)- description of Tp*M(NO) (M = Co, Ni). *J Am Chem Soc* **2011,** *133* (46), 18785-801.
24. Ribas-Ariño, J.; Novoa, J. J., The mechanism for the reversible oxygen addition to heme. A theoretical CASPT2 study. *Chemical Communications* **2007,** (30), 3160-3162.
25. Neese, F., The ORCA program system. *Wiley Interdisciplinary Reviews: Computational Molecular Science* **2012,** *2* (1), 73-78.
26. Becke, A. D., Density-functional Thermochemistry. III. The Role of Exact Exchange. *J. Chem. Phys.* **1993,** *98* (7), 5648-5652.
27. Lee, C.; Yang, W.; Parr, R. G., Development of the Colle-Salvetti Correlation-energy Formula into a Functional of the Electron Density. *Phys. Rev. B* **1988,** *37* (2), 785-789.
28. Grimme, S.; Antony, J.; Ehrlich, S.; Krieg, H., A consistent and accurate ab initio parametrization of density functional dispersion correction (DFT-D) for the 94 elements H-Pu. *The Journal of Chemical Physics* **2010,** *132* (15), 154104.
29. Grimme, S.; Ehrlich, S.; Goerigk, L., Effect of the damping function in dispersion corrected density functional theory. *Journal of Computational Chemistry* **2011,** *32* (7), 1456-1465.
30. Weigend, F.; Ahlrichs, R., Balanced basis sets of split valence, triple zeta valence and quadruple zeta valence quality for H to Rn: Design and assessment of accuracy. *Physical Chemistry Chemical Physics* **2005,** *7* (18), 3297-3305.
31. Weigend, F., Accurate Coulomb-fitting basis sets for H to Rn. *Physical Chemistry Chemical Physics* **2006,** *8* (9), 1057-1065.
32. Marenich, A. V.; Cramer, C. J.; Truhlar, D. G., Universal Solvation Model Based on Solute Electron Density and on a Continuum Model of the Solvent Defined by the Bulk Dielectric Constant and Atomic Surface Tensions. *The Journal of Physical Chemistry B* **2009,** *113* (18), 6378-6396.
33. Ruedenberg, K.; Cheung, L. M.; Elbert, S. T., MCSCF optimization through combined use of natural orbitals and the brillouin–levy–berthier theorem. *International Journal of Quantum Chemistry* **1979,** *16* (5), 1069-1101.
34. Roos, B. O.; Taylor, P. R.; Si�doteqgbahn, P. E. M., A complete active space SCF method (CASSCF) using a density matrix formulated super-CI approach. *Chemical Physics* **1980,** *48* (2), 157-173.
35. Angeli, C.; Cimiraglia, R.; Evangelisti, S.; Leininger, T.; Malrieu, J.-P., Introduction of n-electron valence states for multireference perturbation theory. *The Journal of Chemical Physics* **2001,** *114* (23), 10252-10264.

Appendix 1

Table A1.1. Crystal data and structure refinement for [MnII(dpaq2Me)(OTf)].a

Empirical formula	C27 H25 F3 Mn N6 O4 S	
Formula weight	641.53	
Temperature	100(2) K	
Wavelength	1.54178 Å	
Crystal system	Triclinic	
Space group	P -1	
Unit cell dimensions	a = 11.9552(16) Å	α= 107.482(4)°.
	b = 14.164(2) Å	β= 90.366(4)°.
	c = 18.528(3) Å	γ = 109.556(4)°.
Volume	2799.9(7) $Å^3$	
Z	4	
Density (calculated)	1.522 Mg/m^3	
Absorption coefficient	5.109 mm^{-1}	
F(000)	1316	
Crystal size	0.270 x 0.210 x 0.065 mm^3	
Theta range for data collection	2.518 to 67.864°.	
Index ranges	-9<=h<=14, -16<=k<=16, -21<=l<=21	
Reflections collected	24462	
Independent reflections	9690 [R(int) = 0.0361]	
Completeness to theta = 66.000°	97.3 %	
Absorption correction	Multi-scan	
Max. and min. transmission	1.000 and 0.665	
Refinement method	Full-matrix least-squares on F^2	
Data / restraints / parameters	9690 / 114 / 902	
Goodness-of-fit on F^2	1.051	
Final R indices [I>2sigma(I)]	R1 = 0.0523, wR2 = 0.1480	
R indices (all data)	R1 = 0.0543, wR2 = 0.1498	
Extinction coefficient	n/a	
Largest diff. peak and hole	1.014 and -0.430 $e.Å^{-3}$	

[a] The asymmetric unit for this structure contains three disordered triflate anions and two ordered acetonitrile solvent molecules of crystallization. The first and third triflates are 50/50 disordered about crystallographic inversion centers located at (½, 0, 0) and (½, 0, ½) in the unit cell. Disorder for the first of these triflates gives rise to checkCIF A-alerts for short O---O contacts between the disordered pair.

Table A1.2. Crystal data and structure refinement for [Mn(OH)(dpaq^{2Me})(OTf)].

Empirical formula	C31 H36 F3 Mn N6 O6 S	
Formula weight	732.66	
Temperature	100(2) K	
Wavelength	1.54178 Å	
Crystal system	Monoclinic	
Space group	P 21/c	
Unit cell dimensions	a = 8.4929(5) Å	α = 90°.
	b = 14.2757(8) Å	β = 96.229(3)°.
	c = 27.9728(16) Å	γ = 90°.
Volume	3371.5(3) Å^3	
Z	4	
Density (calculated)	1.443 Mg/m^3	
Absorption coefficient	4.359 mm^{-1}	
F(000)	1520	
Crystal size	0.350 x 0.330 x 0.050 mm^3	
Theta range for data collection	3.178 to 67.952°.	
Index ranges	-9<=h<=10, -10<=k<=17, -28<=l<=33	
Reflections collected	17082	
Independent reflections	5876 [R(int) = 0.0438]	
Completeness to theta = 66.000°	98.0 %	
Absorption correction	Multi-scan	
Max. and min. transmission	1.000 and 0.645	
Refinement method	Full-matrix least-squares on F^2	
Data / restraints / parameters	5876 / 0 / 581	
Goodness-of-fit on F^2	1.043	
Final R indices [I>2sigma(I)]	R1 = 0.0615, wR2 = 0.1692	
R indices (all data)	R1 = 0.0678, wR2 = 0.1741	
Extinction coefficient	n/a	
Largest diff. peak and hole	0.961 and -0.621 e.Å^{-3}	

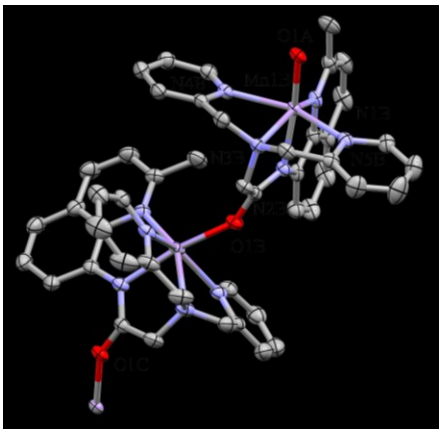

Figure A1.1. ORTEP diagram showing two manganese(II) species in the polymeric crystal structure of $[Mn^{II}(dpaq^{2Me})](OTf)$. Hydrogen atoms, solvent and noncoordinating triflate counter-ions are excluded for clarity.

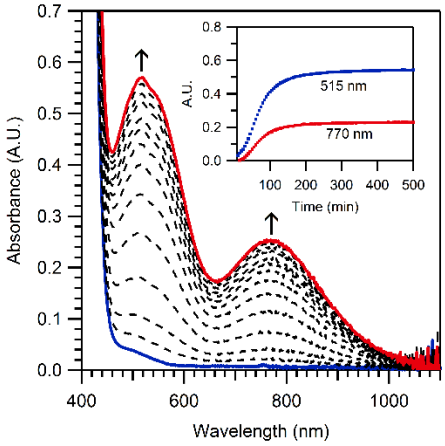

Figure A1.2. Electronic absorption spectra of 2.5 mM $[Mn^{II}(dpaq^{2Me})]^+$ upon addition of O_2 gas at 25°C in MeCN (initial and final bands are blue and red traces, respectively). Inset shows the growth of selected bands over time.

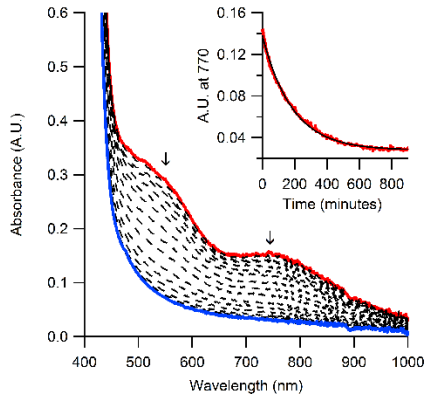

Figure A1.3. Electron absorption spectra of 1.25 mM $[Mn^{III}(OH)(dpaq^{2Me})]^+$ upon the addition of 250 equiv xanthene at 50ºC in MeCN (initial and final spectra are red and blue traces, respectively). Inset shows the decay of the 770 nm band over time (red dots are experimental data points; the black line is a fit to first-order decay).

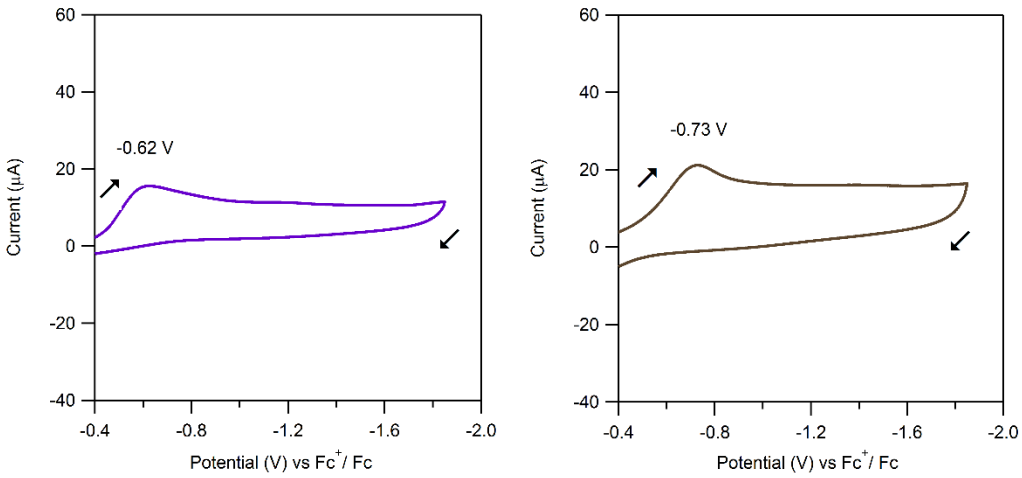

Figure A1.4. Cyclic voltammetry of $[Mn^{III}(OH)(dpaq^{2Me})]^+$ (left) and $[Mn^{III}(OH)(dpaq)]^+$ (right) showing the Mn^{III}/Mn^{II} process. The a scan rate was 100 mV s^{-1}.

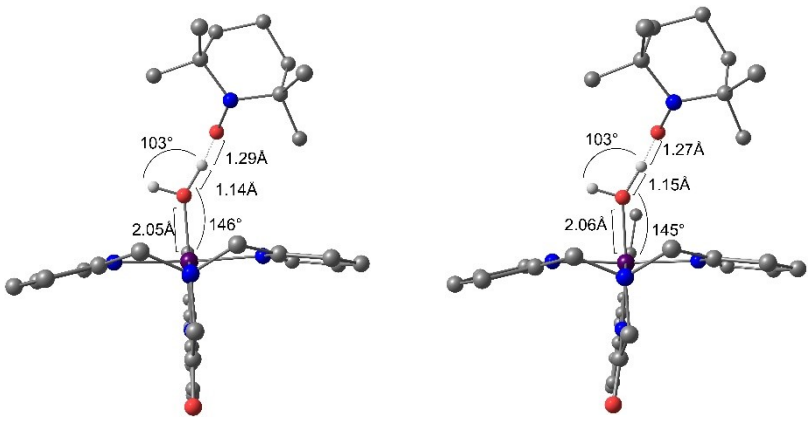

Figure A1.5. Comparison of the transition state structures of 2-H (left) and 2-Me (right). Viewed from a different angle.

Table A1.3. Table of DFT calculated activation parameters for the reaction of 2-H and 2-Me with TEMPOH.

complex	$\Delta H^{\ddagger}$ (kcal mol^{-1})	$T\Delta S^{\ddagger}$ (kcal mol^{-1})	$\Delta G^{\ddagger}$ (kcal mol^{-1})
$[Mn^{III}(OH)(dpaq^{H})]^{+}$	8.57	-10.73	19.30
$[Mn^{III}(OH)(dpaq^{2Me})]^{+}$	8.48	-9.29	17.77

A relatively accurate method for determining theoretical reduction potential, pK_a, and BDFE values has been outlined by Solis et al.[3] This method relies on using a reference complex, for which accurate, experimental reduction potential and pK_a values have been determined, and which is chemically similar to the system under consideration. Importantly, this approach bypasses the need to rely upon calculated proton free energies (for pK_a calculations) and electrode potentials (for reduction potential calculations). Furthermore, the use of a chemically similar reference complex can lead to favorable cancellation of systematic errors intrinsic to the theoretical treatment. Appropriate reference systems include the two Mn^{III}-hydroxo complexes $[Mn^{III}(OH)(S^{Me2}N_4(tren))]^{+}$ and $[Mn^{III}(OH)(PY5)]^{+}$, as both complexes that are capable of initiating PCET and experimental reduction potential and pK_a values have been determined experimentally.[1,4] We used $[Mn^{III}(OH)(PY5)]^{+}$ as the reference complex for two reasons. First, $[Mn^{III}(OH)(S^{Me2}N_4(tren))]^{+}$ contains an N_4S^{-} ligand, which differs from the N_5^{-} coordinate sphere of $[Mn^{III}(OH)(dpaq)]^{+}$ and $[Mn^{III}(OH)(dpaq^{2Me})]^{+}$. Second, and most importantly, we were unable to obtain an energy-minimized structure of the Mn^{II}-aqua complex $[Mn^{II}(OH_2)(S^{Me2}N_4(tren))]^{+}$ due to the water dissociation during the optimization process. Although $[Mn^{III}(OH)(PY5)]^{2+}$ is diacationic, which is unlike $[Mn^{III}(OH)(dpaq)]^{+}$ and $[Mn^{III}(OH)(dpaq^{2Me})]^{+}$, this complex has an N_5 ligand sphere and all required structures are able to be optimized. The choice of $[Mn^{III}(OH)(PY5)]^{2+}$ as a reasonable reference complex is reinforced by the good agreement between the calculated and experimental reduction potentials of $[Mn^{III}(OH)(dpaq)]^{+}$ and $[Mn^{III}(OH)(dpaq^{2Me})]^{+}$ when using this approach (Table A1.4). The pK_a values and reduction potentials collected in Table A1.4 rely upon the DFT optimized structures of the $Mn^{III}(OH)$, $Mn^{II}(OH)$ and the $Mn^{II}(OH_2)$ adducts of the dpaq, $dpaq^{2Me}$, and PY5 ligands. These structures were then used to calculate free energy differences between $Mn^{III}(OH)$ and the $Mn^{II}(OH)$ species to determine the reduction potential and between the

$Mn^{II}(OH_2)$ and $Mn^{II}(OH)$ to determine the pK_a values. These values were then used to calculate the corresponding O-H BDFEs for the $Mn^{II}(OH_2)$ adducts using the Bordwell relationship (Table A1.4).

Table A1.4. Values calculated and used in the determination of the DFT BDFE.

Ligand	$\Delta G(Mn^{II} - Mn^{III})$[a]	$\Delta G(Mn^{II}(OH) - Mn^{II}(OH2))$[a]	Exp. $E_{1/2}$[b]	Exp. pK_a	DFT $E_{1/2}$[b]	DFT pK_a	DFT BDFE[a]
$(dpaq^{H})$	-78.1	294.0	-0.6	-	-0.80	21	65.33
$(dpaq^{2Me})$	-83.4	292.6	-	-	-0.57	20	69.17
$(PY5)^{c}$	-100.4	283.1	0.17	13	-	-	-

[a] Values in kcal mol^{-1}. [b] Values in V vs Fc^{+}/Fc in MeCN. [c] Experimental values taken from reference 1.

Table A1.5. Selected bond lengths from the DFT optimized [MnIII(OH)(dpaqR)]+ structures. All values in Å.

Bond	**2-H**	**2-Me**
Mn-O2	1.846	1.849
Mn-N1	2.084	2.163
Mn-N2	1.986	1.983
Mn-N3	2.233	2.242
Mn-N4	2.246	2.217
Mn-N5	2.235	2.213

Table A1.6. Table of DFT calculated activation parameters for the reaction of 2-H and 2-Me with xanthene at 50 ºC.

Complex	$\Delta H^{‡}$ (kcal mol^{-1})	$\Delta S^{‡}$ (kcal mol^{-1})	$\Delta G^{‡}$ (kcal mol^{-1})
$[Mn^{III}(OH)(dpaq^{H})]^{+}$	22.68	-11.96	34.64
$[Mn^{III}(OH)(dpaq^{2Me})]^{+}$	25.63	-10.94	36.57

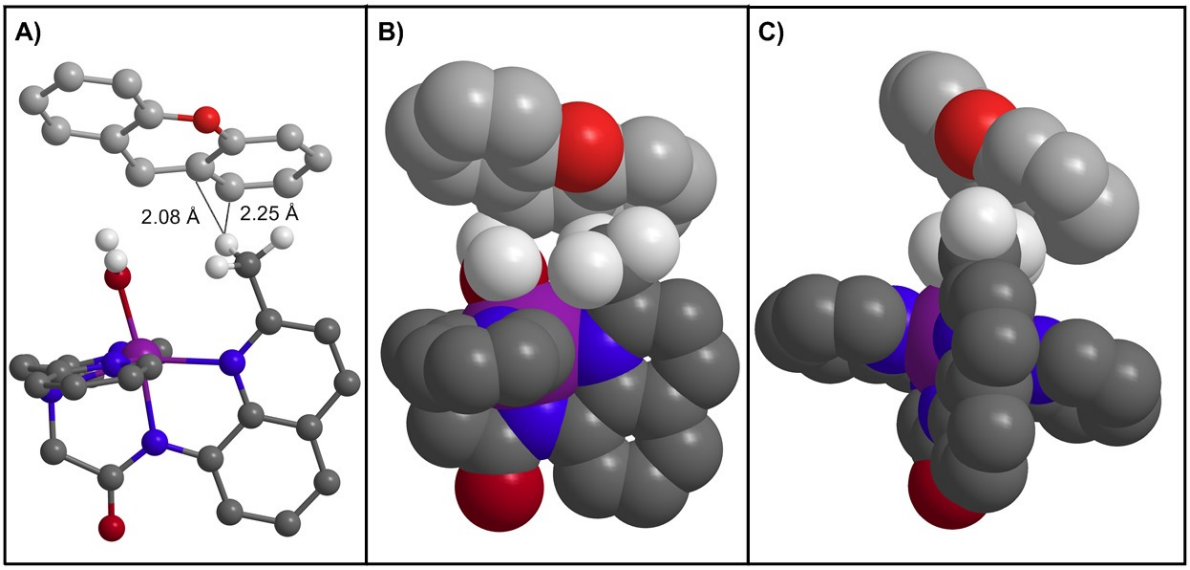

Figure A1.6. Transition state structure of 2-Me with superimposed xanthene structure from the 2-H transition state optimization. The close contacts of the methyl group are shown (A). Panels B and C display filling structures displaying overlap of van der Walls radii showing the methyl groups ability to limit certain structures available to 2-H.

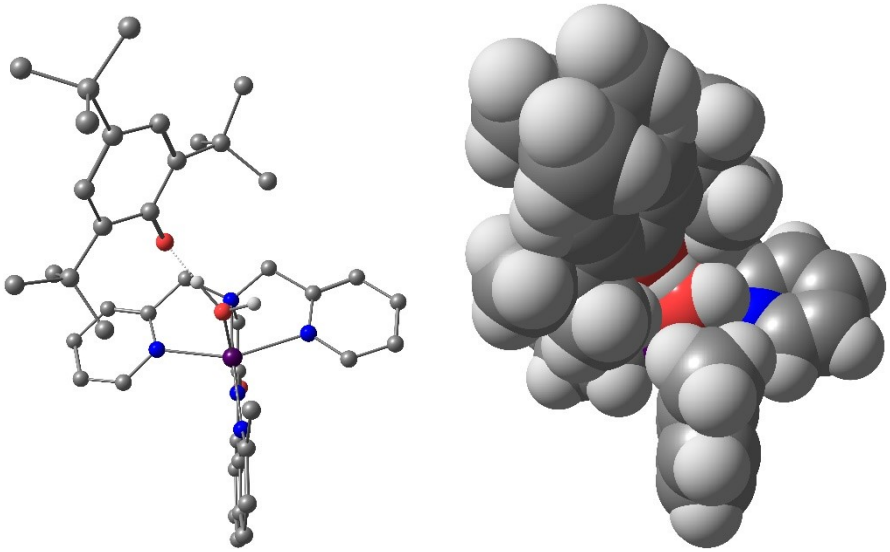

Figure A1.7. Ball and stick model of the DFT structure of 2-Me with 2,4,6-TTBP from the geometry scan with a O_{Mn} –H_{TEMPOH} distance of 1.05 Å (left). Spacefill model of the same structure and orientation (right).

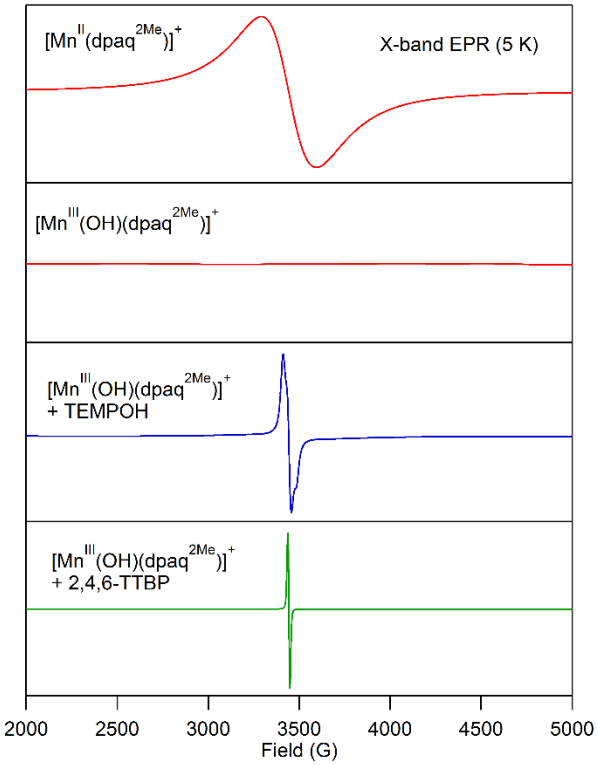

Figure A1.8. Perpendicular-mode 5 K X-band EPR spectrum of 1-Me (top), the final products of TEMPOH oxidation by 2-Me (middle) and the final products of the 2,4,6-tri-*tert*-butylphenol oxidation by 2-Me (bottom). All samples shown here were EPR silent in parallel-mode experiments at 5 K.

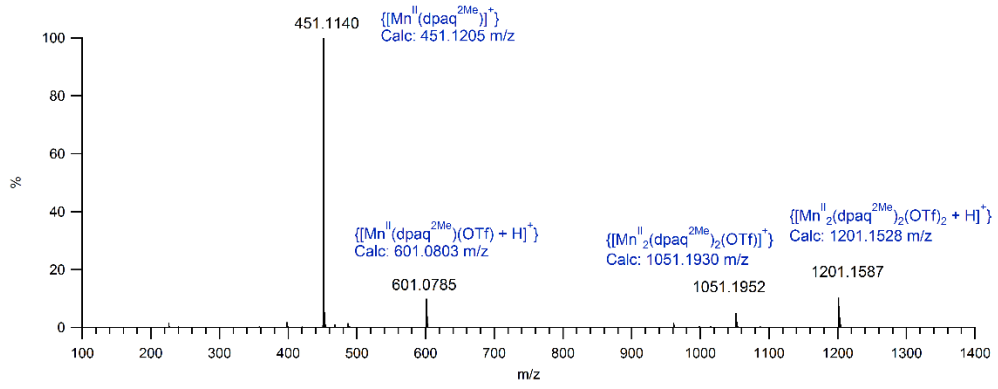

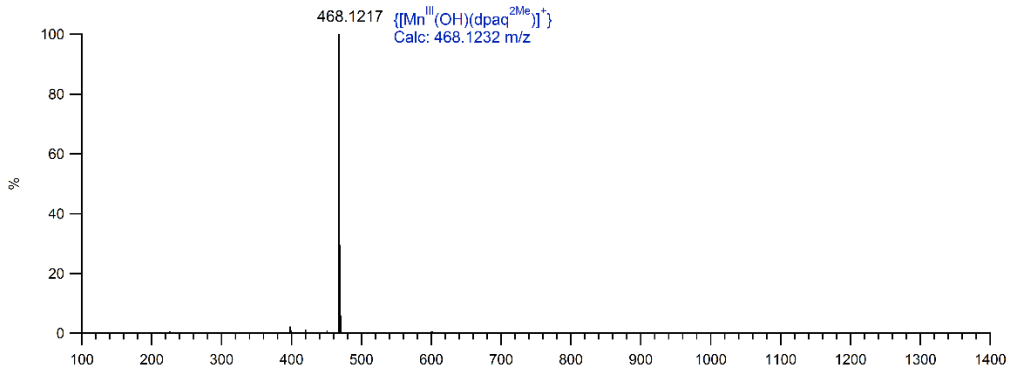

Figure A1.9. ESI-MS of $[Mn^{II}(dpaq^{2Me})]^+$ (top) and $[Mn^{III}(OH)(dpaq^{2Me})]^+$ (bottom).

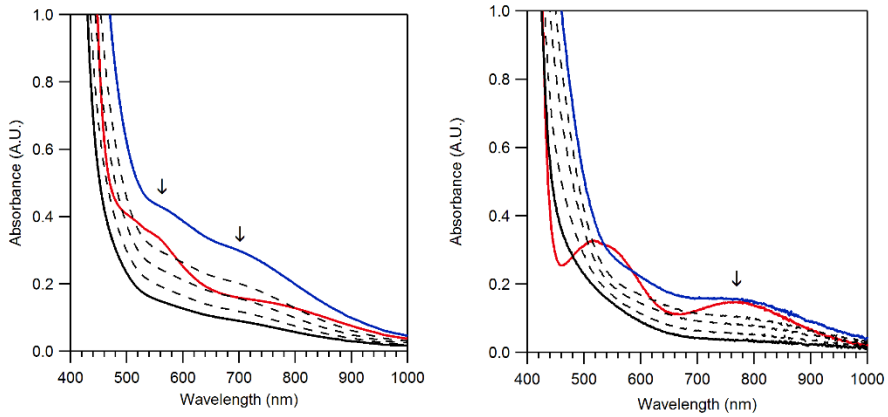

Figure A1.10. Electronic absorption spectra for 1.25mM 2-H (left) and 2-Me (right) upon the addition of 2,4-di-*tert*-butylphenol at 50 °C in MeCN. The initial spectra of the Mn^{III}-hydroxo adducts are red, spectra collected immediately following the addition of 2,4-di-*tert*-butylphenol are blue, and decay spectra are black, dashed traces.

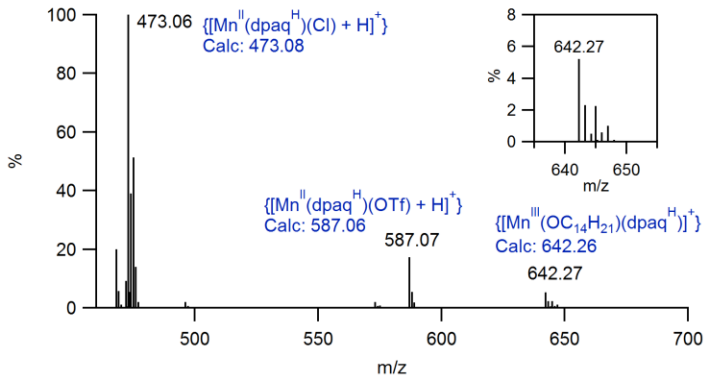

Figure A1.11. ESI-MS taken of room temperature O_2 free mixture of 2-H and 2,4-DTBP in MeCN. Inset is zoomed in on the peak corresponding to the Mn^{III}-phenolate complex.

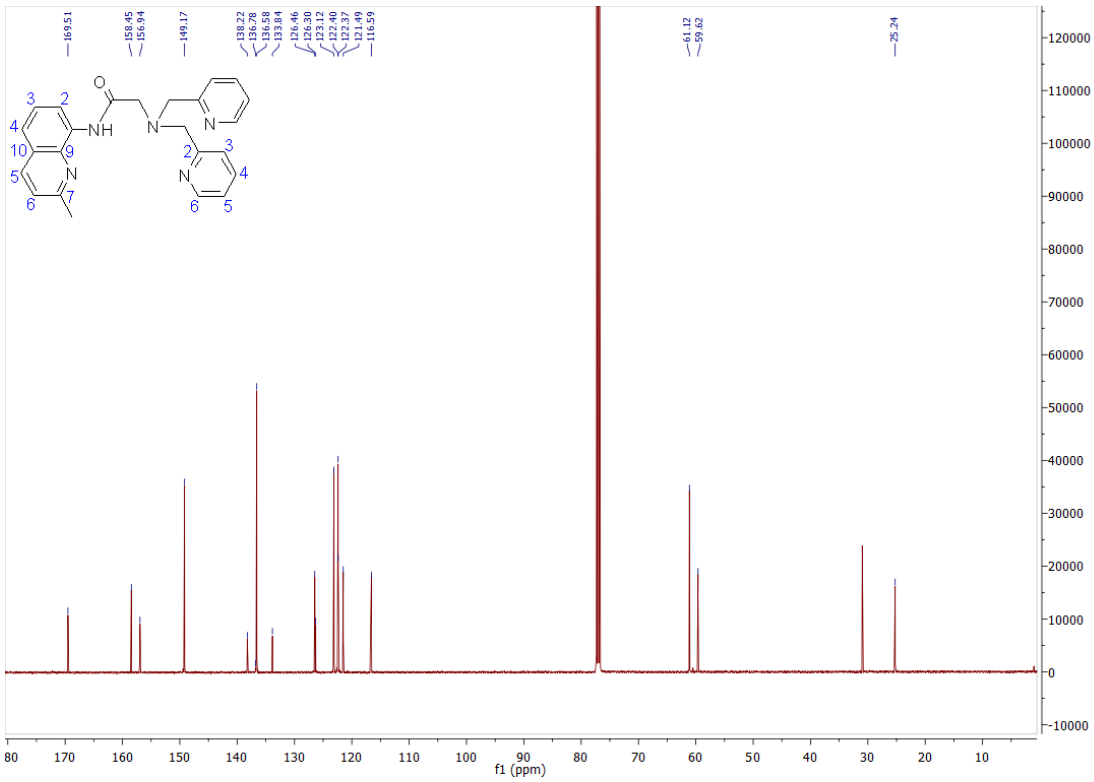

Figure A1.12. ^{13}C NMR of $Hdpaq^{2Me}$ in $CDCl_3$ with structure showing the numbering for the quinoline and pyridines. The peak around 32 ppm is attributed to residual acetone.

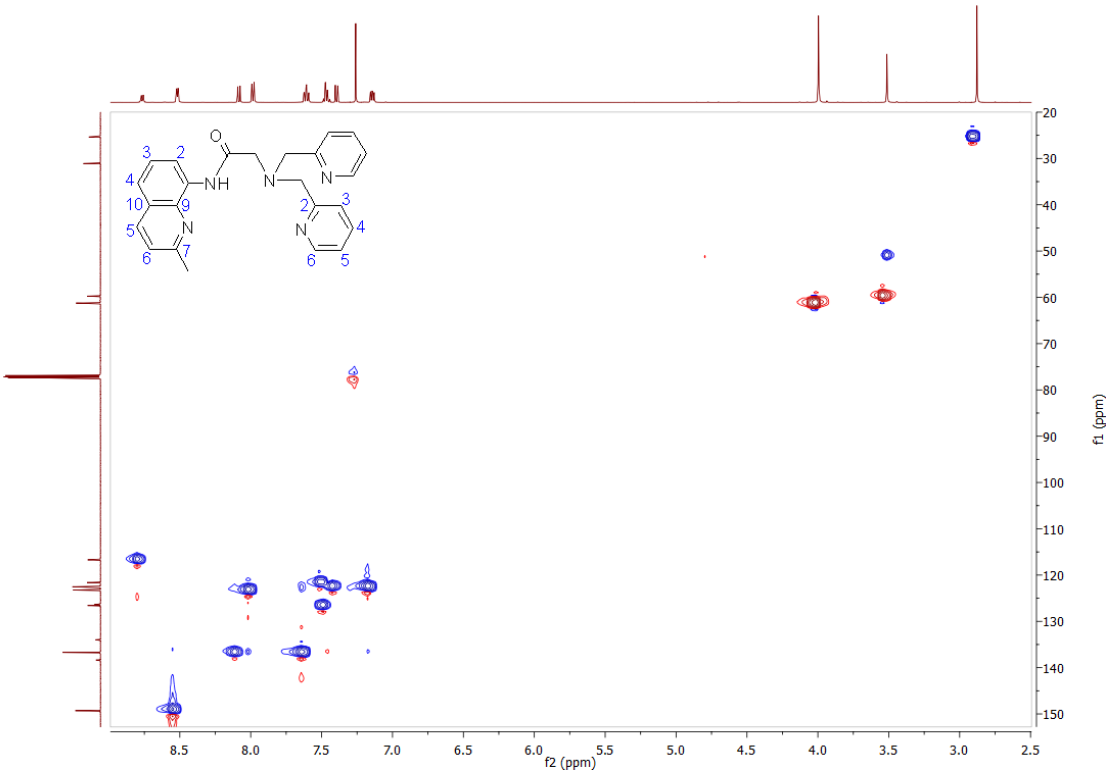

Figure A1.13. ^{1}H – ^{13}C HSQC of $Hdpaq^{2Me}$ in $CDCl_3$ (500 MHz).

References

(1) Goldsmith, C. R.; Cole, A. P.; Stack, T. D. P. *Journal of the American Chemical Society* **2005**, *127*, 9904.
(2) Wijeratne, G. B.; Corzine, B.; Day, V. W.; Jackson, T. A. *Inorg Chem* **2014**, *53*, 7622.
(3) Solis, B. H.; Hammes-Schiffer, S. *Inorganic Chemistry* **2014**, *53*, 6427.
(4) Coggins, M. K.; Brines, L. M.; Kovacs, J. A. *Inorg Chem* **2013**, *52*, 12383.

Appendix 2

Table A2.1. EXAFS fitting for 1-H(MeCN) with best fit bolded. Using DFT structure of $[Mn^{II}(dpaq^{H})(MeCN)]^{+}$ for *FEFF* input.

$[Mn^{II}(dpaq^{H})](OTf)$ (Acetonitrile)									
Mn—N			Mn—N			Mn•••C			
N	R (Å)	σ^2	N	R (Å)	σ^2	N	R (Å)	σ^2	R-factor
			6	2.26	0.00746				0.408
			6	**2.27**	**0.00773**	**8**	**3.15**	**0.00631**	**0.274**
2	2.18	-0.00077	4	2.32	0.00166	8	3.15	0.00643	0.200
4	2.22	0.00182	2	2.35	-0.0093	8	3.15	0.00617	0.207
3	2.2	0.00041	3	2.33	0.00025	8	3.15	0.00647	0.203

Table A2.2. EXAFS fitting for 1-H(solid) with best fit bolded. Using crystal structure of $[Mn^{II}(dpaq^{H})](OTf)$ for *FEFF* input.

$[Mn^{II}(dpaq^{H})](OTf)$ (Solid)									
Mn—O			Mn—N			Mn•••C			
N	R (Å)	σ^2	N	R (Å)	σ^2	N	R (Å)	σ^2	R-factor
			6	2.24	0.00455				0.472
			6	**2.24**	**0.00495**	**8**	**3.12**	**0.00142**	**0.270**
1	2.02	-0.00277	5	2.22	0.00052	8	3.10	0.0027	0.186
3	2.09	0.00514	3	2.25	-0.00177	8	3.10	0.00254	0.207

Table A2.3. EXAFS fitting for 1-Me(MeCN) with best fit bolded. Using DFT structure of $[Mn^{II}(dpaq^{2Me})(MeCN)]^{+}$ for *FEFF* input.

$[Mn^{II}(dpaq^{2Me})](OTf)$ (Acetonitrile)									
Mn—N			Mn—N			Mn•••C			
N	R (Å)	σ^2	N	R (Å)	σ^2	N	R (Å)	σ^2	R-factor
			6	2.20	0.00502				0.371
			6	**2.21**	**0.00519**	**8**	**3.06**	**0.00394**	**0.221**
2	2.17	-0.00063	4	2.28	0.00391	8	3.08	0.00465	0.178
4	2.20	0.00076	2	2.33	0.00009	8	3.07	0.00471	0.175
3	2.23	-0.00001	3	2.32	0.00194	8	3.08	0.00468	0.178

Table A2.4. EXAFS fitting for 1-Me(solid) with best fit bolded. Using crystal structure of $[Mn^{II}(dpaq^{2Me})](OTf)$ for *FEFF* input.

$[Mn^{II}(dpaq^{2Me})](OTf)$ (Solid)									
Mn—O			Mn—N			Mn•••C			
N	R (Å)	σ^2	N	R (Å)	σ^2	N	R (Å)	σ^2	R-factor
			6	2.23	0.00685				0.357
			6	**2.23**	**0.00723**	**7**	**3.09**	**0.00581**	**0.247**
3	2.21	0.00387	3	2.28	0.02414	7	3.09	0.0056	0.233
4	2.21	0.00422	2	2.42	0.00646	7	3.10	0.00599	0.232
2	2.21	0.00169	4	2.26	0.01872	7	3.08	0.00587	0.223

Table A2.5. EXAFS fitting for 2-H(H_2O) with best fit bolded. Using DFT structure of $[Mn^{III}(OH)(dpaq^{H})]^+$ for *FEFF* input.

$[Mn^{III}(OH)(dpaq^{H})](OTf)$ (Water)									
Mn—O			Mn—N			Mn•••C			
N	R (Å)	σ^2	N	R (Å)	σ^2	N	R (Å)	σ^2	R-factor
			6	2.35	0.03028				0.629
2	1.88	0.00522	4	2.15	0.00455				0.368
1	1.85	-0.00022	5	2.15	0.00946				0.347
2	**1.87**	**0.00481**	**4**	**2.14**	**0.00521**	**6**	**2.91**	**0.00889**	**0.166**
1	1.84	-0.00056	5	2.13	0.01067	6	2.93	0.00886	0.166

Table A2.6. EXAFS fitting for 2-H(solid) with best fit bolded. Using crystal structure of $[Mn^{III}(OH)(dpaq^{H})](OTf)$ for *FEFF* input.

$[Mn^{III}(OH)(dpaq^{H})](OTf)$ (Solid) - **2H(solid)**													
Mn—O			Mn—N			Mn—N			Mn•••C			
n	R (Å)	σ^2 (x10^{-3})	*n*	R (Å)	σ^2 (x10^{-3})	*n*	R (Å)	σ^2 (x10^{-3})	*n*	R (Å)	σ^2 (x10^{-3})	R-factor
			6	2.51	37.38							0.765
2	1.90	11.68	4	2.19	8.44							0.538
1	1.79	1.0	2	1.99	1.61	3	2.18	2.7				0.454
1	**1.79**	**0.54**	**2**	**1.98**	**1.32**	**3**	**2.17**	**3.02**	**5**	**2.92**	**5.22**	**0.191**
2	*1.88*	*10.56*	*4*	*2.18*	*9.63*				*5*	*2.94*	*6.3*	0.295
1	1.79	1.0[a]	2	1.98	1.72	3	2.18	3.18	5	2.94	5.31	0.192
1	1.79	2.0[a]	2	1.99	2.59	3	2.18	3.51	5	2.93	5.48	0.200

[a]σ^2 for Mn-O is held constant in this fit.

Table A2.7. EXAFS fitting for 2-Me(MeCN) with best fit bolded. Using DFT structure of $[Mn^{III}(OH)(dpaq^{2Me})]^+$ for *FEFF* input.

$[Mn^{III}(OH)(dpaq^{2Me})](OTf)$ (Acetonitrile)									
Mn—O			Mn—N			Mn•••C			
N	R (Å)	σ^2	N	R (Å)	σ^2	N	R (Å)	σ^2	R-factor
			6	2.20	0.0067				0.606
2	1.90	0.00925	4	2.18	0.00256				0.300
1	1.88	0.00386	5	2.19	0.00448				0.343
2	**1.89**	**0.00868**	**4**	**2.17**	**0.00279**	**5**	**2.93**	**0.00409**	**0.152**

Table A2.8. EXAFS fitting for 2-Me(solid) with best fit bolded. Using crystal structure of $[Mn^{III}(OH)(dpaq^{2Me})](OTf)$ for *FEFF* input.

$[Mn^{III}(OH)(dpaq^{2Me})](OTf)$ (Solid)									
Mn—O			Mn—N			Mn•••C			
N	R (Å)	σ^2	N	R (Å)	σ^2	N	R (Å)	σ^2	R-factor
			6	2.23	0.01489				0.623
			6	2.21	0.01798	7	2.97	0.01623	0.558
1	1.85	0.00149	5	2.17	0.01001	7	2.94	0.00997	0.184
2	**1.87**	**0.00807**	**4**	**2.16**	**0.00561**	**7**	**2.93**	**0.00896**	**0.190**

Table A2.9. EXAFS fitting for 1-Me(MeCN) with best fit bolded. Using crystal structure of $[Mn^{II}(dpaq^{2Me})](OTf)$ for *FEFF* input.

$[Mn^{II}(dpaq^{2Me})](OTf)$ (Acetonitrile)												
Mn—O			Mn—N			Mn—N			Mn•••C			
n	R (Å)	σ^2 (x10^{-3})	*n*	R (Å)	σ^2 (x10^{-3})	*n*	R (Å)	σ^2 (x10^{-3})	*n*	R (Å)	σ^2 (x10^{-3})	R-factor
			6	2.21	5.07	6	2.21	5.07				0.37
			6	**2.21**	**5.23**	**6**	**2.21**	**5.23**	**8**	**3.06**	**4.0**	**0.223**
			2	1.65	20.83	4	2.21	3.09	8	3.06	3.97	0.21
2	2.17	0.079				4	2.28	6.74	8	3.07	4.4	0.19
4	2.18	0.074				2	2.34	2.74	8	3.07	4.21	0.194
			4	2.19	0.08	2	2.33	0.17	8	3.07	4.77	0.178
			3	2.18	0.05	3	2.3	2.01	8	3.07	4.74	0.18

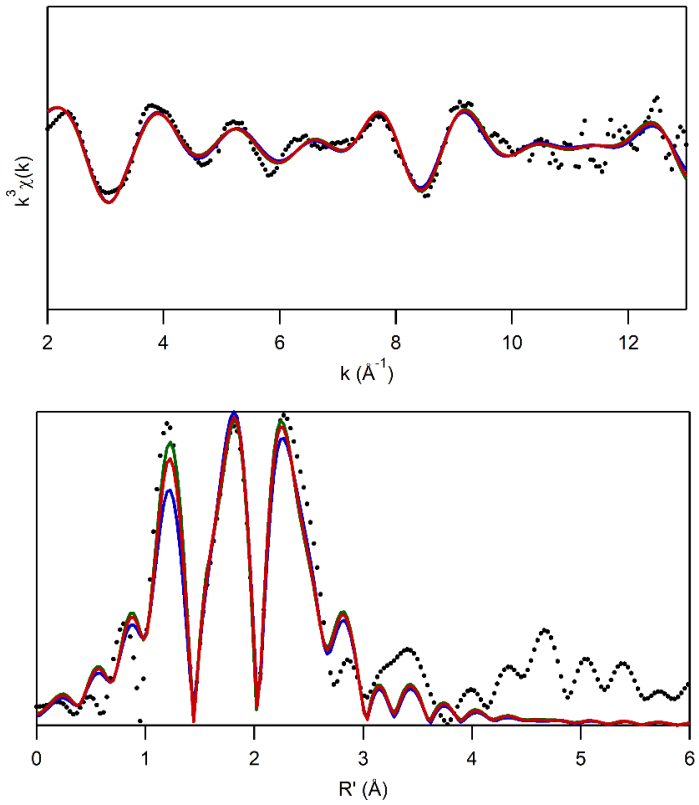

Figure A2.1. 2-H(solid) EXAFS (top) and Fourier transform (bottom) with experimental (•••), optimal fit (—), and fits with a constrained σ^2 of 1 x 10^{-3} (—) and 2 x 10^{-3} (—).

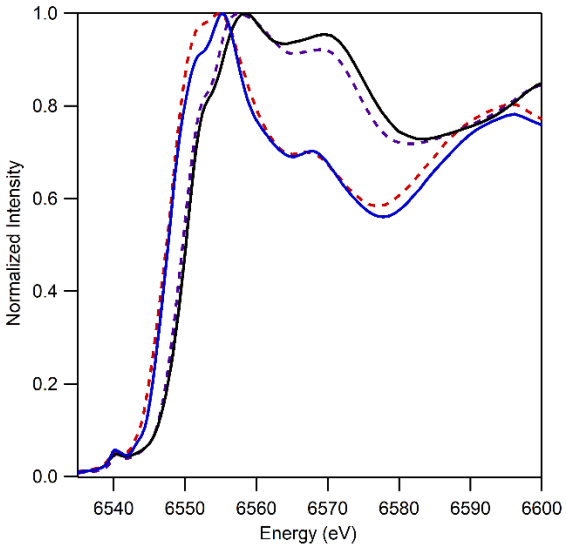

Figure A2.2. Experimental XANES of 1-H(solid)(—), 1-Me(solid)(---), 2-H(solid) (—), and 2-Me(solid) (---).

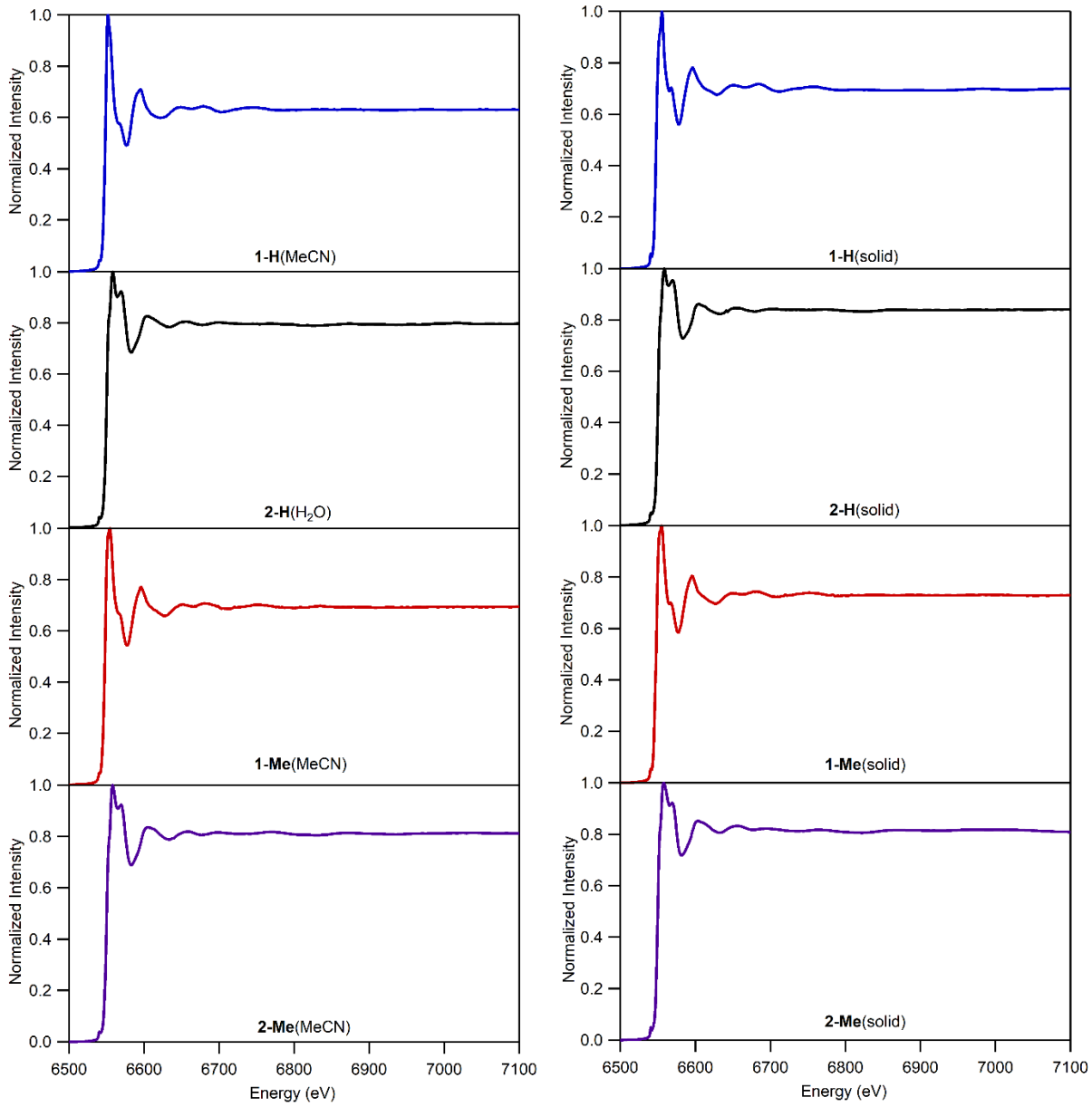

Figure A2.3. Normalized XAS data for solution samples (left) and solid samples (right) from 6.5 keV to 7.1 keV.

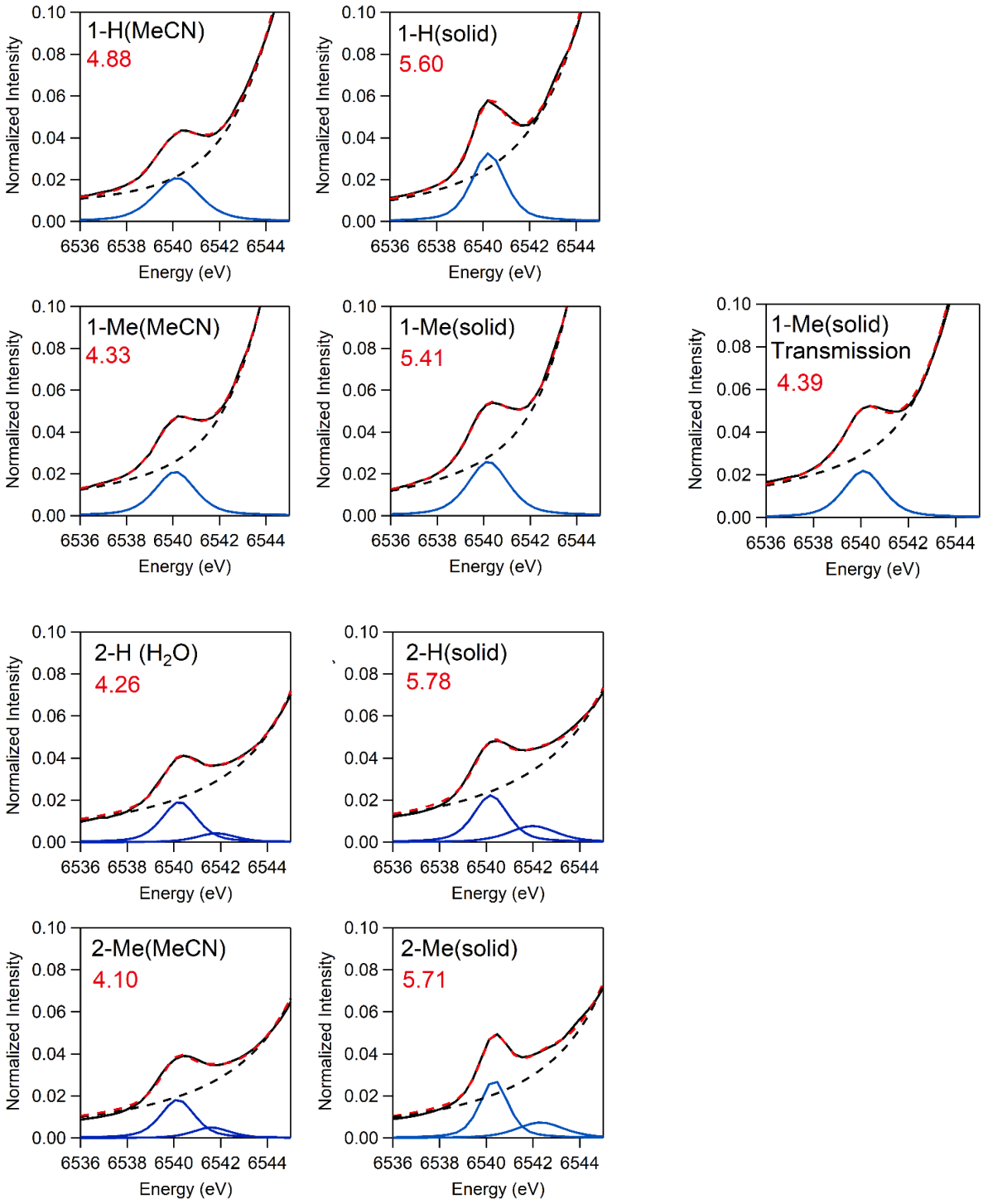

Figure A2.4. Fits for the experimental pre-edge areas of Mn^{II} and Mn^{III}-OH complexes showing data (solid black line), fit (dashed red line), background subtraction (dashed black line), and pseudo-voidt fitted functions (blue lines). Areas determined from fit are shown below the complex name.

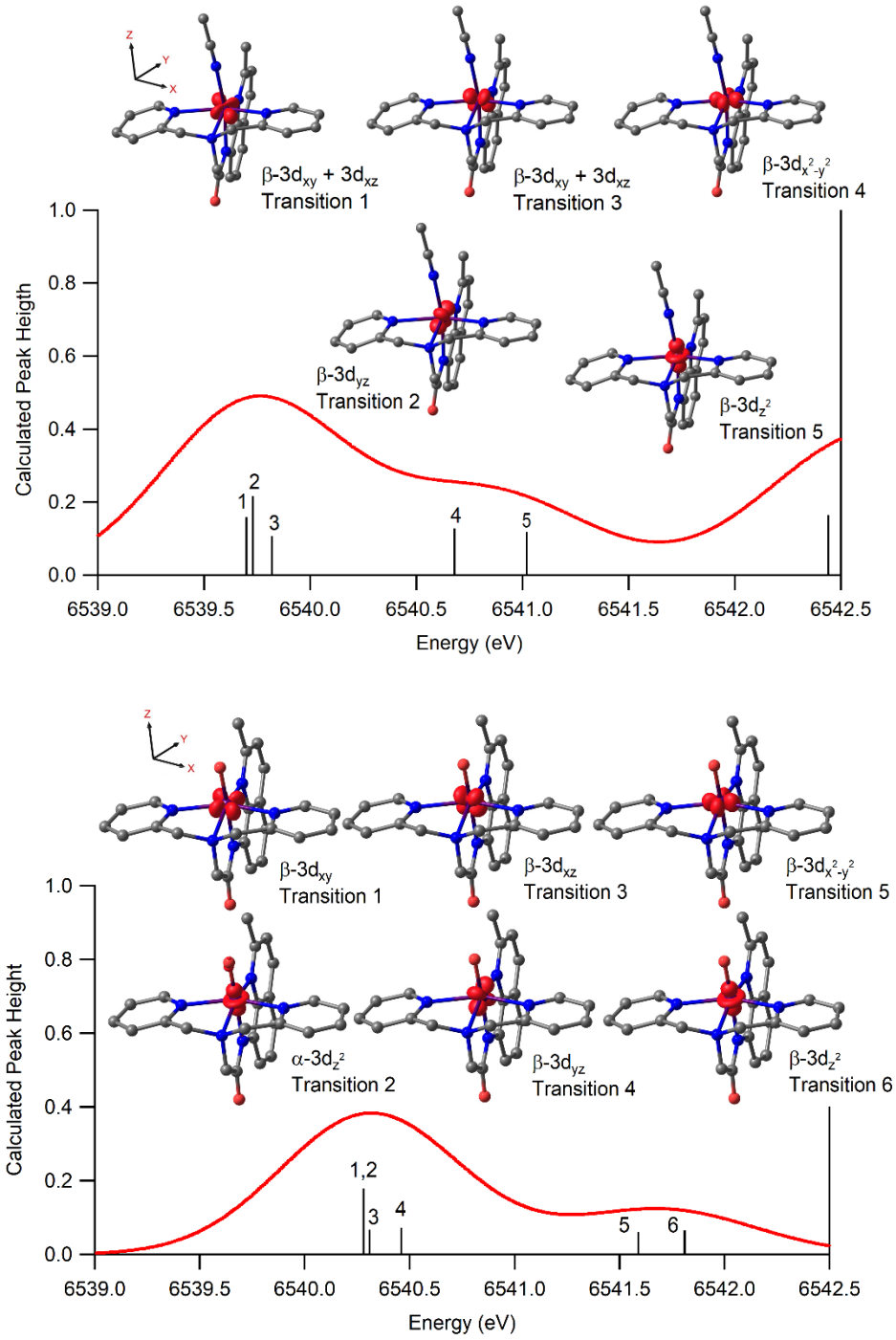

Figure A2.5. TD-DFT simulated pre-edge spectra with vertical lines showing transitions for 1-Me(MeCN) (top) and 2-H(MeCN) (bottom). Electron density difference maps (EDDM) for the specified transitions are depicted and labeled by their primary acceptor orbital. The simulated spectra employed Gaussian functions with a 1 eV bandwidth.

Appendix 3

Table A3.1. Results from the Inversion Recovery Experiments on $[Mn^{III}(OMe)(dpaq)]^+$.

peak	d – ^{1}H (ppm)	I_0^{raw} (arb)	A (arb)	T_1 (ms)
1	127.5	0.99	0.62	0.09 ± 0.02
2	60.8	0.42	1.56	1.12 ± 0.02
3	57.2	0.14	2.87	0.89 ± 0.02
4	53.9	0.20	2.99	1.22 ± 0.02
5	38.5	0.12	5.05	0.07 ± 0.02
6	-4.2	1.05	0.62	3.55 ± 0.15
7	-15.7	0.37	1.03	0.87 ± 0.04
8	-33.6	0.54	0.73	3.21 ± 0.05
9	-52.7	0.11	4.93	1.69 ± 0.04

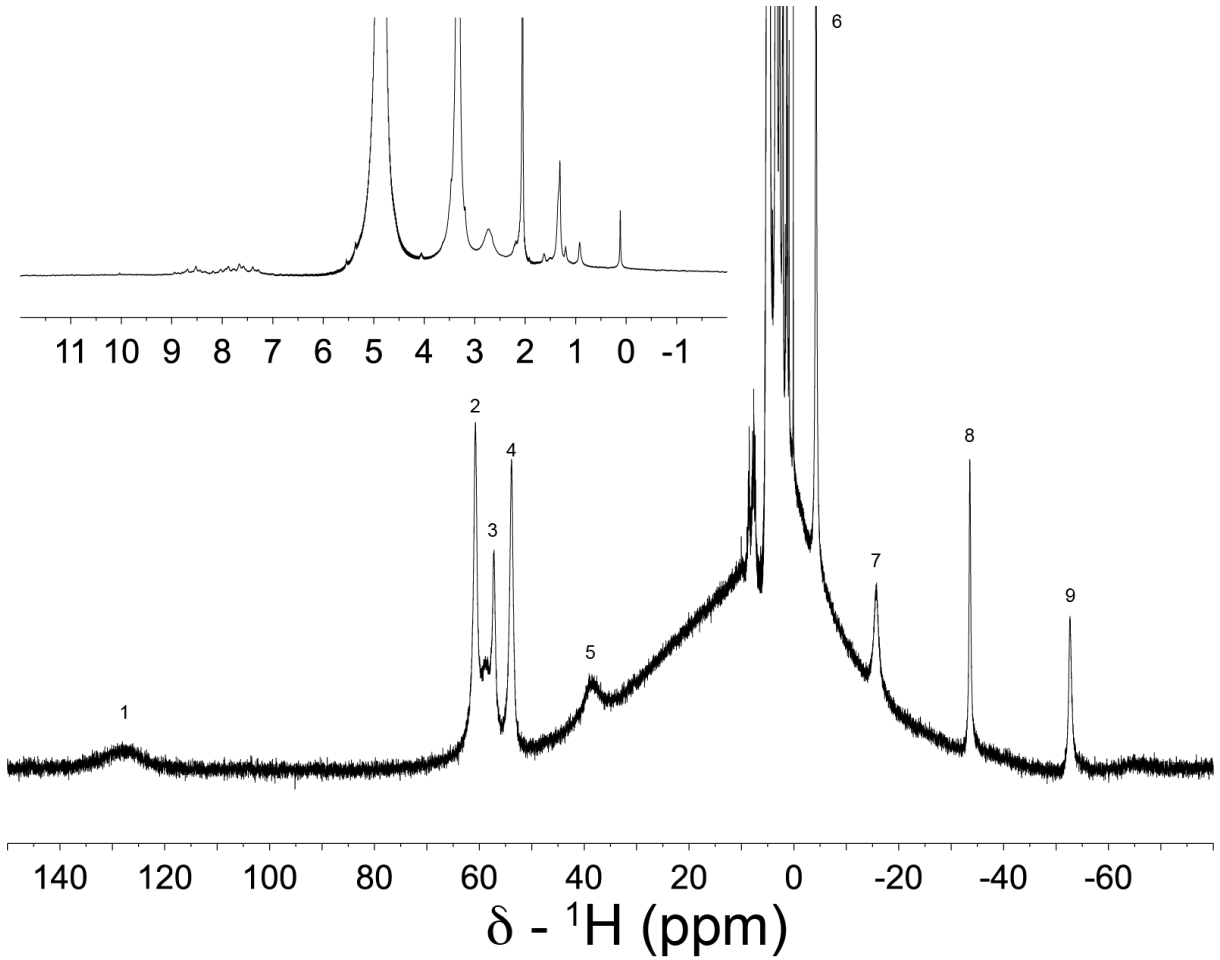

Figure A3.1. 1D ^{1}H NMR spectrum of 80 mM $[Mn^{III}(OMe)(dpaq)]^+$ with region between 12 to -2 ppm inset. T_1 values were measured for peaks marked 1 – 9.

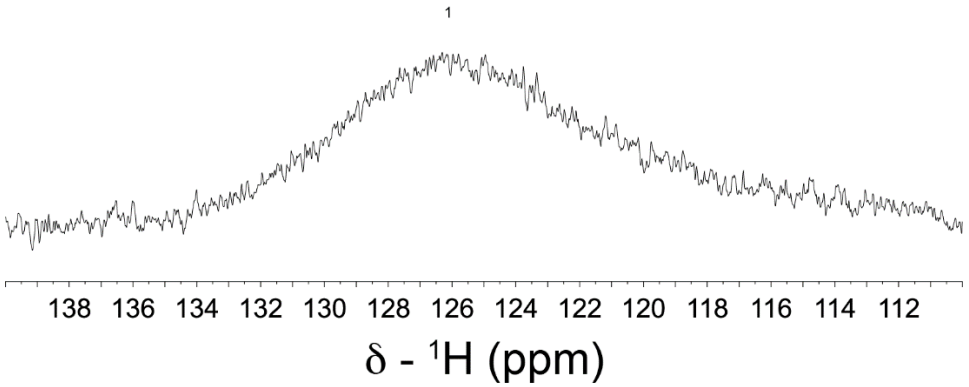

Figure A3.2. 1D ^{1}H NMR spectrum of region between 139 to 111 ppm of $[Mn^{III}(OMe)(dpaq)]^{+}$.

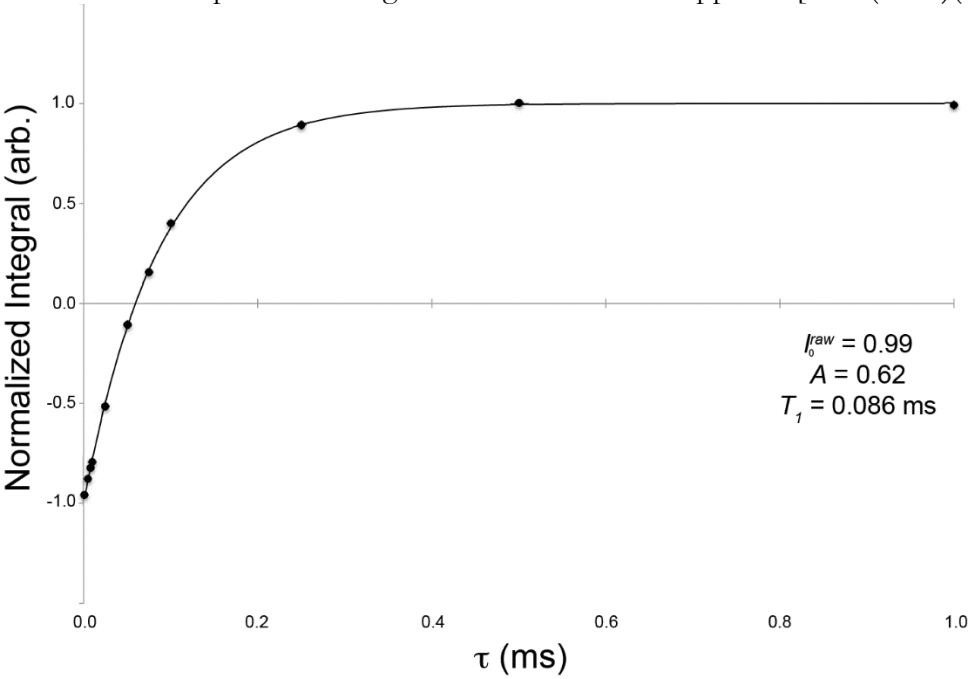

Figure A3.3. Normalized integral versus *t* for peak 1 (127.5 ppm) for inversion recovery experiment.

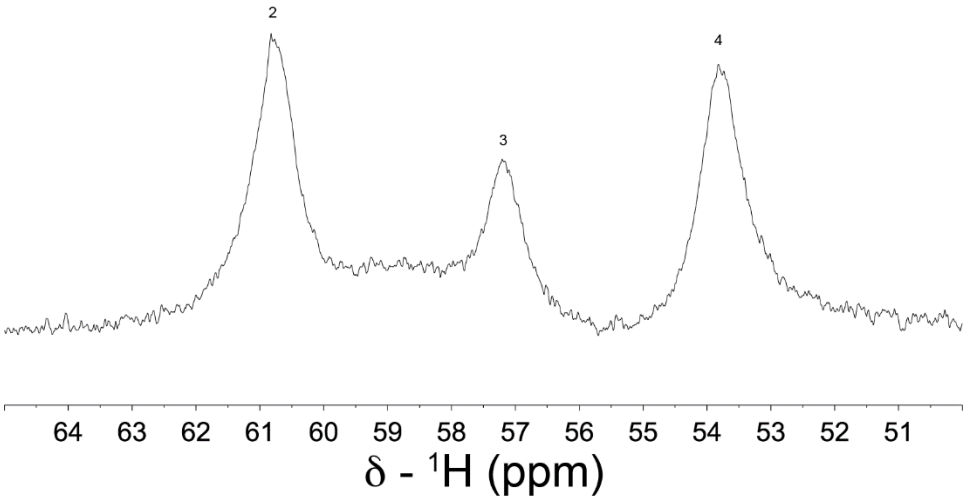

Figure A3.4. 1D ^{1}H NMR spectrum of region between 65 to 50 ppm of $[Mn^{III}(OMe)(dpaq)]^{+}$.

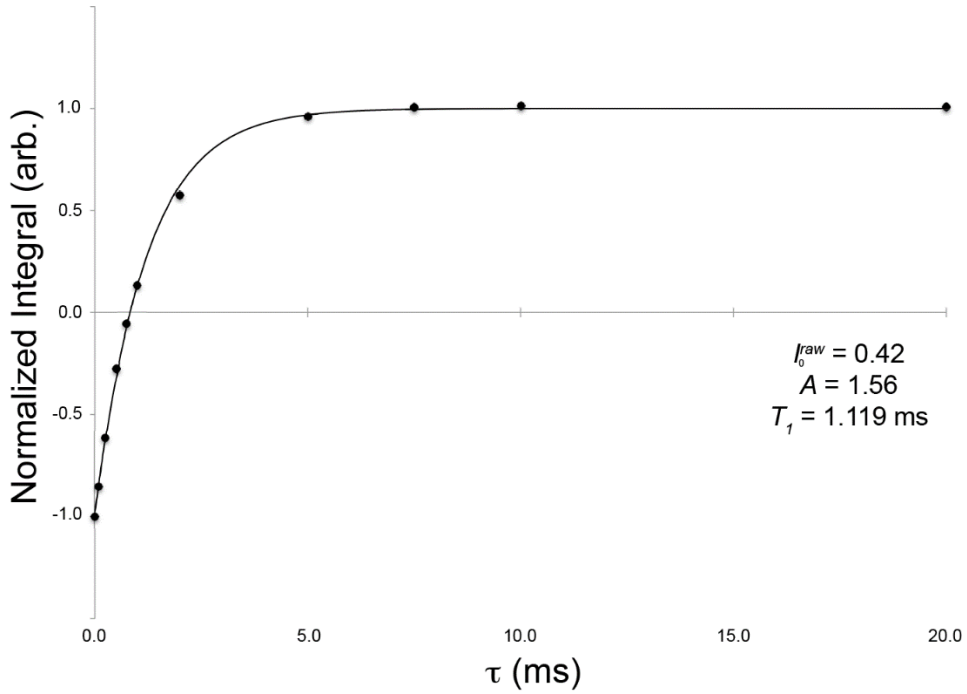

Figure A3.5. Normalized integral versus *t* for peak 2 (60.8 ppm) for inversion recovery experiment.

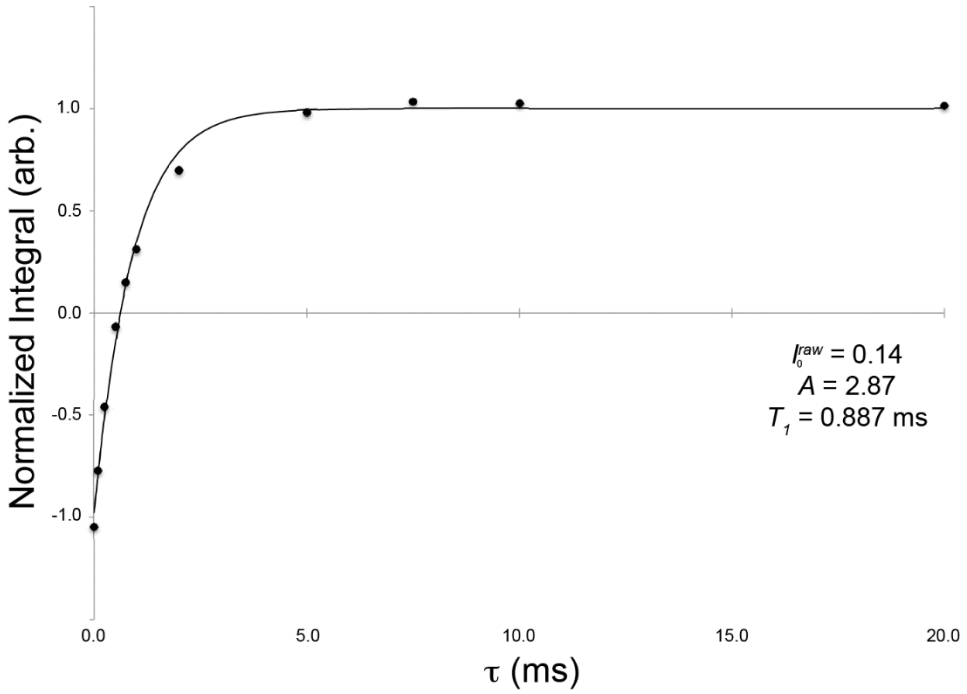

Figure A3.6. Normalized integral versus *t* for peak 3 (57.2 ppm) for inversion recovery experiment.

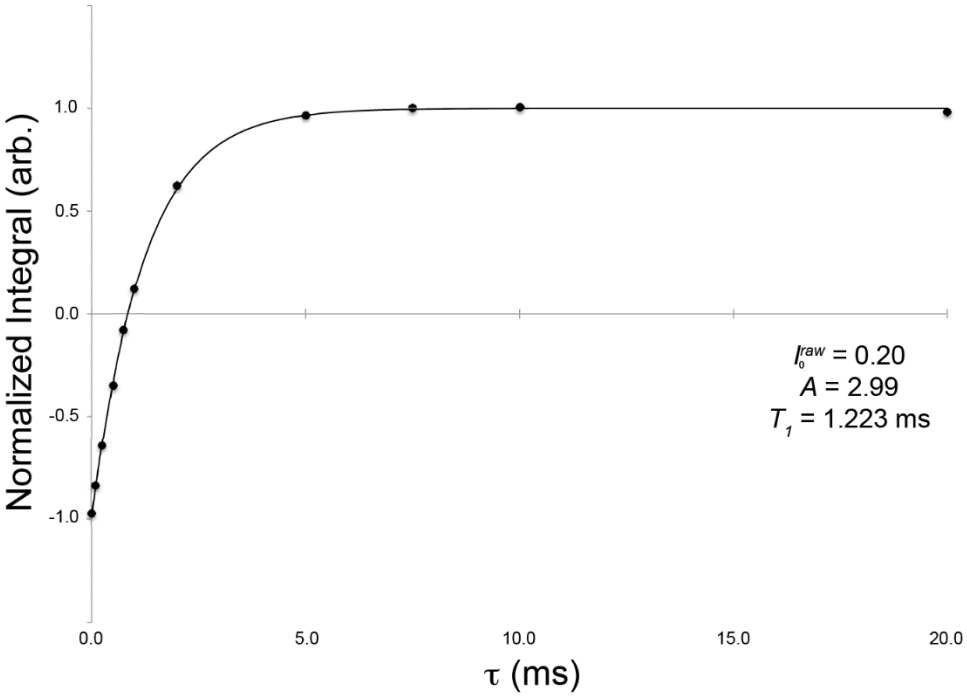

Figure A3.7. Normalized integral versus *t* for peak 4 (53.9 ppm) for inversion recovery experiment.

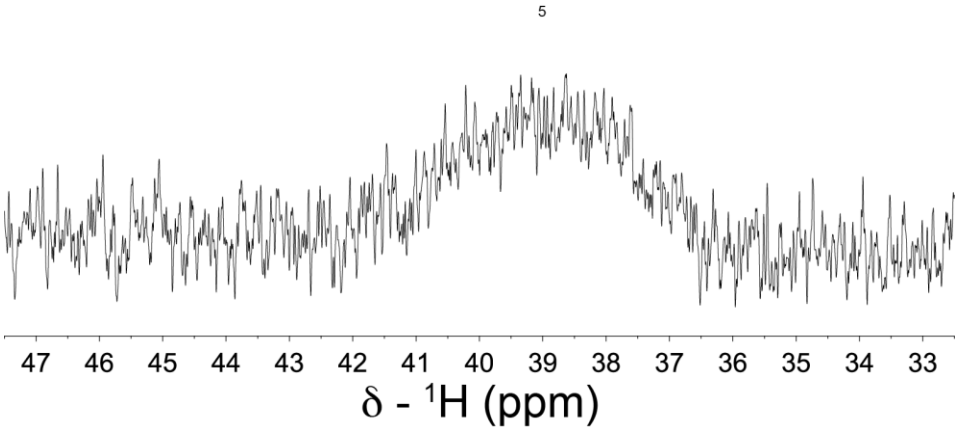

Figure A3.8. 1D ^{1}H NMR spectrum of region between 48 to 32 ppm of $[Mn^{III}(OMe)(dpaq)]^{+}$.

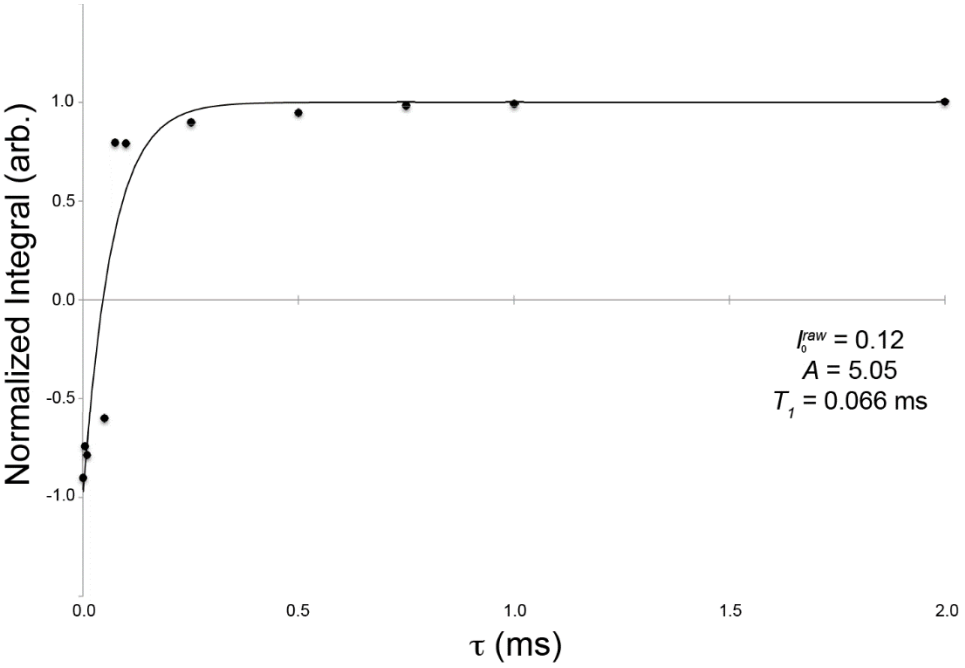

Figure A3.9. Normalized integral versus *t* for peak 5 (38.5 ppm) for inversion recovery experiment.

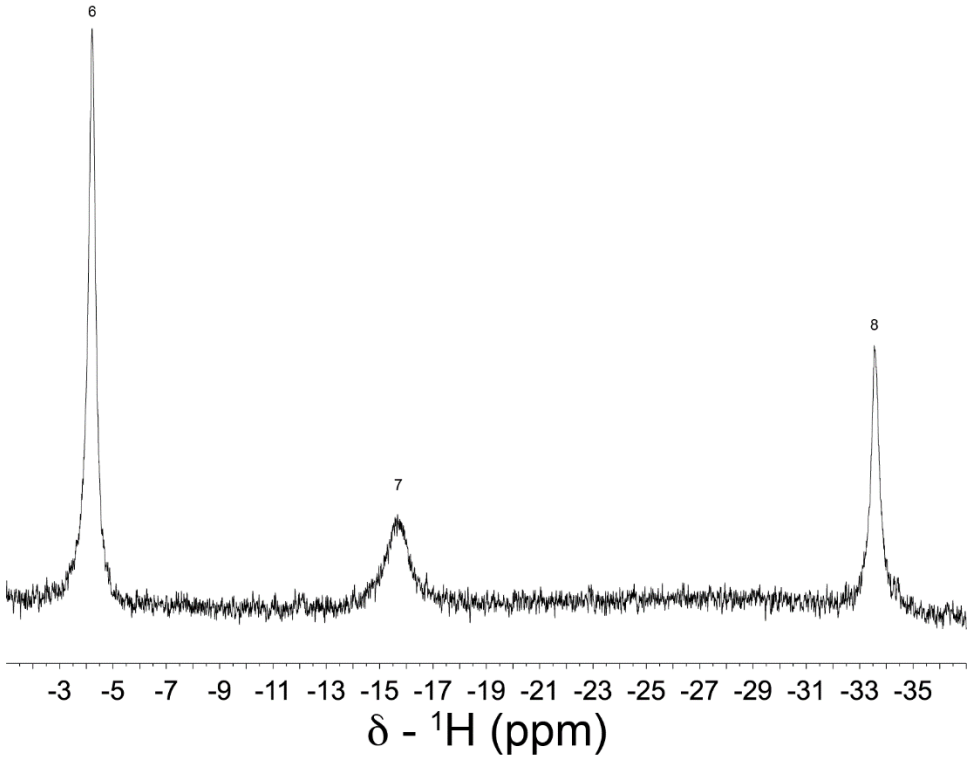

Figure A3.10. 1D ^{1}H NMR spectrum of region between -1 to -37 ppm of $[Mn^{III}(OMe)(dpaq)]^{+}$.

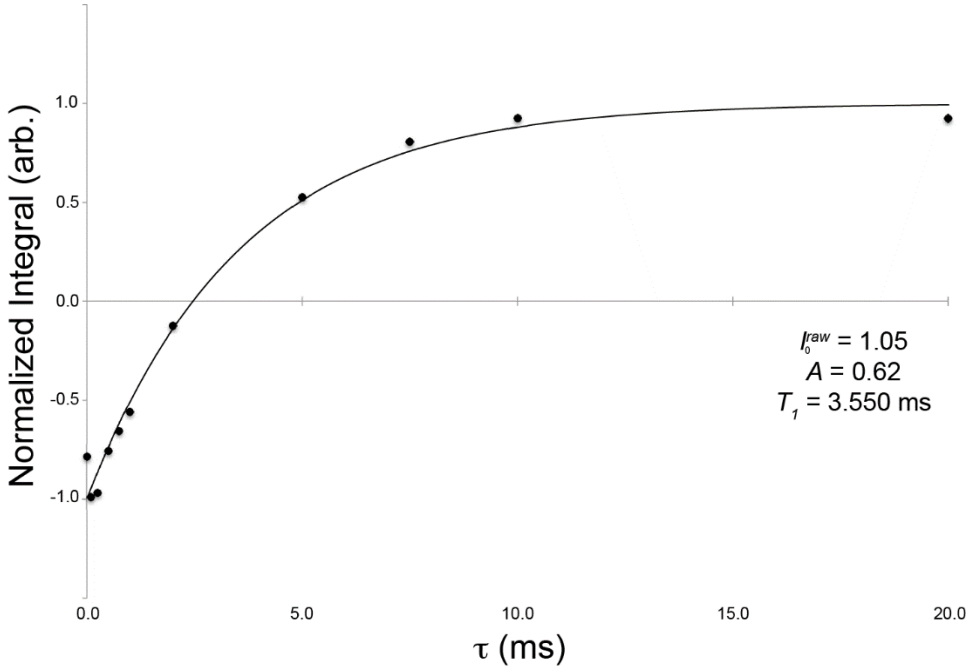

Figure A3.11. Normalized integral versus *t* for peak 6 (-4.2 ppm) for inversion recovery experiment.

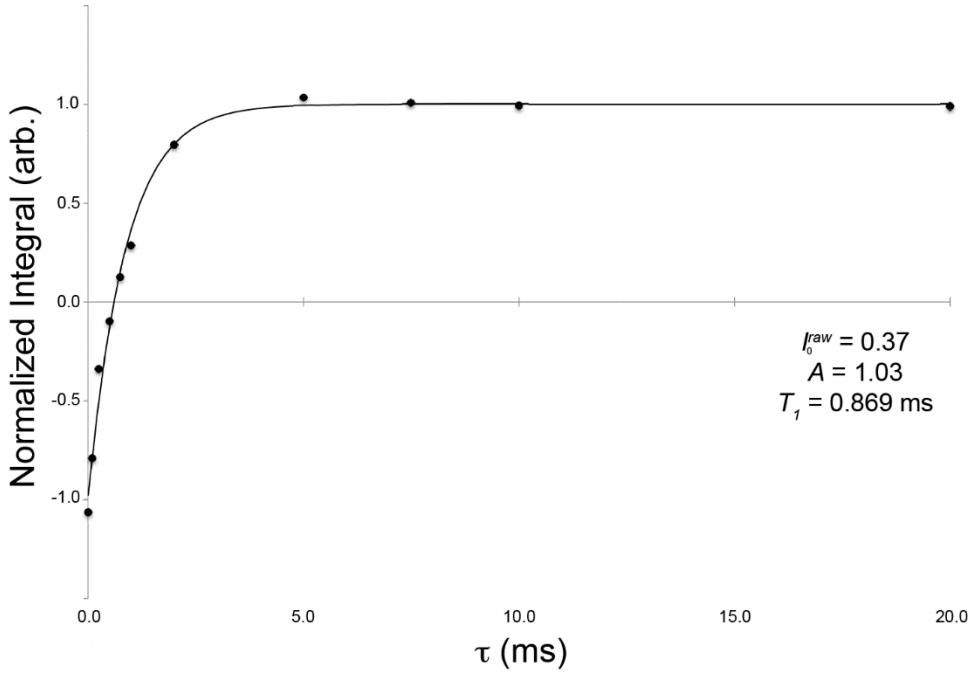

Figure A3.12. Normalized integral versus *t* for peak 7 (-15.7 ppm) for inversion recovery experiment.

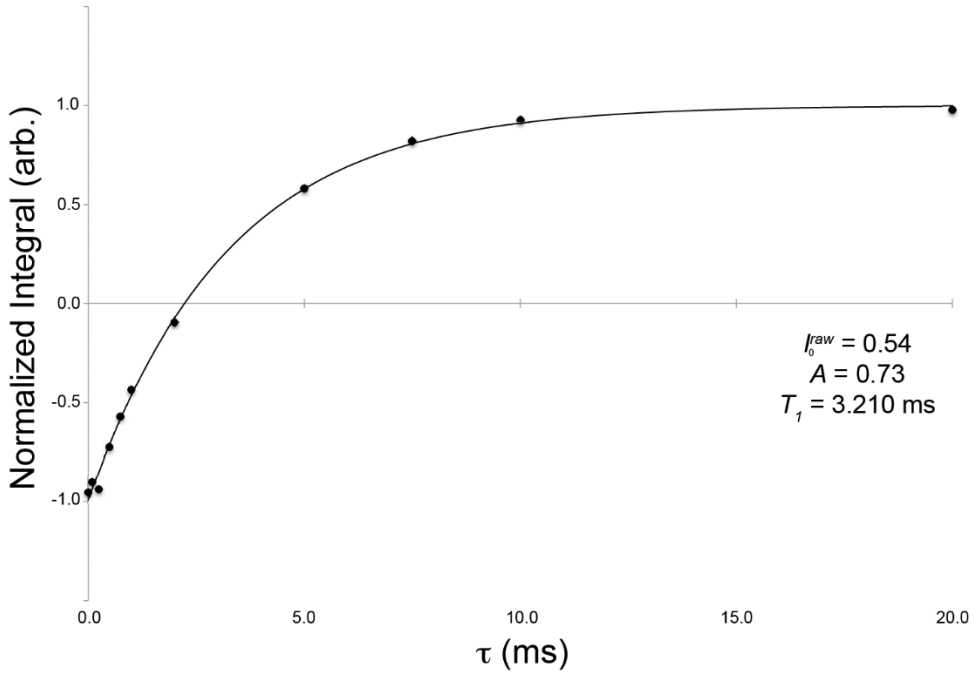

Figure A3.13. Normalized integral versus *t* for peak 8 (-33.6 ppm) for inversion recovery experiment.

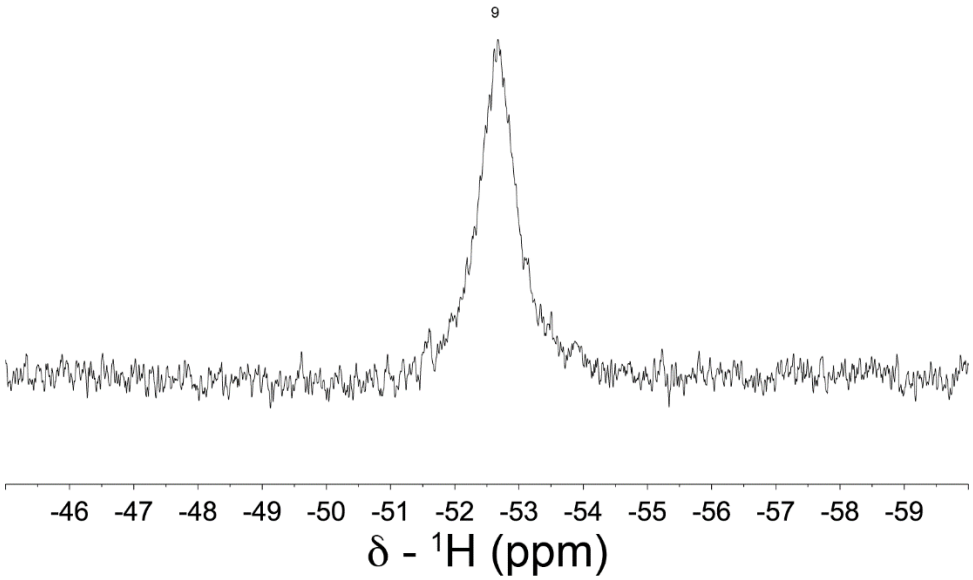

Figure A3.14. 1D ^{1}H NMR spectrum of region between -45 to -60 ppm of $[Mn^{III}(OMe)(dpaq)]^{+}$.

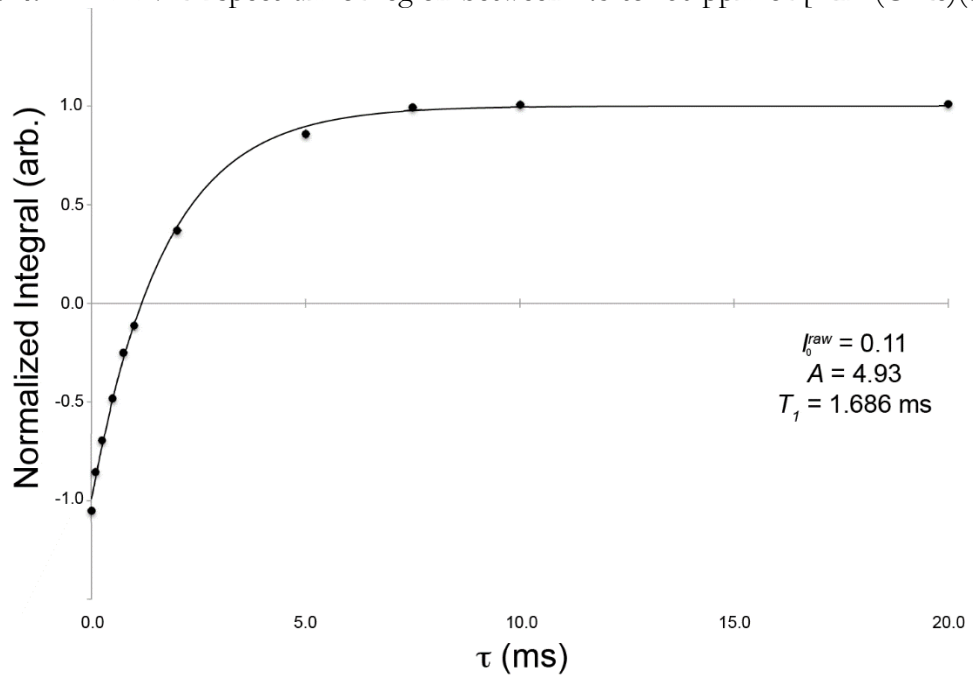

Figure A3.15. Normalized integral versus *t* for peak 9 (-52.7 ppm) for inversion recovery experiment.

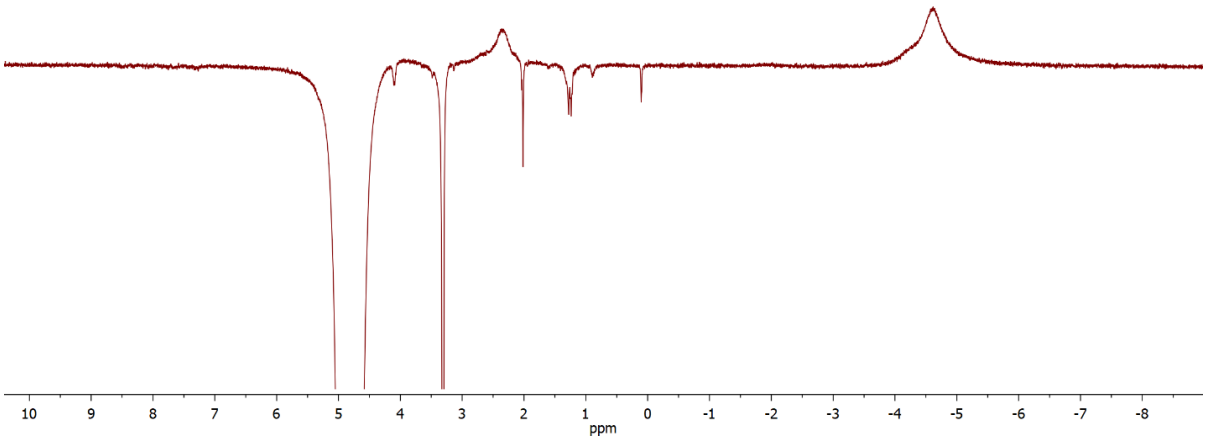

Figure A3.16. 1D ^{1}H-NMR spectrum of an 80 mM solution of $[Mn^{III}(OMe)(dpaq)]^{+}$ in MeOD using the inversion recovery method, with a τ of 0.01s.

Table A3.2. ^{1}H-NMR Chemical Shifts (ppm) for [Mn^{III}(OH)(dpaq)](OTf) Dissolved in CD_3CN, 300 uL of CD_3CN and 45 mL D_2O, and D_2O.

CD_3CN		$CD_3CN + D_2O$	D_2O
paramagnetic	diamagnetic		
130		130	133
65		62	66
60		60	61
54		54	55
33		38	
	27		
	26		
	16.2		
	15.2		
	14.5		
	14.3		
	12.2		
	11.6		
	9.1		
	8.2		
	6.9		
	6.8		
	6.5		
	5.9		
4.7		4.7	
	4.33		
	~2.9		
	1.3		
	-2		
-3		-4	-6
	-5		
-18		-16	-11
-35		-34	-30
-54		-54	-53
		~ -65	~ -60

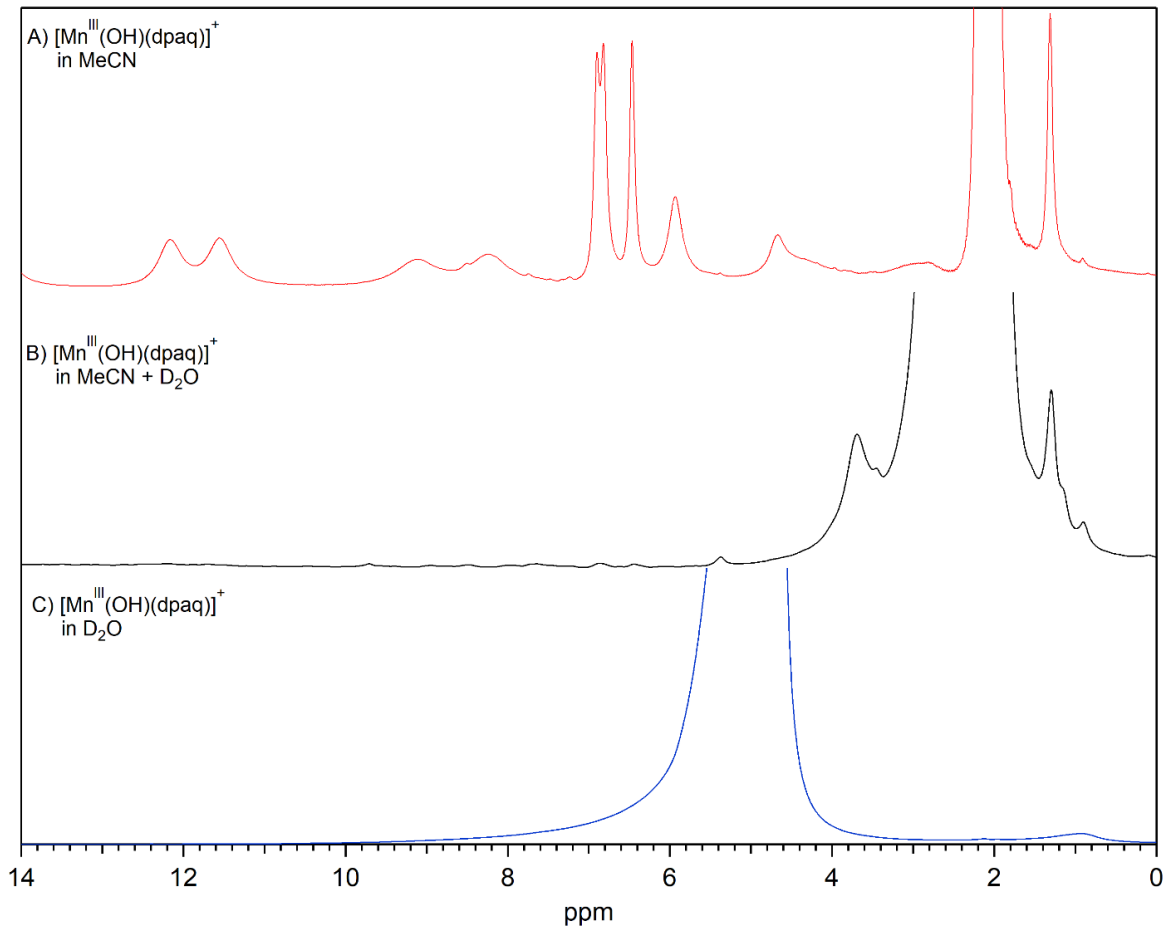

Figure A3.17. Expanded view of the diamagnetic regions of the ^{1}H-NMR spectra of 15 mM [Mn^{III}(OH)(dpaq)](OTf) dissolved in CD_3CN (A), CD_3CN and 45 mL added D_2O (B), and pure D_2O (4 mM) (C).

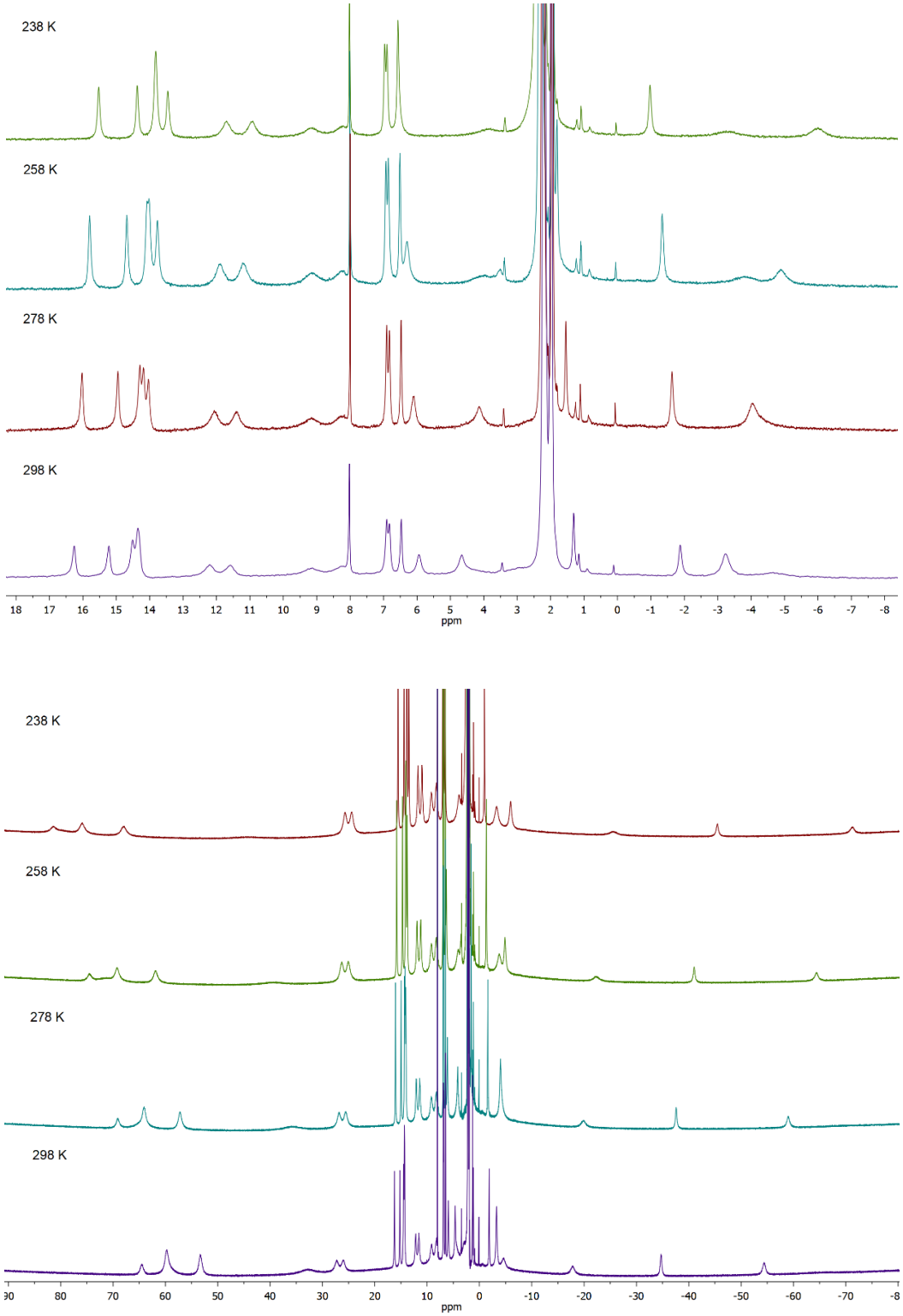

Figure A3.18. Variable-temperature ^{1}H-NMR spectra for 16 mM [Mn^{III}(OH)(dpaq)](OTf) in CD_3CN for diamagnetic region (top) and paramagnetic region (bottom).

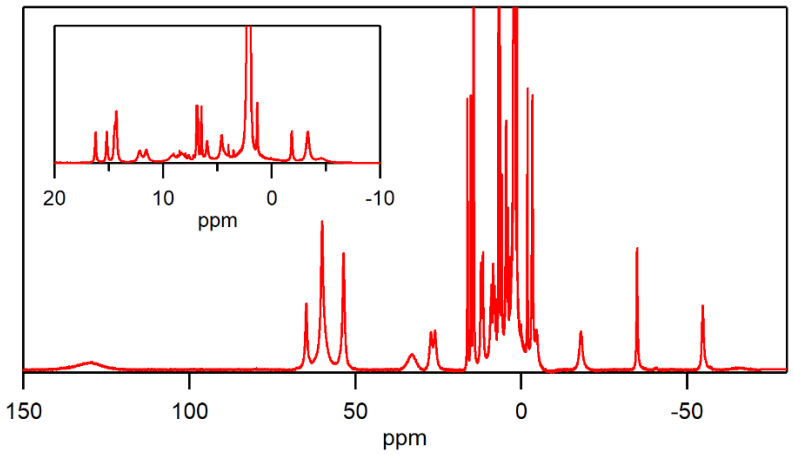

Figure A3.19. ^{1}H-NMR spectrum of 16 mM [Mn^{III}(OH)(dpaq)](OTf) redissolved in CD_3CN after removal of CD_3CN and 45 mL D_2O solvent under vacuum (see Figure 2B).

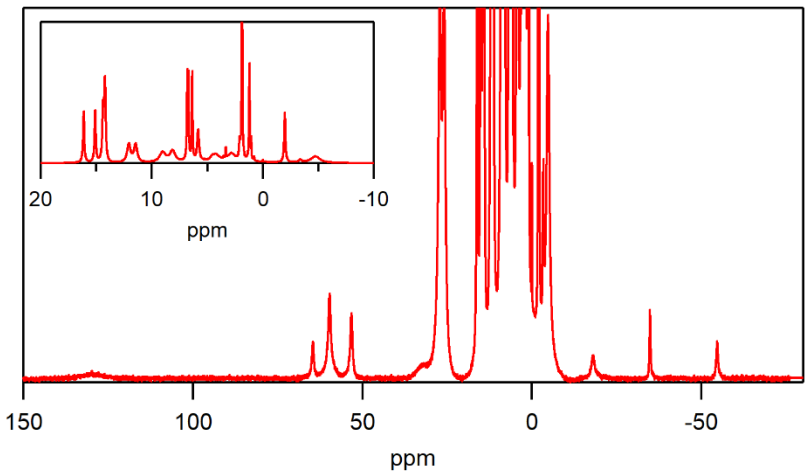

Figure A3.20. ^{1}H-NMR spectrum of 20 mM [Mn^{II}(dpaq)](OTf) following oxidation to the Mn^{III} state using dried O_2.

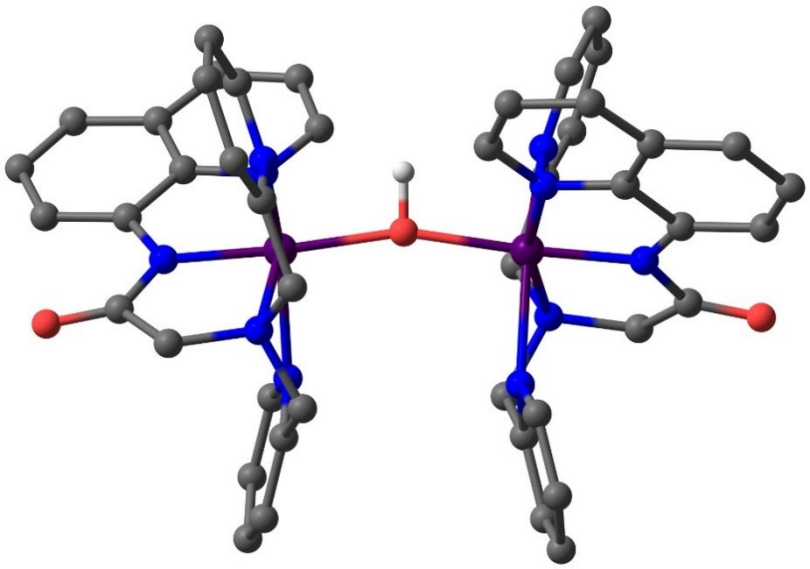

Figure A3.21. Molecular structure of $[Mn^{III}_2(\mu\text{-}OH)(dpaq)_2]^{3+}$ from broken-symmetry DFT geometry optimization.

Table A3.3. Fitted parameters for the ^{1}H NMR resonances of the diamagnetic component of $[Mn^{III}(OH)(dpaq)](OTf)$ in CD_3CN.

d (ppm)	Height	Width(Hz)	L/G	area (x16^5)	Equiv. H
27.29	9	391	0.14	2.96	2
26.04	8	349	0.39	2.43	2
16.23	84	41	0.11	3.03	2
15.19	78	40	0.62	2.52	2
14.48	76	48	0.32	3.11	2
14.31 [a]	113	63	1.39	5.15	4 [a]
12.16	23	127	0.4	2.47	2
11.55	24	130	0.24	2.65	2
9.12	12	200	0.1	2.19	2
8.22	14	200	1.15	2.06	2
6.87	141	26	0.38	3.12	2
6.79	133	26	0.75	2.78	2
6.44	184	19	0.75	2.75	2
5.90	44	61	0.62	2.18	2
4.33	ND [b]	ND [b]	ND [b]	ND [b]	ND [b]
2.95	3	181	2	0.41	2 [c]
1.27	203	19	0.12	3.40	2
-1.92	87	40	0.12	3.03	2
-4.70	5	283	1.36	1.10	2 [c]

[a] Variable-temperature and COSY NMR data demonstrate that the resonance at 14.31 ppm is actually overlapping resonances with chemicals shifts of 14.29 and 14.33 ppm.

[b] Not determined, as this resonance overlaps with an adjacent resonance.

[c] The integrations for these broad bands were 0.54 (resonance at 2.95 ppm) and 0.96 (resonance at -4.70 ppm.

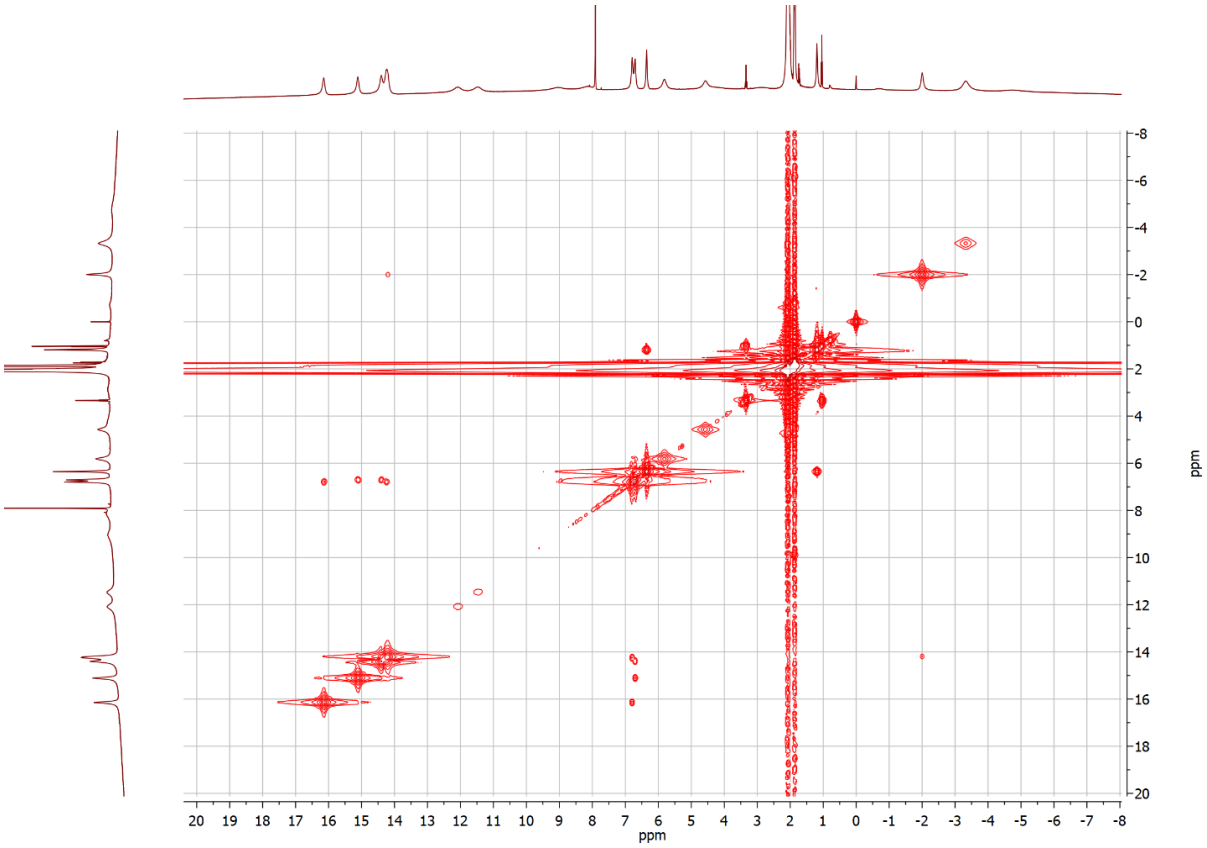

Figure A3.22. COSY NMR data for 16 mM $[Mn^{III}(OH)(dpaq)](OTf)$ in CD_3CN showing cross-peaks for $[Mn^{III}_2(\mu\text{-}O)(dpaq)_2]^{2+}$ protons.

Comment on COSY NMR data for $[Mn^{III}(OH)(dpaq)](OTf)$ in CD_3CN.

The COSY NMR data collected for this diamagnetic species (Figure A3.22) show coupling of only the resonances with narrow linewidths. Protons at 6.79 and 6.87 ppm each couple to two other protons (14.48 and 15.19 ppm and 14.33 and 16.23 ppm, respectively). The coupling of the protons at 6.87 and 6.78 ppm is consistent with their assignment as the γ- or β-H(pyridine) protons or as protons at the 3 or 6 position of the quinoline. The similarity of the chemical shifts of these protons, as well as those of their cross-peaks, would tend to suggest that these are two sets of pyridine protons, but further data would be needed to provide definitive assignments. Additional coupling is observed between resonances at -1.92 and 14.29 ppm, and resonances at 1.27 and 6.43 ppm. With coupling only observed for the narrow resonances, it is difficult to give definitive assignments of the peaks.

Table A3.4. Fitted parameters for the ^{1}H NMR resonances of $[Mn^{III}(OMe)(dpaq)]^+$.[a]

assignment	ppm	height	width(Hz)	L/G[b]	area (x10^6)	normalized area[c]	equiv. H
a-H (py)	130.4	375	4721	0.57	2.82	1.84	2
b-H (py)	61.9	5626	359	0.3	3.36	2.19	2
H (qn)	59.9	1198	890	0.59	1.70	1.11	1
H (qn)	58.2	3214	314	0.31	1.67	1.09	1
b-H (py)	54.9	4975	357	0.09	3.03	1.98	2
CH_2 (am)	39.4	916	1778	0.12	2.77	1.81	2
g-H (py)	-4.5	11748	172	0.45	3.28	2.14	2
H (qn)	-16.2	1930	642	1.0	1.85	1.21	1
H (qn)	-34.3	5225	171	0.03	1.54	1.00	1
H (qn)	-53.9	2907	291	0.1	1.44	0.94	1
a-H (qn)	-66.3	141	3993	0.6	0.89	0.58[d]	1

[a] The positions of the resonances for this sample are slightly shifted compared to the sample use for the T_1 measurements (see Tables 4 and S1). These shifts reflect minor changes in water present in the CD_3OD solutions.
[b] Ratio of Lorentzian to Gaussian lineshape used in the fit.
[c] Peak area normalized relative to the peak at -34 ppm.
[d] Broadening of the peak at -66 likely causes loss of area due to the baseline correction.

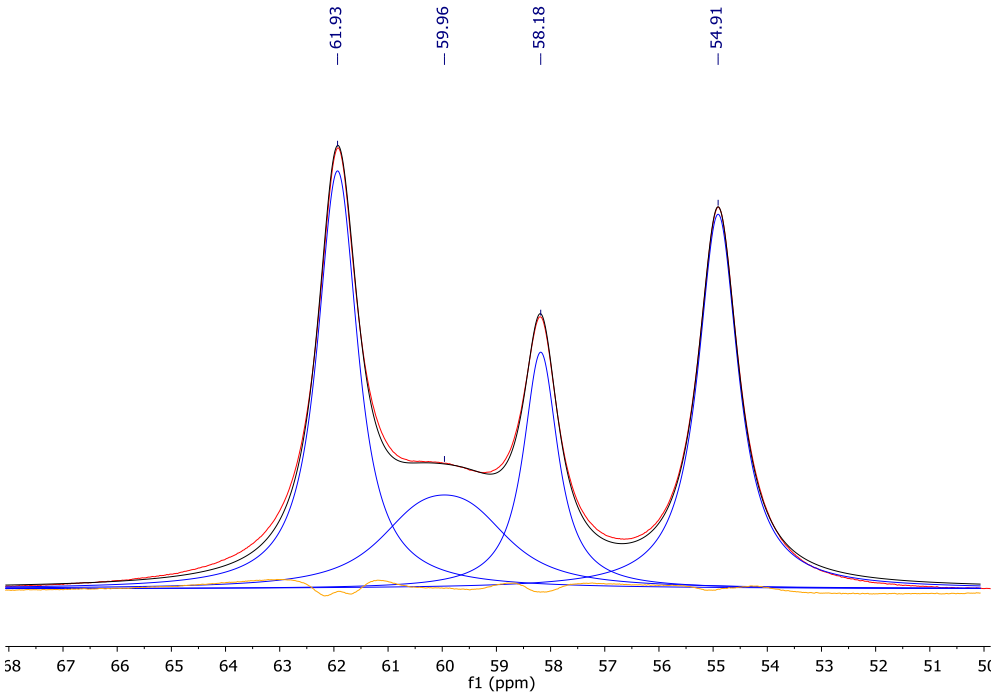

Figure A3.23. Plot showing deconvolution of the peaks between 50 and 58 ppm for $[Mn^{III}(OMe)(dpaq)]^{+}$. Data (red), sum of fits (black), individual fits (blue) and residual (orange) are shown.

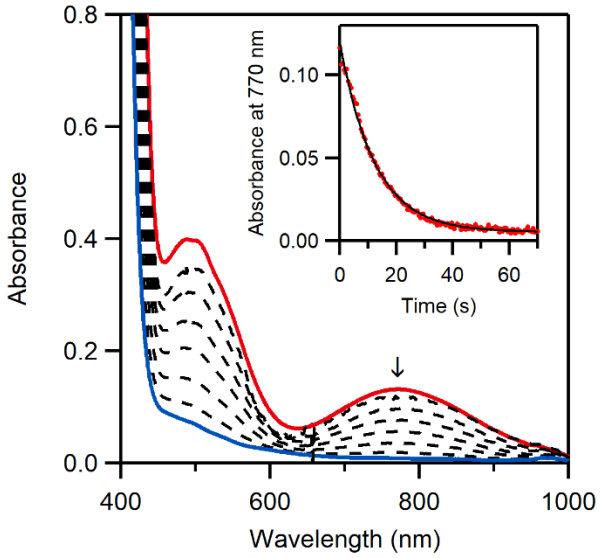

Figure A3.24. Electronic absorption changes upon the addition of 60 equivalents TEMPOH to 1.25 mM $[Mn^{III}(OH)(dpaq)](OTf)$ in CH_3CN with 880 equivalents water.

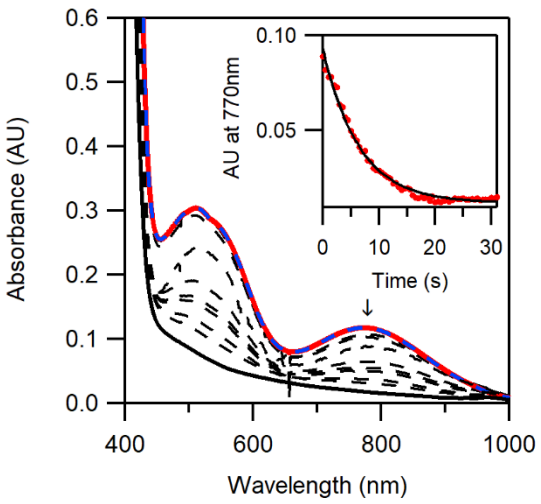

Figure A3.25. Electronic absorption of a 1.25 mM [Mn^{III}(OH)($dpaq^{2Me}$)](OTf) in CH_3CN before (solid red) and after (dashed blue) the addition of 440 equivalents of H_2O. Changes upon addition of 40 equivalents of TEMPOH are shown in dashed and solid black lines. Inset follows 770 nm after the addition of TEMPOH.

Comment of the accuracy and precision of measured integration values for fast relaxing signals.

Ignoring causality and modulation, the NMR signal of a single peak can be represented as a decaying exponential.

$$g(\omega) = \int_{-\infty}^{\infty} Ae\frac{-|t|}{T_2}e^{-i\omega t}dt$$

It can be shown that the total integral of this spectrum equals *A*, the value of the decaying term at time equals zero. In other words, the measured integral of the NMR spectrum should equal the intensity of the time domain signal at time equals zero. Unfortunately, it is not possible to measure the FID at time equals zero. After excitation, but prior to acquisition, a short delay is executed during with the preamplifier is switched from transmit to receive, the receiver gating is opened, the intermediate frequency is added and the digitizer enabled. On the DRX 500 spectrometer used for the bulk of the NMR measurements for this project, the instrument dead time equals 6 μs for the default parameter set. For NMR signals with T_2* equal to 1 s (a conservative estimate for a diamagnetic organic molecule), the expected error in the measured integral value is less than 0.001% ($= e^{-\frac{0.000006}{1}}$). Hence, signal loss during the instrument dead time is not an issue for most

compounds. For signals with very small T_2* (*e.g.* due to relaxation with unpaired electrons in paramagnetic compounds), the error in the integral value can become significant. Neither T_2 nor T_2* values were measured for any compound in this study. T_1 values were measured for $[Mn^{III}(OMe)(dpaq)]^+$ (Table 4) and line width were measured for $[Mn^{III}(OMe)(dpaq)]^+$. (Table A3.3). Estimating T_2* as the inverse of p times the line width, and recalling that $T_1 \geq T_2$*, we can estimate the error due signal loss during dead time. For signals with T_2* greater than 20 μs, the expected error is less than ca. 10%. For the fastest relaxing signals, a-H (py) and a-H (qn) errors greater than 25% are anticipated ($= e^{-\frac{0.000006}{0.000017}}$).

Appendix 4

Table A4.1. Crystal data and structure refinement for $[Mn^{III}Mn^{III}(\mu\text{-}O)(dpaq^{5Cl})_2](OTf)_2$.

Identification code	q54h (**1**)	
Empirical formula	C50.80 H38 Cl2 F6 Mn2 N11.40 O9 S2	
Formula weight	1311.05	
Temperature	200(2) K	
Wavelength	1.54178 Å	
Crystal system	Monoclinic	
Space group	$P2_1/n$	
Unit cell dimensions	a = 22.5110(4) Å	α= 90°.
	b = 11.9178(2) Å	β= 122.9220(10)°.
	c = 24.3401(4) Å	γ = 90°.
Volume	5481.35(17) $Å^3$	
Z	4	
Density (calculated)	1.589 Mg/m^3	
Absorption coefficient	6.123 mm^{-1}	
F(000)	2658	
Crystal size	0.185 x 0.055 x 0.010 mm^3	
Theta range for data collection	2.156 to 70.507°.	
Index ranges	-16<=h<=27, -14<=k<=14, -29<=l<=28	
Reflections collected	54994	
Independent reflections	10108 [R(int) = 0.0810]	
Completeness to theta = 66.000°	98.4 %	
Absorption correction	Multi-scan	
Max. and min. transmission	1.000 and 0.625	
Refinement method	Full-matrix least-squares on F^2	
Data / restraints / parameters	10108 / 60 / 745	
Goodness-of-fit on F^2	1.014	
Final R indices [I>2sigma(I)]	R1 = 0.0698, wR2 = 0.1863	
R indices (all data)	R1 = 0.0890, wR2 = 0.2057	
Extinction coefficient	n/a	
Largest diff. peak and hole	1.030 and -1.098 $e.Å^{-3}$	

Table A4.2. Crystal data and structure refinement for [Mn^{III}(OH)($dpaq^{5Cl}$)](OTf).

Identification code	q70g (**2**)	
Empirical formula	C26 H23 Cl F3 Mn N6 O5 S	
Formula weight	678.95	
Temperature	200(2) K	
Wavelength	1.54178 Å	
Crystal system	Monoclinic	
Space group	P21/n	
Unit cell dimensions	a = 9.2731(2) Å	α= 90°.
	b = 24.9494(5) Å	β= 96.7746(10)°.
	c = 12.5251(2) Å	γ = 90°.
Volume	2877.55(10) Å3	
Z	4	
Density (calculated)	1.567 Mg/m3	
Absorption coefficient	5.868 mm-1	
F(000)	1384	
Crystal size	0.180 x 0.170 x 0.075 mm3	
Theta range for data collection	3.543 to 70.193°.	
Index ranges	-9<=h<=11, -30<=k<=30, -14<=l<=15	
Reflections collected	32798	
Independent reflections	5367 [R(int) = 0.0577]	
Completeness to theta = 66.000°	99.9 %	
Absorption correction	Multi-scan	
Max. and min. transmission	1.000 and 0.623	
Refinement method	Full-matrix least-squares on F2	
Data / restraints / parameters	5367 / 19 / 427	
Goodness-of-fit on F2	1.052	
Final R indices [I>2sigma(I)]	R1 = 0.0445, wR2 = 0.1101	
R indices (all data)	R1 = 0.0490, wR2 = 0.1145	
Extinction coefficient	0.00153(16)	
Largest diff. peak and hole	1.013 and -0.404 e.Å-3	

Table A4.3. Crystal data and structure refinement for $[Mn^{III}Mn^{III}(\mu\text{-}O)(dpaq^{5OMe})_2](OTf)_2$.

Identification code	v37d (**3**)	
Empirical formula	C25 H23 F3 Mn N5 O6 S	
Formula weight	633.48	
Temperature	200(2) K	
Wavelength	1.54178 Å	
Crystal system	Monoclinic	
Space group	C2/c	
Unit cell dimensions	a = 15.9338(4) Å	α= 90°.
	b = 13.7093(4) Å	β= 97.5194(11)°.
	c = 24.2609(7) Å	γ = 90°.
Volume	5254.0(3) $Å^3$	
Z	8	
Density (calculated)	1.602 Mg/m^3	
Absorption coefficient	5.484 mm^{-1}	
F(000)	2592	
Crystal size	0.360 x 0.100 x 0.045 mm^3	
Theta range for data collection	3.675 to 68.063°.	
Index ranges	-18<=h<=18, -16<=k<=14, -29<=l<=28	
Reflections collected	16874	
Independent reflections	4663 [R(int) = 0.0303]	
Completeness to theta = 66.000°	99.3 %	
Absorption correction	Multi-scan	
Max. and min. transmission	1.000 and 0.610	
Refinement method	Full-matrix least-squares on F^2	
Data / restraints / parameters	4663 / 1 / 376	
Goodness-of-fit on F^2	1.089	
Final R indices [I>2sigma(I)]	R1 = 0.0751, wR2 = 0.2025	
R indices (all data)	R1 = 0.0808, wR2 = 0.2071	
Extinction coefficient	n/a	
Largest diff. peak and hole	1.448 and -0.984 $e.Å^{-3}$	

Table A4.4. Crystal data and structure refinement for $[Mn^{III}Mn^{III}(\mu\text{-}O)(dpaq^{5NO2})_2](OTf)_2$.

Identification code	v44d (**4**)	
Empirical formula	C26 H19 F3 Mn N7 O6.50 S	
Formula weight	677.48	
Temperature	200(2) K	
Wavelength	1.54178 Å	
Crystal system	Monoclinic	
Space group	C2/c	
Unit cell dimensions	a = 18.8904(6) Å	α= 90°.
	b = 15.0186(4) Å	β= 90.4914(8)°.
	c = 20.3612(6) Å	γ = 90°.
Volume	5776.4(3) $Å^3$	
Z	8	
Density (calculated)	1.558 Mg/m^3	
Absorption coefficient	5.069 mm^{-1}	
F(000)	2752	
Crystal size	0.280 x 0.190 x 0.190 mm^3	
Theta range for data collection	3.760 to 68.116°.	
Index ranges	-20<=h<=22, -17<=k<=17, -23<=l<=24	
Reflections collected	22831	
Independent reflections	5157 [R(int) = 0.0246]	
Completeness to theta = 66.000°	99.4 %	
Absorption correction	Multi-scan	
Max. and min. transmission	1.000 and 0.824	
Refinement method	Full-matrix least-squares on F^2	
Data / restraints / parameters	5157 / 50 / 506	
Goodness-of-fit on F^2	1.036	
Final R indices [I>2sigma(I)]	R1 = 0.0561, wR2 = 0.1608	
R indices (all data)	R1 = 0.0586, wR2 = 0.1644	
Extinction coefficient	n/a	
Largest diff. peak and hole	0.875 and -0.871 $e.Å^{-3}$	

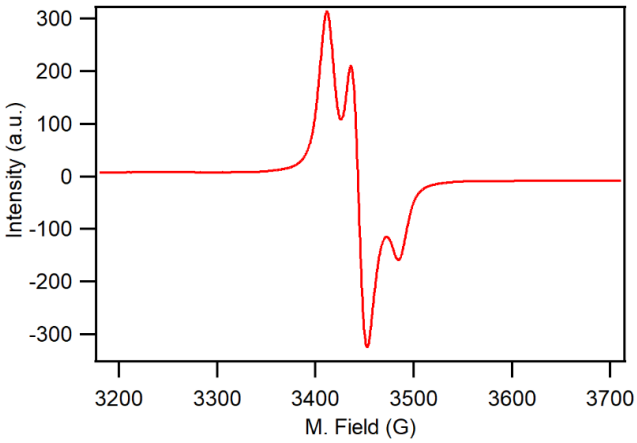

Figure A4.1. Perpendicular-mode, X-band EPR spectrum at 10 K of a solution of $[Mn^{III}(OH)(dpaq^{5Cl})]^+$ following reaction with TEMPOH.

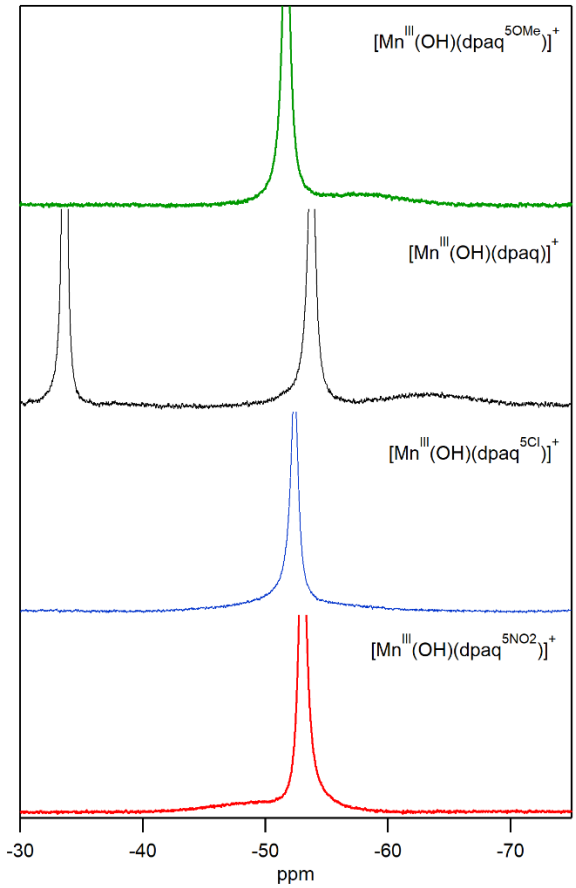

Figure A4.2. ^{1}H NMR spectra of 15 mM solutions of $[Mn^{III}(OH)(dpaq^{5R})]^+$ complexes from Figure 3 magnified from -30 to -75 ppm to show the weak, broad resonance observed for $[Mn^{III}(OH)(dpaq^{5OMe})]^+$, $[Mn^{III}(OH)(dpaq)]^+$, and $[Mn^{III}(OH)(dpaq^{5NO2})]^+$. The resonance is not observed for $[Mn^{III}(OH)(dpaq^{5Cl})]^+$.

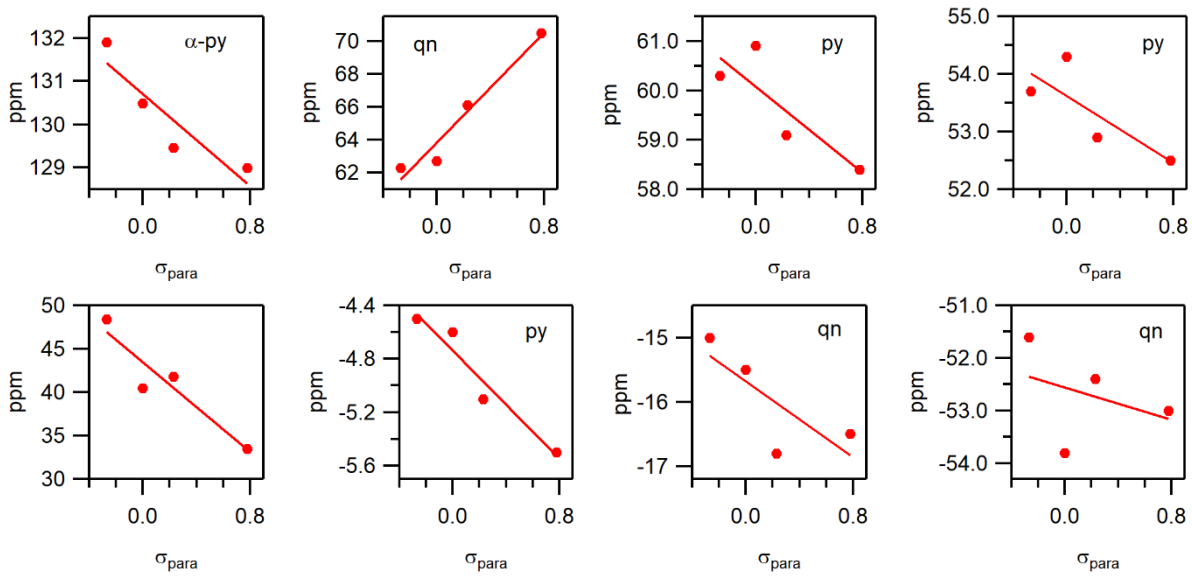

Figure A4.3. NMR chemical shifts (ppm) for $[Mn^{III}(OH)(dpaq^{5R})]^+$ as a function of Hammett σ_{para} parameter.

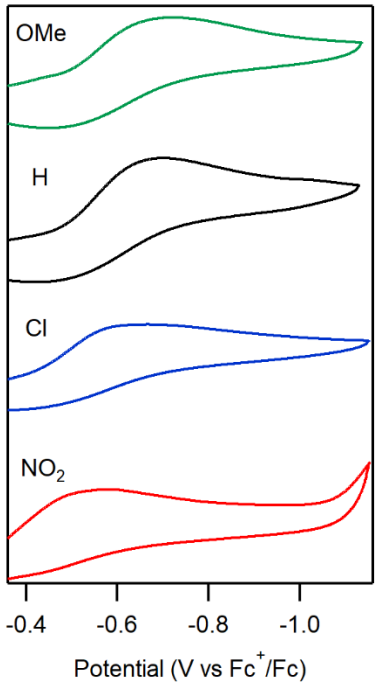

Figure A4.4. Cyclic voltammetry traces of $[Mn^{III}(OH)(dpaq^{5R})]^+$ complexes showing the Mn^{III}/Mn^{II} wave with a scan rate of 100 mV s^{-1}.

Table A4.5. DFT-Calculated Thermodynamic Parameters Used to Determine Mn^{II}-OH_2 BDFEs for the $[Mn^{II}(OH_2)(dpaq^{R})]^{+}$ Complexes.

Ligand	$\Delta G(Mn^{II}(OH) - Mn^{III}(OH))^{a}$	$\Delta G(Mn^{II}(OH_2) - Mn^{II}(OH))^{a}$	$E_{1/2}{}^{b}$	pK_a	BDFE[a]
$dpaq^{5OMe}$	-76.8	-294.0	-0.66	19.5	66.3
dpaq	-77.7	-293.7	-0.62	19.3	67.0
$dpaq^{5Cl}$	-79.2	-293.0	-0.56	18.8	67.7
$dpaq^{5NO2}$	-81.8	-291.8	-0.44	17.9	69.2
$dpaq^{2Me}$	-80.1	292.9	-0.52	18.7	68.5
PY5	-96.0	-285.1	-	-	-

[a]Values in kcal mol^{-1}. [b] Values based on the experimental PY5 Mn^{III}/Mn^{II} potential of 0.17 V vs Fc^{+}/Fc in MeCN. [c]Values based on using the experimental pK_a of $[Mn^{II}(OH_2)(PY5)]^{2+}$ of 13.

Appendix 5

Coordinates for Chapter 2

Cartesian coordinates (Å) for a DFT-optimized model of $[Mn^{III}(OH)(dpaq)]^{+}$.

Mn	0.000000	0.000000	0.000000
O	-0.000000	0.000000	-1.845954
O	-0.027796	1.211379	3.939820
N	-0.044325	-2.064887	0.278338
N	0.003548	-0.067270	1.984492
N	0.019128	2.201008	0.374748
N	-2.180663	0.532706	0.073101
N	2.170215	0.532706	-0.017678
C	-0.054256	-3.012534	-0.666678
C	-0.091747	-4.389927	-0.347535
C	-0.120990	-4.778027	0.987755
C	-0.109501	-3.793251	2.018075
C	-0.134402	-4.089895	3.412918
C	-0.116349	-3.046618	4.331527
C	-0.072804	-1.684158	3.927923
C	-0.047166	-1.346625	2.565345
C	-0.068382	-2.419026	1.609643
C	0.012246	1.100904	2.699417
C	4.801256	1.468625	0.032485
C	4.533731	0.093814	0.132661
C	0.116779	2.379461	1.857746
C	-1.242540	2.757271	-0.179958
C	-2.426749	1.863610	0.117549
C	-3.715232	2.366437	0.356808
C	-4.774262	1.462630	0.536828
C	-4.513173	0.084476	0.478265
C	-3.196695	-0.337113	0.250273
C	1.208834	2.739893	-0.336359
C	2.420099	1.858443	-0.123590
C	3.729083	2.365606	-0.092725
C	3.198765	-0.330156	0.108797
H	-0.909056	-0.041104	-2.215959
H	-0.030155	-2.656976	-1.707539
H	-0.097993	-5.130390	-1.159339
H	-0.152050	-5.843976	1.261187
H	-0.166727	-5.139450	3.741200
H	-0.135329	-3.270221	5.409220
H	-0.058229	-0.886643	4.678745
H	5.836208	1.841143	0.058269
H	5.342161	-0.643605	0.235676
H	1.091021	2.846358	2.110686
H	-0.660264	3.086916	2.212986
H	-1.123491	2.810932	-1.282057
H	-1.424997	3.790737	0.183742
H	-3.881455	3.452741	0.399125
H	-5.793108	1.832244	0.726157
H	-5.311349	-0.658782	0.614107
H	-2.940091	-1.406771	0.207286
H	0.971591	2.745184	-1.420343
H	1.422847	3.787794	-0.035990
H	3.900194	3.449503	-0.166944
H	2.937521	-1.395960	0.195542

Cartesian coordinates (Å) for a DFT-optimized model of $[Mn^{III}(OH)(dpaq^{2Me})]^{+}$.

Mn	0.000000	0.000000	0.000000
O	-0.013679	-1.688142	3.762031
O	-0.000000	0.000000	-1.849270

N	0.011953	2.091849	0.548243
N	-0.024356	-0.175889	1.975466
N	-0.007939	-2.239472	0.114437
N	2.157544	-0.507150	0.026664
N	-2.153803	-0.507150	-0.057463
C	0.023592	3.196355	-0.229269
C	-0.004413	4.497283	0.353376
C	-0.033638	4.653711	1.727585
C	-0.040879	3.506706	2.569512
C	-0.071973	3.586047	3.992027
C	-0.082085	2.415834	4.739221
C	-0.063835	1.141226	4.117217
C	-0.034725	1.019181	2.716716
C	-0.020204	2.222795	1.928054
C	-0.025933	-1.424084	2.543478
C	-0.066900	-2.598563	1.560191
C	1.246766	-2.692966	-0.535250
C	2.423555	-1.825118	-0.141002
C	3.726476	-2.331407	-0.012183
C	4.775559	-1.445352	0.279031
C	4.491363	-0.080107	0.442185
C	3.163123	0.345607	0.314479
C	-1.212543	-2.675883	-0.635484
C	-2.411985	-1.812771	-0.305795
C	-3.724523	-2.312036	-0.312353
C	-4.789218	-1.429624	-0.072797
C	-4.511618	-0.075747	0.175677
C	-3.174634	0.341764	0.179935
C	0.095004	3.065749	-1.723502
H	0.895193	0.132931	-2.229742
H	-0.000584	5.371721	-0.312494
H	-0.052940	5.657672	2.179171
H	-0.086660	4.575391	4.473542
H	-0.106377	2.464612	5.838764
H	-0.072359	0.231238	4.726043
H	-0.998376	-3.163544	1.771711
H	0.765872	-3.284172	1.820279
H	1.457327	-3.761413	-0.315401
H	1.104457	-2.601380	-1.631795
H	3.910397	-3.408134	-0.139274
H	5.804710	-1.819734	0.384970
H	5.280542	0.648863	0.673313
H	2.885929	1.401984	0.450084
H	-1.439098	-3.749081	-0.458286
H	-0.991686	-2.552303	-1.715591
H	-3.903397	-3.380020	-0.504161
H	-5.826030	-1.797954	-0.073394
H	-5.313411	0.650158	0.371481
H	-2.904493	1.389596	0.381880
H	-0.514883	2.220415	-2.090661
H	1.142387	2.866134	-2.037522
H	-0.221904	4.006925	-2.209176

Cartesian coordinates (Å) for a DFT-optimized model of the transition state for $[Mn^{III}(OH)(dpaq)]^+$ and TEMPOH.

Mn	0.000000	0.000000	0.000000
O	-0.000000	0.000000	-2.053069
H	-0.919986	-0.002761	-2.395068
O	-0.206516	1.179370	4.042980
N	-0.033306	-2.135899	0.350983
N	-0.082407	-0.095004	2.078190
N	-0.010587	2.246661	0.495194

N	-2.190477	0.570851	-0.099085
N	2.177957	0.570851	0.056982
C	-0.001639	-3.105961	-0.568833
C	-0.024598	-4.479780	-0.229397
C	-0.084087	-4.838829	1.111518
C	-0.120037	-3.831948	2.120288
C	-0.180681	-4.119014	3.515862
C	-0.210901	-3.068319	4.425278
C	-0.183177	-1.711711	4.006037
C	-0.122863	-1.374730	2.641568
C	-0.091810	-2.460903	1.687470
C	-0.119001	1.056552	2.798607
C	4.766463	1.507513	0.563697
C	4.513399	0.129763	0.474414
C	-0.015932	2.361152	1.984420
C	-1.236674	2.808822	-0.123078
C	-2.430566	1.896228	0.067242
C	-3.718819	2.384373	0.336456
C	-4.787695	1.477411	0.420496
C	-4.535438	0.108719	0.238149
C	-3.218765	-0.299882	-0.013527
C	1.224213	2.803325	-0.112519
C	2.416855	1.903429	0.139587
C	3.701834	2.407869	0.397150
C	3.200965	-0.292983	0.223463
H	0.043540	-2.778466	-1.619179
H	0.004434	-5.235972	-1.026442
H	-0.104078	-5.898714	1.409509
H	-0.202271	-5.167228	3.850354
H	-0.257700	-3.282260	5.504511
H	-0.208820	-0.904112	4.746417
H	5.781546	1.879458	0.768430
H	5.314717	-0.611782	0.601640
H	0.914017	2.865782	2.320488
H	-0.846564	3.020353	2.312774
H	-1.047920	2.895824	-1.213710
H	-1.461764	3.830734	0.252413
H	-3.877842	3.463644	0.476115
H	-5.806095	1.836796	0.631165
H	-5.340553	-0.637475	0.294810
H	-2.970421	-1.363540	-0.153646
H	1.058842	2.857748	-1.209266
H	1.433292	3.837114	0.239150
H	3.860673	3.493853	0.468896
H	2.953038	-1.363469	0.153220
C	1.403392	0.430001	-7.209609
C	0.793646	1.155623	-5.975952
N	1.623081	0.799285	-4.752449
C	3.135794	0.942068	-4.800529
C	3.652922	0.222418	-6.079572
C	2.914899	0.644892	-7.355361
C	3.733038	0.273383	-3.552601
C	3.551972	2.429711	-4.777527
C	-0.649604	0.672945	-5.751285
C	0.746698	2.686665	-6.181894
O	1.210308	-0.323583	-4.131743
H	1.198197	-0.657450	-7.098999
H	0.863868	0.767114	-8.120365
H	4.744358	0.408155	-6.170801
H	3.524163	-0.871655	-5.928338
H	3.292314	0.053853	-8.216259
H	3.135773	1.706571	-7.600110

H	3.496291	-0.804473	-3.506105
H	4.834175	0.394232	-3.579265
H	3.356825	0.753071	-2.627478
H	4.640827	2.489461	-4.579470
H	3.366004	2.959205	-5.727606
H	3.026006	2.972820	-3.967875
H	-0.703838	-0.421995	-5.615123
H	-1.103627	1.163205	-4.866261
H	-1.253904	0.948626	-6.638360
H	-0.053886	2.920470	-6.911740
H	0.506804	3.204454	-5.232582
H	1.683755	3.111275	-6.582634
H	0.634788	-0.110827	-3.001203

Cartesian coordinates (Å) for a DFT-optimized model of the transition state for $[Mn^{III}(OH)(dpaq^{2Me})]^+$ and TEMPOH.

Mn	0.000000	0.000000	0.000000
O	0.492438	1.816095	-3.763377
N	0.034916	-2.099009	-0.694713
N	0.206867	0.235634	-2.050310
N	-0.013983	2.294376	-0.143017
N	2.191661	0.555642	0.202820
N	-2.177843	0.555642	0.014208
C	-0.100315	-3.230089	0.025706
C	0.033267	-4.510195	-0.584664
C	0.306816	-4.610056	-1.938038
C	0.441524	-3.431637	-2.724531
C	0.709895	-3.464109	-4.124153
C	0.816509	-2.269343	-4.823570
C	0.660334	-1.017280	-4.175899
C	0.394488	-0.933140	-2.796050
C	0.289843	-2.169781	-2.051645
C	0.264604	1.490182	-2.574590
C	-0.063775	2.629169	-1.593119
C	1.228271	2.774422	0.507760
C	2.421100	1.893456	0.193273
C	3.704187	2.418905	-0.026571
C	4.778339	1.536723	-0.226850
C	4.536678	0.154327	-0.206512
C	3.224710	-0.290698	0.004668
C	-1.232930	2.728270	0.583158
C	-2.426403	1.876648	0.199372
C	-3.721657	2.405688	0.078332
C	-4.785494	1.542284	-0.228871
C	-4.521924	0.176485	-0.416561
C	-3.199867	-0.270965	-0.290726
C	-0.391533	-3.128358	1.497971
H	-0.083847	-5.410281	0.035219
H	0.415952	-5.595116	-2.418020
H	0.826043	-4.436656	-4.625981
H	1.024030	-2.281591	-5.904950
H	0.743475	-0.086442	-4.747634
H	-1.090743	2.962802	-1.851042
H	0.602549	3.487099	-1.822233
H	1.448347	3.831996	0.244730
H	1.063581	2.740136	1.604795
H	3.855392	3.508219	-0.038008
H	5.792298	1.926483	-0.401876
H	5.345917	-0.573918	-0.358016
H	2.984923	-1.365508	0.016206
H	-1.455435	3.806138	0.425530
H	-1.040561	2.581671	1.666749

H	-3.889709	3.483434	0.219753
H	-5.808356	1.935145	-0.329228
H	-5.321728	-0.535589	-0.664232
H	-2.942200	-1.330653	-0.442546
H	-1.235813	-2.440647	1.697824
H	0.483881	-2.725499	2.046910
H	-0.633797	-4.121271	1.918754
O	-0.000000	0.000000	2.056920
H	0.926012	-0.006626	2.381743
C	-1.167727	0.167846	7.179719
C	-0.751099	1.012702	5.942028
N	-1.653551	0.624931	4.779488
C	-3.161056	0.624860	4.968803
C	-3.487882	-0.204343	6.245150
C	-2.672670	0.225397	7.471566
C	-3.809753	-0.032560	3.739678
C	-3.708478	2.064978	5.076681
C	0.704975	0.697553	5.557659
C	-0.834066	2.528650	6.228447
O	-1.213088	-0.460887	4.107618
H	-0.873578	-0.886301	6.983871
H	-0.578881	0.509620	8.057605
H	-4.577858	-0.129079	6.445998
H	-3.275561	-1.272129	6.019593
H	-2.910489	-0.440906	8.327371
H	-2.967019	1.247566	7.794491
H	-3.504083	-1.087541	3.625752
H	-4.910899	0.007390	3.857129
H	-3.542411	0.509741	2.810809
H	-4.810132	2.032460	4.960984
H	-3.500441	2.546410	6.047984
H	-3.298701	2.707520	4.272987
H	0.858610	-0.377019	5.351646
H	1.014696	1.279741	4.665934
H	1.365239	0.992771	6.397122
H	0.006065	2.806515	6.895563
H	-0.734528	3.112252	5.292120
H	-1.764261	2.840378	6.734046
H	-0.623592	-0.182433	3.009978

Cartesian coordinates (Å) for a DFT-optimized model of $[Mn^{III}(OH)(dpaq^{2Me})]^+$ and 2,4,6-tri-*tert*-butylphenol from a relaxed surface scan.

Mn	-0.088049000	0.008857000	0.045245000
O	0.529370000	-1.028959000	3.979237000
O	-0.571917000	-0.303334000	-1.876057000
N	0.338203000	2.120992000	0.164760000
N	0.289215000	0.153444000	1.979241000
N	-0.232965000	-2.178980000	0.558161000
N	1.955228000	-0.789273000	-0.421533000
N	-2.229626000	-0.237686000	0.554245000
C	0.400015000	3.058798000	-0.805595000
C	0.555472000	4.435553000	-0.478625000
C	0.655450000	4.837702000	0.842616000
C	0.618768000	3.867892000	1.882179000
C	0.734287000	4.199422000	3.263499000
C	0.699080000	3.186956000	4.212527000
C	0.555431000	1.825800000	3.838364000
C	0.437745000	1.457488000	2.487690000
C	0.461760000	2.495479000	1.492721000
C	0.324702000	-0.981405000	2.753004000
C	0.124271000	-2.300144000	2.001909000

C	0.733411000	-2.893181000	-0.316056000
C	2.046168000	-2.143224000	-0.407502000
C	3.282440000	-2.797754000	-0.520126000
C	4.448962000	-2.029687000	-0.663058000
C	4.347299000	-0.629759000	-0.677275000
C	3.078993000	-0.050557000	-0.545517000
C	-1.639672000	-2.578027000	0.281087000
C	-2.614991000	-1.522151000	0.752956000
C	-3.864850000	-1.834988000	1.308591000
C	-4.736087000	-0.790010000	1.655220000
C	-4.332447000	0.536699000	1.438003000
C	-3.065203000	0.767837000	0.887930000
C	0.317932000	2.643161000	-2.247042000
H	0.180245000	-0.277948000	-2.504349000
H	0.596940000	5.169528000	-1.295314000
H	0.772170000	5.902135000	1.098068000
H	0.850688000	5.254307000	3.553505000
H	0.786912000	3.431255000	5.282117000
H	0.538693000	1.044506000	4.605025000
H	-0.647073000	-2.885602000	2.543225000
H	1.068505000	-2.873054000	2.106381000
H	0.899640000	-3.936386000	0.026226000
H	0.288854000	-2.947947000	-1.331071000
H	3.325735000	-3.896296000	-0.492991000
H	5.428994000	-2.521286000	-0.753283000
H	5.234048000	0.011230000	-0.779981000
H	2.951406000	1.042637000	-0.534449000
H	-1.874571000	-3.565021000	0.731713000
H	-1.756456000	-2.671095000	-0.820679000
H	-4.145976000	-2.886005000	1.468167000
H	-5.719096000	-1.010969000	2.096989000
H	-4.980671000	1.385870000	1.695797000
H	-2.698858000	1.790921000	0.712315000
H	-0.660726000	2.178467000	-2.477143000
H	1.105803000	1.903096000	-2.493862000
H	0.454380000	3.516089000	-2.909900000
C	-2.226013000	-2.540633000	-5.151289000
C	-2.706023000	-2.499329000	-6.474401000
C	-3.698347000	-1.600530000	-6.912036000
C	-4.237519000	-0.726908000	-5.941556000
C	-3.818082000	-0.696927000	-4.601497000
C	-2.754913000	-1.597259000	-4.182013000
C	-4.216193000	-1.562047000	-8.366112000
C	-3.476295000	-2.564111000	-9.276959000
C	-4.017376000	-0.139231000	-8.949593000
C	-5.726479000	-1.916285000	-8.384506000
C	-4.509575000	0.264527000	-3.601642000
C	-5.683332000	1.037419000	-4.246528000
C	-3.503907000	1.325620000	-3.086256000
C	-5.092954000	-0.540655000	-2.411527000
C	-1.168946000	-3.602887000	-4.753712000
C	-0.789592000	-4.532237000	-5.929914000
C	0.141187000	-2.916998000	-4.290937000
C	-1.735168000	-4.502673000	-3.623566000
O	-2.314016000	-1.593271000	-2.928100000
H	-2.287419000	-3.206116000	-7.199996000
H	-5.033779000	-0.036644000	-6.252669000
H	-3.869255000	-2.491693000	-10.312049000
H	-3.617260000	-3.612065000	-8.941283000
H	-2.386666000	-2.359365000	-9.317416000
H	-4.396539000	-0.089856000	-9.992274000
H	-4.559249000	0.627739000	-8.360082000

H	-2.942849000	0.138666000	-8.962536000
H	-6.324615000	-1.206277000	-7.778179000
H	-6.121349000	-1.887007000	-9.422342000
H	-5.899109000	-2.936028000	-7.981800000
H	-6.159665000	1.681813000	-3.478944000
H	-6.466692000	0.359485000	-4.643441000
H	-5.351426000	1.701154000	-5.071558000
H	-4.012519000	2.033439000	-2.397549000
H	-2.662795000	0.862103000	-2.539967000
H	-3.091322000	1.916530000	-3.930647000
H	-5.849661000	-1.271609000	-2.767107000
H	-4.296380000	-1.092695000	-1.878955000
H	-5.595480000	0.143936000	-1.695867000
H	-0.041980000	-5.274143000	-5.580681000
H	-1.661172000	-5.097408000	-6.318544000
H	-0.332610000	-3.976763000	-6.774506000
H	0.905667000	-3.678356000	-4.026953000
H	-0.036843000	-2.283707000	-3.403579000
H	0.561766000	-2.278200000	-5.094976000
H	-2.620253000	-5.067992000	-3.982921000
H	-0.973101000	-5.241589000	-3.295962000
H	-2.046309000	-3.896944000	-2.751875000
H	-1.345040000	-0.822024000	-2.361588000

Cartesian coordinates (Å) for a DFT-optimized model of [Mn^{II}(OH)(dpaq)].

Mn	0.16157563006697	-0.05305730408339	-0.23741110998064
O	0.10022214925830	-0.46641419029615	-2.16192226696871
O	-0.39866272025980	1.21073265128428	3.88932693769492
N	0.07170976568465	-2.22295523176211	0.32965478970340
N	-0.05800920944394	-0.11842226418204	1.97884633421319
N	0.10490374335725	2.27044813656157	0.40996795971019
N	-2.13545335877994	0.57160758203680	-0.17535632094410
N	2.30993041543467	0.70052579682779	-0.20148963088046
C	0.11476143254932	-3.21077971935643	-0.56747242864760
C	-0.05881935520884	-4.57013371961507	-0.20519418736216
C	-0.27606599137380	-4.88434080848825	1.13245988446497
C	-0.33656954349950	-3.84747204185010	2.11302212983185
C	-0.55783932175046	-4.08329406912970	3.50217637796683
C	-0.60186473509955	-2.99828108532411	4.37444289467042
C	-0.44544041468339	-1.66131533329102	3.92618946451998
C	-0.22954662671526	-1.36402563307108	2.56136523226348
C	-0.16398306199819	-2.49473531302797	1.64795381430351
C	-0.13247928917362	1.03971267440542	2.67752404752713
C	4.90009597269906	1.76506564360375	-0.17744374251171
C	4.70238843604526	0.37434137375742	-0.18057221628726
C	0.26579712387451	2.30351863418014	1.87971603279403
C	-1.19494878162951	2.81185772388652	-0.02668457020569
C	-2.34450124258446	1.85069981638090	0.21640745009480
C	-3.57559188208281	2.27137210336754	0.74953395003340
C	-4.62343427444488	1.34181060986796	0.86254605640045
C	-4.40466582452294	0.01931499718759	0.44414314572073
C	-3.13972781734856	-0.31838416845101	-0.06186852912793
C	1.23878784906334	2.89412267655523	-0.29480593049405
C	2.49305391898159	2.04238445116706	-0.20761242814108
C	3.77950909761294	2.61104323893742	-0.18503896777052
C	3.38722144003756	-0.11145999959839	-0.18647993387178
H	-0.81423496681085	-0.74511904445704	-2.36521550707978
H	0.28852812207201	-2.87623245964961	-1.60592430335954
H	-0.01149391744932	-5.35382856849650	-0.97598334052869
H	-0.40607769146033	-5.93136703369712	1.45046108394490
H	-0.69428926148095	-5.11469481225335	3.86273517817122
H	-0.77337436482681	-3.17434298900934	5.44905644136982

H	-0.50190263252916	-0.82318891162972	4.63055717821934
H	5.91628002658434	2.18765660891090	-0.16147030353011
H	5.55002891766821	-0.32625921368183	-0.16981876172886
H	1.34057273212854	2.46437995442521	2.11209466134172
H	-0.27657850682519	3.16672631089631	2.32775305186837
H	-1.13457812696161	2.98705975812003	-1.12230338675413
H	-1.41487178738282	3.79634760767716	0.44819812338427
H	-3.71064805616288	3.31687546224099	1.06567707911997
H	-5.59690644861109	1.64734843680253	1.27561691540794
H	-5.19592794808857	-0.74201394662677	0.50903136455380
H	-2.91946385740974	-1.34638486446738	-0.39633216267063
H	0.96280528781236	2.98516609416983	-1.36809258043990
H	1.45505746351277	3.92720800463791	0.06505515363656
H	3.89611355110935	3.70526456652011	-0.17224895262301
H	3.18250894104576	-1.19493218891291	-0.17497717102284

Cartesian coordinates (Å) for a DFT-optimized model of $[Mn^{II}(OH_2)(dpaq)]^+$.

Mn	0.000000	0.000000	0.000000
O	0.000000	-0.000000	-2.285916
H	-0.113553	0.780630	-2.869564
H	-0.142386	-0.772503	-2.873883
O	0.921895	0.436546	4.142353
N	-2.189051	0.119266	0.253826
N	-0.246906	0.166403	2.119306
N	2.223779	-0.023105	0.716237
N	0.608780	2.152383	-0.145942
N	0.608780	-2.136949	-0.160392
C	-3.113270	0.074928	-0.711826
C	-4.500260	0.195754	-0.456483
C	-4.924869	0.370748	0.854015
C	-3.971173	0.424896	1.912369
C	-4.336076	0.604758	3.279055
C	-3.340729	0.646758	4.248370
C	-1.967518	0.515166	3.915946
C	-1.550130	0.332408	2.583268
C	-2.580670	0.290593	1.562473
C	0.853751	0.210301	2.907553
C	1.483012	-4.778205	0.177049
C	0.129467	-4.503799	-0.074042
C	2.176727	-0.153774	2.200025
C	2.838273	1.252537	0.275862
C	1.866048	2.415259	0.296164
C	2.261033	3.709956	0.669987
C	1.338947	4.763706	0.567544
C	0.045231	4.490409	0.096525
C	-0.276573	3.169121	-0.239953
C	2.852884	-1.202384	0.071536
C	1.921577	-2.398203	0.075388
C	2.389719	-3.709565	0.256997
C	-0.262613	-3.168174	-0.229009
H	-2.738478	-0.060546	-1.738570
H	-5.213629	0.150479	-1.291515
H	-5.995838	0.469648	1.090872
H	-5.399245	0.708229	3.544063
H	-3.614669	0.785851	5.306137
H	-1.202755	0.553115	4.700413
H	1.829613	-5.813140	0.316646
H	-0.617871	-5.306899	-0.142365
H	2.364455	-1.216144	2.463676
H	2.995157	0.430716	2.671980
H	3.166340	1.119218	-0.776345
H	3.746493	1.499322	0.868327

H	3.283623	3.885809	1.034919
H	1.627374	5.785518	0.856481
H	-0.710551	5.282297	-0.003323
H	-1.284189	2.905694	-0.597996
H	3.060909	-0.935736	-0.986116
H	3.827717	-1.469685	0.535726
H	3.456357	-3.885775	0.459467
H	-1.315794	-2.904808	-0.413770

Cartesian coordinates (Å) for a DFT-optimized model of [Mn^{II}(OH)($dpaq^{2Me}$)].

Mn	-0.08020126101684	0.14436815624536	-0.24536355425644
O	0.23180110882753	-1.66879597553834	3.66974755556420
O	0.18908874852387	0.22944069730683	-2.22628583759472
N	-0.20325894808124	2.25122047626544	0.58636258470627
N	0.05520762204623	-0.09222430193063	1.92609710128613
N	-0.06713905193456	-2.20118440771257	0.04104571289939
N	2.28693118228884	-0.52202404387926	-0.07045105013193
N	-2.28112674939972	-0.55052273739549	-0.37253166390008
C	-0.35456220546699	3.37984841211018	-0.12957065818104
C	-0.15056957669883	4.66193567008545	0.46113187955238
C	0.18746565052900	4.75925028453455	1.80024358938801
C	0.33049424829510	3.57847761709055	2.58659448492407
C	0.65800237399679	3.61049795523457	3.97383481715240
C	0.76961328295188	2.41367267417421	4.67230046264996
C	0.57057145091729	1.16351177279984	4.03494312878606
C	0.25699080900208	1.07167957292489	2.66194289219994
C	0.12762666830632	2.31725610518760	1.92267932723839
C	0.06532936006295	-1.33086364868120	2.46462279261580
C	-0.26640847764972	-2.47732102727941	1.48324147676123
C	1.24013070473293	-2.68564054652589	-0.45416102646232
C	2.40315776471888	-1.86554457780135	0.06967772079388
C	3.55382173022435	-2.46149198674082	0.61452133540540
C	4.62179495101632	-1.64164710754827	1.01686203349753
C	4.50089630847523	-0.25172923149155	0.86692983411972
C	3.31082031582920	0.25844639859521	0.32350231484543
C	-1.18245074747267	-2.68651721409344	-0.79975139123556
C	-2.44615448476536	-1.88321816820319	-0.56188001791251
C	-3.72138087438122	-2.47549998840904	-0.57463381155200
C	-4.85412795895848	-1.66438644334055	-0.40175746074559
C	-4.67824506884260	-0.28513276538527	-0.20835767032846
C	-3.37128594466132	0.22289517617054	-0.19516091891969
C	-0.78059831660785	3.25782036672915	-1.56769600600962
H	1.14923334563195	0.16783772725737	-2.40838689936526
H	-0.27324974624326	5.56287634967534	-0.15813986064694
H	0.34521276359542	5.74249114035830	2.27152215730882
H	0.81504265739754	4.58184873342252	4.46784215060456
H	1.02083944284919	2.42640586051489	5.74512626357374
H	0.66257241976858	0.23082693574282	4.60343706046790
H	-1.33835920093698	-2.71253634518197	1.65425320787813
H	0.29989210023655	-3.38015893019705	1.80219420674203
H	1.39475420595998	-3.76363522457713	-0.21685025446081
H	1.22608717780481	-2.58329630815972	-1.55933536824391
H	3.61056494822082	-3.55557988464380	0.71743741335678
H	5.53402474912072	-2.08457737041049	1.44483583407317
H	5.30968005711337	0.43122476640911	1.16528470333981
H	3.17161339546647	1.34437285677758	0.19181288590761
H	-1.38512199672013	-3.77299537989172	-0.65812989157208
H	-0.87896293510119	-2.53967600192366	-1.85847368644542
H	-3.82036342746447	-3.56209668499673	-0.71627219548312
H	-5.86186932481142	-2.10671687668094	-0.40884559399612
H	-5.53417772191742	0.38923761175831	-0.06162031145430
H	-3.18219801574535	1.29616512459209	-0.03325495994155

H	-0.38741009574962	2.31740181812032	-2.01607220788677
H	-0.44861380257276	4.13426167231539	-2.15766256084644
H	-1.89075761071016	3.22229224622109	-1.63448407006605

Cartesian coordinates (Å) for a DFT-optimized model of $[Mn^{II}(OH_2)(dpaq^{2Me})]^+$.

Mn	0.000000	0.000000	0.000000
O	0.562007	-2.149035	3.636748
N	0.072902	2.023684	0.903215
N	0.225937	-0.420007	2.076432
N	-0.001528	-2.332930	-0.006642
N	2.170847	-0.515665	-0.331666
N	-2.156122	-0.550788	-0.234232
C	-0.040515	3.208217	0.273734
C	0.085237	4.436140	0.982190
C	0.332592	4.423228	2.345056
C	0.453504	3.184634	3.036602
C	0.704292	3.106247	4.438043
C	0.804320	1.859230	5.041763
C	0.659358	0.662461	4.295081
C	0.408467	0.682697	2.908766
C	0.309567	1.979477	2.262945
C	0.300700	-1.707989	2.488227
C	-0.068630	-2.757401	1.418392
C	1.254984	-2.755770	-0.669000
C	2.426797	-1.850125	-0.343519
C	3.722250	-2.353844	-0.142007
C	4.783129	-1.456335	0.059273
C	4.515957	-0.078474	0.059095
C	3.193635	0.343921	-0.131911
C	-1.204688	-2.737091	-0.773773
C	-2.401130	-1.874307	-0.424539
C	-3.701495	-2.399946	-0.348508
C	-4.776273	-1.536963	-0.083233
C	-4.518222	-0.170864	0.110751
C	-3.192513	0.274310	0.033182
C	-0.298608	3.205093	-1.209919
H	-0.014851	5.384065	0.434626
H	0.435741	5.365786	2.905241
H	0.813862	4.035867	5.016913
H	0.998836	1.786929	6.123445
H	0.739268	-0.312018	4.790580
H	-1.112831	-3.057153	1.649017
H	0.554213	-3.661424	1.590284
H	1.510055	-3.812696	-0.433619
H	1.087856	-2.697550	-1.764770
H	3.893079	-3.440388	-0.145479
H	5.805579	-1.830279	0.219104
H	5.313124	0.662915	0.211285
H	2.935827	1.414681	-0.124005
H	-1.452656	-3.812799	-0.636838
H	-0.978976	-2.587435	-1.850160
H	-3.863700	-3.477880	-0.495279
H	-5.802356	-1.929276	-0.020064
H	-5.325513	0.543058	0.326984
H	-2.942807	1.334445	0.195477
H	-1.205363	2.616645	-1.458641
H	0.550623	2.749403	-1.759462
H	-0.440487	4.232452	-1.592222
O	-0.000000	-0.000000	-2.319404
H	0.814086	0.189458	-2.833709
H	-0.731322	0.300418	-2.900699

Cartesian coordinates (Å) for a DFT-optimized model of $[Mn^{III}(OH)(PY5)]^{2+}$.

Mn	11.87674873344544	5.68872998471093	9.84473877616198
O	13.01968639681329	5.45226893328496	5.39668190408872
O	15.24994747509050	8.24591792849658	11.65879283015922
O	10.47921450822749	4.87877695879256	10.68062512623894
H	10.49230386671992	4.93501883744973	11.66230199541453
N	13.48985630407773	6.53573446086772	8.90083582430225
N	10.73605749570045	6.52033163628179	8.07076408051459
N	12.11231263469323	3.97524456327117	8.57408490789432
N	13.45507333833717	5.11306325913795	11.47929310774610
N	11.72055151898134	7.39765062062384	11.04543409559049
C	13.71625931723417	6.23801759534619	7.59267464630739
C	14.98219073198898	6.43432293471924	7.02137496717716
H	15.17078043441129	6.13209546533281	5.98674944481971
C	16.01156892506356	6.96757014484921	7.80242029696528
H	17.01937712691117	7.09579765484480	7.38190326551958
C	15.74812039043586	7.32304001025851	9.12757265767484
H	16.54266086536160	7.71968539317596	9.76807758846465
C	14.46397820663889	7.11315630860716	9.65145688812998
C	12.61051087113838	5.54736976580616	6.74916608982025
C	13.14940401177922	6.68753416121523	4.63791825982294
H	13.00897744320748	7.58803005622034	5.26678013083976
H	12.40086396687420	6.69297703032054	3.82223373861273
H	14.16123984516692	6.70738842497906	4.18902432096873
C	11.18837737620381	6.16173493737936	6.85006610269642
C	10.36358333139926	6.21953795612202	5.71286997647875
H	10.72347214119372	5.85390246850113	4.74470465148968
C	9.06411667963745	6.73145666659090	5.83720475760149
H	8.40768285788836	6.78836464694457	4.95641530300167
C	8.61834786708676	7.15665562887048	7.09597727122304
H	7.61193426803470	7.57144428997087	7.24568352182133
C	9.48220450428203	7.01261389170848	8.18613147166292
H	9.15353747365909	7.29248375239642	9.19495656930045
C	12.48411397709019	4.10123457532206	7.27632605011083
C	12.68566424522708	2.98848041286544	6.44989950976739
H	12.98532191674006	3.13587427104171	5.40546500420496
C	12.48437179086481	1.70634666594701	6.98469976731869
H	12.64188483495150	0.81641090704527	6.35755191077392
C	12.06145512270377	1.57877891455495	8.31538132540213
H	11.86646780522401	0.59732778951697	8.76903499812108
C	11.87775073909591	2.73921335971976	9.07386377996084
H	11.50514271776186	2.70070032358647	10.10610092756076
C	14.22034435363397	7.41771268067645	11.15175191978779
C	15.37990790277160	9.58429165332450	11.10128651274708
H	14.54205372689090	9.84474080062543	10.42560558310150
H	16.33319914612262	9.65783411068908	10.54254309068403
H	15.40737458636009	10.30004483322364	11.94509769688725
C	14.33008192470871	6.05897478437706	11.88739939255466
C	15.26349208200656	5.83912291536858	12.90929746702874
H	15.95198150046669	6.63943638181659	13.20630148054160
C	15.28406632696988	4.58046161679742	13.53205117459447
H	16.00532889364771	4.37474757188073	14.33689942932868
C	14.37355582136975	3.59791838014464	13.11830416750639
H	14.35078882994590	2.60096061753664	13.57985694097069
C	13.47440946439215	3.90963758327236	12.09035709824788
H	12.74005335501691	3.16890143996564	11.74519643853826
C	12.83373430314144	7.99955535335689	11.52757744185870
C	12.73510267230904	9.03663575979116	12.47131467563993
H	13.64031073693250	9.47293693685929	12.90649343487702
C	11.47208294502608	9.48794540132143	12.87736954803222
H	11.38910372542157	10.30389534009954	13.61012371089270
C	10.32751633789382	8.86911187571793	12.35728539789871

H	9.31450138125762	9.17325600690719	12.65408944954303
C	10.49776008338230	7.81235933878200	11.46175102860414
H	9.63731984298954	7.24578103078950	11.08340507840401

Cartesian coordinates (Å) for a DFT-optimized model of $[Mn^{II}(OH)(PY5)]^{+}$.

Mn	-0.09891598601442	-0.12226928785995	0.20278372817446
O	-0.16595668703952	-0.25114303379589	2.15618241173907
H	0.54107409391698	-0.79820832246485	2.55433217606753
O	-2.75320594584617	2.31452034206204	-2.87795432789991
O	2.77299027514859	-2.17507309431207	-2.98512221135512
N	0.01815577789224	0.05935622711579	-2.08064924185099
N	-0.43358898887266	2.10459423124969	-0.02274691049776
N	-2.39121193432844	-0.04027298597700	-0.14037084662201
N	0.45212375769901	-2.36455534763556	-0.20358944978557
N	2.15644610955339	0.01952104808786	-0.08835506555725
C	-1.13093638408889	0.50833782995452	-2.64369748322732
C	-1.68407954318090	-0.08371127969578	-3.79227270595751
C	-1.01309129709910	-1.15618130119217	-4.39321227217932
C	0.18550556491763	-1.60580724994276	-3.82639412302178
C	0.67846069104149	-0.96407195665000	-2.67655760054658
C	-1.96838247975460	1.59464038348728	-1.92577862083026
C	-2.02453818652292	2.97863614161225	-3.93637828167124
C	-1.24798734678155	2.59848586598991	-0.98328704543081
C	-1.57790164426732	3.96814746564395	-1.02414867332664
C	-1.01992598928322	4.83971532050375	-0.07771870116120
C	-0.17192996837338	4.32082785651227	0.91054064661259
C	0.07649891309902	2.94393778716937	0.90466134738036
C	-2.95940255967754	0.81648120698901	-1.02115082075183
C	-4.34783566025165	1.00308271456182	-1.10328492692409
C	-5.17416717455246	0.26748479931476	-0.23806904149348
C	-4.58864951638647	-0.61444841541482	0.68278106667001
C	-3.19223808483302	-0.72962375852774	0.70022502627750
C	1.93014248885465	-1.57408176378820	-1.99961569431311
C	3.25678491211691	-1.30191462551365	-4.03087945830737
C	1.39451552981663	-2.72307934372940	-1.10600151197823
C	1.86947645318161	-4.03912598877490	-1.22010527140825
C	1.33634015496894	-5.01916969223154	-0.36736667789584
C	0.36168445302154	-4.65126637476937	0.57270868734120
C	-0.04257724157247	-3.31063593631584	0.62320622716677
C	2.78552885183912	-0.68096575981168	-1.05959163004708
C	4.19269447107902	-0.73923130162096	-1.12102535626301
C	4.95398297207032	-0.02052516717827	-0.18849046571015
C	4.29499787704052	0.71622290902976	0.80569011198016
C	2.89641915145717	0.68961653382979	0.82232225650104
H	-2.64118051568824	0.27595931302461	-4.19223313552355
H	-1.42844593325275	-1.64684942972535	-5.28564974191375
H	0.72522872186306	-2.46157809620181	-4.25289815721122
H	-1.08529656559078	3.44299870662573	-3.57247295513026
H	-2.69910906706122	3.76673835531658	-4.31984908006365
H	-1.77753412525781	2.27814666833626	-4.76035474413567
H	-2.28345440377564	4.34843642698400	-1.77166241029735
H	-1.26494972662623	5.91207027804063	-0.10520560837645
H	0.27411753505996	4.95958977947537	1.68591559765075
H	0.68700970151498	2.47504667835348	1.69021174716259
H	-4.76498700411943	1.71003629313143	-1.83111822815043
H	-6.26701608237291	0.38916192691503	-0.28220457439007
H	-5.19768706963213	-1.20555017083053	1.38128770144003
H	-2.68028164148337	-1.38864283194835	1.41781469069585
H	3.58971758045608	-0.31969698592869	-3.63721238142271
H	2.48465327941137	-1.12861113601713	-4.80839430562612
H	4.11832963870473	-1.82584596155217	-4.48490032863302
H	2.63953750031728	-4.28241934577330	-1.96270779631192

H	1.68538130919492	-6.06055964911210	-0.43622327221168
H	-0.08039005578661	-5.38523534697727	1.26124595172034
H	-0.78543188905173	-2.96523835621281	1.35872378295292
H	4.69017635102459	-1.35886857508117	-1.87600314756978
H	6.05294571331209	-0.05299256107735	-0.23233790045880
H	4.84605699674005	1.28461886347566	1.56822571389657
H	2.33138387211165	1.20492148084783	1.61270031201039

Cartesian coordinates (Å) for a DFT-optimized model of $[Mn^{II}(OH_2)(PY5)]^{2+}$.

Mn	9.43774517316696	10.72334194566695	2.95458527895734
O	4.88818459121814	9.71429978587734	2.88043340116796
O	10.43582527756265	9.75634440010401	7.40193546689340
O	10.72312900448370	11.51402653837999	1.35056866857902
H	11.68984296601533	11.68208760364483	1.38513770209613
H	10.47354503637802	11.67952432528135	0.41553691004256
N	8.14492869681115	9.94404386619627	4.54741466705127
N	8.34532042749577	9.25864844896144	1.67874867926867
N	7.64135740799190	12.01931731111628	2.32468524240921
N	10.40710818362524	12.03642867020718	4.57410977740541
N	10.92542896624365	9.28218707305983	3.77656814639375
C	6.81863889656870	10.08111629396038	4.31808736757899
C	5.92726349373833	10.42574791435885	5.34913301141305
H	4.86420746297343	10.58836651758245	5.13210555112016
C	6.42999059969272	10.60756862222693	6.64289719934852
H	5.75839807805764	10.89934787734677	7.46348210647844
C	7.80028269299149	10.44147172222119	6.87693855613236
H	8.22398950607477	10.61672342669342	7.87367441209835
C	8.63448254162067	10.09619438659192	5.79945236115602
C	6.27530224087857	10.03896965368852	2.86399208503676
C	4.52880191195302	8.44047854442010	3.47036555835773
H	5.24866735027868	7.63868959769063	3.20948749557772
H	3.53353567991816	8.19010145210275	3.05932520812520
H	4.45958452678965	8.51010832446723	4.57469954640293
C	7.00151775980830	9.15217487787906	1.81105198651154
C	6.24542515344583	8.37486096479222	0.91237117593065
H	5.15259408206469	8.34624782580476	0.98661761437658
C	6.89736941320540	7.65993217788282	-0.10232155300171
H	6.31384702868547	7.04709765224247	-0.80524839850840
C	8.29100100722543	7.75330991430029	-0.21529234463497
H	8.84828943129881	7.22069307282017	-0.99829903521697
C	8.96700537390969	8.57665676658333	0.68962422564416
H	10.05444008792950	8.71603286897584	0.60968820331966
C	6.39093075795048	11.49498452457683	2.33924640724805
C	5.26875553195930	12.21387387173129	1.90315300990877
H	4.27582445104586	11.74895182506255	1.93302088644662
C	5.45100878987980	13.52538659021801	1.43523509072228
H	4.58753361366203	14.11281276812406	1.08903511248085
C	6.74271846526554	14.07033745314808	1.41323662501194
H	6.93324791325209	15.09093021308538	1.05330940330167
C	7.80661827180374	13.27936557282603	1.86464938848623
H	8.83632595430476	13.66650195252887	1.85449850695054
C	10.16822066150199	10.06724625542940	6.03799605782678
C	9.93480065593664	8.48578318368007	7.88702886133779
H	10.00206935154661	7.68700338251209	7.12123933678805
H	8.88137065850105	8.56842892135428	8.22252584947777
H	10.57045992787847	8.22111727878345	8.75221540346794
C	10.65112402681013	11.52392446022056	5.80540190450139
C	11.30530610633078	12.25447310947600	6.80771685074440
H	11.48172915420900	11.79994421999785	7.79016847188509
C	11.72246074417156	13.56429459225962	6.52028189777809
H	12.23679836906498	14.16062040348105	7.28865632599792
C	11.47866743515677	14.09646102655082	5.24609887951318

H	11.79015214765832	15.11504398233143	4.97603837931800
C	10.82058687483202	13.29481694063089	4.30514448846270
H	10.61847635480770	13.66995896745112	3.29087366958712
C	11.05792273389298	9.17725256968480	5.12081623006990
C	12.08758311413829	8.40126534860979	5.68745703700285
H	12.22649405841443	8.37118162514819	6.77382275072721
C	12.95723337104176	7.68751300656149	4.85075000139343
H	13.76033919675944	7.07508831285226	5.28675725851647
C	12.79824499336215	7.78201081642859	3.46185869168837
H	13.45920996720135	7.25103039330368	2.76288677599094
C	11.77735217168558	8.60307409805031	2.97461409783548
H	11.64544612587295	8.74205491077345	1.89211907602069

Cartesian coordinates (Å) for a DFT-optimized model of the transition state for $[Mn^{III}(OH)(dpaq)]^+$ and xanthene

Mn	0.000000	0.000000	0.000000
O	0.000000	0.000000	-2.063540
H	-0.910133	0.075569	-2.429315
O	-0.250848	1.157296	4.025002
N	-0.045789	-2.132422	0.317659
N	-0.089605	-0.105990	2.057504
N	0.009529	2.242349	0.492053
N	-2.164659	0.565296	-0.120440
N	2.169008	0.565296	-0.028602
C	-0.011423	-3.095341	-0.609648
C	-0.074055	-4.470591	-0.282588
C	-0.174637	-4.839729	1.053118
C	-0.211814	-3.841071	2.069545
C	-0.313082	-4.137026	3.460793
C	-0.342520	-3.092940	4.377599
C	-0.274474	-1.733958	3.970568
C	-0.173649	-1.389534	2.610972
C	-0.143007	-2.467720	1.650017
C	-0.124176	1.044333	2.784982
C	4.788900	1.489507	0.309300
C	4.523935	0.112380	0.243004
C	0.064418	2.344321	1.981492
C	-1.237969	2.816259	-0.071365
C	-2.419577	1.882303	0.086653
C	-3.716060	2.347228	0.356702
C	-4.776208	1.427537	0.397490
C	-4.508133	0.068158	0.172149
C	-3.185060	-0.319210	-0.076014
C	1.221654	2.805055	-0.156411
C	2.419350	1.897117	0.031788
C	3.720731	2.394588	0.207594
C	3.196291	-0.304171	0.079759
H	0.070183	-2.761041	-1.655782
H	-0.044388	-5.221578	-1.084034
H	-0.226940	-5.901539	1.339748
H	-0.366277	-5.186707	3.786587
H	-0.420823	-3.313758	5.453507
H	-0.300191	-0.932070	4.716886
H	5.816888	1.856603	0.447255
H	5.327527	-0.633097	0.324194
H	1.053582	2.748326	2.282567
H	-0.684466	3.078072	2.345614
H	-1.073170	2.967582	-1.158709
H	-1.467065	3.812775	0.364352
H	-3.888617	3.419531	0.529527
H	-5.800583	1.769677	0.607647
H	-5.306009	-0.687460	0.193480

H	-2.923729	-1.375119	-0.246831
H	1.013313	2.880971	-1.244386
H	1.449416	3.831746	0.203650
H	3.889680	3.479877	0.264251
H	2.937326	-1.373566	0.037354
C	-0.571546	1.815094	-6.671882
C	-1.401937	0.860446	-7.295099
C	-1.286216	-0.498673	-6.955962
C	-0.347844	-0.888053	-5.989681
C	0.497959	0.050606	-5.332615
C	0.362851	1.413695	-5.707967
O	-0.283541	-2.247352	-5.699023
C	0.757828	-2.736131	-4.918766
C	1.645160	-1.857257	-4.231956
C	1.410165	-0.422745	-4.299629
C	0.887652	-4.130768	-4.849556
C	1.927236	-4.689952	-4.086035
C	2.832406	-3.849188	-3.405976
C	2.691102	-2.457033	-3.479930
H	-0.655203	2.878703	-6.942842
H	-2.137459	1.171874	-8.052136
H	-1.912640	-1.265238	-7.436071
H	1.011849	2.159523	-5.221838
H	2.241580	0.245195	-4.011799
H	0.177933	-4.763996	-5.402543
H	2.034201	-5.783739	-4.030464
H	3.653546	-4.285291	-2.817001
H	3.402013	-1.801029	-2.952825
H	0.626624	-0.175812	-2.968611

Cartesian coordinates (Å) for a DFT-optimized model of the transition state for $[Mn^{III}(OH)(dpaq^{2Me-})]^{+}$ and xanthene

Mn	0.000000	0.000000	0.000000
O	-0.444836	-1.812593	3.751886
N	-0.000384	2.092418	0.677055
N	-0.188003	-0.236444	2.032963
N	0.041990	-2.289411	0.129896
N	2.170309	-0.515882	-0.111435
N	-2.171042	-0.562216	-0.168678
C	0.144102	3.222580	-0.043999
C	-0.012566	4.503262	0.558862
C	-0.310798	4.606374	1.906795
C	-0.448193	3.430156	2.695693
C	-0.735314	3.464798	4.091473
C	-0.842272	2.271766	4.793544
C	-0.669946	1.018509	4.152034
C	-0.387691	0.933750	2.776079
C	-0.278995	2.167248	2.030012
C	-0.229339	-1.492206	2.561200
C	0.105666	-2.626791	1.579525
C	1.257394	-2.723292	-0.603618
C	2.440406	-1.837386	-0.270165
C	3.748826	-2.336634	-0.173550
C	4.803367	-1.445654	0.080953
C	4.517605	-0.080992	0.243961
C	3.184914	0.338139	0.146460
C	-1.203380	-2.775270	-0.511830
C	-2.400060	-1.898782	-0.199009
C	-3.688403	-2.428879	-0.022407

C	-4.766442	-1.551015	0.174490
C	-4.523874	-0.168694	0.195674
C	-3.206982	0.280318	0.027289
C	0.477193	3.119894	-1.506759
H	0.110026	5.401785	-0.062096
H	-0.435421	5.592516	2.380564
H	-0.865169	4.437972	4.588536
H	-1.063353	2.285958	5.872103
H	-0.753936	0.089395	4.726241
H	-0.547958	-3.493380	1.811887
H	1.138677	-2.947292	1.829333
H	1.502882	-3.790218	-0.412375
H	1.046611	-2.625180	-1.688971
H	3.933428	-3.413954	-0.295342
H	5.836483	-1.815745	0.159856
H	5.309264	0.652562	0.451581
H	2.910859	1.395531	0.282943
H	-1.416694	-3.832848	-0.244639
H	-1.039998	-2.744837	-1.609297
H	-3.840118	-3.518061	-0.040440
H	-5.784324	-1.944094	0.315609
H	-5.335943	0.556210	0.347762
H	-2.965640	1.354398	0.052563
H	-0.376468	2.710089	-2.084984
H	1.340470	2.446772	-1.675141
H	0.726198	4.113543	-1.921364
O	0.000000	0.000000	-2.060648
H	0.889447	0.118821	-2.462918
C	-2.455310	3.562708	-4.567028
C	-1.512666	3.987920	-5.525861
C	-0.607763	3.065437	-6.079048
C	-0.647866	1.728161	-5.659915
C	-1.576511	1.268594	-4.683798
C	-2.484725	2.223591	-4.154812
O	0.272888	0.863794	-6.243403
C	0.134064	-0.508502	-6.062035
C	-0.771478	-1.038726	-5.100152
C	-1.516418	-0.119398	-4.252193
C	0.932380	-1.332607	-6.868142
C	0.838708	-2.728545	-6.732400
C	-0.061323	-3.287136	-5.801433
C	-0.853929	-2.452647	-5.001754
H	-3.171357	4.282219	-4.141505
H	-1.485582	5.038782	-5.851503
H	0.128042	3.368714	-6.838730
H	-3.223023	1.889839	-3.408535
H	-2.402781	-0.519812	-3.738586
H	1.614752	-0.872114	-7.598069
H	1.463746	-3.379738	-7.361962
H	-0.145563	-4.380207	-5.703383
H	-1.565367	-2.890915	-4.283642
H	-0.682546	-0.047728	-2.965616

Coordinates for Chapter 3

All coordinates besides those for $[Mn^{II}(MeCN)(dpaq^{R})]^{+}$ are the same coordinates as used in Chapter 1.

Coordinates for $[Mn^{II}(MeCN)(dpaq^{H})]^{+}$

	x	y	z
Mn	0.000000000000	0.000000000000	0.000000000000
O	-0.205113000000	1.396386000000	4.037102000000
N	-0.001879000000	-2.160988000000	0.552506000000
N	0.000000000000	0.000000000000	2.154734000000
N	0.002982000000	2.304113000000	0.467859000000
N	-2.185498000000	0.567241000000	0.024792000000
N	2.114371000000	0.679461000000	-0.335457000000
C	0.019520000000	-3.199342000000	-0.288845000000
C	-0.031615000000	-4.545917000000	0.145276000000
C	-0.112179000000	-4.805486000000	1.506882000000
C	-0.138666000000	-3.725938000000	2.437686000000
C	-0.222880000000	-3.918143000000	3.848077000000
C	-0.242866000000	-2.808099000000	4.684338000000
C	-0.180900000000	-1.485711000000	4.173248000000
C	-0.093768000000	-1.237075000000	2.789253000000
C	-0.076983000000	-2.388229000000	1.906835000000
C	-0.040835000000	1.186311000000	2.808072000000
C	4.734374000000	1.670087000000	-0.360662000000
C	4.496516000000	0.287152000000	-0.404528000000
C	0.247442000000	2.423123000000	1.933084000000
C	-1.319328000000	2.844314000000	0.072409000000
C	-2.450476000000	1.865728000000	0.314148000000
C	-3.725705000000	2.285165000000	0.727682000000
C	-4.757557000000	1.338171000000	0.825427000000
C	-4.482822000000	-0.001536000000	0.508786000000
C	-3.179843000000	-0.341013000000	0.120159000000
C	1.107120000000	2.900478000000	-0.322790000000
C	2.338735000000	2.017610000000	-0.301841000000
C	3.639859000000	2.547123000000	-0.304731000000
C	3.169801000000	-0.162021000000	-0.384338000000
H	0.077108000000	-2.956650000000	-1.361298000000
H	-0.008802000000	-5.357882000000	-0.595407000000

H	-0.156767000000	-5.839867000000	1.882398000000
H	-0.271124000000	-4.941277000000	4.250857000000
H	-0.308155000000	-2.947576000000	5.775051000000
H	-0.199261000000	-0.628441000000	4.855957000000
H	5.762147000000	2.063094000000	-0.363803000000
H	5.321788000000	-0.437695000000	-0.446780000000
H	1.324549000000	2.643356000000	2.090397000000
H	-0.310616000000	3.285901000000	2.355225000000
H	-1.286983000000	3.042768000000	-1.019611000000
H	-1.533645000000	3.815540000000	0.570204000000
H	-3.903881000000	3.344097000000	0.966135000000
H	-5.764227000000	1.643769000000	1.148160000000
H	-5.259185000000	-0.777531000000	0.567083000000
H	-2.913615000000	-1.381531000000	-0.123973000000
H	0.762854000000	2.984151000000	-1.375451000000
H	1.360619000000	3.929735000000	0.014461000000
H	3.787695000000	3.636246000000	-0.262925000000
H	2.935103000000	-1.237761000000	-0.406274000000
C	-0.241613000000	-0.418966000000	-3.348941000000
N	-0.156620000000	-0.457577000000	-2.186285000000
C	-0.345898000000	-0.370256000000	-4.794094000000
H	-0.381586000000	-1.399884000000	-5.201999000000
H	0.532531000000	0.157224000000	-5.215518000000
H	-1.269349000000	0.168029000000	-5.085714000000

Coordinates for $[Mn^{II}(MeCN)(dpaq^{2Me})]^{+}$

	x	y	z
Mn	0.000000000000	0.000000000000	0.000000000000
O	0.628295000000	-1.966652000000	3.750112000000
N	0.056123000000	2.066442000000	0.829331000000
N	0.249701000000	-0.319223000000	2.111339000000
N	0.012260000000	-2.342982000000	0.137287000000
N	2.210012000000	-0.570337000000	-0.194999000000
N	-2.175032000000	-0.628540000000	-0.101679000000
C	-0.085410000000	3.222271000000	0.153986000000
C	0.076582000000	4.481527000000	0.798767000000
C	0.386416000000	4.530904000000	2.147084000000
C	0.530948000000	3.324327000000	2.889279000000
C	0.836276000000	3.311147000000	4.281724000000

C	0.950985000000	2.093515000000	4.940570000000
C	0.769158000000	0.864624000000	4.257798000000
C	0.466780000000	0.820470000000	2.881614000000
C	0.349922000000	2.085477000000	2.179197000000
C	0.337140000000	-1.583372000000	2.587174000000
C	-0.063596000000	-2.683682000000	1.583742000000
C	1.273737000000	-2.806519000000	-0.485132000000
C	2.451565000000	-1.905070000000	-0.168711000000
C	3.738686000000	-2.418154000000	0.063978000000
C	4.805744000000	-1.526103000000	0.256820000000
C	4.552866000000	-0.146173000000	0.216177000000
C	3.237043000000	0.283721000000	-0.005696000000
C	-1.183013000000	-2.803998000000	-0.607356000000
C	-2.397013000000	-1.955744000000	-0.281542000000
C	-3.689384000000	-2.502794000000	-0.212051000000
C	-4.779472000000	-1.654374000000	0.036779000000
C	-4.544564000000	-0.282717000000	0.221121000000
C	-3.225011000000	0.182547000000	0.149081000000
C	-0.403684000000	3.162235000000	-1.315740000000
H	-0.048409000000	5.403493000000	0.213097000000
H	0.517208000000	5.497570000000	2.658336000000
H	0.974242000000	4.266720000000	4.810189000000
H	1.186176000000	2.071464000000	6.016408000000
H	0.859827000000	-0.086421000000	4.794948000000
H	-1.116119000000	-2.937269000000	1.830725000000
H	0.533921000000	-3.593626000000	1.806671000000
H	1.508966000000	-3.857800000000	-0.206266000000
H	1.128378000000	-2.790789000000	-1.585756000000
H	3.898210000000	-3.506161000000	0.090867000000
H	5.822018000000	-1.905771000000	0.441131000000
H	5.355819000000	0.590703000000	0.360392000000
H	2.990057000000	1.356961000000	-0.031853000000
H	-1.405990000000	-3.879398000000	-0.428649000000
H	-0.966187000000	-2.696839000000	-1.691177000000
H	-3.833773000000	-3.584443000000	-0.350477000000
H	-5.799859000000	-2.062121000000	0.094869000000
H	-5.365072000000	0.419694000000	0.425309000000
H	-2.992206000000	1.248233000000	0.301077000000
H	-1.143780000000	2.369575000000	-1.538481000000
H	0.510624000000	2.936202000000	-1.904519000000
H	-0.801263000000	4.129232000000	-1.675890000000
C	0.040858000000	-0.038131000000	-3.427726000000
N	0.000000000000	0.000000000000	-2.263300000000

C	0.093431000000	-0.083058000000	-4.876004000000
H	-0.430606000000	-0.987642000000	-5.243069000000
H	1.148734000000	-0.112318000000	-5.212034000000
H	-0.398842000000	0.815392000000	-5.298041000000

Coordinates for Chapter 4

Coordinates for $[Mn^{III}Mn^{III}(\mu\text{–}O)(dpaq)_2]^{2+}$

	x	y	z
Mn	-0.126837930467	-0.220471956024	-3.658465508066
O	-0.073803850000	-0.108989947607	-1.852320088727
O	-0.127821853491	-1.656795804278	-7.525425347525
N	-0.037120011609	1.796898097208	-4.078328655136
N	-0.104943498984	-0.284164577155	-5.638614397249
N	-0.380786630598	-2.423243218120	-3.933672106391
N	-2.434823294101	-0.592251656693	-3.876555596146
N	2.033110772323	-1.073708116918	-3.866789169584
C	-0.056673397314	2.803700649149	-3.198312787721
C	0.019111498128	4.155989438425	-3.601038888469
C	0.124883007125	4.460750258075	-4.955336135862
C	0.143234482391	3.414719842120	-5.919828141297
C	0.238197573012	3.616242207885	-7.327202193409
C	0.230218353878	2.513525227741	-8.174278807470
C	0.124790853605	1.182849385424	-7.687259040291
C	0.029258038106	0.941260858430	-6.306129829385
C	0.049466627869	2.068548042981	-5.426212046647
C	-0.194477951597	-1.485009366880	-6.309050899565
C	4.366353229635	-2.448046697401	-4.567434584488
C	4.313485077112	-1.047756922664	-4.646187613022
C	-0.441267068480	-2.700658939193	-5.405195203210
C	-1.647043503226	-2.787339965596	-3.245914750368
C	-2.769020021085	-1.893527086928	-3.732262491066
C	-4.058842603570	-2.363890113279	-4.024743070149
C	-5.025506164429	-1.453211564852	-4.483024202186
C	-4.666644086054	-0.105549062907	-4.642977971219
C	-3.354857182265	0.279351063155	-4.329316919978
C	0.795500150906	-3.074359886614	-3.307037876833
C	2.073695845290	-2.423195731994	-3.794122625519
C	3.225730685772	-3.147707096176	-4.139035345943
C	3.119862552582	-0.402621581948	-4.290931839560
Mn	-0.000757002868	-0.014866170993	-0.046145407317
O	1.332427410740	-0.109503228666	3.855420416258
N	-2.021879345727	0.170819896011	0.320432113558
N	0.013354500453	0.020616608294	1.934941076591
N	2.205613585841	-0.070734794708	0.280933562258

N	0.696254169117	2.221341995395	0.109741233248
N	0.521699575709	-2.271670899065	0.257535407337
C	-2.997313777855	0.285249613529	-0.587453067976
C	-4.356623709010	0.402321410258	-0.219724140659
C	-4.703133514451	0.392185727121	1.128591681409
C	-3.690866296675	0.275254574060	2.121717225485
C	-3.935353342619	0.261793176142	3.525460000653
C	-2.861095492870	0.155835041908	4.402003388966
C	-1.517586513857	0.064494379347	3.948581775048
C	-1.233851288957	0.075310227846	2.572198650149
C	-2.333259452365	0.172293694378	1.662548559467
C	1.199274709576	-0.045751741853	2.634074683895
C	1.527918265112	-4.740588565309	1.103248933085
C	0.147564051535	-4.488109715669	1.126515244762
C	2.456604650971	0.013516982673	1.755933631562
C	2.762248265083	1.099635774304	-0.447428471004
C	2.033880320456	2.358283574294	-0.023404570621
C	2.682210709360	3.577783887550	0.227814961995
C	1.915446257465	4.683138694173	0.632761080463
C	0.528289347310	4.528652237081	0.783051635134
C	-0.038496959484	3.274574245169	0.512309221384
C	2.693687451404	-1.355079657664	-0.278821089183
C	1.853342619995	-2.504841720226	0.237538820639
C	2.395793317331	-3.730348699052	0.655503466787
C	-0.310031854903	-3.233036484210	0.699030799599
H	-0.130450736149	2.512344287384	-2.142507626000
H	-0.004601442772	4.947832940808	-2.839287962292
H	0.189945807164	5.507213273221	-5.292148562577
H	0.313718821190	4.639072198178	-7.724947018821
H	0.303061126159	2.664120714686	-9.262113932792
H	0.112940620535	0.336520921631	-8.383205471662
H	5.279326368173	-2.992337883187	-4.852398459742
H	5.176760145352	-0.461173687191	-4.992497261364
H	0.288421804694	-3.486939240602	-5.683835939835
H	-1.439631578556	-3.100704894331	-5.673567960527
H	-1.488568274462	-2.627877231330	-2.159007891925
H	-1.901041324171	-3.858882449203	-3.401932418159
H	-4.300152003113	-3.431214778826	-3.907726258219
H	-6.041815961222	-1.796763983776	-4.728203184749
H	-5.385576012066	0.637594487878	-5.017455728925
H	-3.022872044392	1.322625974076	-4.447242996331
H	0.702527362529	-2.932909145992	-2.211251303666
H	0.809048369868	-4.167857014871	-3.509618413996

H	3.225361727355	-4.246898911426	-4.085441388206
H	3.023092124023	0.692532246456	-4.359171820967
H	-2.675363725319	0.276813310691	-1.636985056181
H	-5.121145234481	0.498218023924	-1.003403234535
H	-5.756404349659	0.477903898216	1.438474230572
H	-4.967971185194	0.337498027744	3.896994128387
H	-3.044828913120	0.144877465817	5.487127113837
H	-0.693365175208	-0.011471590429	4.666700126207
H	1.927749758063	-5.707112725101	1.445201475375
H	-0.566305336344	-5.244077666727	1.484505476928
H	3.142665098682	-0.793172350830	2.082727995254
H	2.968119517165	0.966904546157	1.997116398144
H	2.597500783035	0.921420400846	-1.530468451372
H	3.856755966362	1.201553741258	-0.278034820980
H	3.774602060730	3.657795139939	0.121229820061
H	2.399358014139	5.648406066916	0.845173658082
H	-0.107412575800	5.361247040598	1.117772503329
H	-1.120104023398	3.101331508970	0.625228082328
H	2.591980523666	-1.291753984220	-1.380888874304
H	3.768617098977	-1.516252933526	-0.043609787317
H	3.484985952270	-3.887262546690	0.642839673180
H	-1.382016510982	-2.980507036622	0.720629453274

Coordinates for $[Mn^{III}Mn^{III}(\mu\text{–}OH)(dpaq)_2]^{3+}$

	x	y	z
Mn	-0.065694156513	-0.426027146042	-3.867049043932
O	-0.196170875050	-0.089871033411	-1.849020211535
O	-0.113763615890	-2.099575484977	-7.570039994302
N	0.417037723258	1.522117342255	-4.367306118029
N	0.013419905008	-0.618662475299	-5.784740517017
N	-0.670601149976	-2.544649581818	-3.975300763781
N	-2.378245614803	-0.355334657013	-3.959236572699
N	1.926702278907	-1.548938357987	-3.801721549609
C	0.570010960880	2.584032162367	-3.560172068757
C	0.907759470899	3.863260058356	-4.048375054803
C	1.099668076612	4.044352374320	-5.417498547690
C	0.946860340437	2.945120669475	-6.305256576178
C	1.116573282228	3.022577226329	-7.718966667914
C	0.932318577531	1.882118616391	-8.491018134109

C	0.573637313614	0.630587682677	-7.918865553350
C	0.395392153215	0.517083166163	-6.530659184685
C	0.591643836543	1.677866283801	-5.727280584720
C	-0.238450686964	-1.852946950685	-6.379161856147
C	4.026657506097	-3.273223695471	-4.478258938632
C	4.193960095179	-1.881364489220	-4.555509848377
C	-0.758288377505	-2.924011689949	-5.421207815730
C	-1.995822752989	-2.651658483567	-3.298139081618
C	-2.934055073821	-1.584810025762	-3.823557783835
C	-4.276584109833	-1.830424875644	-4.147286226372
C	-5.066987707917	-0.768457017767	-4.622738503035
C	-4.485158925753	0.500986238014	-4.763329248715
C	-3.133421775878	0.660353100200	-4.425479042221
C	0.384253611191	-3.326747492405	-3.266978129570
C	1.757639855498	-2.891925569188	-3.730898854521
C	2.785848148781	-3.786738606418	-4.061746395265
C	3.113142526795	-1.056078733746	-4.214539589734
Mn	0.063984717584	-0.208256740254	0.180348754119
O	1.633516927800	-0.278792425368	3.928499623271
N	-1.945800455004	-0.399120277888	0.636711352427
N	0.195880308029	-0.258824649582	2.104054186882
N	2.244810829278	0.095248845032	0.333453418265
N	0.317935192354	2.088947363889	0.216665994906
N	0.896847319049	-2.339237493956	0.194130588189
C	-2.998949606733	-0.426790920756	-0.195555813799
C	-4.324785920407	-0.564579066208	0.265043523277
C	-4.564649687918	-0.684137196388	1.633267616189
C	-3.476699467535	-0.659195223506	2.547296838438
C	-3.612492100921	-0.769120296134	3.962472573809
C	-2.476970158492	-0.722315159048	4.761823069181
C	-1.173404734056	-0.563824139400	4.216098815192
C	-1.001281518618	-0.449935208580	2.827096153255
C	-2.157958797500	-0.506048143022	1.996173017794
C	1.437735781691	-0.162704879778	2.727279279804
C	2.291565068691	-4.640026118931	0.969795075542
C	0.888649006277	-4.607964965245	1.013951865359
C	2.597421644060	0.163637237505	1.787392387176
C	2.556333602232	1.375055381703	-0.366918513745
C	1.615346802099	2.465935390073	0.101759433610
C	2.035560910113	3.771792122569	0.394653813858
C	1.081192679008	4.715375049463	0.815671328336
C	-0.259629150735	4.318078247786	0.935087919309
C	-0.595297192653	2.990775469642	0.631397813400

C	2.885963517770	-1.077000758327	-0.330359186900
C	2.251603655866	-2.362504705614	0.155040649316
C	2.984454725856	-3.496209198039	0.535722297297
C	0.232168552286	-3.432315404189	0.623499573274
H	0.420429911850	2.411079892939	-2.484748413978
H	1.014638270853	4.699998090899	-3.344013521934
H	1.366106628659	5.034270184012	-5.819918603523
H	1.389984430985	3.982774368963	-8.181029408363
H	1.062151004605	1.935289505113	-9.582577043541
H	0.432680812455	-0.244881178076	-8.562271515698
H	4.846317572046	-3.953491401218	-4.755608990978
H	5.142619291611	-1.437889195364	-4.891722424559
H	-0.211705574659	-3.867395974679	-5.618092758961
H	-1.814781589057	-3.113173869643	-5.698667306447
H	-1.824121650445	-2.496835671434	-2.212720046479
H	-2.430091709773	-3.665681560112	-3.429282952332
H	-4.698023361120	-2.841830858090	-4.042619445846
H	-6.120245873228	-0.936811039870	-4.894636271698
H	-5.063087294773	1.356041414003	-5.143445565915
H	-2.631603302350	1.633792075878	-4.539804562097
H	0.281301503682	-3.114787109022	-2.183155126182
H	0.235983196046	-4.417299297469	-3.416040111189
H	2.615882243345	-4.872722401000	-4.008317555782
H	3.192748091392	0.040058246751	-4.284018244527
H	-2.781724749527	-0.338190787659	-1.269750472505
H	-5.150799805097	-0.575078816355	-0.459706074457
H	-5.591892039609	-0.794607790034	2.014631512874
H	-4.613045149982	-0.888369042237	4.403952364905
H	-2.575115694785	-0.806636725840	5.854725494110
H	-0.302918909458	-0.526861562749	4.880284025510
H	2.842815606078	-5.538654928614	1.286209728106
H	0.308187641658	-5.474797486230	1.362266608562
H	3.441416289607	-0.514601931611	2.022330742050
H	2.939168934650	1.185880258823	2.046397513668
H	2.414474278303	1.199584268916	-1.453526907222
H	3.616374961964	1.667643849341	-0.209787881790
H	3.097813628368	4.046709719030	0.307866823792
H	1.386364524752	5.743784012147	1.062369029771
H	-1.036140617063	5.019778072415	1.273107112596
H	-1.631132759945	2.630860251154	0.731258607956
H	2.713488394579	-0.974766521122	-1.421226853837
H	3.983060129255	-1.079259842590	-0.157451132769
H	4.084489844486	-3.482129200960	0.507229819012

H	-0.865525037018	-3.355056553920	0.665680877364
H	-0.847490847583	0.642755559082	-1.869893116813

Coordinates for Chapter 5

Coordinates for the DFT optimized structure of $[Mn^{III}(OH)(dpaq)]^{+}$

	x	y	z
Mn	-0.14426131020374	-0.03093342279741	-0.00466336956423
O	0.23388381326148	-1.19005653117820	-3.90369805667658
O	-0.16204487979994	-0.06337053907345	1.82208654520205
H	-1.00906352441536	-0.25319643182657	2.24570366489495
N	-0.72344738692287	1.95040854142632	-0.28187478589552
N	-0.11457970656179	0.04371692412957	-1.97153490500201
N	0.49585868875434	-2.13087279635700	-0.36047560186977
N	-2.12328891241805	-1.18166039719147	-0.15290877672204
N	2.12998405441231	0.05288701353682	0.07094523129664
C	-0.98272376033025	2.85198709038693	0.65480460758677
H	-0.86610636038968	2.51989840990834	1.68911309897017
C	-1.38111490970005	4.16492116576356	0.33419159938008
H	-1.58431899230619	4.87552100080890	1.13713099086231
C	-1.50770399373446	4.52419656264373	-0.99569838702441
H	-1.81754948678480	5.53621432481510	-1.27034092100907
C	-1.23185778351161	3.58189154392293	-2.02065459288280
C	-1.32647529212874	3.85515393488782	-3.41170682163829
H	-1.63455320729541	4.84830352863531	-3.74611242363447
C	-1.02396256251373	2.85796287466187	-4.31795073250682
H	-1.09375203344759	3.06333704601959	-5.38922106523533
C	-0.61670403630933	1.56295310970377	-3.91025117164000
H	-0.38159903077933	0.80293583845329	-4.65176811870286
C	-0.51017759725053	1.25323687280934	-2.55551785146134
C	-0.82834433605778	2.27700392424580	-1.60902980328031

C	0.22830923146456	-1.06729470362236	-2.68875045863972
C	0.68976576500431	-2.26132063373001	-1.83705675144537
H	1.75918373003565	-2.40019262587799	-2.05622077565596
H	0.17747345572376	-3.15803473665778	-2.21732735224247
C	-0.57241366548874	-3.01596184318065	0.15353296875642
H	-0.48827743889937	-3.02953757153917	1.25170151570962
H	-0.43720194426498	-4.05277874099375	-0.19971549180479
C	-1.95522205152819	-2.51236181298915	-0.19979133860598
C	-3.01519137982397	-3.37357549817794	-0.49113411770115
H	-2.84998864648045	-4.45250599989918	-0.53350862673330
C	-4.28194179777214	-2.83203281936540	-0.72456331437625
H	-5.12749680625871	-3.48465085780797	-0.95456390963145
C	-4.44668025352696	-1.44670922221474	-0.66692936395381
H	-5.41705867589321	-0.98015096298024	-0.84630184269320
C	-3.33210541015756	-0.65808842655700	-0.38384885277463
H	-3.40786909094460	0.43159521199769	-0.34258326149394
C	1.75412858110456	-2.31611507291824	0.39955450687092
H	1.48886307604837	-2.36129610240280	1.46729400326908
H	2.24827189738051	-3.26661198527743	0.13285367929188
C	2.70114003216062	-1.15177174708998	0.20916543621761
C	4.08922657628272	-1.30494866014771	0.23772075490986
H	4.53014433325380	-2.29899052495356	0.33998038759136
C	4.89532799893663	-0.16856541172352	0.13903777810596
H	5.98407704366057	-0.25997487865758	0.16200272767349
C	4.28875860373235	1.08202990735718	0.00440427989374
H	4.87953252774636	1.99603527949601	-0.07885106373252
C	2.89643458697364	1.14285289083706	-0.03138254772005
H	2.37611363896358	2.09667937874124	-0.14694496053243

Coordinates for the DFT optimized structure of $[Mn^{III}(OH)(dpaq^{5NO2})]^+$

	x	y	z
Mn	0.00206989831817	-0.03075268229229	0.00168294629819

O	-0.10695397752293	1.17572481666391	3.90246778301491
O	0.02438412189161	-0.00972849363748	-1.82006002125526
N	-0.01563116393975	-2.09721695421493	0.28667711437044
N	-0.00760084617355	-0.10915178440571	1.97238814861714
N	0.02016400829163	2.15951129883998	0.36787868920678
N	-2.21875806604327	0.50919832811402	0.09284848759516
N	2.20561294126281	0.52034153749373	-0.00870890044735
C	0.02046819307589	-3.01739997383194	-0.66540625319217
C	-0.01235110232935	-4.38884976151593	-0.36035946158687
C	-0.09820900663601	-4.79378888447531	0.95862718570479
C	-0.14172756974146	-3.82697932215331	2.00477092025112
C	-0.20497005047677	-4.07641105814939	3.41402270461015
N	-0.30036352500143	-5.43736624250359	3.97619425297262
C	-0.18645308276379	-3.02878656082847	4.31715091406426
C	-0.12949578309441	-1.68401962269905	3.90850838106611
C	-0.07723228597459	-1.36961875829454	2.55074703947593
C	-0.08177599459647	-2.45568941937648	1.60704426501720
C	-0.02104418994755	1.06019890054931	2.69259922195192
C	0.13595821220235	2.33291417072935	1.84697973883497
C	-1.24319055132787	2.71096010938834	-0.17136289135552
C	-2.43529864537771	1.83312794597746	0.14392745031825
C	-3.70333808346224	2.35695575728451	0.40436303225661
C	-4.77188727467423	1.47772886033638	0.59767704977747
C	-4.53741438408994	0.10266520974082	0.53208380899070
C	-3.23768409890109	-0.33667515726736	0.28422953149496
C	1.19605137992888	2.69314778882610	-0.36024602948877
C	2.42398252053747	1.83692059527365	-0.14022228284406
C	3.71561940151165	2.36864916425545	-0.13593508317420
C	4.80236966842956	1.50004549063784	-0.01070251870433
C	4.56324064836596	0.12998349835743	0.11574308103225
C	3.24210939277817	-0.31463336714688	0.11783161192818

O	-0.04840405105798	-5.57582260060464	5.15975128371517
O	-0.64211134999580	-6.34676796333631	3.23021794300737
H	-0.82814416716187	-0.06310956614858	-2.27143293226448
H	0.08471045462219	-2.64985254162223	-1.69213198976430
H	0.02839595117521	-5.12244350975508	-1.16767254491613
H	-0.13378770388784	-5.85132120095002	1.21071511459645
H	-0.22517898004832	-3.26612679973050	5.38099414010343
H	-0.12784616712836	-0.88818876135123	4.64905899163236
H	1.12864197951014	2.73967946033573	2.09218558799500
H	-0.59630412879346	3.06810505415564	2.21271085800040
H	-1.14014045881449	2.75925603389925	-1.26680560635727
H	-1.41565469707407	3.73957274661978	0.18899407814365
H	-3.85108338769203	3.43823636201625	0.45262706437253
H	-5.77364841697867	1.86297181556817	0.80245184788935
H	-5.34165557896563	-0.62061917126717	0.67939167989049
H	-3.00231147151447	-1.40314857206119	0.24016422192399
H	0.95728050493923	2.66909009578461	-1.43487419005987
H	1.39722938223945	3.74215044114453	-0.08185840053152
H	3.86649475745890	3.44620908318028	-0.23290840507626
H	5.82315860969195	1.88980358140474	-0.00689045748900
H	5.38232868907650	-0.58429550112906	0.21838750716695
H	3.00489852587960	-1.37600891582856	0.22393729122007

Coordinates for the DFT optimized structure of $[Mn^{III}(OH)(dpaq^{5Cl})]^+$

	x	y	z
Mn	-0.02729750414760	-0.02846443871729	-0.00343947351222
O	-0.06950560057508	1.17522803673720	3.89849088712581
O	-0.01284777556264	-0.00120573513385	-1.82907369039879
N	-0.04796898541558	-2.09726137488702	0.27031059622213
N	-0.02096870597623	-0.09894038429317	1.96253999865293
N	0.00888754728600	2.16259799987210	0.35846801574127

N	-2.24729213357222	0.53848970157265	0.09017896094294
N	2.18556889754924	0.50173693656971	-0.01785990329107
C	-0.03183968782090	-3.02906506733044	-0.67177274241706
C	-0.05578871134863	-4.40189244749028	-0.35920850227425
C	-0.09656648276848	-4.79051771825098	0.96725590122334
C	-0.10701263977157	-3.81424797434743	1.99593887305346
C	-0.13864865261199	-4.09471295820619	3.39477897988116
Cl	-0.17350129274634	-5.74551251786372	3.94900299515773
C	-0.13843181291734	-3.05534398916759	4.30561571996927
C	-0.10433566246361	-1.70240135715098	3.89475689013777
C	-0.07141853800246	-1.37134024913211	2.54174228883883
C	-0.07832459524082	-2.44365790962379	1.59629599655839
C	-0.01617869621059	1.06144073132608	2.68382673629848
C	0.10809276904881	2.33991788464431	1.83961689939648
C	-1.24237301181389	2.72329776573611	-0.19771158875874
C	-2.44703807106058	1.86540394323089	0.12336094065591
C	-3.70868963482393	2.40911492352079	0.37408922294206
C	-4.78864467696641	1.54642130652835	0.57764360454312
C	-4.57115261006393	0.16781956594965	0.53281201340042
C	-3.27655347919284	-0.29136040392651	0.29303138821713
C	1.19588613520462	2.68389878583570	-0.35953476168341
C	2.41497167975171	1.81790760457923	-0.12979711799240
C	3.71006726785463	2.34045004032195	-0.09983394282025
C	4.78866905878464	1.46260657643649	0.03121304236870
C	4.53796147185896	0.09296216296748	0.13719082721239
C	3.21362949119993	-0.34199544734315	0.11410487262236
H	-0.86761465088589	-0.06025153533029	-2.27505012382817
H	0.00665461523084	-2.67164191642791	-1.70343656062507
H	-0.04157319825240	-5.13840744842453	-1.16458419683487
H	-0.11752180965015	-5.84696727234908	1.24195192770237
H	-0.16232154688280	-3.28372262085161	5.37296995145097

H	-0.10134600447879	-0.91077892375871	4.64091892797584
H	1.08256826973070	2.78366733195508	2.09336415275333
H	-0.65407222959991	3.04866309211756	2.19634677011083
H	-1.13145432456689	2.75361815195929	-1.29303944191438
H	-1.40403786207687	3.75926840241915	0.14677703764806
H	-3.84232123057137	3.49281302145440	0.40721246489832
H	-5.78583320178605	1.94720451252996	0.77479635768822
H	-5.38459669326383	-0.54294919910170	0.68997455333286
H	-3.05388131515164	-1.36112694912982	0.26532168688660
H	0.96622969592145	2.65960484945890	-1.43620613241567
H	1.40416464081606	3.73159886189913	-0.08130175194980
H	3.86978396699176	3.41798185842243	-0.18166378863042
H	5.81199862257707	1.84492468529605	0.05523876580259
H	5.35031070572653	-0.62845846841161	0.24349560913723
H	2.96676619270731	-1.40263942669090	0.20439086279728

Coordinates for the DFT optimized structure of $[Mn^{III}(OH)(dpaq^{5OMe})]^+$

	x	y	z
Mn	-0.02811930811197	-0.02583631317549	-0.00068992545160
O	-0.07844612423624	1.19057137023633	3.89580482438139
O	-0.00754653593750	0.00164685589186	-1.82913383377025
N	-0.06135981683381	-2.09058378394525	0.27368930362183
N	-0.03015360728317	-0.08495273001340	1.96207404738247
N	0.00972700141061	2.16663207182737	0.35227482923148
N	-2.25325578949353	0.54843652148808	0.08321530513971
N	2.18829201679281	0.50460894292722	-0.01324147058116
C	-0.04690404367421	-3.02966383247745	-0.66329619816956
C	-0.08150293544333	-4.39951774211728	-0.34570402857810
C	-0.13161010237214	-4.78139259726152	0.98536675648466
C	-0.14070006064184	-3.79866928700317	2.00274916340407
C	-0.18169353107492	-4.09795927090842	3.40532247151508

O	-0.21841815176371	-5.41591106843498	3.71545422921950
C	-0.17857409979482	-3.05068333561726	4.31382204231389
C	-0.13273651613178	-1.69807443388269	3.89398798621831
C	-0.09146797151499	-1.36182501476204	2.54472074156902
C	-0.10070445089524	-2.43119387248723	1.60183873255310
C	-0.02335037002901	1.07278127016668	2.67962037684929
C	0.10547677795405	2.34969419697590	1.83345929146273
C	-1.23895710688139	2.72744804670439	-0.20908059415345
C	-2.44690321911585	1.87599982511483	0.11655155673135
C	-3.70500650494144	2.42568948106205	0.37212538281805
C	-4.78797597488412	1.56786966716456	0.58049051946902
C	-4.57671224121017	0.18840831011799	0.53553141285059
C	-3.28489447746310	-0.27659018432643	0.29087147271484
C	1.19829596675360	2.68441385925093	-0.36499534262725
C	2.41724675402140	1.82039763896650	-0.12738539780890
C	3.71187077372065	2.34402715432137	-0.09259146970528
C	4.79035935795469	1.46717589169865	0.04560871437543
C	4.53995089746751	0.09768023692789	0.15381672593762
C	3.21585210178776	-0.33810417380479	0.12581384171765
C	-0.24900789609835	-5.79771652656307	5.08983076820971
H	-0.86134871485677	-0.06711517389576	-2.27531582270476
H	-0.00101668060056	-2.67750807382320	-1.69655711898761
H	-0.06792380061319	-5.13906009446622	-1.14824633218740
H	-0.16069846210265	-5.83603694474767	1.26539759644131
H	-0.20855831972052	-3.24844830290984	5.38514093287229
H	-0.12741541056392	-0.90535722522706	4.63934864533162
H	1.07977052018338	2.79371560361749	2.08741224315189
H	-0.65723699745072	3.06062602848290	2.18479283001660
H	-1.12684814715251	2.74921696598184	-1.30447990110955
H	-1.39751139862146	3.76634351694809	0.12823866223704
H	-3.83355921578670	3.50999638305393	0.40541843888732

H	-5.78256252445805	1.97318971163041	0.78151219467657
H	-5.39269494980272	-0.51865066665641	0.69626704948095
H	-3.06639647063954	-1.34726441790275	0.26318581561007
H	0.97181364988633	2.65361643781047	-1.44219202241821
H	1.40552019907736	3.73373689229734	-0.09182183551447
H	3.87118503280738	3.42148335579399	-0.17622356244998
H	5.81334276324422	1.85019291281185	0.07340348065029
H	5.35228204039154	-0.62295696696125	0.26548229209827
H	2.96848894838464	-1.39852413080482	0.21786522441846
H	-0.26985722642223	-6.89471541301246	5.10000692514602
H	-1.15126843361537	-5.40832337110955	5.59026224263012
H	0.64976678639555	-5.44209020097335	5.62061978639788

Coordinates for the DFT optimized structure of $[Mn^{III}(OH)(dpaq^{2Me})]^{+}$

	x	y	Z
Mn	0.00352679364053	0.03444464890673	-0.01198517679091
O	0.03698730560003	-1.66325701510633	3.69825286184205
O	-0.00784037745586	0.03688374371595	-1.84247328527495
N	-0.00946644958313	2.11514782223165	0.52408924129305
N	-0.01616144682697	-0.14805579391185	1.93978629199204
N	-0.00561309318158	-2.19098262395468	0.07288206371325
N	2.21692692987599	-0.50286360783685	0.05212634817536
N	-2.19637052162701	-0.50700411687126	-0.06458681955266
C	-0.03384108260267	3.20749938114921	-0.24756430107462
C	-0.03921411434479	4.50224940016430	0.33330576983668
C	-0.01578918447744	4.65525911268209	1.70057976581564
C	0.00454494994490	3.51428558588747	2.53962203663618
C	0.01942856089346	3.58884519017406	3.95695070407331
C	0.02824316586667	2.42408033641634	4.69513528158348
C	0.01999561365436	1.15425759136625	4.07321408850553
C	0.00516697886485	1.03932080745965	2.68247060414618
C	0.00253429955981	2.23834869702800	1.90030375468475

C	-0.00666970651429	-1.39257966534649	2.50781275353208
C	-0.09104626500502	-2.55965292684188	1.51378305291115
C	1.25220822164800	-2.64180953772307	-0.55925927342643
C	2.43931544993829	-1.81747444908795	-0.10713583064040
C	3.70715565187581	-2.37078337445205	0.08537283483118
C	4.76574285793523	-1.53100144257191	0.44086649625948
C	4.52223699196495	-0.16551914950782	0.60139892697639
C	3.22449862463114	0.30394370928703	0.40249959799558
C	-1.19174454638810	-2.61705570347849	-0.70353311263239
C	-2.41404377886462	-1.80122930018870	-0.34153029834789
C	-3.70277541320764	-2.34023674049056	-0.34264547531276
C	-4.78562250453033	-1.50383495776864	-0.06135200534382
C	-4.54594458404138	-0.15744973492077	0.22044373845569
C	-3.22772022757626	0.29645732862371	0.21299121404638
C	-0.03939373391662	3.08344069460183	-1.74582018679264
H	0.82316665153920	0.24608668649108	-2.28668507752040
H	-0.06227173452054	5.37163791961234	-0.32572393437478
H	-0.01779927220754	5.65234626642833	2.14930415196556
H	0.02140517998545	4.56822691331891	4.44059993656605
H	0.03924078943404	2.46905675638118	5.78707210671855
H	0.02358092412150	0.25049054310429	4.67686010772108
H	-1.04550006092863	-3.06991804901158	1.71266661320430
H	0.69958166101925	-3.27726961608079	1.77957614417018
H	1.43481074724432	-3.71360332888739	-0.36909651023569
H	1.13937857281693	-2.51082191534805	-1.64645154539232
H	3.86085182950859	-3.44489037903927	-0.03997053851899
H	5.76639786069397	-1.94050598302380	0.59863440948670
H	5.31766867510865	0.52582750138493	0.88539321339411
H	2.97995199108615	1.36100321994193	0.53327182965208
H	-1.39239599813264	-3.69438536566169	-0.57135073204897
H	-0.97067372510727	-2.43780583231122	-1.76683489676318

H	-3.85417213786460	-3.39976399932197	-0.56064994488156
H	-5.80345002824787	-1.90133181950814	-0.05517652666212
H	-5.36130065680401	0.53039779311053	0.45141120981863
H	-2.98716766351009	1.33785108143317	0.44005549978454
H	-0.71713469400224	2.29276888672409	-2.09059333650397
H	0.96740847357123	2.82433407353475	-2.11526175196994
H	-0.32016475055412	4.03914573709343	-2.20815408972584

Coordinates for the DFT optimized structure of $[Mn^{III}(OH)(PY5)]^{2+}$

	x	y	z
Mn	0.02687446516361	-0.01230068144856	-0.00024619064534
O	-2.50003534195310	-2.55835921745760	-2.86983266280121
O	2.64773904312533	2.43964238777140	-2.87257456712938
O	0.02660494309340	-0.05968989320208	1.79567977137234
H	0.69779295206334	0.44854416639960	2.27268267529110
N	0.04865455172443	-0.02898177524621	-2.06615633103882
N	-2.23183233990028	0.00406240442556	-0.26882259696143
N	-0.28111844427934	-2.15878923875642	-0.06146086739138
N	2.37717286217987	0.01303154331269	-0.22954479066589
N	0.32119078626860	2.08081874655843	-0.06725941318931
C	-0.68547993285075	-0.96083593081001	-2.71409702798121
C	-0.38235112065040	-1.31393725836624	-4.03068337090828
H	-0.93344608889780	-2.11123620219534	-4.52077985816339
C	0.66680599877064	-0.67566877045451	-4.68503262454689
H	0.94091050666771	-0.96450506899937	-5.70262829954109
C	1.37123795864229	0.32394008810400	-4.02239952074804
H	2.21070660624719	0.82185577893675	-4.50069881754140
C	1.02797346137977	0.64353863705098	-2.70724427992450
C	-1.78244878168479	-1.75999885941239	-1.96214433656228
C	-3.34410320708691	-1.93268478435199	-3.85904025158629
H	-3.30888915949911	-0.83460568718214	-3.81244637427983

H	-4.38069345496956	-2.26610526810507	-3.70882083420908
H	-3.02288438355366	-2.26403596726784	-4.85729743014463
C	-2.75041192233095	-0.93878265644396	-1.06955027400313
C	-4.10533352479414	-1.28186985840821	-1.00319736527512
H	-4.49797963952681	-2.09888700365065	-1.60298225511297
C	-4.94578988909935	-0.58534146618334	-0.13288237288456
H	-6.00690169109915	-0.83935135230975	-0.07209149979843
C	-4.40567595489614	0.42285501426858	0.66433191743545
H	-5.01991602727929	0.99413177901480	1.36275870051612
C	-3.03903494266090	0.66563479651302	0.57454612910859
H	-2.57207010303424	1.40866608800247	1.21834825364167
C	-1.05108061039495	-2.72970314118588	-1.00705053834524
C	-1.23060387825366	-4.11004759461665	-1.07819931631638
H	-1.86040023369020	-4.53206473662945	-1.85944570249514
C	-0.60359051911348	-4.91858879392507	-0.12573110747079
H	-0.72503962108930	-6.00421976988043	-0.16099944038795
C	0.15480735180489	-4.31922618965032	0.88065511845797
H	0.63536479566237	-4.90939584495181	1.66304260293955
C	0.28287254615734	-2.93319474869388	0.88050617548214
H	0.82425686581477	-2.41142220233962	1.66902813742228
C	1.90394205370480	1.67837086741961	-1.95489175241510
C	1.95599750344187	3.29830348842160	-3.80408492110970
H	0.88209880344816	3.38434433508175	-3.58260104410072
H	2.08154448321675	2.91552593595886	-4.82720789425446
H	2.41719082852901	4.29478494058717	-3.75437471364118
C	2.91866583480085	0.85409689283420	-1.12568090344460
C	4.29643540234674	0.98786150337479	-1.29362773793701
H	4.69111774848410	1.68261071802433	-2.03335962107075
C	5.14139882422913	0.21409228306225	-0.49180304017795
H	6.22623102605868	0.29360404607100	-0.59873523352802
C	4.58116199355838	-0.65344670830531	0.44668339606598

H	5.20406978941521	-1.27117625393176	1.09634816810129
C	3.19225185255568	-0.71844820976411	0.54373283845427
H	2.71676855132621	-1.37913663759073	1.26962624583752
C	1.18111107356605	2.61276694848938	-0.95335871185720
C	1.53550717266488	3.96472302720977	-0.87536904635128
H	2.28365490127968	4.37188215569872	-1.55035898557518
C	0.95096649709133	4.77962586538437	0.09425106786165
H	1.21926058751246	5.83710070544096	0.15737495029028
C	0.04169493863029	4.21811698463078	0.99117395258197
H	-0.43305879405471	4.80992972120271	1.77590375867252
C	-0.22587909702681	2.85939909174229	0.88622667852182
H	-0.87315890095603	2.35934070372386	1.60514206245809

Coordinates for the DFT optimized structure of [Mn^{II}(OH)(dpaq)]

	x	y	z
Mn	-0.11873007276243	0.00960123780735	-0.30116535063017
O	0.23377683569716	-0.09024367383950	-2.22066264691802
H	0.14006915306660	0.67331264127701	-2.79811305272783
O	0.83400999929236	0.44726988533393	3.89912509373677
N	-2.34444485233638	0.07568762784014	0.08877212246357
N	-0.33824891289822	0.18555092597007	1.89318424955436
N	2.13722759784669	0.01169099071994	0.49642335117645
N	0.59374370689551	2.39247482208965	-0.03751567654870
N	0.55600831775578	-2.27235293618899	-0.00356945744288
C	-3.27309486048795	0.00108341567027	-0.84657364905107
C	-4.65188901415506	0.09686727113614	-0.55745071492499
C	-5.03746589395877	0.27843979221480	0.75501596675119
C	-4.06245606447004	0.36397737603161	1.78427374261757
C	-4.39048747251291	0.55118770361717	3.15209443972038
C	-3.37030555545570	0.62320196951117	4.08095076376422
C	-2.01051160872704	0.51479646282733	3.71549370080057

C	-1.62243324273120	0.32383240037167	2.38099021579843
C	-2.68625897880343	0.25247645300433	1.39673476865934
C	0.75423885464279	0.24704771962476	2.68091837902528
C	1.63429179607888	-4.79000560483148	0.47108686141639
C	0.25359266939541	-4.62260338114986	0.35549351308698
C	2.10458563645716	-0.03271035263910	1.97353731335461
C	2.73038746775824	1.24310017351988	-0.03914203084272
C	1.89965309911723	2.47518567187409	0.25508308552783
C	2.46599053849516	3.65095119941030	0.75921211483091
C	1.65110421140233	4.76942056671137	0.95016912506056
C	0.29477772326777	4.67416705366036	0.63801921967116
C	-0.18628522060579	3.45597961550811	0.15136267107191
C	2.72265595836366	-1.18120097804803	-0.12812717323589
C	1.88387887677697	-2.42208982902866	0.09766910730861
C	2.46183176101204	-3.67239205597414	0.34557784187986
C	-0.23702970230650	-3.33615151651360	0.12361968650803
H	-2.91421519022446	-0.14097817633142	-1.87106817631220
H	-5.38440727514560	0.02681989201705	-1.36470016660443
H	-6.09600948481787	0.35744491487400	1.02092125682571
H	-5.43947860409359	0.63389975971052	3.44823504044327
H	-3.61264370662893	0.76824065486282	5.13814782471850
H	-1.23180017070123	0.57645286783699	4.47225058692652
H	2.06318492183886	-5.77697564417621	0.66326791284045
H	-0.43381926080023	-5.46582781763110	0.45032620043026
H	2.40675497420114	-1.03659839542945	2.31220939093027
H	2.84201058189388	0.66384815308159	2.40638826555916
H	2.77666386661140	1.13113661970339	-1.13437865774842
H	3.76387507215806	1.39559028381243	0.33189152399532
H	3.53075708872665	3.68495315766897	1.00121722750169
H	2.07025977702222	5.69829568898886	1.34555356759566
H	-0.38356349247242	5.51874944645302	0.77661696087248

H	-1.24557547563391	3.32906167418037	-0.09276456411372
H	2.74490566842349	-1.00074013681313	-1.21571853166595
H	3.76240894672350	-1.36570997587184	0.20942810982160
H	3.54675535257635	-3.76423812456747	0.43778590077526
H	-1.31183060076757	-3.15101897688764	0.03755347474587

Coordinates for the DFT optimized structure of [Mn^{II}(OH)(dpaq^{5NO2})]

	x	y	z
Mn	0.52958905463093	0.82962402637142	0.04969544821730
O	-0.59902444810990	0.50975747591622	4.21955475573197
O	0.88393300443529	1.59087428350356	-1.70446165094208
N	0.36784568227504	-1.40169807695913	-0.24122718499817
N	0.03018643804922	-0.05493305870645	2.03837150636967
N	0.47648477057829	2.72224259769702	1.51811973563010
N	-1.82901027018418	1.57143690499581	0.24216576059291
N	2.75435578649115	1.24457373045457	0.80347139808319
C	0.58560861368480	-1.97420486631895	-1.41071910763716
C	0.43062703565162	-3.35922954200869	-1.59566185351873
C	0.02296215095048	-4.13919765320196	-0.53155672516062
C	-0.23138371973174	-3.54820732079734	0.73989277231485
C	-0.64862870606247	-4.23370769859570	1.93154037415177
N	-0.91790254144636	-5.66497051367782	1.98327035930451
C	-0.82262694309388	-3.52313138523383	3.11506249136289
C	-0.62495324708320	-2.14467435719302	3.20442311190965
C	-0.21948809325971	-1.39396567390229	2.08491051232288
C	-0.02488879042238	-2.13062143641704	0.83678575325472
C	-0.14865543318727	0.77092016444191	3.10369440825954
C	0.35594555649490	2.21950968203719	2.90184780066602
C	-0.67677828816685	3.52847597223397	1.09558276264812
C	-1.94442713599739	2.71359712270332	0.93443497057364
C	-3.17750230299258	3.15126214455120	1.42860016885667
C	-4.31782517206194	2.38249103127226	1.18295122789891

C	-4.18797993587856	1.19892839724845	0.45593340577692
C	-2.91511471968356	0.83385837664463	0.01165961789186
C	1.74655497073683	3.41122046856990	1.24888805811377
C	2.93362828740264	2.47098861751390	1.31326318737219
C	4.16810853583388	2.87322823187140	1.83516781132549
C	5.23884784740507	1.97723007643611	1.81177696736221
C	5.04125628686438	0.70424013233419	1.27467857899328
C	3.77368578626974	0.38479480066115	0.78506960950592
O	-1.10134485981249	-6.18001178138162	3.08181273021426
O	-0.96254922751584	-6.30623969683606	0.93264398777673
H	0.18665729635281	1.77978694039907	-2.33939701853713
H	0.89392558453237	-1.30685881926079	-2.22173367963988
H	0.62972615458963	-3.80711027069641	-2.57160133378788
H	-0.11212010571591	-5.21063547153867	-0.64983185007418
H	-1.13689060021838	-4.07927458727805	3.99816666912800
H	-0.78965518639622	-1.63035865017194	4.14737095912867
H	1.35012392106628	2.23964219025796	3.37534978323031
H	-0.28732610329774	2.87512817851548	3.51307557498674
H	-0.43303506242896	3.95549232760817	0.10933488435880
H	-0.86074329556896	4.37210081993668	1.78983882889754
H	-3.24040933815160	4.07972837624861	2.00053222949454
H	-5.29222491229105	2.70135601946113	1.56174377360464
H	-5.04902848640840	0.56218334932364	0.24274957970191
H	-2.76133565165548	-0.09196137631434	-0.55084669863410
H	1.69422476689887	3.80352418192563	0.21978585454731
H	1.91173224722039	4.26959174037206	1.92982553606066
H	4.28334373078062	3.87456079956923	2.25638155371487
H	6.21235034856110	2.26813092446826	2.21476358991048
H	5.84689999674589	-0.03203855497814	1.23950055760723
H	3.56634197432075	-0.60180744107589	0.36120082307629

Coordinates for the DFT optimized structure of [Mn^{II}(OH)(dpaq^{5Cl})]

	x	y	z
Mn	0.08346296813730	-0.11183605491858	-0.21361755768074
O	-0.50568115315907	1.02270615180450	3.92076191049417
N	0.04980560009126	-2.31848252948830	0.28818835460577
N	-0.15705690932527	-0.23315683746645	1.98090857171010
N	0.00467295264056	2.18663193106887	0.47435444225463
N	-2.30437550757261	0.56600735509696	-0.09104013426730
N	2.33655475802065	0.63617203649854	0.11740551623608
C	0.16968428996959	-3.27998788982843	-0.60746045657857
C	0.09555827583675	-4.64620360391038	-0.26207183850524
C	-0.11004329107650	-4.98380787083573	1.05964186234060
C	-0.24133386580580	-3.96893225665739	2.04404439703071
C	-0.45385850728625	-4.21633721934666	3.42895910674250
Cl	-0.55897065686124	-5.86647219721218	4.02366010461227
C	-0.57466947385145	-3.15947445674672	4.30918541918393
C	-0.49066014201387	-1.82060600151868	3.87451032337344
C	-0.27549268419369	-1.49379478801365	2.52850879750845
C	-0.15312593688907	-2.60511322431968	1.60369824028077
C	-0.26940929505391	0.89347107385641	2.71363274677564
C	-0.00846478470394	2.21790569961593	1.95326237994712
C	-1.21588140730624	2.73377665330727	-0.13062691032869
C	-2.44036142401097	1.88096709310188	0.13118596318506
C	-3.66103262662764	2.43570875801450	0.53046441857541
C	-4.76787800974961	1.59813319980618	0.68788611751963
C	-4.61696209144511	0.23200404714853	0.44834508414771
C	-3.35728315245229	-0.23556029035955	0.06602619324214
C	1.21004478923733	2.77557310026663	-0.12254354557249
C	2.45787477693159	1.96938364619720	0.17401228181664
C	3.68832439929167	2.58183926123710	0.43702265230222
C	4.81788811011597	1.78258766124377	0.62409642496395

C	4.68110710417685	0.39554135398467	0.55281072021390
C	3.41185675277933	-0.12969013705726	0.30272701950843
H	0.33075988524903	-2.95477952090995	-1.64035820972563
H	0.20081465623325	-5.41182289672552	-1.03382246628807
H	-0.17455433384457	-6.02793129132775	1.37179571984550
H	-0.73835266101878	-3.36651590417942	5.36918750095420
H	-0.59208218466061	-1.01068342407306	4.59322010670645
H	0.96972692778900	2.57157458245040	2.31637228139908
H	-0.74674676038935	2.94807039101566	2.32457535603291
H	-1.05860677634183	2.75557117935347	-1.22122866511734
H	-1.40903963677233	3.77322706790647	0.20244061330577
H	-3.73912270205836	3.50942148387770	0.71682997504037
H	-5.73161201938278	2.00801693185039	1.00098159341027
H	-5.45120113405441	-0.46328814729570	0.56354003159742
H	-3.18654955295927	-1.30084405598023	-0.11795371860644
H	1.07164913381451	2.76640636604706	-1.21643140177114
H	1.36224940162762	3.82823066421423	0.19008971422131
H	3.75607973425086	3.67102882210216	0.49245369786813
H	5.79013044821865	2.23827094385798	0.82899160110550
H	5.53462142358705	-0.27046050770234	0.69536020086767
H	3.25070142085619	-1.21037664661732	0.24930821790893
O	0.25686601710871	0.02320974175957	-2.15054713680945
H	-0.49585714509686	-0.06866944419318	-2.74228861758368

Coordinates for the DFT optimized structure of [Mn^{II}(OH)(dpaq^{5OMe})]

	x	y	z
Mn	0.58611048593865	0.63849351640675	0.26550285457201
O	-0.15171938758221	0.60861151538862	4.52269237320760
O	0.89889552466070	1.35798240823600	-1.52310307155302
N	0.23270216460918	-1.59332882685684	0.08129612087915
N	0.15443972217157	-0.06496445577391	2.30683633652349

N	0.87756120226072	2.60563974049798	1.61210441197121
N	-1.64490928908698	1.72795323184944	0.55126098835369
N	2.89867930823638	0.76967531648678	0.87185499035514
C	0.32244465849595	-2.27928888551276	-1.04322089219527
C	0.04119063386527	-3.65971287846873	-1.11450324499559
C	-0.35390911326208	-4.31312965499990	0.03683036967596
C	-0.46163196902332	-3.59787510100589	1.25579354095863
C	-0.86613996516011	-4.20879382046914	2.48292543942036
O	-1.15703819442676	-5.54824184531379	2.40927377838926
C	-0.93628819792248	-3.43288331277296	3.62518813021483
C	-0.61352745490179	-2.05417497717944	3.60865449903833
C	-0.20801325859901	-1.39601599029309	2.44437600358190
C	-0.14386461045125	-2.20047695283186	1.24245088060357
C	0.16539672337901	0.79539705734738	3.33935331172709
C	0.71156814746848	2.21350227449525	3.02929145221296
C	-0.14598640015162	3.54442724102285	1.13814044996711
C	-1.53482785233337	2.93969726958977	1.11327999000309
C	-2.65140447172298	3.62399970647561	1.60610432482464
C	-3.91178322813923	3.03132295969955	1.50014911934454
C	-4.01477866681593	1.76976831377630	0.91347681760803
C	-2.84499981608953	1.15668111341386	0.45839062750703
C	2.22866750426830	3.06925015248155	1.27372854423946
C	3.26034996536404	1.96298814820518	1.36257030769523
C	4.54153697981028	2.18231854813417	1.88126768634749
C	5.46658612900861	1.13629135334251	1.87060650072955
C	5.07966247100757	-0.10009138870868	1.35158333751218
C	3.77667241312258	-0.23300610991331	0.86777512000378
C	-1.54727578777707	-6.21197670909737	3.59830462860179
H	0.17335749299876	1.56678864533932	-2.11918091581830
H	0.63017269730998	-1.71091095429401	-1.92694813092638
H	0.13568508580960	-4.18762138049121	-2.06588965467751

H	-0.58671544506266	-5.37934652321689	0.02876234942670
H	-1.24353391680058	-3.87170224756639	4.57523128017546
H	-0.67596036824629	-1.47667219765644	4.52848527511528
H	1.68831479937020	2.26463690106142	3.53618140020498
H	0.06155778625158	2.92829984216342	3.56089565413465
H	0.11471837942243	3.81349313028952	0.10151872140808
H	-0.15895899207345	4.47717872202390	1.73738942189461
H	-2.53045684888692	4.60515627342655	2.07054261625321
H	-4.79858630203293	3.54519047936718	1.87981980966474
H	-4.97696502905822	1.26251357211840	0.81572124727680
H	-2.87351708583188	0.16213027284374	0.00292242352213
H	2.20474463350620	3.40800874948810	0.22473547336711
H	2.54766473565739	3.92788907124619	1.89846093345610
H	4.80605929626868	3.16094173395170	2.28862119067636
H	6.47323110685109	1.28387808832108	2.27018902140647
H	5.76619165565734	-0.94897090485621	1.32561237594705
H	3.42069168259039	-1.18390723820569	0.46114366085941
H	-1.72490413151465	-7.26101716347684	3.32445770659682
H	-2.47621185926937	-5.78477677758116	4.01671194741126
H	-0.75593892713823	-6.16671247094749	4.36770573229972

Coordinates for the DFT optimized structure of [Mn^{II}(OH)(dpaq^{2Me})]

	x	y	z
Mn	0.05530498069775	0.14074240690049	-0.23995985510844
O	0.53148363739411	-2.00528939539340	3.46644020915830
N	0.01144912773928	2.19125391534447	0.79082298281494
N	0.25288396287313	-0.29218066553366	1.89763262110324
N	0.03561683413415	-2.24898363501679	-0.15711143799705
N	2.42802289764071	-0.63256361878489	-0.23213744674200
N	-2.22691452871606	-0.55746476051507	-0.12001142406722

C	-0.14552790524538	3.36696016220992	0.19656906725990
C	-0.03847554074754	4.57950472586522	0.93270463844312
C	0.22830942661642	4.53509658295061	2.27968095544068
C	0.39030836582627	3.28657176300780	2.93662461553579
C	0.66054418726866	3.18152276941230	4.32474342213781
C	0.79663829787297	1.92769270225580	4.88688530501216
C	0.67102570520275	0.75222310378775	4.11765400146081
C	0.40538205130315	0.79418682664024	2.73991079162727
C	0.26671540084950	2.10595316502401	2.13607498973416
C	0.31821083565918	-1.56864241577772	2.32842714769646
C	0.02082396318694	-2.65385137386995	1.26258914857367
C	1.24963441560109	-2.65831883726795	-0.87250731203245
C	2.49751780828033	-1.96550886031195	-0.36288728362080
C	3.67578878863617	-2.66816909524276	-0.08790074855733
C	4.80916350861165	-1.96126595868962	0.32114721800762
C	4.72670122489102	-0.57469393171468	0.44996764065859
C	3.50591765321633	0.04230098416839	0.16611328369507
C	-1.17796523037229	-2.60457365393773	-0.90274358769085
C	-2.39773009290622	-1.85615356182194	-0.40528280505407
C	-3.65020263220658	-2.47000957330545	-0.28864748195062
C	-4.74527616108302	-1.70709860321277	0.12242735958176
C	-4.55420462687535	-0.35589875532868	0.41471997872634
C	-3.26822708905395	0.17114022446659	0.28206525516433
C	-0.46177461511205	3.41387608485648	-1.27555185691544
H	-0.17019070321741	5.53180593517694	0.41365232898452
H	0.31744293866400	5.45652966022949	2.86314365492331
H	0.75496482872972	4.09114429270996	4.92363771788805
H	1.00429764413269	1.83139261795655	5.95679508092151
H	0.77622165702206	-0.22326965776686	4.58590992411361
H	-0.97551892428477	-3.04710245315578	1.51944506138375
H	0.72567785059058	-3.48231454005850	1.44491329380775

H	1.39654888377161	-3.75653242141652	-0.83790310138580
H	1.11739908290208	-2.36569249683541	-1.92641952254167
H	3.69955400773214	-3.75573296078497	-0.18884126742947
H	5.73999084176544	-2.48895533666864	0.54484430687307
H	5.58312441102061	0.02081433521211	0.77297446418042
H	3.38917599676705	1.12579650415034	0.26760075067801
H	-1.37751915428786	-3.69487089250782	-0.88786845769727
H	-1.01508731933738	-2.29960199811299	-1.94963974432004
H	-3.76077243252900	-3.53288610667054	-0.51577514839373
H	-5.73300114370056	-2.16499909183612	0.22129149214946
H	-5.37836847124899	0.27884793043211	0.74631310397138
H	-3.06301162834571	1.22090460437168	0.51058849851595
H	-0.36541565784165	2.42426180806834	-1.75146683645765
H	0.19827257801303	4.13151319415871	-1.79078190068497
H	-1.49533162428185	3.77213505496908	-1.42919594559650
O	-0.01637696362056	0.23507192352794	-2.20522742586402
H	0.77711365040165	0.40615737368581	-2.72246372011542

Coordinates for the DFT optimized structure of $[Mn^{II}(OH)(PY5)]^{+}$

	x	y	z
Mn	-0.10023488183438	-0.14827858923473	0.27575433980624
O	-0.30212508034304	-0.28856507362011	2.18425261447672
H	0.25925359254134	-0.73575478837913	2.82317310945738
O	-2.71021278903052	2.30133960554355	-2.88931331434676
O	2.76669608169168	-2.15098665336797	-3.00493228827475
N	0.00774718104461	0.02933719170479	-2.08329364646268
N	-0.45603840783145	2.10019121023881	-0.00672530747772
N	-2.44173579118143	0.00165967010743	-0.12188546109360
N	0.50430636499214	-2.42278958990507	-0.21075305653003
N	2.18005109420117	-0.00359870129503	-0.09184163159396
C	-1.12894597321161	0.48338318570796	-2.62861468975407
C	-1.68384098011235	-0.10606493245652	-3.77169327173281

C	-1.01846914601487	-1.17410302472060	-4.36686019963931
C	0.18002032258380	-1.61637291653010	-3.81330842764893
C	0.67089332485575	-0.97817173247507	-2.66757576132655
C	-1.95915593489431	1.58213609879059	-1.92306624031536
C	-1.98759695065469	2.95648987701490	-3.93818327720735
C	-1.23886467216165	2.58473630092122	-0.98009226980490
C	-1.55599382402535	3.95008287355086	-1.03340069293801
C	-1.01898173793665	4.81614962522847	-0.07989169115720
C	-0.20901712980657	4.29641031820769	0.92868874759194
C	0.02745940671128	2.92407258641301	0.93050874931621
C	-2.97700592200967	0.83130098395789	-1.02888741550461
C	-4.35393484807746	1.03380649162852	-1.13600801129080
C	-5.19437015385337	0.34591934351120	-0.25544801952741
C	-4.63351260384258	-0.49598778917635	0.70528639097215
C	-3.24495867389442	-0.63069528246674	0.74043360585467
C	1.93426257672675	-1.58108772194674	-2.00544341544773
C	3.23789809601693	-1.29046818137223	-4.04845478073591
C	1.42989753985284	-2.74953991601890	-1.12353646634570
C	1.92093704865952	-4.05010787968025	-1.25807962718399
C	1.41769542848803	-5.03962219457299	-0.40859608076325
C	0.45880462023121	-4.69637148528496	0.54541082459227
C	0.03740237180160	-3.36829093846636	0.61221932320572
C	2.79076748213196	-0.68330645966716	-1.07180575048837
C	4.19097707216003	-0.72272696250982	-1.15514368238203
C	4.95356328231599	-0.00842927953617	-0.23064086145989
C	4.30433148332435	0.70694897186545	0.77479497308246
C	2.91313951713685	0.66407133250261	0.80758688783013
H	-2.63606923654952	0.25044328349322	-4.16284732567413
H	-1.43760902799124	-1.66737612351535	-5.24721082935754
H	0.71554381942631	-2.46519662070142	-4.23726319483788
H	-1.02222586783705	3.36072546514348	-3.59502248936043

H	-2.62130689670585	3.78583471958790	-4.28347219148764
H	-1.79938026700054	2.27844768847782	-4.78560017125452
H	-2.23886855550912	4.32947260562491	-1.78975535091416
H	-1.25488187390429	5.88270627412576	-0.11444748510508
H	0.21027864438174	4.92974221711249	1.71259601224528
H	0.59523869712174	2.45093289588989	1.73429594487320
H	-4.74862781286725	1.71670207679479	-1.88672966725905
H	-6.27775838255152	0.47890351013100	-0.31433053629104
H	-5.25446480782855	-1.03540885472029	1.42295198369276
H	-2.74510636649191	-1.24365889493286	1.49430306425598
H	3.44766669054323	-0.27042554345873	-3.69045791818678
H	2.51572442273156	-1.22684590206090	-4.87759196655643
H	4.16895042935741	-1.73777862327519	-4.42513653431333
H	2.67656172451716	-4.27301933823475	-2.00989633562810
H	1.77801150533877	-6.06816010690722	-0.49000549010372
H	0.04539969453382	-5.43817450558267	1.23126115234052
H	-0.69141196548912	-3.03717488173246	1.35634716962746
H	4.68105326432709	-1.32608309788125	-1.91574481822236
H	6.04485098907784	-0.02865813066678	-0.28785612901813
H	4.85735599611935	1.26746827165010	1.53088532477068
H	2.35604079649855	1.16374904142655	1.60241055401222

Coordinates for the DFT optimized structure of $[Mn^{II}(OH_2)(dpaq)]^+$

	x	y	z
Mn	-0.04773479258761	-0.01505703574667	-0.00451492772222
O	-0.01650995218003	0.02540215829301	-2.37139801859562
H	0.08450540592819	0.83689338313545	-2.88869463740517
H	0.03790884218960	-0.70981295037284	-2.99799197485480
O	0.91558731459443	0.48752870450065	4.05829567720975
N	-2.24203105382364	0.10598489471000	0.22748819076366
N	-0.26649841220723	0.15989233129978	2.07360633947324
N	2.21008393278003	-0.02958017933879	0.66206593841021

N	0.60060682263444	2.18652446631889	-0.17002944547568
N	0.61318865880358	-2.18758987382867	-0.18468442648650
C	-3.17214509526798	0.05540419368362	-0.71479276144624
C	-4.54831669162835	0.18105157345239	-0.44208292822941
C	-4.94464475394547	0.37007725800556	0.86735904727649
C	-3.97976420467968	0.43303665105814	1.90533375335900
C	-4.32249304234759	0.63111083635679	3.26816140774910
C	-3.31904007898165	0.68404258489004	4.21425549011197
C	-1.95604880928521	0.54296041571414	3.86659979327989
C	-1.56180036705059	0.33800455165364	2.54128728357247
C	-2.60099317029659	0.28909101460399	1.53869827266377
C	0.83299991390081	0.23313327096880	2.85907778701550
C	1.51110484618877	-4.78419327386171	0.25563771281540
C	0.16152863084023	-4.53761937650852	-0.00250037700669
C	2.15734806795323	-0.13807118512479	2.14871199832871
C	2.81140853107818	1.23680990801749	0.20439062483418
C	1.85263804645194	2.40954902545341	0.27169641474454
C	2.25912475332880	3.67154981248343	0.71012979623481
C	1.34715054291119	4.72964095866451	0.67978618934944
C	0.05271882152853	4.49114452795609	0.21594674290989
C	-0.27608587256371	3.19880467938876	-0.19059179771209
C	2.83511364323862	-1.20879642397365	0.03581863467735
C	1.91700745815843	-2.41591814981532	0.06356297989095
C	2.39961648843553	-3.70688285434176	0.29296727509910
C	-0.24123631417737	-3.21955552333659	-0.21032508787126
H	-2.82040423188921	-0.08816989563338	-1.74081745115859
H	-5.27216473961382	0.12914359336035	-1.25763798044890
H	-6.00378097490614	0.47310035848075	1.11988399806596
H	-5.37322922207502	0.73841385048307	3.54731133327542
H	-3.57385538691828	0.83776861384481	5.26625021116928
H	-1.18763182363295	0.59074962540846	4.63538209484354

H	1.86815254786531	-5.80128254150003	0.43518003103678
H	-0.57110812237814	-5.34640589397835	-0.03229258784501
H	2.34970340771720	-1.18557368628084	2.42851372019631
H	2.95978145889866	0.45866935516852	2.61095317820979
H	3.10066065348340	1.11002002033183	-0.85185739921480
H	3.73411749398644	1.47640063484731	0.76264833650565
H	3.27704310874304	3.82081988422197	1.07635192062748
H	1.64295851725112	5.72409848053563	1.02262852782158
H	-0.69606918465092	5.28469894369851	0.17965276809986
H	-1.28490220748394	2.96100670283031	-0.53855207118810
H	3.04092489914314	-0.96463537607957	-1.01956181049831
H	3.80588282871752	-1.46419113217197	0.49846340153201
H	3.45989666026235	-3.86340220113395	0.50375305866963
H	-1.29112879244164	-2.97676171079272	-0.39597924666337

Coordinates for the DFT optimized structure of $[Mn^{II}(OH_2)(dpaq^{5NO2})]^+$

	x	y	z
Mn	0.50137963056382	0.76033840171174	0.50797732855214
O	-0.59966961497679	0.46507228921139	4.56183404552647
O	0.78907550102851	1.41444746451083	-1.74951583585498
N	0.30962397859647	-1.39872151661614	0.05925276605542
N	0.02801617198833	-0.09041006891029	2.38283104320003
N	0.46933079254707	2.68570868794988	1.86391353916946
N	-1.63790870787818	1.55172892486923	0.29751214541316
N	2.68463276204891	1.32437393102879	0.79599349438681
C	0.50137339175921	-1.97745996806105	-1.11637157820798
C	0.32063492722293	-3.35546728780375	-1.31602200258678
C	-0.09458074998747	-4.13712742350990	-0.25643762793703
C	-0.32764441573635	-3.55040193861072	1.01998389255816
C	-0.74585178848094	-4.24519789235374	2.20021380940715
N	-1.05500856120812	-5.68301360123887	2.21400473798902

C	-0.88934148853622	-3.56804963644541	3.39920461636666
C	-0.66128730042325	-2.18970503070067	3.50912035635196
C	-0.25401901024130	-1.43670866138169	2.40169017046759
C	-0.08762062286994	-2.13956907990241	1.13977505320397
C	-0.14151557810807	0.72964049718339	3.45694940110691
C	0.40456640098931	2.16092256783159	3.25573099306872
C	-0.72727347563616	3.46701686821606	1.49657538976182
C	-1.90649274741976	2.60252893337126	1.09566977207450
C	-3.21277138912729	2.91662033577089	1.47638846510489
C	-4.26741996610548	2.13046529081657	1.00526815279945
C	-3.98201781640134	1.04929797187339	0.16981335614164
C	-2.64917009541448	0.79392599978743	-0.14846795085921
C	1.72380191648565	3.41555985516915	1.60235368222939
C	2.90434943057689	2.47351497098051	1.46401705559410
C	4.16873252488041	2.79617844823199	1.96246911537441
C	5.23051601830705	1.91183027127782	1.75669182567969
C	4.99414668614487	0.72409217652516	1.06223955540901
C	3.70146454502611	0.47117785567743	0.60675640907598
O	-1.07465043444475	-6.24414016602735	3.29709594244723
O	-1.29533198748516	-6.24110332066354	1.14813536617816
H	0.06918972196310	1.74802976048717	-2.30399628918574
H	0.81036968125606	-1.32606865955093	-1.93856277596438
H	0.50400875399893	-3.79415137180379	-2.29859802732987
H	-0.25422166867676	-5.20498210478308	-0.38557060439722
H	-1.20185309730699	-4.13537935571996	4.27631367689097
H	-0.80444292913006	-1.69041995483995	4.46402405219504
H	1.42602426862258	2.13654067458732	3.66610735997381
H	-0.17808237769097	2.83511629855930	3.90390877283164
H	-0.46815697657727	4.09086926486423	0.62556929552962
H	-1.02610066721693	4.15718884090876	2.30520684189558
H	-3.40014832840056	3.76581451841030	2.13713286151226

H	-5.29687429488364	2.35579632266955	1.29401112445316
H	-4.77161609797427	0.40443324444834	-0.21998042314993
H	-2.37843738274991	-0.05714141304721	-0.77937051788202
H	1.60858237683352	3.95780934770286	0.64918206647649
H	1.93595349475258	4.17597513397304	2.37580610659340
H	4.31678737307580	3.72932109664439	2.51018438478906
H	6.22626170833774	2.14435232354001	2.14190748863716
H	5.78993374602741	-0.00136256174273	0.88361525586186
H	3.46670303284628	-0.45435619100440	0.07445492872301
H	1.61239973520885	1.68828363592788	-2.17814206370181

Coordinates for the DFT optimized structure of $[Mn^{II}(OH_2)(dpaq^{5Cl})]^+$

	x	y	z
Mn	0.43328383932598	0.76126936956302	0.48259809103258
O	-0.16798325067309	0.08103945272459	4.58411338255153
O	0.56621403025412	1.73483067435555	-1.67662947717229
N	-0.33167917208394	-1.20155232424350	-0.21246297040422
N	0.02609670610468	-0.23796981517338	2.28240141931274
N	1.05902551345557	2.41333701580603	2.04239581584777
N	-1.45236394375595	2.05072269210218	0.71638656401118
N	2.70642940818525	0.76847607885077	0.46086185975818
C	-0.45744475356276	-1.62957129285457	-1.45965570843032
C	-0.97862122796555	-2.89593312673565	-1.78457454475748
C	-1.38565071703582	-3.72540633200827	-0.75879196938514
C	-1.27313066826937	-3.30020995230161	0.58906109905917
C	-1.67736384355953	-4.08621888238407	1.70703619861132
Cl	-2.35776884515827	-5.67579032360278	1.45991840724190
C	-1.53386090515997	-3.58854185190552	2.98687088162551
C	-0.98674336715458	-2.30998938816708	3.22390910656022
C	-0.55989049418093	-1.49047861373943	2.17609022318694
C	-0.71976932759435	-1.99817692136374	0.83388095211538

C	0.19238584792927	0.41311083271234	3.45786010907706
C	1.03144850858069	1.70838057449043	3.35547940393844
C	0.06283027692643	3.49768412532301	1.95881369792930
C	-1.33875522225673	3.00023101865844	1.66431382839675
C	-2.46100875043577	3.54414135370049	2.29251367214550
C	-3.73242952462251	3.10106295915669	1.91939216753768
C	-3.84202175108772	2.12145174249643	0.93123916466080
C	-2.67116991047217	1.61952218390649	0.36537247074709
C	2.41422295135582	2.86330541647889	1.67713358378292
C	3.29184226322522	1.71288378174429	1.22187986981414
C	4.65280611214575	1.65709398973360	1.53334004051500
C	5.42537301734711	0.60605499248741	1.03391775441009
C	4.81045834145385	-0.36658755547726	0.24329751882762
C	3.44511954014340	-0.24663088396123	-0.00904246253858
H	-0.13485702712483	2.28950507051271	-2.04722219035402
H	-0.13529987479210	-0.94157532666871	-2.24663283332450
H	-1.05695234352522	-3.20276606129099	-2.82918572752493
H	-1.79893148037219	-4.71426538666626	-0.96456272810688
H	-1.85022597484417	-4.19864049883367	3.83512000289148
H	-0.88910063200765	-1.94594690629308	4.24453493178143
H	2.05970952201741	1.40533766012412	3.60741868462382
H	0.69978135490147	2.38766761163246	4.15691032018406
H	0.35528139010869	4.15964514360044	1.12735749624936
H	0.05526014776835	4.11729866862565	2.87337552145732
H	-2.33815045426212	4.30251727379819	3.06890626751040
H	-4.62355300417539	3.51012274864205	2.40160833449262
H	-4.81317485475940	1.73969637916758	0.61091267724229
H	-2.70907789652800	0.83263537648137	-0.39314637598424
H	2.32355893877176	3.57144141721351	0.83660259180328
H	2.91061132943285	3.41017140581118	2.49948727801325
H	5.09953109436849	2.42917759275339	2.16364711482080

H	6.49110973597885	0.54398883471787	1.26711332139318
H	5.37113866270032	-1.21061376321215	-0.16260527192792
H	2.91780144543811	-0.99667880929197	-0.60498987218309
H	1.33244623950068	1.83367757880377	-2.25915169306649

Coordinates for the DFT optimized structure of $[Mn^{II}(OH_2)(dpaq^{5OMe})]^+$

	x	y	z
Mn	-0.05461455443020	-0.06486951627826	0.00957368481984
O	-0.04905690598084	-0.05903287939118	-2.36030843701589
H	0.04611924229320	0.74634172517958	-2.88808953477810
H	0.01277247788932	-0.80205246010111	-2.97685080691902
O	0.92937425807506	0.48051527145807	4.06019911512923
N	-2.25008299481045	0.05445960205739	0.25226903213882
N	-0.25462646803486	0.14148108946032	2.08020062372738
N	2.21065082661188	-0.04978356783449	0.65765482201721
N	0.57551784541782	2.14047098412478	-0.19817441189965
N	0.62584191247838	-2.23371342124615	-0.14830786816588
C	-3.18757050337926	-0.01350207191087	-0.68237184473986
C	-4.55932138732730	0.12534651671304	-0.40551392364988
C	-4.94774731663516	0.34819004181949	0.90326318086336
C	-3.97420757264169	0.42761962889530	1.92613021570664
C	-4.31498838865816	0.66052386276297	3.29782484823647
C	-3.30074205754856	0.72553191937604	4.23706048461181
C	-1.94387804289216	0.56452710439195	3.87014397637422
C	-1.55230473451941	0.33175192254793	2.55245789724149
C	-2.59689218222736	0.26816479283783	1.56313273259191
C	0.84371301510584	0.22301680262919	2.85956089497102
C	1.55044010005514	-4.81486352456801	0.32712176574607
C	0.19698430303257	-4.58459213994663	0.07426064086780
C	2.16956182825073	-0.13834641771485	2.14664249537128
C	2.79627279973083	1.21561416847116	0.17832897322687

C	1.82674185052328	2.38004775236797	0.23682714365234
C	2.22215759801003	3.65033687587729	0.66106852181342
C	1.29962621950248	4.69908015516162	0.62319616483370
C	0.00614833626410	4.44326854016172	0.16622765059427
C	-0.31113805689809	3.14357582670458	-0.22595777064588
C	2.84016702611722	-1.23152730630042	0.04185615246773
C	1.93326733114934	-2.44627905835381	0.09469837851348
C	2.42913481820844	-3.72905109190761	0.34140659309972
C	-0.21918028715260	-3.27365012822118	-0.15152360293133
H	-2.84172044338666	-0.18256903134542	-1.70668623077486
H	-5.28936361154801	0.05797699356969	-1.21421614048243
H	-6.00050026853722	0.46459808440829	1.16659656038693
H	-3.52832906827781	0.90260330990825	5.28837073571783
H	-1.17268532379167	0.62219362139101	4.63593015725665
H	1.91803668271773	-5.82563842317623	0.52047737837695
H	-0.52843505611701	-5.40032413918896	0.06239433581276
H	2.38359839485111	-1.17787332830215	2.44009856114614
H	2.96493242827570	0.47910959478227	2.59376607295154
H	3.07913509450570	1.07750702240086	-0.87825440029201
H	3.72061921427495	1.47155598174058	0.72663732087056
H	3.23977897825485	3.81345371818891	1.02219044356831
H	1.58678281485328	5.69984174798570	0.95490285514828
H	-0.75063057076735	5.22893367030589	0.12421898606838
H	-1.31876155089323	2.89198251483072	-0.56771424477689
H	3.03373637051532	-1.00039724461430	-1.01880254954463
H	3.81742331715202	-1.47288587176905	0.49852672404597
H	3.49220325350899	-3.87242119059681	0.54753807788545
H	-1.27258193484272	-3.04333252322944	-0.33331709259971
O	-5.64340708819194	0.80032498991626	3.55261370149399
C	-6.05922649590380	1.01674385745427	4.89721089297653
H	-5.76333368276287	0.17627205355935	5.54764983906598

H	-5.64079632519335	1.95499992071323	5.29966925384392
H	-7.15413487827558	1.08878033184340	4.87063219498372

Coordinates for the DFT optimized structure of $[Mn^{II}(OH_2)(dpaq^{2Me})]^+$

	x	y	z
Mn	-0.01927447816826	0.02470431522159	0.01249840430398
O	0.64200384084535	-2.11388374162405	3.56568025252559
N	0.07348838356380	2.06897927092278	0.89125396399948
N	0.21672064745139	-0.39393197425876	2.04714715734276
N	-0.00746997179540	-2.32298303750185	-0.03657793449010
N	2.19696009937090	-0.52154209880846	-0.36690846636803
N	-2.20280865001035	-0.57032480400282	-0.25260593261489
C	-0.03215801190779	3.24791523691324	0.28023104888017
C	0.09575824724520	4.46318318745405	0.99321797519706
C	0.33975041776363	4.43126659497760	2.34935268104817
C	0.45637519157052	3.19254952817080	3.02560590952476
C	0.70976577126697	3.10151788350993	4.41896915734758
C	0.80941996012744	1.85690953112569	5.00469991542250
C	0.66051399073796	0.67086728272304	4.25163146696692
C	0.40469444555588	0.70358462872810	2.87726391619804
C	0.30755312074279	1.99970411194423	2.24556755750814
C	0.33448658369935	-1.67784821907169	2.45872477469064
C	-0.05307962563259	-2.73244533962362	1.39525050443926
C	1.23922706858673	-2.73592841997866	-0.70567899147640
C	2.41972418180361	-1.84990938506712	-0.35897762461882
C	3.68759589458206	-2.37644763369869	-0.10250619671617
C	4.75219620599199	-1.50458393295050	0.13978377180170
C	4.51399423313138	-0.12959052871574	0.12515394307640
C	3.21560027593121	0.31341525539779	-0.12426427254108
C	-1.20957221440196	-2.73537363496282	-0.78263556719692
C	-2.41606921604853	-1.88910468133906	-0.42417322001577

C	-3.69589230373077	-2.43979266988595	-0.31529475583144
C	-4.77751614409706	-1.60374836939881	-0.02860581252362
C	-4.54569831035063	-0.23900495657317	0.15176931029470
C	-3.23812951175974	0.22953632307825	0.03649479899826
C	-0.28538461070258	3.26203076152844	-1.20625608803976
H	0.00148810416622	5.41123676665864	0.46084624333052
H	0.44480324485991	5.36013056468012	2.91675913547643
H	0.82238789277444	4.01762189769202	5.00324911306859
H	1.00540720862455	1.77364961318461	6.07689821626754
H	0.74269567763787	-0.29872146341643	4.73751725012188
H	-1.08422630436730	-3.02829763529678	1.64325230099760
H	0.57396259811535	-3.62184918633070	1.56663163341635
H	1.48813446863681	-3.79055867150583	-0.48999457966896
H	1.07699365144161	-2.65952410600692	-1.79278386799880
H	3.83656147487707	-3.45837519022739	-0.08853255356353
H	5.75120675144801	-1.89608902685563	0.34635055858722
H	5.31211070444378	0.59022444136025	0.31602084238361
H	2.97892380409532	1.38099819741468	-0.12041082009587
H	-1.44637724390763	-3.80500743655121	-0.63623420751134
H	-1.00570692066541	-2.59515055534591	-1.85642980823856
H	-3.83949482565008	-3.51432223816098	-0.44873986346878
H	-5.78549754235380	-2.01543569655583	0.06379329002095
H	-5.35699521330739	0.45164257268180	0.38871614919930
H	-3.00728075635061	1.28713836191158	0.18954516966693
H	-1.18655010546026	2.68152048099377	-1.46303701958684
H	0.56151976310050	2.82068445163623	-1.75680996925726
H	-0.42716639538488	4.28576037975082	-1.57763798010994
O	0.01554031785079	0.05147878513666	-2.40627012880591
H	0.86572509821028	0.19232910368710	-2.84717514683761
H	-0.66240596419768	0.37070610523156	-3.01873260452660

Coordinates for the DFT optimized structure of $[Mn^{II}(OH_2)(PY5)]^{2+}$

	x	y	z
Mn	0.09809792626194	-0.10821106915380	-0.02207160494306
O	-2.60469489475054	-2.23553142947104	-3.13486993821644
O	2.78728382899304	2.42396622010892	-2.83414025560985
O	0.16743880375853	-0.30434278491477	2.26494277538893
H	0.76207494395170	0.16929861305084	2.86560353307411
H	-0.40252991852321	-0.85446892183716	2.82287265393248
N	0.06351214616185	0.07586586617726	-2.21047036325380
N	-2.13886663788162	-0.08670033238904	-0.19546395679651
N	-0.30435721891997	-2.37632605534700	-0.35304995485567
N	2.41529243320912	-0.02733059329234	-0.20363226011174
N	0.39940047043633	2.11798277049140	-0.06311526500901
C	-0.60874831379618	-0.89233563071418	-2.85247341925544
C	-0.16186591676010	-1.38457676020809	-4.08331113671001
H	-0.67873012409410	-2.21116412048117	-4.56745970310152
C	0.98654692611267	-0.83496663097259	-4.64932093201932
H	1.37126293081134	-1.21889325850392	-5.59730686903768
C	1.65591009224309	0.18968968005939	-3.98338009054337
H	2.57658979593829	0.60625548960423	-4.38809620527080
C	1.15547198398576	0.63489929991803	-2.75511048119357
C	-1.79810407698866	-1.61328986239387	-2.15823992605483
C	-3.21480478005210	-1.41567680961303	-4.14947496902323
H	-3.39088122119883	-0.38453517858397	-3.80815602088931
H	-4.17692589815032	-1.88535554905441	-4.39755466787127
H	-2.59585036693776	-1.38540307728600	-5.05830769962678
C	-2.70399106222015	-0.80253544791605	-1.18441720675489
C	-4.09664712940756	-0.94865318729979	-1.25292932230554
H	-4.54631559206072	-1.58116024294001	-2.01391619361518
C	-4.90818155854972	-0.30372164628825	-0.31893078584833
H	-5.99466615900820	-0.41031759045711	-0.36978089499360

C	-4.31119154579215	0.46007514265785	0.68369843776676
H	-4.90188952418149	0.97869235733472	1.44105380115690
C	-2.92262469838215	0.52484107827710	0.70747009261289
H	-2.41297839885647	1.08021798021822	1.49693124119527
C	-1.16947000217537	-2.75290005921622	-1.31389578489508
C	-1.49088618415723	-4.09226047642079	-1.54197569496810
H	-2.19653132277210	-4.35325879908819	-2.32907329772500
C	-0.89178255013406	-5.07231306471220	-0.74589220118381
H	-1.12516322339683	-6.12822956153508	-0.90396307712569
C	0.00425671919049	-4.68316480527868	0.25102437747838
H	0.49529868316911	-5.41435869299700	0.89580621029984
C	0.26348989760273	-3.32399461842473	0.40906530515878
H	0.95654368013688	-2.98006590930764	1.18043510803934
C	1.99527735558927	1.66307166453566	-1.94688411624656
C	2.12553057537812	3.21359033341715	-3.84051080272699
H	2.00135047286943	2.64698299417895	-4.77509006550045
H	2.77731757813547	4.07596054433026	-4.03753475236637
H	1.13796805477401	3.57221219842676	-3.51300326032524
C	2.97503910812313	0.82232705393480	-1.08608046019074
C	4.35877655585504	0.94693697821548	-1.22195239774066
H	4.77055104512057	1.64637507114368	-1.94764767542728
C	5.18702469116632	0.16243098669136	-0.41458951787042
H	6.27382009812294	0.23980690399817	-0.50163124778692
C	4.60799691824170	-0.71657170227161	0.50195405721890
H	5.21685065058284	-1.34738209497814	1.15235455022127
C	3.21817699749069	-0.77409037952328	0.57026102166489
H	2.72651146052590	-1.44745405958752	1.27626463800366
C	1.26627675122397	2.62174208938479	-0.95983247359870
C	1.63132916849141	3.97482943171421	-0.91704223950006
H	2.38187975547175	4.36293765793552	-1.60090239284807
C	1.04910656317686	4.82046805652315	0.02765498668676

H	1.32604869482965	5.87693732698641	0.06308936787438
C	0.12406528468521	4.29355852143748	0.92854138593439
H	-0.35746995650074	4.91305195713037	1.68737014625771
C	-0.15434102574168	2.93391832509509	0.84888600645989
H	-0.84409591842710	2.47383130148136	1.55853154851148

Coordinates for Chapter 7

Coordinates for $[Mn^{IV}(O)(N4py)]^{2+}$

	x	y	z
Mn	0.000000000000	0.000000000000	0.000000000000
O	0.000000000000	0.000000000000	1.661741976868
N	0.020925255957	0.020620979039	-2.120285175849
N	1.996153422665	0.000000000000	-0.324993678296
N	0.113348179204	1.993901244293	-0.325401144778
N	-1.981378793872	0.043028460471	-0.293066827332
N	-0.060891896865	-1.980635829015	-0.292021173088
C	1.104839544261	1.043300992798	-2.282157850432
C	-1.315583325321	0.460219103328	-2.596744199772
C	0.381575955645	-1.338697787557	-2.598711151606
C	2.312453247937	0.508798633141	-1.534984446174
C	3.625468476068	0.559510218090	-1.975138735752
C	4.625761646308	0.061574006339	-1.131201567275
C	4.279366452531	-0.463837088180	0.114079502162
C	2.938282075580	-0.479426649935	0.490003315611
C	0.641625826881	2.279920489023	-1.534792884010
C	0.769695187975	3.587468257818	-1.975152494361
C	0.330898238040	4.615455919384	-1.131601096098
C	-0.215121664441	4.300598631292	0.113167200585
C	-0.310216403618	2.962769223601	0.489201612079
C	-2.381143629921	0.159222554920	-1.576916451385
C	-3.729798945772	0.068018856055	-1.909486889532
C	-4.666344249534	-0.134076581225	-0.895491203607
C	-4.231503428713	-0.239599287270	0.428062589438
C	-2.871686177148	-0.150960510531	0.692270206319
C	0.034442559606	-2.386945000101	-1.575363316159
C	-0.118753195625	-3.730669971524	-1.905500597316
C	-0.359713526780	-4.655552208718	-0.889380793913

C	-0.442670527397	-4.214473446486	0.433823742148
C	-0.292761492060	-2.859602943845	0.695364834871
H	1.334824210095	1.260309174131	-3.333208644041
H	-1.555977436819	-0.002731083782	-3.562613331609
H	-1.300855793304	1.546141090115	-2.766652430881
H	1.464789613272	-1.384107016471	-2.780911641032
H	-0.104089694056	-1.553323083738	-3.559477427232
H	3.859994541053	0.972385420482	-2.956859901261
H	5.669852700739	0.083705786424	-1.450164212464
H	5.034121379234	-0.858835624746	0.795098870990
H	2.601547541661	-0.872937140077	1.449445589760
H	1.196719531651	3.797288624578	-2.956445555475
H	0.414823103846	5.656459224566	-1.450306561144
H	-0.564797757162	5.077512855298	0.794060096050
H	-0.724158956521	2.649842374114	1.448120000751
H	-4.034652137971	0.157079916239	-2.953245091473
H	-5.728384996250	-0.210620482761	-1.137812049469
H	-4.931774795037	-0.397405763872	1.249213385574
H	-2.462219934594	-0.236647536576	1.698535141814
H	-0.046528438796	-4.040847745203	-2.949000560759
H	-0.484000858076	-5.713559566442	-1.129660603126
H	-0.629149944058	-4.905982695921	1.256441946795
H	-0.357940253819	-2.444630082838	1.701021216530

Coordinates for $[Mn^{IV}(O)(N4py)]^{2+}$ with cyclohexane (RC)

	x	y	z
Mn	-0.245661000000	0.438382000000	0.112316000000
O	-0.363405000000	0.834757000000	1.720463000000
N	-0.074863000000	-0.100621000000	-1.933620000000
N	-0.200213000000	-1.574325000000	0.282542000000
N	1.769294000000	0.335899000000	-0.060026000000
N	-0.207379000000	2.288859000000	-0.650019000000
N	-2.200666000000	0.369764000000	-0.318038000000
C	0.978823000000	-1.153598000000	-1.754112000000
C	0.367594000000	1.095701000000	-2.695227000000
C	-1.390331000000	-0.616503000000	-2.391289000000
C	0.413385000000	-2.158937000000	-0.768614000000
C	0.517989000000	-3.537235000000	-0.866775000000
C	-0.048192000000	-4.317770000000	0.148905000000
C	-0.694110000000	-3.695904000000	1.217985000000
C	-0.747858000000	-2.304357000000	1.256195000000

C	2.149659000000	-0.469671000000	-1.074781000000
C	3.485864000000	-0.638977000000	-1.400616000000
C	4.442339000000	0.064290000000	-0.658188000000
C	4.029569000000	0.906298000000	0.374431000000
C	2.668840000000	1.016393000000	0.653009000000
C	-0.006955000000	2.368580000000	-1.982078000000
C	-0.083373000000	3.595438000000	-2.635981000000
C	-0.357755000000	4.744185000000	-1.893542000000
C	-0.550350000000	4.639446000000	-0.513645000000
C	-0.472703000000	3.385577000000	0.076422000000
C	-2.512623000000	-0.049963000000	-1.562380000000
C	-3.829063000000	-0.009662000000	-2.013185000000
C	-4.824867000000	0.461010000000	-1.156964000000
C	-4.480730000000	0.880262000000	0.130611000000
C	-3.148434000000	0.824322000000	0.516004000000
H	1.273992000000	-1.627996000000	-2.698766000000
H	-0.046372000000	1.082245000000	-3.711846000000
H	1.460965000000	1.073122000000	-2.807182000000
H	-1.407250000000	-1.711000000000	-2.291264000000
H	-1.543150000000	-0.401987000000	-3.457136000000
H	1.018615000000	-3.990798000000	-1.722834000000
H	0.011223000000	-5.406695000000	0.097092000000
H	-1.151210000000	-4.275445000000	2.020748000000
H	-1.229369000000	-1.756055000000	2.065767000000
H	3.771094000000	-1.293819000000	-2.224613000000
H	5.503289000000	-0.040048000000	-0.893489000000
H	4.749693000000	1.472490000000	0.965939000000
H	2.282158000000	1.651102000000	1.450243000000
H	0.073027000000	3.641975000000	-3.714720000000
H	-0.423604000000	5.714779000000	-2.389743000000
H	-0.766132000000	5.513775000000	0.101580000000
H	-0.622247000000	3.228060000000	1.144453000000
H	-4.063328000000	-0.344935000000	-3.024518000000
H	-5.862638000000	0.502711000000	-1.494418000000
H	-5.230063000000	1.254409000000	0.829204000000
H	-2.806679000000	1.144350000000	1.500110000000
C	2.098276000000	-0.886049000000	5.880905000000
C	2.807341000000	0.027381000000	4.874423000000
C	3.364010000000	-0.765939000000	3.686593000000
C	2.266920000000	-1.596633000000	3.010135000000
C	1.019558000000	-1.741986000000	5.205755000000
C	1.589044000000	-2.530000000000	4.020355000000
H	1.658123000000	-0.287106000000	6.696620000000

H	2.845281000000	-1.552642000000	6.351421000000
H	3.615821000000	0.590405000000	5.371573000000
H	2.088339000000	0.779308000000	4.498367000000
H	4.165651000000	-1.441090000000	4.039957000000
H	3.833806000000	-0.080223000000	2.963943000000
H	2.680833000000	-2.173312000000	2.164637000000
H	1.508458000000	-0.913464000000	2.588337000000
H	0.207882000000	-1.082978000000	4.844024000000
H	0.561893000000	-2.427985000000	5.939044000000
H	2.330016000000	-3.262360000000	4.392093000000
H	0.795806000000	-3.119422000000	3.532857000000

Coordinates for $[Mn^{IV}(O)(N4py)]^{2+}$ with cyclohexane TS ($^4B_1$)

	x	y	z
Mn	0.000000000000	0.000000000000	0.000000000000
O	0.000000000010	0.000000000098	1.770648789129
N	-0.069403907140	-0.048544702789	-2.083799992200
N	1.983130196365	0.000000000000	-0.400218287346
N	-0.014213480764	1.982544305764	-0.380462594326
N	-2.004562920223	-0.066025247198	-0.185792003106
N	-0.041142297092	-2.003770118739	-0.210317755453
C	0.975114050772	1.004542754827	-2.321633585157
C	-1.441520666513	0.328301596519	-2.518312863948
C	0.314266502031	-1.411520923734	-2.541218856124
C	2.231603147351	0.524830126558	-1.618740838893
C	3.519099423753	0.609213777105	-2.127166777402
C	4.572919534393	0.125522296465	-1.343003042948
C	4.299392249537	-0.436583473651	-0.095343216233
C	2.978448092417	-0.488674122951	0.344005845363
C	0.494452208719	2.250275905703	-1.601629270652
C	0.558103687345	3.544124303440	-2.095835232358
C	0.069410187170	4.583492496305	-1.295007869561
C	-0.476701194211	4.289162340167	-0.045260348769
C	-0.506504524854	2.962810600964	0.380476690654
C	-2.459477836646	0.012699156945	-1.451619069898
C	-3.817136420547	-0.127676475162	-1.732159677476
C	-4.707312064916	-0.332531180853	-0.677745890784
C	-4.216917284353	-0.396064086265	0.629440890417
C	-2.849192251541	-0.265714268128	0.835089662056

C	0.027081298212	-2.444882330446	-1.481649803319
C	-0.097887222465	-3.801696615744	-1.773887936840
C	-0.276921743081	-4.704575770420	-0.725749624914
C	-0.330455191664	-4.227823848729	0.587058873663
C	-0.216039003154	-2.860762893223	0.804968173321
H	1.152429294928	1.192797949970	-3.388753136907
H	-1.696764396171	-0.167254737547	-3.464054991301
H	-1.474258680735	1.409026676087	-2.714688184403
H	1.391738666342	-1.429885336533	-2.756609032055
H	-0.194008391517	-1.659765940248	-3.482155413684
H	3.693065410592	1.033026165269	-3.116928777336
H	5.598829021016	0.177416979989	-1.713543443797
H	5.094394469255	-0.835737800327	0.535701788945
H	2.701911976974	-0.932032776600	1.300309994940
H	0.970344012944	3.734326421084	-3.087532761937
H	0.104213633289	5.613968598220	-1.654447697967
H	-0.879624860425	5.072118433972	0.598467191047
H	-0.935687999321	2.667148066972	1.337002373660
H	-4.165352953853	-0.072216795222	-2.764822940627
H	-5.775468782402	-0.444932891743	-0.875729041500
H	-4.880340380192	-0.555272656263	1.480696980703
H	-2.393185984353	-0.317984293388	1.824384941143
H	-0.050484066275	-4.139078209321	-2.810473231009
H	-0.376556764547	-5.772377590669	-0.932244759544
H	-0.468929045780	-4.902016686695	1.433430552724
H	-0.261517410919	-2.414566135211	1.798994283020
C	0.150489046504	1.679291363685	5.462132466491
C	-0.036450712559	2.581920426507	4.236797879388
C	1.250635230848	2.665457307464	3.407304043958
C	1.786903942903	1.295752902625	3.055284540094
C	0.649368288225	0.283660216163	5.068124725649
C	1.935427854999	0.354546259963	4.232933192186
H	-0.796535883210	1.598649577233	6.022480524784
H	0.880426866901	2.147926125920	6.148606921988
H	-0.355657560982	3.591454033819	4.545155953931
H	-0.847020685025	2.170842082892	3.608050194007
H	2.026253944292	3.195992010229	3.998761465288
H	1.106425933104	3.275733630119	2.500973437426
H	2.654636207444	1.319347925331	2.379462009903
H	0.871329139019	0.687470356634	2.325107092755
H	-0.128947171877	-0.225691490725	4.473187953834
H	0.817611163116	-0.331029453295	5.968297941059
H	2.767368795974	0.720517767721	4.870095120595

H	2.232728760057	-0.651141970446	3.890413186541

Coordinates for $[Mn^{IV}(O)(N4py)]^{2+}$ with cyclohexane TS ($^4E_1$)

	x	y	z
Mn	-0.249593955935	0.087668149765	0.016703044468
O	-0.500627255753	0.176036809606	1.729546959484
N	-0.074056953106	-0.021090968341	-2.090161739311
N	2.028597803727	0.069377709137	-0.388069370421
N	-0.084379106525	2.101940049522	-0.466578457897
N	-0.209738116812	-1.978090023752	-0.167920880938
N	-2.376610050104	-0.107226676878	-0.604434236789
C	3.052848038788	-0.360526792814	0.348832943465
C	4.369233447304	-0.283058068019	-0.106193448561
C	4.609040370237	0.250071958480	-1.373227270047
C	3.528436438370	0.680310795289	-2.150627536114
C	2.251391864245	0.567052537356	-1.614017938139
C	0.988790605015	1.016551091147	-2.325135375307
C	0.515775349431	2.295332896312	-1.660079021762
C	0.712273649576	3.569724595717	-2.173273618450
C	0.268152821669	4.664405697829	-1.423627527179
C	-0.364197944218	4.447940045969	-0.198457360980
C	-0.528171740476	3.139592680420	0.248757557670
C	-0.499025619807	-2.828419968476	0.826205835685
C	-0.643235885983	-4.191411424537	0.598699155893
C	-0.496278914482	-4.669215625164	-0.706011326449
C	-0.200908945583	-3.773605931657	-1.734766329853
C	-0.056730922172	-2.421390201720	-1.431625922398
C	0.340336334215	-1.405693057777	-2.470207499405
C	-1.363268733270	0.354519823074	-2.737737345170
C	-2.536138833695	-0.142017879346	-1.937473411908
C	-3.734436539588	-0.551938073416	-2.517641385753
C	-4.789894931156	-0.922310420806	-1.680913751794
C	-4.612976887540	-0.876997451945	-0.296200001271
C	-3.379260151205	-0.468051557031	0.203163221162
H	2.815234975985	-0.786197805034	1.324962703071
H	5.184744372453	-0.640475096794	0.524168284500
H	5.627375816025	0.322071509220	-1.761247893033
H	3.674463331274	1.085992604699	-3.152779242592
H	1.170558870521	1.168490692401	-3.397152794740
H	1.196935811973	3.703332347492	-3.141208258815
H	0.407912868256	5.679020458546	-1.802410384857

H	-0.733373547724	5.276981199703	0.406580990735
H	-1.030166195834	2.906094861877	1.187875912239
H	-0.618808219905	-2.386970952480	1.816873892201
H	-0.876478540735	-4.859259061394	1.428961238719
H	-0.615418922787	-5.732849958441	-0.923226520026
H	-0.083083552521	-4.114559088657	-2.764524316920
H	-3.835483408460	-0.579782120069	-3.603823285542
H	-5.740169851253	-1.249503963178	-2.108573932014
H	-5.411870827720	-1.162727042452	0.389744750895
H	-3.179620277890	-0.429374198829	1.276179391670
H	-0.074680794439	-1.668796041089	-3.451818150845
H	1.432964083165	-1.437175929960	-2.577709268457
H	-1.390137522917	-0.011422168745	-3.772545774055
H	-1.424492194271	1.450511279537	-2.784422653577
C	0.288871461193	1.156701770473	5.735776369771
C	-0.224911132955	2.205354789280	4.742338192766
C	0.848617690120	2.574442584987	3.712753120068
C	1.427312795078	1.348864376699	3.029020901295
C	0.819364413245	-0.089690506278	5.018250418509
C	1.896248221604	0.267135171420	3.986707037851
H	-0.511701735794	0.875979929132	6.440667146885
H	1.100615254180	1.599164622285	6.342676695100
H	-0.561224682386	3.109915885092	5.275358353483
H	-1.108547364238	1.804836003040	4.212687384341
H	1.683773341518	3.095956896186	4.222214397731
H	0.459429535333	3.288866942715	2.969854440059
H	2.163627504380	1.599384845059	2.249746036752
H	0.529543427342	0.845280349203	2.405416107265
H	-0.015670163140	-0.596745636790	4.501904904372
H	1.223065241389	-0.811366095634	5.747454624715
H	2.799002330508	0.644024801264	4.507823268185
H	2.215533765863	-0.632440602909	3.435227784494

Coordinates for $[Mn^{IV}(O)(N4py)]^{2+}$ with ethylbenzene RC

	x	y	z
Mn	0.195794376448	-0.133857710957	0.010456881679
O	0.419728279265	0.067009423219	1.736441546502
N	-0.119267684747	-0.340834156669	-2.043795638946
N	0.025406253905	-2.134553792450	-0.095655772470
N	2.108554003544	-0.310771363903	-0.610367047968
N	0.240558176898	1.824782364887	-0.454399652690

N	-1.807575491871	0.043414887636	0.045719663997
C	0.826611756486	-1.491369326477	-2.248425835027
C	0.285264695382	0.924645472890	-2.713155159915
C	-1.553263214026	-0.668381026084	-2.266275769191
C	0.353739802702	-2.594558479694	-1.321667547639
C	0.254857408619	-3.938036211805	-1.644748775933
C	-0.216284314129	-4.820004511678	-0.664029518960
C	-0.572733953041	-4.327031833506	0.590023617293
C	-0.433202510702	-2.964694945923	0.844222697125
C	2.183601408626	-1.022766221164	-1.754234932890
C	3.400033822486	-1.287228058101	-2.365704915116
C	4.562741944484	-0.777494336130	-1.775249334097
C	4.464997479391	-0.009676638053	-0.613655357867
C	3.207151218814	0.209444509013	-0.057356259394
C	0.178291916858	2.098172417686	-1.772566383775
C	0.084044554491	3.412370279809	-2.223808633589
C	0.073186086523	4.448402524069	-1.289779942618
C	0.152658369111	4.144062714402	0.071617308939
C	0.228307479263	2.810801333767	0.452849301741
C	-2.414946222912	-0.153875695932	-1.141173213153
C	-3.785653488051	0.047350821569	-1.282751720055
C	-4.530008034408	0.438235050462	-0.169414818764
C	-3.883815972696	0.621383028145	1.055623772465
C	-2.511216193908	0.420233335256	1.121896045605
H	0.871343033458	-1.828537227834	-3.291550849498
H	-0.311919955034	1.091224823620	-3.618665657112
H	1.329769592760	0.838095620440	-3.042268126997
H	-1.667864937281	-1.759761728125	-2.314774810775
H	-1.893961796104	-0.277961589098	-3.233555985374
H	0.524809186492	-4.287079100796	-2.641770280941
H	-0.312211498255	-5.883725500257	-0.887990622509
H	-0.951756908750	-4.984449574089	1.371154217100
H	-0.696817626526	-2.517856388248	1.801546398728
H	3.438368247051	-1.865514340366	-3.289370225546
H	5.535408037348	-0.967851685912	-2.231767874609
H	5.348552357150	0.417517097748	-0.138821685548
H	3.063255567248	0.807547837048	0.841676337050
H	0.022886580280	3.614764809464	-3.294032701591
H	0.000039818385	5.485614526926	-1.622428049931
H	0.146569904376	4.925739758526	0.832035547948
H	0.280131490889	2.496401334405	1.495428749883
H	-4.258312802146	-0.106072091752	-2.253905842785
H	-5.605835954498	0.600652630828	-0.258268044841

H	-4.430600345553	0.925516957694	1.948718085059
H	-1.938328650256	0.556112056270	2.039469535811
C	1.594015889774	-3.658453993516	3.392483076728
C	1.625198965507	-4.996449929142	2.997168711769
C	2.289477364440	-5.375092985829	1.825801724989
C	2.936458413276	-4.399163011052	1.056206133200
C	2.920070282168	-3.066415671601	1.457971154788
C	2.246388055968	-2.659611547507	2.635124135355
C	2.226766334890	-1.240477876019	3.019535490305
C	1.823251263054	-0.845224364911	4.421682561076
H	1.065593180172	-3.386996551169	4.308145294125
H	1.120477591247	-5.750813778650	3.606295672807
H	2.303878044533	-6.422203711180	1.513895018826
H	3.462166790112	-4.683103553021	0.140992413659
H	3.451514286810	-2.320196770101	0.864521171834
H	1.302060888873	-0.628421482136	2.286165657140
H	3.112888923989	-0.701664275294	2.654612187176
H	1.855214480850	0.248970079559	4.538203508148
H	2.499216386926	-1.281263092897	5.180753200990
H	0.799529770570	-1.170620975308	4.668061437276

Coordinates for $[Mn^{IV}(O)(N4py)]^{2+}$ with ethylbenzene TS ($^4B_1$)

Mn	0.000000000000	0.000000000000	0.000000000000
O	0.000000000017	-0.000000000017	1.752004054867
N	-0.050219518651	0.029284259056	-2.087744943365
N	-0.022149360615	-1.978905521743	-0.355694905175
N	1.981233971767	0.000000000000	-0.387406008290
N	-0.030533500555	2.000399640273	-0.227674065906
N	-2.000312081382	0.067138674450	-0.200998809270
C	0.988255642037	-1.036859856752	-2.300346125124
C	0.346616523932	1.386348821318	-2.550370545305
C	-1.421730970781	-0.342828397003	-2.527761483407
C	0.481808402705	-2.268055414102	-1.574272449796
C	0.512719781019	-3.565344530998	-2.059223736635
C	-0.013321409997	-4.583775948895	-1.254406348528
C	-0.550716166163	-4.266835926068	-0.008017037711
C	-0.534314372623	-2.940328708413	0.416432860167
C	2.241264150066	-0.562122881526	-1.586324314972
C	3.537559610267	-0.686277977243	-2.063554391457
C	4.583774453109	-0.192638792885	-1.274813755862
C	4.295390454301	0.421466580427	-0.054933880198

C	2.967770562844	0.505264008113	0.357453077550
C	0.048639936556	2.429079226464	-1.502878414099
C	-0.078120216594	3.781841900596	-1.808793657773
C	-0.270915506678	4.694097791007	-0.771242871381
C	-0.336196543402	4.230358948655	0.545201239978
C	-0.218129897818	2.866281448290	0.777582413626
C	-2.445397652175	-0.015095447871	-1.470516295392
C	-3.799355188354	0.130303096957	-1.762120225417
C	-4.697128867870	0.343051472770	-0.715643043627
C	-4.217252850093	0.408630416241	0.594794384114
C	-2.852334636912	0.272601739629	0.812460483793
H	1.181031442539	-1.241350573983	-3.360918576924
H	-0.146682720968	1.630939483500	-3.499665154317
H	1.426645279642	1.395109090070	-2.751014348417
H	-1.456394515532	-1.424595669594	-2.715314849631
H	-1.668511184683	0.144511016115	-3.479461659414
H	0.923790119628	-3.775513456516	-3.046951519000
H	-0.010156945441	-5.615732031121	-1.609257747302
H	-0.976443788522	-5.033539096447	0.637694336081
H	-0.940856271097	-2.628052101588	1.377074464560
H	3.725703603753	-1.144672429430	-3.034902727276
H	5.614974171113	-0.274951383790	-1.622055302984
H	5.084601121113	0.832885883113	0.574757480962
H	2.676723998216	0.980814178142	1.293313878984
H	-0.023032679362	4.109938409897	-2.847736144627
H	-0.372569450825	5.758942757592	-0.989383731705
H	-0.486298259197	4.911955474635	1.383168245487
H	-0.271634540234	2.430060503942	1.775257052138
H	-4.139996112615	0.072217667471	-2.796854987491
H	-5.762798543903	0.458892734428	-0.922063225776
H	-4.886957105260	0.572570216252	1.439606243661
H	-2.404784365407	0.325056603721	1.805210152439
C	1.212281280603	-3.833592311188	3.106420074213
C	1.380367367261	-5.109859280908	2.567561536585
C	2.205016917861	-5.307556864081	1.455084473574
C	2.873445432734	-4.212622887035	0.891502457456
C	2.719585058704	-2.941576179194	1.438005430521
C	1.883039718713	-2.717162635780	2.558209239040
C	1.722294020772	-1.358542619111	3.097106836604
C	1.126941988259	-1.158988765316	4.472171675244
H	0.560223273103	-3.703840412855	3.972065190734
H	0.857391761845	-5.958190664545	3.016643282088
H	2.326959604751	-6.306569902191	1.029599171159

H	3.523596206854	-4.354944275840	0.024520506572
H	3.267680169395	-2.101841172802	1.006849667166
H	0.854036216846	-0.710479967939	2.326609345037
H	2.607957408280	-0.733822496665	2.912638881954
H	1.071357631140	-0.087039647616	4.716496775779
H	1.733965886825	-1.648673908333	5.256375987221
H	0.105035289449	-1.564866640168	4.546736157195

Coordinates for $[Mn^{IV}(O)N4py)]^{2+}$ with ethylbenzene TS ($^4E_1$)

	x	y	z
Mn	0.126441880294	-0.184600673258	0.055238997476
N	0.042842928201	-0.080368134098	-2.063185291889
N	2.150864187859	-0.016342885922	-0.431723800342
N	0.017601775729	2.033581438622	-0.417267816215
N	0.040983678461	-2.331575417688	-0.488961707145
N	-1.948170070432	-0.272665004640	-0.181993076856
O	0.208841847032	-0.270798786037	1.763487176242
C	3.186729376098	-0.468548351884	0.280579003226
C	4.489770825528	-0.364738698993	-0.197971734395
C	4.705136878694	0.237622791620	-1.437056415610
C	3.612992446475	0.705001907049	-2.176231381168
C	2.342710297481	0.549977604543	-1.641062102773
C	1.059260695754	1.001661230205	-2.310723631904
C	0.580524970197	2.261671764922	-1.613654718831
C	0.728954139241	3.544397340668	-2.127949178376
C	0.254824522274	4.617799596483	-1.365830101736
C	-0.359144187550	4.367923005978	-0.137072388551
C	-0.460888992068	3.048527341006	0.303261511109
C	-0.268612563969	-3.322051918201	0.355271805878
C	-0.615806900341	-4.591579523342	-0.097928904656
C	-0.654271197032	-4.820283506186	-1.475233675820
C	-0.336865407935	-3.778827242170	-2.349919466244
C	0.013953102723	-2.540791142100	-1.815845906865
C	0.453726022276	-1.380456516105	-2.666375367987
C	-1.345320592109	0.289468582324	-2.470516160929
C	-2.363380367205	-0.169326927792	-1.460688662463
C	-3.690325335253	-0.418634445123	-1.803126929172
C	-4.593657779949	-0.768724999960	-0.798275862881
C	-4.146929303907	-0.864051679224	0.521776618933
C	-2.806080900495	-0.613694902685	0.788517980755
H	2.957921421001	-0.929774609288	1.241180641296

H	5.316805870304	-0.746551998977	0.399995340241
H	5.717172838437	0.338679763076	-1.834034676011
H	3.744648851426	1.167728966932	-3.155008267393
H	1.209321974722	1.175702835443	-3.384352960143
H	1.193526296193	3.700284841463	-3.102554840550
H	0.353968679387	5.639654664319	-1.737956306031
H	-0.755574893814	5.178621957239	0.475759182543
H	-0.939401651988	2.797253981185	1.251402322701
H	-0.239393632937	-3.083657939547	1.420537616226
H	-0.860507258115	-5.377823240127	0.617811374259
H	-0.935310150085	-5.799932648452	-1.867972543495
H	-0.360687693353	-3.920617013870	-3.431661982199
H	-4.006146306663	-0.339177257933	-2.844477625587
H	-5.637895776891	-0.970372885530	-1.046320906429
H	-4.821015419923	-1.137447689308	1.334594783085
H	-2.392981990825	-0.687978141026	1.795911625154
H	0.070568972382	-1.461121772640	-3.692061986590
H	1.549907825694	-1.405882296864	-2.732621615954
H	-1.569560373744	-0.115322887702	-3.465866024282
H	-1.416230349652	1.381931314037	-2.554980360790
C	4.071648998734	1.406579770613	2.960771395345
C	5.332400971682	1.632612375404	2.406166080698
C	5.470721456950	2.440720441411	1.272696279496
C	4.336868117181	3.029462076809	0.699515600905
C	3.080225229776	2.812469585519	1.260540347570
C	2.921595068960	1.998484447755	2.403091333335
C	1.559075602653	1.775285204851	2.968943121336
C	1.444036158178	1.309204204837	4.410158888561
H	3.983900205235	0.768147366656	3.841603381113
H	6.213350677745	1.169383888190	2.857728388551
H	6.457526393205	2.607808369515	0.833875581424
H	4.435686413313	3.661778733708	-0.186223591159
H	2.204426800127	3.291993339244	0.819794515551
H	1.046381555430	0.946004628978	2.338440122383
H	0.919489283606	2.650452961664	2.778156086521
H	0.385039138067	1.215014171235	4.695278223759
H	1.918322064506	2.028602482279	5.099621128801
H	1.918154124468	0.328071041070	4.569373333396